ISSN-e 2594-0317

JOURNAL *of the* MEXICAN CHEMICAL SOCIETY

(J. Mex. Chem. Soc.)
Former Revista de la Sociedad Química de México (Rev. Soc. Quím. Mex.)

Regular Issue

J. Mex. Chem. Soc.
Volume 68
Issue 2
April-June
Year 2024

Quarterly publication
www.jmcs.org.mx
Mexico City

ISSN-e 2594-0317

JOURNAL *of the* MEXICAN CHEMICAL SOCIETY

(J. Mex. Chem. Soc.)
Former Revista de la Sociedad Química de México (Rev. Soc. Quím. Mex.)

Regular Issue

J. Mex. Chem. Soc.
Volume 68
Issue 2
April-June
Year 2024

Quarterly publication
www.jmcs.org.mx
Mexico City

J. Mex. Chem. Soc. **2024**, *68(2)*
Regular Issue

ISSN-e 2594-0317

The *Sociedad Química de México* was founded in 1956 as a non-profit association to promote the development of the professionals and students of chemistry in education, research, services and industry, and for the diffusion of chemical knowledge. The *Sociedad Química de México* organizes annually the *Mexican Congress of Chemistry* and the *National Congress of Chemical Education*, both congresses include activities of current interest for professionals and students of the chemical sciences. It grants annually the "*Andrés Manuel del Río*" *National Award of Chemistry* in the Academic area (field of research and field of education) and in the Technological area (field of technological development). It also grants each year the *Rafael Illescas Frisbie Best Bachelor, Master and Doctoral Thesis in Chemical Sciences Awards* and the biennial *Award of the Sociedad Química de México in honor of the Doctor Mario J. Molina, directed to the professionals in Chemistry Sciences*.

The *Journal of the Mexican Chemical Society* (*J. Mex. Chem. Soc*) is the official journal of the *Sociedad Química de México*, it was published as *Revista de la Sociedad Química de México* (*Rev. Soc. Quím. Mex.*) from 1957 to 2003, changing its name in 2004. The Journal of the Mexican Chemical Society (J. Mex. Chem. Soc.) is a scientific, blind, peer reviewed, and open access, free of charge publication that covers all areas of chemistry and its sub-disciplines (i.e. medicinal chemistry, natural products, electrochemistry, material science, computational chemistry, organic chemistry, bioinorganic chemistry, etc). It is devoted to facilitating the worldwide advancement of our understanding of chemistry. It will primarily publish original contributions of research in all branches of the theory and practice of chemistry in its broadest context as well as critical reviews in active areas of chemical research where the author has published significant contributions. The J. Mex. Chem. Soc. is a quarterly publication in which language of submission and publication is English. To be suitable for publication in J. Mex. Chem. Soc., manuscripts must describe novel aspects of chemistry, high quality of results and discussion an excellent bibliographic support, and contribute to the development of the field. Routine or incremental works are not suitable for publication in J. Mex. Chem. Soc. Authors are encouraged to send contributions in electronic form. Our online submission system guides you stepwise through the process of entering your article details and uploading your files. The *Sociedad Química de México* also publishes since 2007 articles of general interest in the *Boletín de la Sociedad Química de México*.

La *Sociedad Química de México* fue fundada en 1956 como una agrupación sin fines de lucro para promover el desarrollo de los profesionales y estudiantes de la química en las áreas educativa, investigación, servicios e industria, y para difundir el conocimiento de la química. La *Sociedad Química de México* organiza anualmente el *Congreso Mexicano de Química* y el *Congreso Nacional de Educación Química*, en los cuales se desarrollan diversas actividades de interés para los profesionales y estudiantes de las ciencias químicas. Asimismo, otorga anualmente el *Premio Nacional de Química "Andrés Manuel del Río"* en el área Académica (campos de docencia e investigación) y en el área Tecnológica (campo de Desarrollo Tecnológico). También otorga anualmente el *Premio a las Mejores Tesis de Licenciatura, Maestría y Doctorado en Ciencias Químicas, Rafael Illescas Frisbie*. De manera bienal otorga el *Premio de la Sociedad Química de México en Honor al Doctor Mario J. Molina, dirigido a los profesionistas de las Ciencias Químicas*.

El *Journal of the Mexican Chemical Society* (*J. Mex. Chem. Soc.*), es la revista oficial de la *Sociedad Química de México*. Desde 1957 y hasta 2003 fue publicada como *Revista de la Sociedad Química de México* (*Rev. Soc. Quím. Mex.*), cambiando su nombre en 2004. Es una publicación trimestral que tiene como objetivo coadyuvar al avance del entendimiento de la química; las instrucciones para los autores aparecen en cada fascículo. La *Sociedad Química de México* también publica desde 2007 artículos de interés general en el *Boletín de la Sociedad Química de México*

Journal of the Mexican Chemical Society
(*J. Mex. Chem. Soc.*)

ISSN-e: 2594-0317
ISSN 1870-249X

former

Revista de la Sociedad Química de México
(*Rev. Soc. Quím. Mex.*) ISSN 0583-7693

Journal of the Mexican Chemical Society (*J. Mex. Chem. Soc.*)
Quarterly publication.
Editor-in-Chief: Prof. Alberto Vela Amieva

Indexed Journal

Certificate of reserved rights granted by the Instituto Nacional del Derecho de Autor (INDAUTOR): 04-2005-052710530600-102
Certificate of lawful title and content: Under procedure
Postal registration of printed matter deposited by editors or agents granted by SEPOMEX: IM09-0312

The Figures/schemes quality and the general contents of this publication are full responsability of the authors.

Edited and distributed by Sociedad Química de México, A.C.
Barranca del Muerto 26, Col. Crédito Constructor,
Del. Benito Juárez, C.P. 03940, Mexico City.
Phone: +5255 56626837; +5255 56626823
Contact: soquimex@sqm.org.mx
https://www.sqm.org.mx

Editorial assistance: jmcs@sqm.org.mx
https://www.jmcs.org.mx

J. Mex. Chem. Soc. **2024**, *68(2)*
Regular Issue

ISSN-e 2594-0317

Table of Contents

Articles

* The asterisk indicates the name of the author to whom inquiries about the paper should be addressed.

J. Mex. Chem. Soc. **2024**, *68(2)*
Regular Issue

ISSN-e 2594-0317

Table of Contents

Articles

* The asterisk indicates the name of the author to whom inquiries about the paper should be addressed.

J. Mex. Chem. Soc. **2024**, *68(2)*
Regular Issue

ISSN-e 2594-0317

Table of Contents

Articles

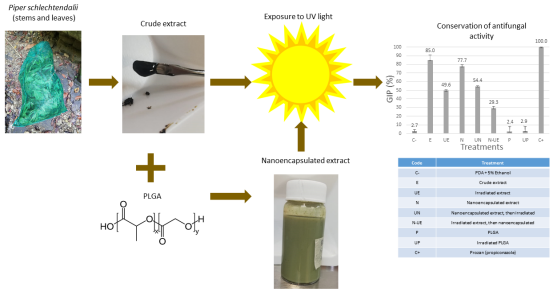

* The asterisk indicates the name of the author to whom inquiries about the paper should be addressed.

Article

J. Mex. Chem. Soc. **2024**, *68*(2)
Regular Issue

ISSN-e 2594-0317

Experimental and Numerical Comparison of Dispersion and Sorption of Cr(VI) on Maize Cane Biomass

María de Jesús Marín-Allende[1,2], Elizabeth Teresita Romero-Guzmán[1*], Carlos Enrique Alvarado-Rodríguez[3], Lázaro Raymundo Reyes-Gutiérrez[4]

[1]Instituto Nacional de Investigaciones Nucleares, Departamento de Química, Gerencia de Ciencias Básicas; Carretera México-Toluca, S/N. La Marquesa Ocoyoacác, Estado de México, México. ZP 52750.
[2]Universidad Autónoma del Estado de México, Paseo Colón y Paseo Tollocan S/N. C.P. 50000. Toluca, México.
[3]Universidad de Guanajuato, División de Ciencias Naturales y Exactas. Noria Alta S/N C. P. 36050.
[4]Universidad Autónoma Metropolitana, Unidad Lerma. Av. de las Garzas 10, Col. El Panteón, Lerma de Villada, Municipio de Lerma, Estado de México, México. Z. P. 52005.

***Corresponding author:** Elizabeth Teresita Romero-Guzmán, email: elizabeth.romero@inin.gob.mx; Phone: 5253297200 ext 12279; Fax: +52 55 53297301.

Received August 26th, 2022; Accepted May 9th, 2023.

DOI: http://dx.doi.org/10.29356/jmcs.v68i2.1859

Abstract. Computational and theoretical modelling has become an important tool for the characterization, development, and validation of packed beds. Relevant breakthrough curves would provide much valuable information on designing a fixed bed adsorption process in field applications. In this study, the hydrodynamic properties involved in the Navier–Stokes flow equation, such as velocity, pressure, and permeability, in a packed bed were investigated. Experiments in natural porous media such as maize cane biomass for determining the sorption of Cr(VI) are compared with numerical simulations. The relevant ordinary partial equations were solved in COMSOL Multiphysics Software friendly and efficiently. The close agreement between the experimental and numerical results suggests that the theoretical model of advection-hydrodynamic dispersion can be used to model the transport of Cr(VI) in unsaturated porous media composed of maize cane biomass.
Keywords: Numerical simulation; hydrodynamic dispersion; sorption; porous media.

Resumen. El modelado computacional y teórico se ha convertido en una herramienta importante para la caracterización, desarrollo y validación de lechos empacados. Las curvas de avance relevantes proporcionarían información muy valiosa sobre el diseño de un proceso de adsorción de lecho fijo en aplicaciones de campo. En este estudio, se investigaron las propiedades hidrodinámicas involucradas en la ecuación de flujo de Navier-Stokes, como la velocidad, la presión y la permeabilidad, en un lecho empacado. Los experimentos en medios porosos naturales como la biomasa de caña de maíz para determinar la sorción de Cr(VI) se comparan con simulaciones numéricas. Las ecuaciones parciales ordinarias relevantes se resolvieron en COMSOL Multiphysics Software de manera amigable y eficiente. La estrecha concordancia entre los resultados experimentales y numéricos sugiere que el modelo teórico de dispersión hidrodinámica por advección puede usarse para modelar el transporte de Cr(VI) en medios porosos no saturados compuesta por biomasa de caña de maíz.
Palabras clave: Simulación numérica; dispersión hidrodinámica; sorción; medios porosos.

J. Mex. Chem. Soc. **2024**, *68*(2)
Regular Issue

ISSN-e 2594-0317

Introduction

Heavy metal ions ubiquitous in the environment but their increased levels in water are consequences of man–made activities. One of the most toxic metal ions in our environment that has raised global concern is chromium [1].

Chromium contamination of soil and groundwater is a significant problem worldwide and is becoming a serious threat to our environment. The predominant forms of chromium in nature are Cr(III) (trivalent chromium) and Cr(VI) (hexavalent chromium) as chromate ion, which have different physicochemical characteristics including mobility, toxicity and bioavailability [2]. The Cr(VI) is 10 – 100 times more toxic that the Cr(III) when both are introduced by oral ingestion [3]. The World Health Organization (WHO) reported that chromium is a priority pollutant and proposed a provisional guideline value of 0.05 mg L^{-1} for total chromium, mainly soluble Cr(VI), in drinking water [4,5].

A variety of methods and materials have been developed for the Cr(VI) removal including precipitation, membrane separation, or solvent extraction, neutralization and adsorption [6,7]. Among these techniques, biosorption using agricultural waste such as maize cane, has gained considerable attention because of high efficiency, low cost, more availability, and ease of handling [1,8]. These materials have been reported to possess good adsorption capability for Cr(VI) from aqueous system. The use of these waste material as adsorbent also reduces the cost of the Cr(VI) treatment process and makes the application of adsorption technology. The physicochemical and surface characteristics of this biomass and sorption properties, that make it a candidate to absorb Cr(VI) are reported by Marin-Allende et al., 2017 [9].

The computational fluid dynamics (CFD) is a useful tool for the modelling of flow and contaminant transport (hydrodynamics system). The main advantage of computational modelling may be that different physical domains can be coupled and solved efficiently. In fixed beds column, in general, several modes of transport and processes take place simultaneously. For instance, fluid flow, permeation, advection, hydrodynamic dispersion, diffusion, and the chemical reactions involved in adsorption. The CFD simulations can be applied by manually written codes or commercial software programs. Some commercial packages, such as COMSOL Multiphysics (Femlab, formerly COMSOL [10], Inc., Sweden) has become popular for various physics and engineering applications, geoenvironmental phenomena, or multiphysics in last decades since commercial packages are designed to be user friendly. The purpose of these programs is to allow researchers who may not be well versed in fluid dynamics to successfully model the channel fluid flow phenomena in an interdisciplinary field such as column adsorption [11].

The main objective in this research is to evaluate the behaviour of the Cr(VI) sorption in natural porous media such as maize cane biomass through the experimental and simulated breakthrough curves.

Experimental

The work model consists of a cylindrical container in three dimensions (3D), using porous biomass of maize cane as a fixed bed column. The column of internal diameter 0.5 cm and length 15 cm with a cross-sectional area of 0.78 cm^2, is installed in a vertical position. In order to obtain homogeneous porous packaging, the column was placed in a vertical position. The filling of the column with material granular sorbent (biomass), is poured into the column partially by layers of 3 cm, by adding water to prevent the formation of air bubbles and lightly shaking the column to ensure a good compaction. Tests are conducted under a continuous flux of dissolved solute [40 mg L^{-1} of Cr(VI) solution] as an influent for the sorption studies. The flow is described by the average linear velocity or seepage velocity (v=q/n), which transports the dissolved solute by advection-dispersion. The solute continuously moves down the column at seepage velocity v. Solute samples were collected at the outlet of the column in glass tubes.

Numerical Solution using COMSOL software

COMSOL software (COMSOL [10] Multiphysics program, Version 3.5ª) was used as a numerical software package to solving sets of ordinary and/or partial differential equations for modelling predicting and

J. Mex. Chem. Soc. **2024**, *68*(2)
Regular Issue

ISSN-e 2594-0317

optimizing the performance of water treatment process, adsorption, operations, flow behaviour, etc. The numerical solution by COMSOL software is performed based on the finite element method. The software runs the finite elements analysis together using adaptive meshing refinement and error control by a variety of numerical solvers.

The simulation is performed assuming the biomass is as porous and permeable material, and saturated, with a high surface area for capture of retention of Cr(VI) as polluting potential. The velocity field into the cylindrical container was obtained by solving the Navier Stokes and continuity equations. The speed of the porous media was obtained by solving the Brinkman and continuity equations. The dispersion, convection and sorption of biomass were obtained by solving the transport equation. The equations were solved by the finite element method. The COMSOL Multiphysics post processing was used to analyze the simulation results. The analysis is performed by the generation of images of the process and its animation.

Generating of the geometry

The experimental device (Fig. 1) consists of the following elements:

The geometry is based on the experimental device used in the laboratory, in which the biomass is packed in a cylindrical container with the dimensions indicates in Fig. 1.

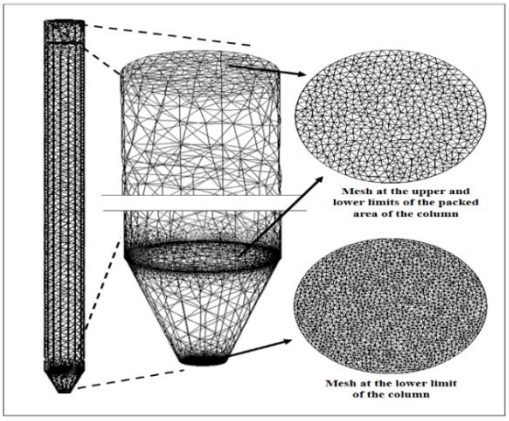

Fig. 1. Mesh for the simulation.

The system is divided into three zones; Zone 1 is the feed injection zone, in this area there is no biomass and the feed flow is constant. In zone 2 the biomass is present, in this zone the interaction between the biomass and Cr(VI) solution occurs, this is considered a saturated porous system. In zone 3, there is no biomass here; it is when the Cr(VI) concentration value in the eluates is measured, to determine the concentrations of Cr(VI) sorbed in the biomass, Fig. 2.

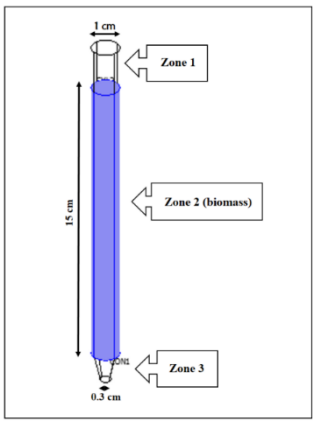

Fig. 2. Geometry, dimensions, and zone subdomains used for the simulation.

J. Mex. Chem. Soc. **2024**, *68*(2)
Regular Issue

ISSN-e 2594-0317

The flow in the interstitial access from the biomass is calculated by solving the equation governing the water flow and continuity which is written in the form:

$$\rho \frac{\boldsymbol{Dv}}{\boldsymbol{D}t} = -\boldsymbol{\nabla} p + \mu \boldsymbol{\nabla}^2 \boldsymbol{v} + \rho \mathbf{g} \tag{1}$$

$$\frac{\partial \rho}{\partial t} = -(\boldsymbol{\nabla} \cdot \rho \boldsymbol{v}) \tag{2}$$

where ρ in the density [M L^{-3}], v is the velocity [L t^{-1}], t is the time [t], p is the pressure [M $L^{-1}t^{-2}$], μ is the viscosity [M $L^{-1}t^{-1}$] and g is the gravity [L t^{-2}]. The equation used for the free flow in this simulation is obtained from equation (1), which is written as follows:

$$\left(-\boldsymbol{\nabla} \cdot \mu(\boldsymbol{\nabla v} + (\boldsymbol{\nabla v})^T)\right) + \rho \boldsymbol{v} \cdot \boldsymbol{\nabla v} + \boldsymbol{\nabla} p = 0 \tag{3}$$

where the density is considered constant and in the steady state equation the time dependent terms are eliminated [12]. For the flow through the biomass (porous system), the Brinkman and the modified continuity equations for the porous systems are:

$$-\boldsymbol{\nabla} p - \frac{\mu}{k} \boldsymbol{v} + \mu \boldsymbol{\nabla}^2 \boldsymbol{v} + \rho \mathbf{g} = 0 \tag{4}$$

$$\varepsilon \frac{\partial p}{\partial t} = -(\boldsymbol{\nabla} \cdot \rho \boldsymbol{v}) \tag{5}$$

where k is the permeability [L t^{-1}], ε is the porosity (the ratio between porous volume and total container volume). The equation used for the porous media flow in this simulation is obtained from equation 4, which is written as follows:

$$\left(-\boldsymbol{\nabla} \cdot \frac{\mu}{\varepsilon}(\boldsymbol{\nabla v} + (\boldsymbol{\nabla v})^T)\right) - \left(\frac{\mu}{k} \boldsymbol{v} + \boldsymbol{\nabla} p\right) = 0 \tag{6}$$

where the density is considered constant and for steady state equation the time dependent terms has been eliminated. The steady state equations (2, 3, 5 and 6) are solved according with the experimental methodology. Cr(VI) transport and its sorption through the biomass are calculated by solving the transport equations. The Freundlich isotherm solution is written as follow:

$$\varepsilon \frac{\partial \mathrm{c}}{\partial t} + \rho_b \frac{\partial c_p}{\partial c} \frac{\partial c}{\partial t} + \boldsymbol{\nabla} \cdot [-\varepsilon D_L \boldsymbol{\nabla} \mathrm{c} + \boldsymbol{v} \mathrm{c}] = \mathrm{R_L} + \mathrm{R_p} + \mathrm{S_c} \tag{7}$$

$$c_p = K_F c^N \quad , \quad \frac{\partial c_p}{\partial c} = N K_F c^{N-1} \tag{8}$$

where ε is the porosity, c is the solute concentration [M L^{-3}], t is the time [t], ρ_b is the density of the porous medium [M L^{-3}], cp is the concentration of the solute sorbed in the biomass (the mass amount of solute sorbed per unit of biomass), v is the velocity [L t^{-1}], D_L is the hydrodynamic dispersion tensor, KF and N are constants of Freunlich isotherms (COMSOL 2008). The equation used for flow and transport in porous medium in this simulation is obtained from equation (7), which is written as follows:

$$\varepsilon \frac{\partial \mathrm{c}}{\partial t} + \rho_b \frac{\partial c_p}{\partial c} \frac{\partial c}{\partial t} + \boldsymbol{\nabla} \cdot [-\varepsilon D_L \boldsymbol{\nabla} \mathrm{c} + \boldsymbol{v} \mathrm{c}] = 0 \tag{9}$$

where the reaction terms are removed if there are no chemical reaction.

J. Mex. Chem. Soc. **2024**, *68*(2)
Regular Issue

ISSN-e 2594-0317

Constants

The values of the constants were obtained according with the results from the physicochemical characterization of the biomass and the interaction between the Cr(VI) as a solute-biomass to determine the sorption rate, Table 1.

Table 1. Values of the constants obtained by experimental procedures [5].

Constants		Value
ρ_s	Biomass density	0.072 kg m^{-3}
ε	Porosity	0.76%
k_s	Permeability	1.4e^{-4} m s^{-1}
K_F	Freundlich constant	0.907 mg g^{-1}
N	Freundlich isotherms exponent	2.015
α1	Longitudinal dispersivity	0.03 m
α2	x Transversal dispersivity	0.005 m
α3	y Transversal dispersivity	0.005 m
C_{in}	Feed concentration	0.04 kg m^{-3}
V_{max}	Feed velocity	0.45 mL min^{-1}

Definition of initial and boundary conditions

The initial and boundary conditions are the follow: for t = 0, c = 0 and cp=0 and the boundary conditions are shown in Fig. 3, where r=sqrt(x^2+y^2+z^2), R is the radius of the cylinder, Fig. 2, v is the velocity, n is a unit vector normal to the plane, N is the total flux of Cr(VI), V_{max} is the feed velocity (Table 1), Uchns is the velocity calculated by the Navier Stokes equation, Cin is the initial concentration of Cr(VI) (Table 1), p is the pressure, c is the Cr(VI) concentration in the solution, cp is the solute concentration sorbed in the biomass, z is the coordinate in the xyz plane and t is the time.

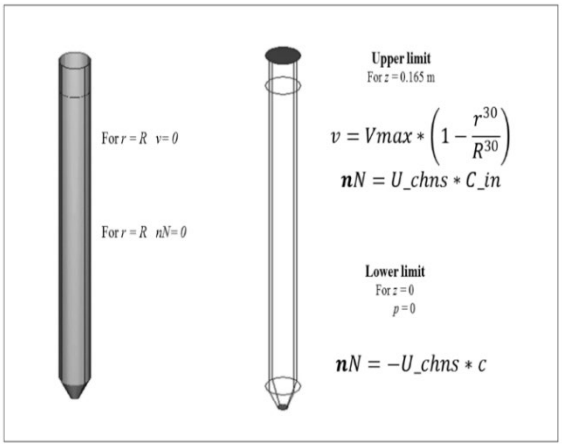

Fig. 3. Initial and boundary conditions for the Cr(VI) sorption simulation.

J. Mex. Chem. Soc. **2024**, *68*(2)
Regular Issue

ISSN-e 2594-0317

Mesh and running solution

The quality of the mesh plays a significant role to achieve accurate results without unnecessary computational demand. The cell shape and cell size have an important effect on the accuracy and stability of the numerical solution. The very fine meshes can obtain more accurate results of solution but will cost higher computer memory and central processing unit time [11]. The mesh elements are prism and we use for the Navier-Stokes equation a total of 34,393 elements (Fig. 1). The finite element method is one of the most popular mathematical techniques used in decades, and it is employed in popular modeling software is commonly used to solve partial differential equations in systems possessing complex geometries [13].

Results and discussion

The Reynolds number value is 23, which were obtained by solving the fluid flow equations. The values indicate that the flow is in the laminar regime, as also reported by Basak, 1977 [14]. In Fig. 4 we present the velocity field at the entrance of the system and in the region occupied by the biomass that is represented as a porous system. The velocity field is deviates when the Cr(VI) solution gets in contact with the biomass because the porosity change and the permeability is modified.

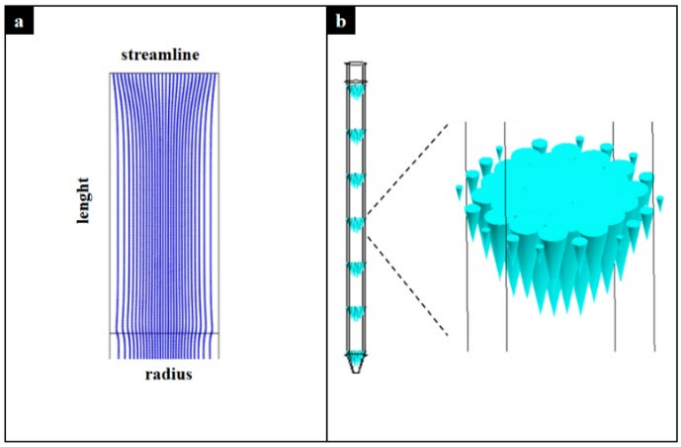

Fig. 4. Flow lines simulation on column.

The input and output speed is shown in Fig. 5. The results indicate that the velocity is greater in the center and zero on the walls. In the first case (Fig. 5**(a)**), the velocity field is uniform; the Cr(VI) solution is injected at a constant rate around the entire surface.

Fig. 5**(b)** shows speed values larger than the maximum speed entry value due to the decrease in the cross-sectional area, as well as a more uniform profile. The multiple core measurement at the outlet column permitted an estimation of the velocity fluctuations. Due to different steady state infiltration rates, the water content distribution in the non-living biomass column varied with depth. In the central region, the velocity is greater than near the walls, this behaviour is correlated with Fig. 4 that indicates that in the core the velocity is greater and so the Cr(VI) sorption is probably lower due of the lower Cr(VI)-biomass interaction time. On the other hands, on the walls, the biomass has more interaction time with the solute, because the velocity of interaction is lower, or the interstitial water is saturating the pores.

J. Mex. Chem. Soc. **2024**, *68*(2)
Regular Issue

ISSN-e 2594-0317

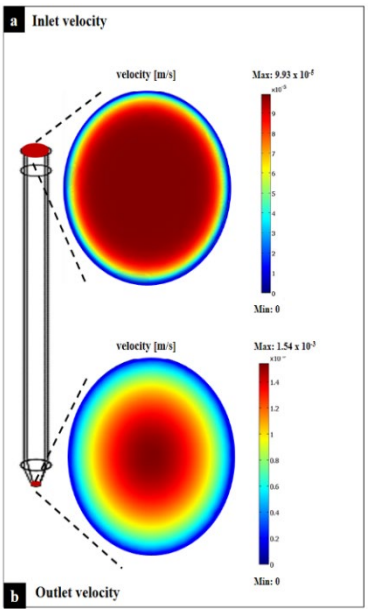

Fig. 5. Input and output velocity field.

The velocity field of the porous biomass is shows in Fig. 6. These results indicate that the pores of the biomass were saturated by the Cr(VI) solution, and then the fluid velocity diminishes through the biomass column, causing that the outlet velocity also decreases. Thus, higher values are obtained at the fluid outlet due of the pressure difference between the input and output of the porous medium.

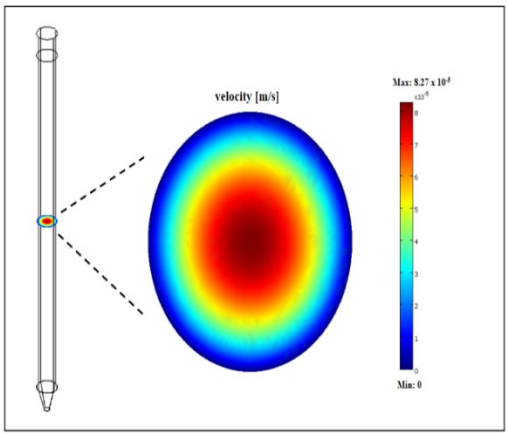

Fig. 6. Cr(VI) solution; velocities in biomass.

Solving the transport equation using the velocity field obtained previously, it was simulated the Cr(VI) transport system and its sorption onto maize cane biomass. Fig. 7 shows the biomass saturation time evolution during the Cr(VI) solution transport through the system at 5, 30, 60, 90 and 125 minutes. In the same Fig. 7 it was observed that the Cr(VI) concentration is not present at the bottom of the column, but it increases when it is transporting through the maize cane biomass. At 60 minutes is observed the Cr(VI) transport, the Cr(VI) is sorbed on the biomass, in the upper of the biomass column; the system is getting saturated depending upon the

J. Mex. Chem. Soc. **2024**, *68*(2)
Regular Issue

ISSN-e 2594-0317

Cr(VI) concentration transport. The Cr(VI) concentration in the solution increases because the biomass is reaching its Cr(VI) saturation or the Cr(VI) concentration in the solution decreases through the biomass because it is sorbed by the biomass. Finally, at 125 minutes the biomass reaches its Cr(VI) saturation, the concentration is constant; the biomass is saturated and already does not sorbs Cr(VI) from solution.

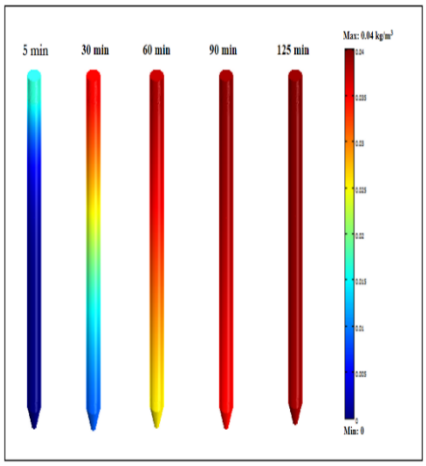

Fig. 7. Transport of the chromium (VI) solution in biomass, through the time, (kg m^{-3}).

Various mathematical models have been developed to predict the dynamic behaviour of sorption column studies [15, 16]. In this case, the experimental and simulated breakthrough curves for Cr(VI) sorption are shown in Fig. 8. Comparison between experimental and simulated breakthrough curves showed good agreement of predicted software COMSOL values, which indicates that the chosen models are suitable for explain the Cr(VI) sorption during the interaction between the biomass and the Cr(VI) solution.

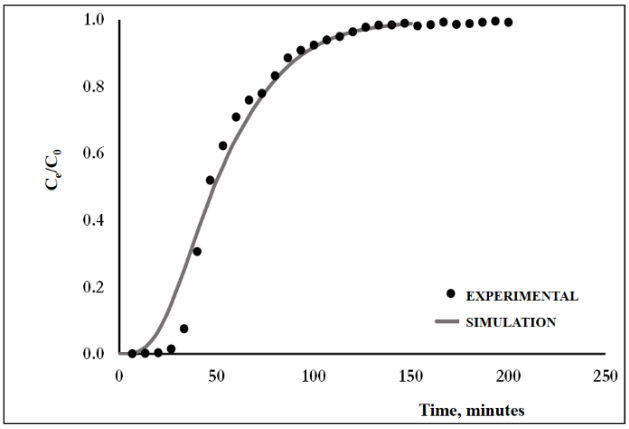

Fig. 8. Experimental and predicted breakthrough curves of Cr(VI) sorption in a fixed column of biomass (*maize cane*) in vertical flux.

According to breakthrough curves obtained with maize cane biomass, the point of rupture and saturation in the vertical flow for experimental and simulated system are given in Table 2. This indicates a greater capacity of sorption in vertical flow and that the COMSOL simulation is able to represent the dynamic conditions observed in a biomass-column test for Cr(VI).

J. Mex. Chem. Soc. **2024**, *68*(2)
Regular Issue

ISSN-e 2594-0317

Table 2. Breakthrough and saturation points of process sorption in maize cane biomass.

Biomass	Process	Procedure	Breakthrough point, minutes	Saturation point, minutes
Maize cane	Sorption	Experimental	12	125
		Simulated	27	125

Conclusions

Model the transport of Cr(VI) in unsaturated porous media composed of maize cane biomass enhances our understanding of the fundamental physical behaviour of hydrodynamic flows and mass transfer in the channels of packed beds. Performing computational modelling reduces the time needed to design and develop adsorption systems because many physical parameters can be tested theoretically prior to the device fabrication. Data obtained from simulations can be used to validate experimental data, thereby providing a theoretical explanation of the performance of a system. Cr(VI) concentration measurements as obtained from experiments during the solute-biomass interaction were used for the simulation of the hydrodynamic dispersion. COMSOL software was proved to be an effective numerical tool to describe the transport and adsorption phenomena of the Cr(VI) adsorption in fixed bed column. Good agreement between the experimental results and the predicted theoretical breakthrough curves was observed. The computational fluid dynamics prediction can be used for analysing the experimental study of the Cr(VI) sorption process in packed bed.

Acknowledgements

The authors want to thank to Dr. Jaime Lázaro Klapp Escribano, for his help.

References

1. Asuquo, E.D.; Martin, A. D. *J. Environ. Chem. Eng.* **2016**, *4*, 4207-4228.
2. Economou-Eliopoulos, M.; Frei, R.; Atsarou, C. *Catena.* **2014***, 122*, 216-228.
3. Polowczyk, I.; Urbano, B. F.; Rivas, B. L.; Bryjak, M.; Kabay, N. *Chem. Eng. J*. **2016***, 284,* 395-404.
4. Wang, S.; Choi, J. H. *Applied Mathematical Modelling.* **2013***, 37*, 102-111.
5. Owalude, S. O.; Tella, A. C. *J. Basic Appl. Sci*. **2016***, 5*, 377-388.
6. Usman, L. U.; Bharat, K. A.; Nakshatra, B. S.; Sushmita, B. *J. Mol. Liq*. **2022***, 354*, 118833.
7. Kavitha, B.; Deepa, R.; Sivakumar, S. *Materials Today Sustainability*. **2022***, 18,* 100124.
8. Ullah, I.; Nedeem, R.; Iqbal, M.; Manzoor, Q. *Ecological Engineering.* **2013***, 60*, 99-107.
9. Marín-Allende, M. J.; Romero-Guzmán, E. T.; Ramírez-García, J. J.; Reyes-Gutiérrez, L. R. *Part. Sci. Technol.* **2016***, 35*, 704–711.
10. COMSOL, Earth Science Module User's Guide, ©1998–2008 by COMSOL AB.
11. Esfandian, H.; Samady-Maybodi, A.; Khoshandam, B.; Parvini, M. *J. Taiwan Inst. Chem. Eng.* **2017***, 75*, 164-173.
12. Bird, R. B.; Stewart, W. E.; Lightfoot, E. N., in: *Fenómenos de transporte*. Editorial reverte, España, **2003**, 4-29.
13. Qian, W.; Wu, J.; Yang, L.; Lin, X.; Chen, Y.; Chen X. *Chem. Eng. J.* **2012**, *197*, 424-434.
14. Basak, P. *J. Irrig. Drain. Div., Am. Soc. Civ. Eng*. **1977**, *103*, 459.
15. Volesky, B. *Hydrometallurgy*. **2003***, 71*, 179-190.
16. Naja, G. Volesky, B. *Environ. Sci. Technol.* **2006**, *40*, 3996-4003.

Article

J. Mex. Chem. Soc. **2024**, *68*(2)
Regular Issue

ISSN-e 2594-0317

Evaluation of Photosensitizing Ability of Antioxidants Used in Skincare Products

Irene Lagunes, Ángel Trigos*

Centro de Investigación en Micología Aplicada (CIMA). Universidad Veracruzana. Calle Médicos 5, Col. Unidad del Bosque. C.P. 91010. Xalapa, Veracruz, México.

***Corresponding author:** Ángel Trigos, email: atrigos@uv.mx

Received December 9th, 2022; Accepted May 11th, 2023.

DOI: http://dx.doi.org/10.29356/jmcs.v68i2.1925

Abstract. Singlet oxygen generation is possible by photosensitizer molecules able to absorb energy from light and transfer it to molecular oxygen. Singlet oxygen is able to react with components of cellular membranes such as cholesterol leading to peroxidation products implicated in photoaging. In order to prevent oxidative damage caused by reactive oxygen species, skincare products enriched with antioxidants have been developed; in spite of some pro-oxidant effects associated with antioxidants has been reported. Based on this data, the photosensitizing ability of 14 antioxidants commonly used in skincare products was evaluated through the photo-oxidation of ergosterol, using ergosterol as oxidizable substrate to quench singlet oxygen. Singlet oxygen indirectly detection was performed through ^{1}H-NMR mixtures analysis by ergosterol peroxide detection. The results revealed that fisetin, retinol, cyanidin and hesperetin they acted as photosensitizer antioxidants in generation of singlet oxygen. Conversely, caffeic acid, luteolin, rutin, vanillic acid, ascorbic acid, apigenin, epigallocatechin gallate, rosmarinic acid, myricetin and kaempferol were not able to generate singlet oxygen through a photosensitized mechanism. Our results allow us to suggest that the incorporation of antioxidants in skincare products as anti-aging treatments should be supported by their evaluation against photosensitizing ability in order to increase their safety.
Keywords: Antioxidants; singlet oxygen; photosensitizing ability; photo-oxidation of ergosterol.

Resumen. La generación del oxígeno singulete es posible a través de moléculas fotosensibilizadoras capaces de absorber energía proveniente de la luz y transferirla al oxígeno molecular. El oxígeno singulete es capaz de reaccionar con componentes de membranas celulares como el colesterol formando productos de peroxidación implicados en el foto-envejecimiento. Para prevenir el daño oxidativo causado por especies reactivas del oxígeno, se han desarrollado productos para el cuidado de la piel enriquecidos con antioxidantes, a pesar de que han sido reportados algunos efectos prooxidantes asociados a los antioxidantes. Con base en lo anterior, se evaluó la capacidad fotosensibilizadora de 14 antioxidantes comúnmente utilizados en productos para el cuidado de la piel mediante la foto-oxidación de ergosterol, utilizando ergosterol como sustrato oxidable para atrapar oxígeno singulete. La detección indirecta del oxígeno singulete se realizó mediante análisis de mezclas de RMN-^{1}H a través de la detección de peróxido de ergosterol. Los resultados mostraron que fisetina, retinol, cianidina y hesperetina actuaron como antioxidantes fotosensibilizadores en la generación de oxígeno singulete. Por el contrario, ácido cafeico, luteolina, rutina, ácido vainillínico, ácido ascórbico, apigenina, galato de epigalocatequina, ácido rosmarínico, miricetina y kaempferol no fueron capaces de generar oxígeno singulete mediante mecanismos fotosensibilizados. Los resultados permiten sugerir que la incorporación de antioxidantes en productos para el cuidado de la piel como tratamiento anti-envejecimiento debe respaldarse con la evaluación de la capacidad fotosensibilizadora para incrementar su seguridad.
Palabras clave: Antioxidantes; oxígeno singulete; capacidad fotosensibilizadora; foto-oxidación de ergosterol.

J. Mex. Chem. Soc. **2024**, *68*(2)
Regular Issue

ISSN-e 2594-0317

Introduction

Constant exposure to solar radiation entails negative skin effects induced by reactive oxygen species (ROS) formation as singlet oxygen ($^1O_2$). $^1O_2$ is the first excited state of molecular oxygen ($^3O_2$) and can be endogenously generated in biological systems through photochemical reactions type II, where UVA/UVB radiation as well as visible light can convert photosensitizer molecules into excited states that transfers absorbed energy to $^3O_2$ to generate $^1O_2$ [1,2]. Of the total solar energy able to reach the earth´s surface, 6.8 % corresponds to UV light, 38.9 % to visible light and 54.3 % to near infrared light [3]. Likewise, from UV light, more than 50 % of UVA can penetrate the dermis, whereas only 14 % of UVB light reaches the epidermis, thereby photochemical generation of $^1O_2$ in the skin is possible due to the presence of endogenous photosensitizer molecules such as porphyrins, bilirubin, B_6 vitamers and vitamin K [2,4]. $^1O_2$ is the predominant ROS from type II reactions that is able to react with nucleic acids, unsaturated lipids and aminoacids to yield endoperoxides from [2 + 4] cycloadditions, dioxetanes from [2 + 2] cycloadditions and hydroperoxides from "ene" reactions [5,6].

In recent years due to multiple benefits attributed to natural antioxidants, the cosmetic and dermatology industry has focused on the development of skincare products such as anti-aging creams or sunscreens enriched with antioxidants in order to prevent oxidative damage caused by ROS [7–9]. In this sense, the term antioxidant has been defined as any substance that delays, prevents or removes oxidative damage to a target molecule [10]. Antioxidants can react by depleting molecular oxygen or decreasing its local concentration, removing pro-oxidative metal ions, trapping aggressive reactive oxygen species such as superoxide anion radical or hydrogen peroxide, scavenging chain-initiating radicals like hydroxyl (HO•), alkoxyl (RO•) or peroxyl (ROO•), breaking the chain of a radical sequence or quenching $^1O_2$ [11]. However, increasingly researches have reported pro-oxidant activities of antioxidants such as resveratrol and quercetin [12–14]. Likewise, we previously reported the photosensitizing ability to generate $^1O_2$ of curcumin, resveratrol and quercetin identified through the photo-oxidation of ergosterol method [15]. Also, through this method, the photosensitizing ability of cosmetic colorants to generate $^1O_2$ and the membrane cell damage caused by two of the nine cosmetic colourants evaluated has been reported [16,17]. Furthermore, we recently reported on the pro-oxidant effect of five synthetic hydroxycoumarin-based antioxidants by acting as photosensitizers in $^1O_2$ generation [18]. Therefore, the present study was aimed to determine whether natural antioxidants commonly used in the development of skincare products are able to generate $^1O_2$ by acting as photosensitizing molecules in the photo-oxidation of ergosterol reactions.

Experimental

Reagents

Fisetin, retinol, cyanidin, hesperetin, luteolin, rutin, L-ascorbic acid, apigenin, epigallocatechin gallate, myricetin, kaempferol, ergosterol, eosin yellowish, sodium azide (NaN_3) were purchased from Sigma-Aldrich (Corp., St. Louis, Mo., U.S.A.). Caffeic acid, vanillic acid and rosmarinic acid were kindly provided by Prof. Zaira Domínguez from the Universidad Veracruzana. Distilled ethanol, analytical grade was employed as a solvent in photo-oxidation reactions.

Photo-oxidation of ergosterol

Ergosterol was used as $^1O_2$ chemical trap in the determination of the photosensitizing ability through reactions of the photo-oxidation of ergosterol. 14 antioxidants were tested: Fisetin (**1**), retinol (**2**), cyanidin (**3**), hesperetin (**4**), caffeic acid (**5**), luteolin (**6**), rutin (**7**), vanillic acid (**8**), ascorbic acid (**9**), apigenin (**10**), epigallocatechin gallate (**11**), rosmarinic acid (**12**), myricetin (**13**) and kaempferol (**14**) (Fig. 1). For each reaction, 1 mM ergosterol and 144 μM antioxidant (initial concentration) was prepared in ethanol [15]. The solution was placed inside a photo-oxidation camera and irradiated (four compact fluorescent lamps) during 2 h under continuous oxygen flux (medicinal grade oxygen, flux rate: 75 mL/s), bubbled using a stainless-steel filter (10 μm HPLC filter). The light intensity was 19623 ±129 lux (YK-10LX light meter). The temperature inside the photo-oxidation camera was 32 °C ± 2. In order to establish reference controls, the photo-oxidation reaction by adding

J. Mex. Chem. Soc. **2024**, *68*(2)
Regular Issue

ISSN-e 2594-0317

eosin yellowish 144 μM was established as positive control (+) and the reaction without a photosensitizer dye as negative control (−). Sodium azide (1 mM) was used to confirm $^1O_2$ generation in photo-oxidation reactions.

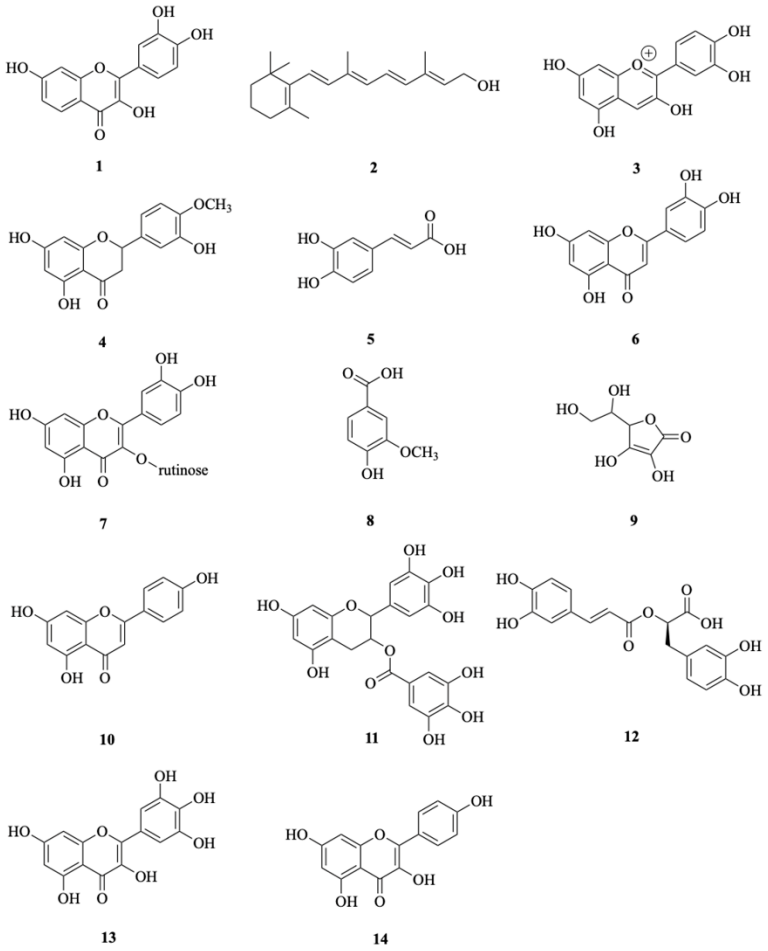

Fig. 1. Tested antioxidants through photo-oxidation of ergosterol.

Determination of singlet oxygen by nuclear magnetic resonance

Indirect detection of $^1O_2$ generation was made by proton Nuclear Magnetic Resonance (^{1}H-NMR) recorded on a Bruker Avance HD III spectrometer (500 MHz) and Agilent DD2 500 MHz spectrometer for NaN_3 reactions, using $CDCl_3$ as solvent and TMS as an internal reference. Ergosterol traps $^1O_2$ to form ergosterol peroxide. Both sterols were detected by ^{1}H-NMR mixtures analysis based on the comparison of integrals of vinyl signals of H-6 and H-7 protons of ring B of ergosterol ($\delta_{H\text{-}6}$= 5.57 ppm, dd, 1H; $\delta_{H\text{-}7}$= 5.38 ppm, dd) and ergosterol peroxide ($\delta_{H\text{-}6}$= 6.50 ppm, d, 1H; $\delta_{H\text{-}7}$= 6.25 ppm, d). Once these signals were identified, integration values were obtained from which the conversion ratio of ergosterol into ergosterol peroxide (E:EP) was calculated. This ratio was also calculated for the positive and negative controls.

Antioxidants classification was established taking into reference the E:EP conversion ratio from the negative control. Therefore, antioxidants used in photo-oxidation reactions where the ratio conversion E:EP was higher than the negative control were considered as photosensitizer antioxidants in the generation of $^1O_2$. Conversely, antioxidants used in photo-oxidation reactions where the ratio conversion E:EP was lower than the negative control were considered as antioxidant quenchers of $^1O_2$. MestReNova software (v6.0.2-5475) was used in ^{1}H-NMR analysis and data processing.

J. Mex. Chem. Soc. **2024**, *68*(2)
Regular Issue

ISSN-e 2594-0317

Results and discussion

$^1O_2$ generation was quantified by ^{1}H-NMR mixtures analysis through the identification of ergosterol peroxide (**EP**), an oxidation product of ergosterol (**E**) formed through a Diels-Alder reaction between $^1O_2$ and a conjugate diene system of B ring of ergosterol. Indirect detection of $^1O_2$ through photo-oxidation of ergosterol reactions allowed us to establish the photosensitizing ability of four out of fourteen screened antioxidants: fisetin (**1**), retinol (**2**), cyanidin (**3**), hesperetin (**4**). Thereby, two double signals at 6.50 and 6.25 ppm attributed to H-6 and H-7 protons from **EP** were identified in the ^{1}H-NMR spectra, also two double-double signals attributed to H-6 and H-7 protons from **E** were observed at 5.57 and 5.38 ppm, respectively (Fig. 2). The E:EP conversion ratio was calculated from integration data of this signals and was also expressed as a percentage. Thus, the results obtained from photo-oxidation reactions carried out with **1** and **2** converted 20 % of **E** into **EP** and **3** and **4** allowed a 9 % of EP formation (Table 1). This suggests that fisetin, retinol, cyanidin and hesperetin were able to generate $^1O_2$ through a photosensitized mechanism because the **EP** quantity detected was higher than negative control (5 %).

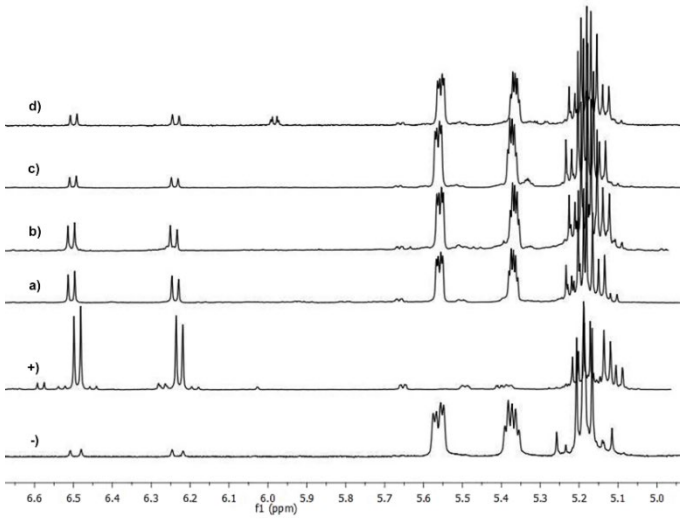

Fig. 2. ^{1}H-NMR spectra of mixtures reaction obtained from photo-oxidation reactions carried out with **(a)** fisetin, **(b)** retinol, **(c)** cyanidin and **(d)** hesperetin. Control (−): reaction without photosensitizer, Control (+): reaction with eosin yellowish as photosensitizer.

Table 1. Conversion ratio of Ergosterol into Ergosterol peroxide (E:PE) calculated from ^{1}H-NMR-signals assignment of H-6 and H-7.

Antioxidant	**Ergosterol**		**Ergosterol peroxide**		**Conversion E:EP**	
	∫ H-6	∫ H-7	∫ H-6	∫ H-7	Ratio	EP Percentage
Control (−)	18H	18H	1H	1H	18:1	5
Control (+)	NS	NS	1H	1H	0:1	100
Fisetin	4H	4H	1H	1H	4:1	**20**
Retinol	4H	4H	1H	1H	4:1	**20**

J. Mex. Chem. Soc. **2024**, *68*(2)
Regular Issue

ISSN-e 2594-0317

Cyanidin	10H	10H	1H	1H	10:1	**9**
Hesperetin	10H	10H	1H	1H	10:1	**9**
Caffeic acid	177H	181H	1H	1H	179:1	1
Luteolin	146H	151H	1H	1H	148:1	1
Rutin	129H	138H	1H	1H	133:1	1
Vanillic acid	191H	203H	1H	1H	133:1	1
Ascorbic acid	76H	77H	1H	1H	76:1	1
Apigenin	62H	64H	1H	1H	63:1	2
Epigallocatequin gallato	51H	52H	1H	1H	52:1	2
Rosmarinic acid	42H	44H	1H	1H	43:1	2
Myricetin	26H	26H	1H	1H	26:1	4
Kaempferol	20H	20H	1H	1H	20:1	5

∫: integration values; NS: no signal detected.

Additionally, in order to confirm the presence of $^1O_2$, photo-oxidation of ergosterol reactions with fisetin, retinol, cyanidin and hesperetin were carried out adding sodium azide (1 mM) as specific quencher of $^1O_2$. After the reaction time, a substantial reduction in the quantity of **EP** generated during photo-oxidation reactions was observed (Fig. 3).

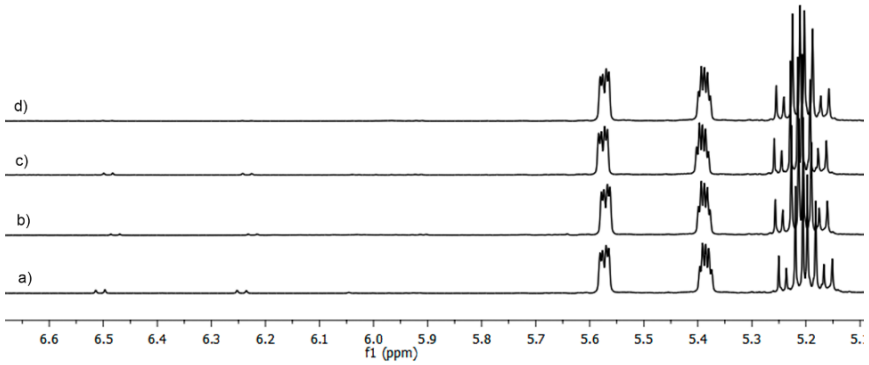

Fig. 3. ^{1}H-NMR spectra of mixtures reaction carried out with **(a)** fisetin, **(b)** retinol, **(c)** cyanidin, **(d)** hesperetin plus NaN_3 (1 mM).

On the other hand, signals attributed to **EP** were barely detected in the ^{1}H-NMR spectra of the remaining antioxidants tested, while signals corresponding to **E** were clearly visible (Fig. 4). Thus, the E:EP conversion ratios obtained were lower than negative control in photo-oxidation reactions carried out with caffeic acid (**5**), luteolin (**6**), rutin (**7**), vanillic acid (**8**) and ascorbic acid (**9**), in which only a 1 % of **EP** was formed. In a similar way, the E:EP conversion ratios in photo-oxidation reactions carried out with apigenin (**10**), epigallocatechin gallate (**11**) and rosmarinic acid (**12**) allowed the formation of 2 % of **EP**. Finally E:EP conversion ratios similar to the 5 % of **EP** detected in the negative control were obtained in photo-oxidation reactions carried out with myricetin (**13**) and

J. Mex. Chem. Soc. **2024**, *68*(2)
Regular Issue

ISSN-e 2594-0317

kaempferol (**14**)(Table 1). Therefore, because of the **EP** quantity detected in photo-oxidation reactions was ≤ 5 % (negative control), we can assume that they were not able to generate $^1O_2$ through a photosensitized mechanism thereby they were considered as antioxidants able to quench $^1O_2$.

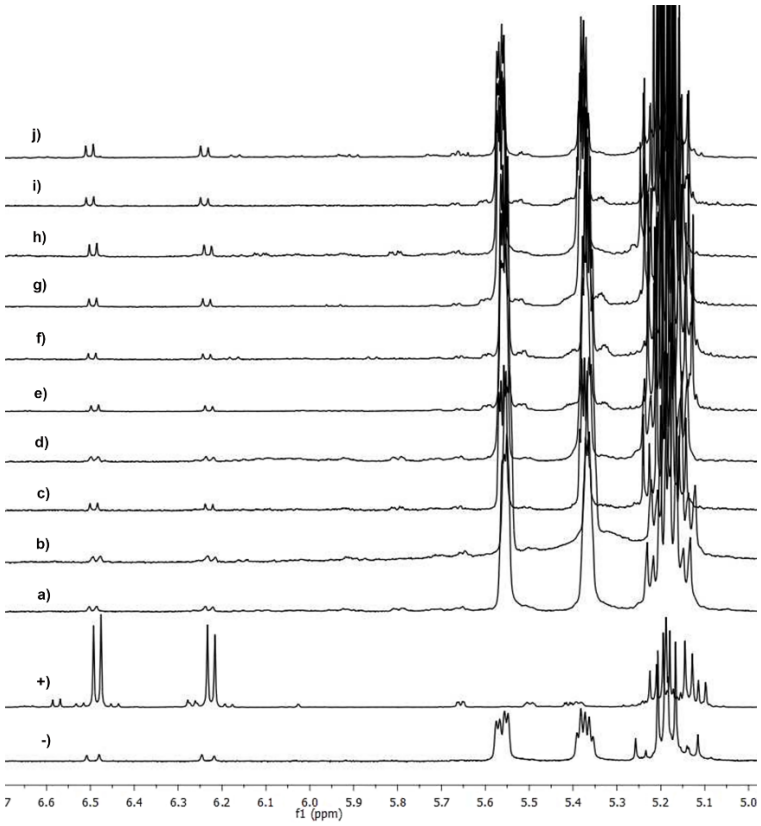

Fig. 4. ^{1}H-NMR spectra of mixtures reaction obtained from photo-oxidation reactions carried out with **(a)** caffeic acid, **(b)** luteolin, **(c)** rutin, **(d)** vanillic acid, **(e)** ascorbic acid, **(f)** apigenin, **(g)** epigallocatechin gallate, **(h)** rosmarinic acid, **(i)** myricetin, **(j)** kaempferol. Control (−): reaction without photosensitizer, Control (+): reaction with eosin yellowish as photosensitizer.

Identification of compounds with the ability to photosensitize the generation of $^1O_2$ should be considered an important issue owing to the fact that the presence of $^1O_2$ in cells is related to skin photoaging. Cholesterol peroxidation can be caused through ene-reaction between $^1O_2$ and the cholesterol double bond in carbons 5 and 6 to form cholesterol 5α-hydroperoxide, as the major product and cholesterol 6α/β-hydroperoxide as the minor products [19]. The significance of cholesterol peroxidation products in photoaging has been clearly established because a mixture of cholesterol 5-hydroperoxide and cholesterol 7-hydroperoxide induces the activation of matrix metalloproteinase-9 (MMP-9), a protein implicated in collagen degradation. Loss of collagen in the skin results in wrinkles appearing and sagging skin, a hallmark associated with skin photoaging [20]. Several researches have shown the efficient antioxidant, anti-inflammatory and anti-aging activity of fisetin [21,22], retinol [23], cyanidin [24] and hesperetin [25], however our results show that under specific conditions they are able to act as photosensitizer compounds in photochemical reactions and stimulate the generation of $^1O_2$. Hence, the evaluation of the photosensitizing ability of compounds used in skincare formulations should be considered an important issue by the dermatology and cosmetic industry.

Concerning antioxidants that show ability to quench $^1O_2$, several researches have reported, not only on their anti-inflammatory, anti-aging and free radical scavenging properties but also their ability to provide a

J. Mex. Chem. Soc. **2024**, *68*(2)
Regular Issue

ISSN-e 2594-0317

protector effect against UVA/UVB-induced skin damage [26–30]. Likewise, no phototoxic effect has been reported on caffeic acid and rutin [31]. Therefore, the ability to quench $^1O_2$ added to all the beneficial properties reported for caffeic acid, luteolin, rutin, vanillic acid, ascorbic acid, apigenin, epigallocatechin gallate, rosmarinic acid, myricetin and kaempferol, allow us to suggest that they could be considered as promising compounds to diminish, prevent or avoid skin photoaging caused by $^1O_2$.

Through the photo-oxidation of ergosterol, the photosensitizing ability of antioxidant compounds was evidenced. Thus, fisetin, retinol, hesperetin and cyanidin aside from their antioxidant activity could show a pro-oxidant effect caused by $^1O_2$. Moreover, the identification of antioxidant compounds with the ability to quench $^1O_2$, was seen to be possible because they provided protection to ergosterol against oxidation caused by $^1O_2$. Consequently, the results obtained allow us to increase the antioxidant classification based on their activity against $^1O_2$ as we previously proposed [15]. Therefore, we suggest that caffeic acid, luteolin, rutin, vanillic acid, ascorbic acid, apigenin, epigallocatechin gallate, rosmarinic acid, myricetin and kaempferol can be classified as type 1 antioxidants: antioxidant quenchers of $^1O_2$; and fisetin, retinol, hesperetin and cyanidin as type 2 antioxidants: photosensitizer antioxidants in generation of $^1O_2$.

Conclusions

Antioxidants provide several health benefits. However, the endogenous generation of $^1O_2$ through photosensitized mechanisms joined to non-photosensitized mechanisms could increase the presence of $^1O_2$ in an organism, which can cause damage to cell membrane components and induce skin photoaging. Hence the incorporation of antioxidants in skincare products as anti-aging treatments or sunscreens should be supported by a previous evaluation of their photosensitizing ability in order to increase their safety.

Acknowledgements

This work has been supported by the Consejo Nacional de Ciencia y Tecnología (Project: 181820). I. Lagunes the PhD scholarships granted under #340331. The authors would like to thank M.C. Israel Bonilla from Clúster Científico y Tecnológico Biomimic, INECOL Campus III and G. A. Vásquez-Reyes from the Instituto de Química Aplicada, Universidad Veracruzana for the NMR experiments performed.

References

1. Onyango, A. N. *Oxid. Med. Cell. Longev.* **2016**, *2016*, 1–22. DOI: https://doi.org/10.1155/2016/2398573.
2. Miyamoto, S.; Martinez, G. R.; Medeiros, M. H. G.; Di, P. *J. Photochem. Photobiol. B.* **2014**, *139*, 24–33. DOI: https://doi.org/10.1016/j.jphotobiol.2014.03.028.
3. Akhalaya, M. Y.; Maksimov, G. V.; Rubin, A. B.; Lademann, J.; Darvin, M. E. *Ageing Res. Rev.* **2014**, *16*, 1–11. DOI: https://doi.org/10.1016/j.arr.2014.03.006.
4. Calori, I. R.; Gusmão, L. A.; Tedesco, A. C. *J. Photochem. Photobiol.* **2021**, *7*, 100041. DOI: https://doi.org/10.1016/j.jpap.2021.100041.
5. Baptista, M. S.; Cadet, J.; Di Mascio, P.; Ghogare, A. A.; Greer, A.; Hamblin, M. R.; Lorente, C.; Nunez, S. C.; Ribeiro, M. S.; Thomas, A. H.; Vignoni, M.; Yoshimura, T. M. *Photochem. Photobiol.* **2017**, *93*, 912–919. DOI: https://doi.org/10.1111/php.12716.
6. Lorente, C.; Serrano, M. P.; Vignoni, M.; Dántola, M. L.; Thomas, A. H. *J. Photochem. Photobiol.* **2021**, *7*, 100045. DOI: https://doi.org/10.1016/J.JPAP.2021.100045.
7. Freitas, J. V.; Praça, F. S. G.; Bentley, M. V. L. B.; Gaspar, L. R. *Int. J. Pharm.* **2015**, *484*, 131–137. DOI: https://doi.org/10.1016/j.ijpharm.2015.02.062.

J. Mex. Chem. Soc. **2024**, *68*(2)
Regular Issue

ISSN-e 2594-0317

8. Pentek, T.; Newenhouse, E.; O'Brien, B.; Singh Chauhan, A. *Molecules.* **2017**, *22*, 1–16. DOI: https://doi.org/10.3390/molecules22010137.
9. Hoang, H. T.; Moon, J. Y.; Lee, Y. C. *Cosmetics.* **2021**, *8*, 106. DOI: https://doi.org/10.3390/COSMETICS8040106.
10. Halliwell, B.; Gutteridge, J. M. C. *Free Radicals in Biology and Medicine*, Illustrate.; Halliwell, B., Gutteridge, J. M. C., Eds.; Oxford University Press: New York, **2015**.
11. Pisoschi, A. M.; Pop, A. *Eur. J. Med. Chem.* **2015**, *97*, 55–74. DOI: https://doi.org/10.1016/j.ejmech.2015.04.040.
12. Fahlman, B. M.; Krol, E. S. *J. Photochem. Photobiol. B.* **2009**, *97*, 123–131. DOI: https://doi.org/10.1016/j.jphotobiol.2009.08.009.
13. Celaje, J. A.; Zhang, D.; Guerrero, A. M.; Selke, M. *Org. Lett.* **2011**, *13*, 4846–4849. DOI: https://doi.org/10.1021/ol201922u.
14. Rajnochová Svobodová, A.; Ryšavá, A.; Psotová, M.; Kosina, P.; Zálešák, B.; Ulrichová, J.; Vostálová, J. *Photochem. Photobiol.* **2017**, *93*, 1240–1247. DOI: https://doi.org/10.1111/php.12755.
15. Lagunes, I.; Trigos, Á. *J. Photochem. Photobiol. B.* **2015**, *145*, 30–34. DOI: https://doi.org/10.1016/j.jphotobiol.2015.02.014.
16. Vázquez-Ortega, F.; Lagunes, I.; Trigos, Á. *Dyes Pigm.* **2020**, *176*, 108248. DOI: https://doi.org/10.1016/j.dyepig.2020.108248.
17. Vázquez-Ortega, F.; Sifaoui, I.; Reyes-Batlle, M.; Piñero, J. E.; Lagunes, I.; Trigos, Á.; Lorenzo-Morales, J.; Díaz-Marrero, A. R.; Fernández, J. J. *Dyes Pigm.* **2020**, *180*, 108481. DOI: https://doi.org/10.1016/j.dyepig.2020.108481.
18. Guerrero, T.; Vázquez-Ortega, F.; Lagunes, I.; Ortiz-Blanco, E.; Sosa-Ortiz, G.; Tovar-Miranda, R.; Medina, M. E.; Trigos, Á. *Dyes Pigm.* **2021**, *192*, 109447. DOI: https://doi.org/10.1016/J.DYEPIG.2021.109447.
19. Yin, H.; Xu, L.; Porter, N. A. *Chem. Rev.* **2011**, *111*, 5944–5972. DOI: https://doi.org/10.1021/cr200084z.
20. Minami, Y.; Kawabata, K.; Kubo, Y.; Arase, S.; Hirasaka, K.; Nikawa, T.; Bando, N.; Kawai, Y.; Terao, J. *J. Nutr. Biochem.* **2009**, *20*, 389–398. DOI: https://doi.org/10.1016/j.jnutbio.2008.04.010.
21. Seo, S. H.; Jeong, G. S. *Int. Immunopharmacol.* **2015**, *29*, 246–253. DOI: https://doi.org/10.1016/j.intimp.2015.11.014.
22. Chiang, H. M.; Chan, S. Y.; Chu, Y.; Wen, K. C. *J. Agric. Food Chem.* **2015**, *63*, 4551–4560. DOI: https://doi.org/10.1021/jf502500t.
23. Shao, Y.; He, T.; Fisher, G. J.; Voorhees, J. J.; Quan, T. *Int. J. Cosmet. Sci.* **2017**, *39*, 56–65. DOI: https://doi.org/10.1111/ics.12348.
24. Pratheeshkumar, P.; Son, Y. O.; Wang, X.; Divya, S. P.; Joseph, B.; Hitron, J. A.; Wang, L.; Kim, D.; Yin, Y.; Roy, R. V.; Lu, J.; Zhang, Z.; Wang, Y.; Shi, X. *Toxicol. Appl. Pharmacol.* **2014**, *280*, 127–137. DOI: https://doi.org/10.1016/j.taap.2014.06.028.
25. Li, M.; Lin, X. F.; Lu, J.; Zhou, B. R.; Luo, D. *J. Photochem. Photobiol. B.* **2016**, *165*, 240–245. DOI: https://doi.org/10.1016/j.jphotobiol.2016.10.037.
26. Choi, K. S.; Kundu, J. K.; Chun, K. S.; Na, H. K.; Surh, Y. J. *Arch. Biochem. Biophys.* **2014**, *559*, 38–45. DOI: https://doi.org/10.1016/j.abb.2014.05.016.
27. Lembo, S.; Balato, A.; di Caprio, R.; Cirillo, T.; Giannini, V.; Gasparri, F.; Monfrecola, G. *Biomed. Res. Int.* **2014**, *2014*, 346793. DOI: https://doi.org/10.1155/2014/346793.
28. Choi, S.; Youn, J.; Kim, K.; Joo, D. H.; Shin, S.; Lee, J.; Lee, H. K.; An, I.; Kwon, S.; Youn, H.J.; Ahn, K. J.; An, S.; Cha, H. J. *Int. J. Mol. Med.* **2016**, *38*, 627–634. DOI: https://doi.org/10.3892/ijmm.2016.2626.
29. Chen, J.; Li, Y.; Zhu, Q.; Li, T.; Lu, H.; Wei, N.; Huang, Y.; Shi, R.; Ma, X.; Wang, X.; Sheng, J. *Mech. Ageing. Dev.* **2017**, *164*, 1–7. DOI: https://doi.org/10.1016/j.mad.2017.03.007.
30. Xie, J.; Zheng, Y. *J. Cosmet. Dermatol.* **2017**, *16*, 444–449. DOI: https://doi.org/10.1111/jocd.12399.
31. Aguiar, B.; Carmo, H.; Garrido, J.; Lobo, J. M. S.; Almeida, I. F. *Molecules.* **2022**, *27*, 189. DOI: https://doi.org/10.3390/MOLECULES27010189.

Article

J. Mex. Chem. Soc. **2024**, *68*(2)
Regular Issue

ISSN-e 2594-0317

Effect of Time of Harvest on the Chemical Composition and Antioxidant Potential of Leaf Essential Oil of *Syzygium guineense* Growing in North Central Nigeria (Willd.) Dc. Var.

Lamidi Ajao Usman*, Ridwan Olanrewaju Ismaeel, Musa Alfanla Kamaldeen

Department of Chemistry, University of Ilorin, P.M.B. 1515, Ilorin, Nigeria.

***Corresponding author:** Lamidi Ajao Usman, email: usmanlamidi@unilorin.edu.ng; lamidiusman09@gmail.com; Phone Number: +2348035032378

Received January 29th, 2023; Accepted May 17th, 2023.

DOI: http://dx.doi.org/10.29356/jmcs.v68i2.2035

Abstract. The use of synthetic antioxidants to ameliorate oxidative stress goes with side effects. Some plants are known to be sources of natural antioxidants and, hence, could be used as alternatives to synthetic antioxidants without side effects. Meanwhile, the presence of the phytochemicals that exhibit antioxidant activity in plants depends on environmental conditions that vary with the time of harvest of plant materials. This study, therefore, investigated the effect of time of harvest on the chemical composition and antioxidant potential of leaf essential oil of *Syzygium guineense* native to North central Nigeria. To accomplish these, pulverized (500 g) leaves of *S. guineense* harvested in the morning and afternoon were separately hydrodistilled and yielded 0.25 ± 0.002 % (w/w) and 0.27 ± 0.003 % (w/w) of essential oils. Characterization of the oils using GC-MS revealed the presence of twenty-two and twenty-three compounds in the oils from morning and afternoon harvests. The most abundant compound in the oils was β-bergamotene (30.1 % and 27.3 %). D-limonene (2.9 % and 5.6 %), β-ocimene (4.2 % and 10.2 %), α-santalene (7.4 % and 7.7 %), α-cedrene (8.6 % and 9.0 %), β-farnesene (9.1 % and 10.2 %) and calamenene (7.1 % and 5.2 %) were detected in significant quantities in the oils. DPPH radial scavenging assay was used to evaluate the antioxidant activity of the oils with butylated hydroxyl toluene (BHT) as standard. The oils exhibited antioxidant activity with IC_{50} of 41.92 μg/mL and 33.12 μg/mL for the oils from morning and afternoon harvests. Although the oils exhibited lower antioxidant activity than the standard (IC_{50} of 28.63 μg/mL), but the oils could be used to ameliorate oxidative stress after clinical trials.
Keywords: *Syzygium guineense;* antioxidant; α-bergamotene; β-farnesene.

Resumen. El uso de antioxidantes sintéticos para mejorar el estrés oxidativo conlleva efectos secundarios. Se sabe que algunas plantas son fuentes de antioxidantes naturales y, por lo tanto, podrían usarse como alternativas a los antioxidantes sintéticos sin efectos secundarios. La presencia de fitoquímicos que exhiben la actividad antioxidante en las plantas depende de las condiciones ambientales que varían con el momento de la cosecha de los materiales vegetales. Por lo tanto, en este estudio se investigó el efecto del momento de la cosecha sobre la composición química y el potencial antioxidante del aceite esencial de hoja de *Syzygium guineense*, originario del centro norte de Nigeria. Para lograr esto, se hidrodestilaron por separado hojas pulverizadas (500 g) de *S. guineense* cosechadas en la mañana y en la tarde que produjeron 0.25 ± 0.002% (p/p) y 0.27 ± 0.003% (p/p) de aceites esenciales. La caracterización de los aceites mediante GC-MS reveló la presencia de veintidós y veintitrés compuestos en los aceites de las cosechas de la mañana y la tarde. Los compuestos más abundantes en los aceites fueron el β-bergamoteno (30.1 % y 27.3 %), D-limoneno (2.9 % y 5.6 %), β-ocimeno (4.2 % y 10.2 %), α-santaleno (7.4 % y 7.7 %), α-cedreno (8.6 % y 9.0 %), β-farneseno (9.1 % y 10.2 %) y calameneno (7.1 % y 5.2 %). Se utilizó el ensayo de eliminación radial DPPH para evaluar la actividad antioxidante de los aceites con hidroxil tolueno butilado (BHT) como estándar. Los aceites exhibieron actividad antioxidante con

J. Mex. Chem. Soc. **2024**, *68*(2)
Regular Issue

ISSN-e 2594-0317

IC50 de 41.92 μg/mL y 33.12 μg/mL para los aceites de las cosechas de la mañana y la tarde. Si bien los aceites exhibieron una actividad antioxidante menor que el estándar (IC50 de 28.63 μg/mL), los aceites podrían usarse para mejorar el estrés oxidativo después de los ensayos clínicos.
Palabras clave: Syzygium guineense; antioxidante; α-bergamoteno; β-farneseno.

Introduction

Syzygium guineense (Willd.) DC. var. belongs to the family Myrtaceae. It is widely grown in the forests and savannah regions of Africa [1]. The plant is commonly called "malmoo" by the Hausas, "sumsum" by the Fulanis and "adere or igi-aro" by the Yorubas in Nigeria [2,3]. Traditionally, the fruit of the plant is used to treat dysentery while the leaf decoction is used to cure stomach-ache, diarrhea, diabetes, ulcers, rheumatism, malaria and inflammations. The bark is used for the treatment of hypertension [4,5]. The crude extracts from the plant have been reported to possess antibacterial, antidiabetes, analgesic, anti-inflammatory, antihypertensive, antioxidant and antimalarial activities [6-8]. Hence, justify its use in traditional medicine. Reports on the phytochemical analysis of the plant extracts revealed the presence of flavonoids, tannins, saponin, alkaloids and cardiac glycosides [9-11]. The phytochemicals detected in its various extracts, were responsible for the reported biological and biochemical activities.

Previous work on the leaf essential oil of *S. guineense* from Natitingou, Peperkou, Tchaourou and Terou locations in Republic of Benin revealed that the oils were of β-caryophyllene, *cis*-calamenen-10-ol, viridiflorol and α-humullene chemotypes respectively. Other major constituents in the oils were humullene-1,2-epoxide, epi-α-muurol, α-cadinol and caryophyllene oxide [9]. The leaf essential oil of the plant native to south-western Nigeria was earlier characterized [12]. The oil was found to be of aromadendrene chemotype. Germacrene D, *tau*- cadinol, caryophyllene oxide and α-cadinol were the other principal constituents in the oil. The chemotypic variation of the oils is attributable to differences in environmental factors at various location of the plant. The oil of the south-western Nigerian grown plant was reported to exhibit antioxidant activity. The activity of the oil was linked to abundance of oxygenated terpenoids in the oil. The presence of these terpenoids in an essential oil may vary with time of harvest of plant materials that bear the oil. It is on this basis that this work investigated the effect of time of harvest on the chemical composition and antioxidant potential of essential oils from leaves of *S. guineense* native to North central, Nigeria.

Experimental

Sample collection

Leaves of *Syzygium giuneense* (1500 g) were separately harvested in the morning (7.00 a.m.) and afternoon (1.00 p.m.) at Oke Odo, Tanke, Ilorin-South LGA, Kwara State, Nigeria. The plant was identified by Mr. Bolu at the Herbarium of Plant Biology Department, University of Ilorin, where voucher specimens were deposited [UILH/002/0673].

Extraction of essential oil

Pulverized leaves (500 g) of *S. guineense* from morning and afternoon harvests were separately hydrodistilled for 3 hours in a Clevenger setup based on British Pharmacopoeia specification [13]. The oils were collected, preserved in a sealed sample tube, and stored under refrigeration at 4 °C until the analyses were carried out.

Gas Chromatography-Mass Spectrometry (GC/MS) analysis of the oils

An Agilent 19091S gas chromatograph coupled with a quadruple focusing mass spectrometer 433HP-5 mass detector was used. Helium was used as the carrier gas at a flow rate of 1.5 mL/min; all analyses were performed at constant flow. The GC was fitted with a 30 m by 0.25 mm fused silica capillary column coated with phenyl methyl siloxane at a split ratio 1:50. The film thickness was 0.25 μm. Oven temperature was initially kept

J. Mex. Chem. Soc. **2024**, *68*(2)
Regular Issue

ISSN-e 2594-0317

at 100 °C for 5 min. and then 150 °C at a rate of 4 °C/min. for 8 min. and to 250 °C at a rate of 20 °C/min. Mass detector conditions were as follows: Transfer line temperature at 300 °C, ionization mode electron impact at 70 eV. The percentage composition of the oil was computed in each case from GC peak areas.

Identification of constituents in the oils

The identification of the constituents in the oils was based on (i) comparison of their retention indices (RI), calculated using a homologous series of n-alkanes (C_7–C_{30}, Supelco Bellefonte, PA, USA) under identical experimental conditions, co-injection with standards and compared with those data from Wiley 275 and NIST 08 libraries (ii) comparison of fragmentation pattern in the mass spectra of each constituent with those data from Wiley 275 and NIST 08 libraries [14-17]. The relative quantity of each constituent was calculated based on the peak area of the GC (FID response) without using a correction factor.

DPPH antioxidant assay of the oils

The antioxidant potential of the oils was measured in terms of its hydrogen-donating or radical scavenging ability against DPPH, using the method reported by Ilhami [18]. In the method, 2,2-diphenyl-1-picryl-hydrazil, DPPH, solution (1.5 ml of 10^{-4} M, in 95 % ethanol) (Meyer, Mexico) was separately mixed with the oil (1.5) at various concentrations (12.5-200 µg/mL). Each of the mixtures was shaken thoroughly and incubated in the dark for 30 minutes at ambient temperature. The control was prepared using the same procedure without the oil. The absorbance of the solution was measured at 517 nm using UV-spectrophotometer. The assay was carried out in triplicate and the results were expressed as mean values ± standard deviation. The concentration of the oil that gave 50 % inhibition (IC_{50}) was calculated from the graph of percentage inhibition against the oil concentration. Butylatedhydroxy toluene (BHT) was used as standard. The percentage inhibitions were calculated using the equation:

$$\% \text{ Inhibition} = \frac{A_0 - A_T}{A_0} \times 100$$

where A_0 is the absorbance of the control sample (containing all reagents except the test compound) and A_T is the absorbance of the test samples. Butylated hydroxytoluene (BHT, 1.0 mg/mL) (Sigma-Aldrich, Mexico) was used as a positive control.

Statistical analysis

Tests were carried out in triplicates. The mean values were calculated from the three values. The data for various biochemical parameters was expressed as mean ± SD (n = 3) and compared using one way analysis of variance (ANOVA) test, followed by Dunnett multiple comparison test with an equal sample size test. Values were considered statistically significant at $p < 0.05$. The IC_{50} values were calculated by non-linear regression analysis from the mean values. Statistics were done using SPSS for Windows version 10.

Results and discussion

Hydrodistilled leaves of *S. guineense* harvested in the morning and afternoon afforded essential oils in the yields of 0.25 ± 0.002 % (w/w) and 0.27 ± 0.003 % (w/w) respectively. The yields were lower than the yield from the leaves of the plants growing in South western Nigeria, but higher than the yields of oils from the leaves of the plant harvested from four different locations in the Republic of Benin [12,19]. The variations in the oil yields could be linked to differences in the number of secretory organs in the leaves of the plant at their respective locations. Meanwhile, the afternoon harvest yielded more oil than the morning harvest. This is attributable to environmental conditions that favoured the formation of more oil in the afternoon than in the morning. The identities, retention indices and percentage composition of constituents of leaf essential oils of the plant harvested in the morning and afternoon are presented in Table 1.

J. Mex. Chem. Soc. **2024**, *68*(2)
Regular Issue

ISSN-e 2594-0317

Table 1. Chemical Composition (%) of Essential Oils from Leaves of *S. guneense*.

S/N	Compound	RI[a]	RI[b]	% Composition		Mass spectra data
				Morning	Afternoon	
1	2-Carene	1001	1001	1.4	-	150,121,**93**,67,53
2	β-Pinene	980	982	3.2	-	**68**,79,93,107,121
3	β-Ocimine	1050	1053	4.2	10.2	**68**,79,93,107,121
4	γ-Terpinene	1062	1057	-	0.5	136,105,**93**,77,65
5	α-Terpinolene	1088	1089	-	1.4	27,53,**93**,121,136
6	Limonene	1031	1027	2.9	5.6	136, 107, 93, **68**,53
7	α-Terpineol	1189	1189	0.7	1.2	43,**59**,81,93,107
8	Thymol	1290	1291	1.5	0.7	51,77,91,121,**135**
9	α-Santalene	1420	1422	7.4	7.7	41,69,**94**,121,161
10	α-Cubebene	1345	1351	0.5	0.4	105,119,**161**,189,204
11	α-Copaene	1378	1376	4.0	3.5	105,119,**161**,189,204
12	α-Cedrene	1409	1410	8.6	9.0	55,93,**119**,136,161
13	β-Santalene	1462	1462	1.3	1.0	41,69,**94**,107,148
14	**α-Bergamotene**	**1436**	**1435**	**30.1**	**27.3**	55, 79,**93**, 119, 161
15	β-Farnesene	1458	1455	9.1	10.2	93,**119,**161,134,147
16	α-Muurolene	1499	1499	1.2	0.8	204,134,**105**,93,81
17	Muurola-3,5-diene	1450	1454	-	0.4	133,145,**161**,175,189
18	Calamenene	1521	1498	7.1	5.2	133,147,**161**,179,189
19	β-Bisabolene	1509	1513	1.5	-	**69**,79,93,109,119
20	Sesquieneole	1541	1541	1.3	1.3	**139**,140,161,176,189
21	δ-Cadinene	1524	1524	2.8	2.4	119,134,**161**,189,204
22	Cadina-1,4-diene	1532	1532	2.1	2.8	91,105,**119**,161,204
23	β-Cadin-4-en-10-ol	1580	1581	1.6	0.6	135,149,**161**,179,189
24	Nerolidol	1564	1564	-	0.6	41,**69**,93,123,161
25	β-Bisabolol	1668	1662	2.9	2.8	69,**82**,93,111,119
26	α-Bisabolol	1683	1685	2.1	1.1	69,**109**,119,134,147

J. Mex. Chem. Soc. **2024**, *68*(2)
Regular Issue

ISSN-e 2594-0317

	% Monoterpenoids			13.9	19.6	
	% Hydrocarbon Sesqquiterpenoids			77.0	72.0	
	% Oxygenated Sesquiterpenoids			6.6	5.1	
	Total (%)			**97.5**	**96.7**	

Compounds are listed in order of elution from fused silica capillary column coated on CP-Sil 5; RI^a = Literature Retention Indices, RI^b = Calculated Retention Indices; Bolded name = Chemotype

In the Table, twenty-two and twenty-three compounds that constituted 97.1 % and 96.7 % of the oils from morning and afternoon harvests were identified from their mass spectra. The percentage composition of monoterpenoids in the oils from morning and afternoon harvests were 13.9 % and 19.6 %. Sesquiterpenoids constituted 91.6 % and 76.8 % of the oils from morning and afternoon harvests respectively. The major constituents of the oils were; β-ocimene (4.2 % and 10.2 %), D-limonene (2.9 % and 5.6 %), α-santalene (7.4 % and 7.7 %), α-copaene (4.0 % and 3.5 %), α-cedrene (8.6 % and 9.0%), α-bergamotene (30.1 % and 27.3 %), β-farnesene (9.1 % and 10.2 %), calamenene (7.1 % and 5.2 %), δ-cadinene (2.8 % and 2.4 %), cadina-1,4-diene (2.1 % and 2.8 %), α-bisabolol (2.9 % and 2.8 %) and β-bisabolol (2.1 % and 1.1 %). Other principal constituents in the oil from morning harvest were β-pinene (3.2 %) and β-ocimene (4.2 %). Terpenoids that were detected in significant quantities in the oils from the two harvests were α-terpineole (0.7 % and 1.2 %), thymol (1.7 % and 0.7 %), β-santalene (1.3 % and 1.0 %), α-muurolene (1.2 % and 0.8 %), and β-cadin-4-en-10-ol (1.6 % and 0.6 %). Sesquieneole constituted 1.3% of each of the oils. 2-Carene (1.4 %) and β-bisabolene (1.5 %) that were present in appreciable amounts in the oil from morning harvest were not detected in the oil from afternoon harvest. Meanwhile, the oil from the afternoon harvest contained appreciable quantities of γ-terpinene (0.5%), α-terpinolene (1.4 %) and nerolidol (0.6 %) but the compounds were not found in the oil of the morning harvest. α-Cubebene (0.5 % and 0.4 %) was detected as a minor constituent in the oils. Irrespective of time of harvest of the leaves, α-bergamotene was the most prominent compound in the oils. This revealed that the oils were of α-bergamotene chemotypes. Aromadendrene and α-hunmullene chemotypes were earlier reported for the leaf essential oils of the plant native to Republic of Benin and south-western Nigeria [12,19]. The chemotypic differences in the oils could be attributed to differences in climatic conditions of the three geographical regions.

It has been found that the synthases of the most abundant mono- and sesquiterpenoids in an essential oil usually facilitate the biosynthesis of all terpenoids in plants [20-22]. The activities of the synthases are influenced by environmental factors that subsequently determine the quantity and the type of compounds in the oil. The predominance of β-ocimene and α-bergamotene in the oils of morning and afternoon harvests implied that their synthases facilitated the transformation of their precursors, (geranyl, neryl and farnesyl pyrophosphates) to all mono- and sesquiterpenoids in the oils. β-Ocimene synthase aided the formation of 2-carene [6] and β-pinene [9] in the oil of morning harvest but the environmental conditions did not favour the activity of the synthase to facilitate the biosynthesis of the compounds in the oil from afternoon harvest. Meanwhiile, the environmental conditions that favour the formation of γ-terpinene [11] and α-terpinolene [14] that constituted the oil from afternoon harvest did not favour their formation in the oil of the morning harvest. The α-bergamotene synthase facilitated the formation of β-bisabolene [21] in the oil of the morning harvest but the environmental condition was not conducive for its activity to mediate the formation of the compound in the oil from afternoon harvest. In contrast, the environmental condition was conducive for the activity of the synthase to aid the biosynthesis of muurola-3,5-diene and nerolidol in the oil of the afternoon harvest but did not favour their formation in the oil of the morning harvest.

β-Ocimene synthase catalyzed the biosynthesis of β-ocimene [16], limonene [7[, α-terpineol [5] and thymol [13] in the oils. However, the compounds were of greater quantities in the oil of the afternoon harvest than that of the morning harvest except thymol. Similarly, both oils contained α-santalene, α-cubebene, α-copaene [25], α-cedrene [37], β-santalene, α-bergamotene [35], β-farnesene [32], α-muurolene [39],

J. Mex. Chem. Soc. **2024**, *68*(2)
Regular Issue

ISSN-e 2594-0317

calamenene [41], α-sesquieneole, δ-cadinene [26], cadina-1,4-diene, β-Cadin-4-en-10-ol, α-bisabolol [28] and β-bisabolol [29]. Their formations in the oils were aided by α-bergamotene synthase. Meanwhile, α-cubebene [33], α-copaene [25], α-bergamotene [35], β-santalene, α-muurolene [39], calamenene [41], δ-cadinene [26], β-cadin-4-en-10-ol [27], α-bisabolol [28] and β-bisabolol [29] were of higher quantities in the oil of morning harvest than the oil of afternoon harvest. On the contrary, the oil from afternoon harvest was richer in α-santalene, α-cedrene [38], β-farnesene [32] and cadina-1,4-diene [30] than the oil from morning harvest. The lower quantity of some compounds in the oils could be attributed to subjection of their reactive intermediates to premature termination [23]. The mechanisms of biogenesis of some of the mono- and sesquiterpenoids in the essential oils from both during their formation harvests are presented in Reaction Schemes 1 and 2.

The DPPH radical scavenging of essential oils from leaves of *S. guineense* harvested in the morning and afternoon is shown in Fig. 1.

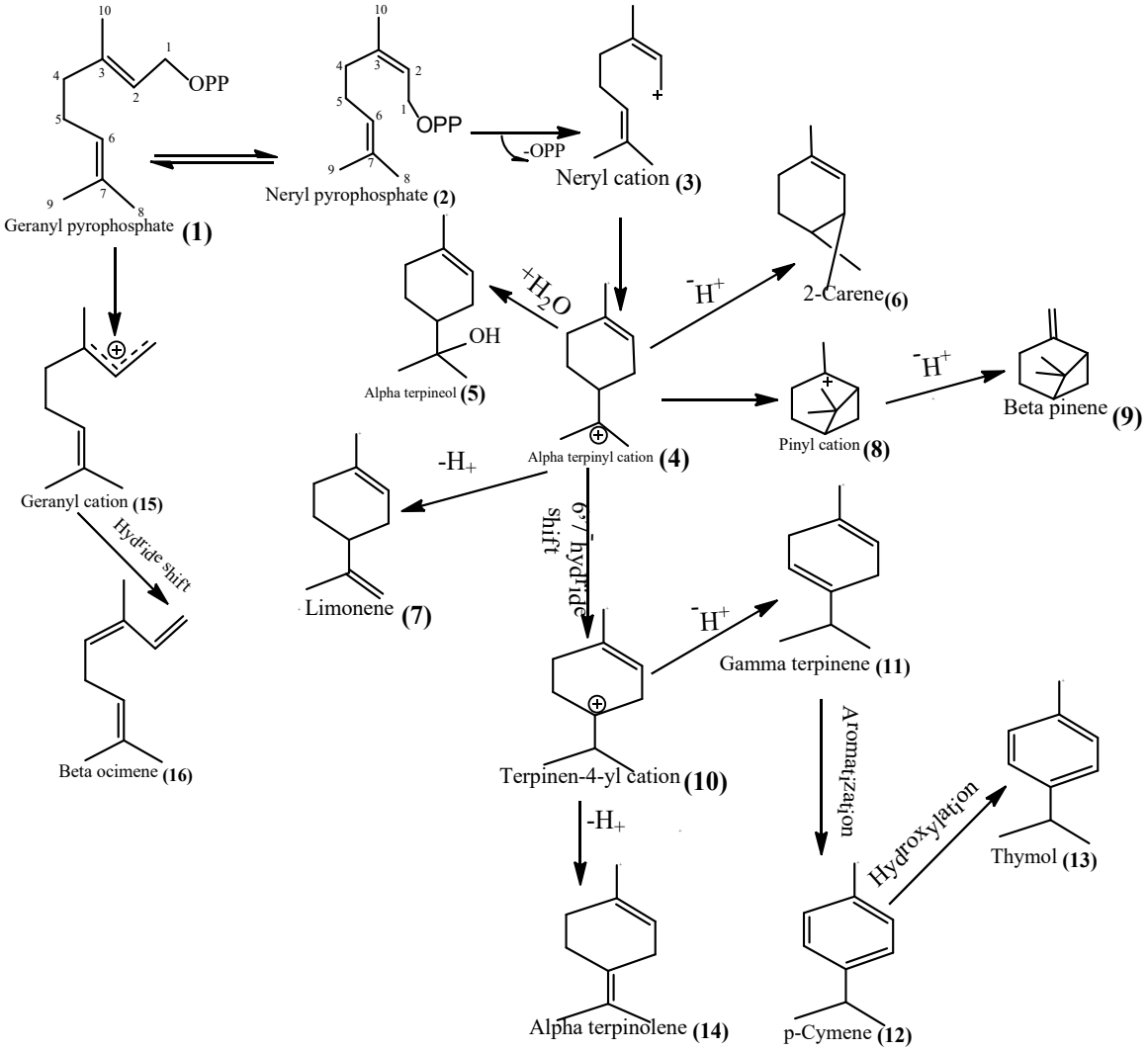

Scheme 1. Mechanism of biogenesis of monoterpenoids in the essential oils from leaves of *S. guineense*.

J. Mex. Chem. Soc. **2024**, *68*(2)
Regular Issue

ISSN-e 2594-0317

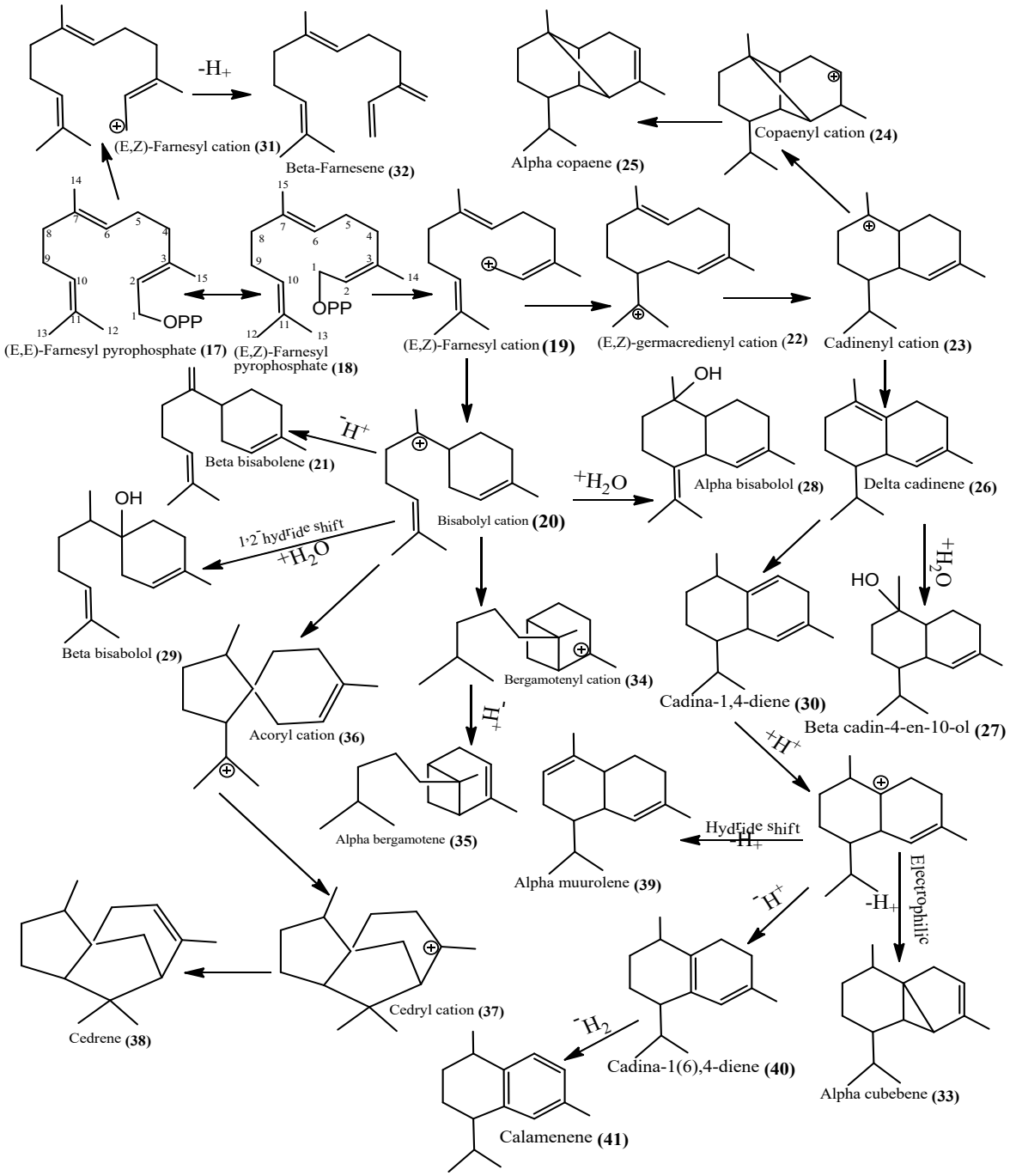

Scheme 2. Mechanisms of biogenesis of sesquiterpenoids in the essential oils from leaves of *S. guineense*.

J. Mex. Chem. Soc. **2024**, *68*(2)
Regular Issue

ISSN-e 2594-0317

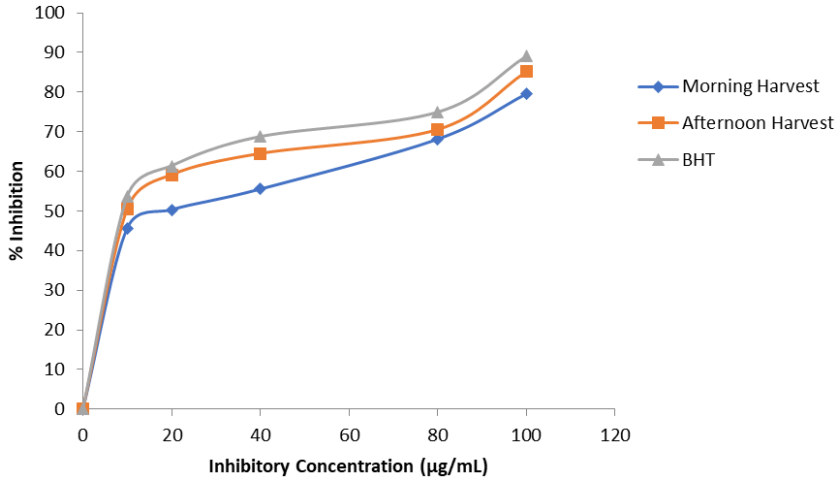

Fig. 1. DPPH Radical Scavenging Activity of Essential Oils from Leaves of *S. guineense* Harvested in the Morning (7.00 a.m.) and Afternoon (1.00 p.m.).

The figure revealed that the antioxidant activity of the oils was concentration dependent. The oils scavenged DPPH radical with IC_{50} of 41.92 µg/mL and 33.12 µl/ml for the oils from morning and afternoon harvests respectively. The oils were less active when compared to the activity of butylated hydroxytoluene, BHT, (IC_{50} = 28.63 µg/mL) that was used as standard. Irrespective of the time of harvest, the oils showed better antioxidant activity than the oil from the leaves of the plant earlier reported from the northern part of Nigeria (12). Interestingly, the oil from afternoon harvest showed higher activity than the oil from morning harvest. The oil was richer in α-terpineol and limonene and also contained γ-terpinene, α-terpinolene and nerolidol which were not found in the oil from morning harvest. It has been established that essential oils containing greater amounts of oxygenated compounds usually possess higher antioxidant activity [24,25]. For instance, the DPPH radical scavenging activity of leaf essential oils of *Ocimum basilicum* and *Scutia buxifolia* was linked to the predominant of linalool, carvacrol, 1,8-cineole and spathulenol in the oils [26,27]. The oils also contained terpinolene and γ-terpinene which were separately reported to show stronger DPPH radical-scavenging activity than trolox which was used as a reference. The DPPH radical scavenging activity of limonene and α-terpineol has also been documented [28,29]. Thus, the stronger DPPH radical scavenging activity of the oil from afternoon harvest could be attributed to the presence and higher quantities of the listed compounds above as compared to the oil from morning harvest.

Conclusions

The yields of essential oils obtained from *S. guineense* harvested in the morning and afternoon differ significantly. More oil was obtained from the afternoon harvest which was linked to a higher number of secretary cells in the afternoon than in the morning. The phytochemical profile of the oils also varied with times of harvest which sample harvested in the subsequently affected plant harvested in their antioxidant activity. Irrespective of the time of harvest of the leaves, the oils scavenged DPPH radicals with the oil from afternoon harvest showing greater antioxidant activity. Hence, the oils could be used as alternative antioxidants to ameliorate oxidative stress after clinical trials.

J. Mex. Chem. Soc. **2024**, *68*(2)
Regular Issue

ISSN-e 2594-0317

Acknowledgements

The authors wish to acknowledge Mr. Bolu, of the department of Plant Biology, University of Ilorin, Ilorin, Nigeria who assisted in the identification of the plant.

References

1. Bankefa, E.; Onileke, F.; Dada, E. *J. Sci. Res*. **2014**, *2*, 21-252.
2. Agwu, C. O. C.; Okeke, G. I. *J. Bot.* **1997**, 9-10, 25–36.
3. Iwu, M. M. in: *Handbook of African Medicinal Plants*, CRP Press, BOC Raton, Florida. **1993**, 12 – 78.
4. Burkill, H. M. in: *The useful plants of west tropical families M-R*, Vol. 4, 2nd Edition, Kew: Royal Botanical Gardens. **1997**, 253–254.
5. Seyoum, G.; Abebe, M.; Asres, K.; Bekuretsion, Y.; Woldkidan, S.; Debebe, E. *Evid.-based Complement. Altern. Med*. **2021**, 5, 1 – 10.
6. Wubneh, Z. B., Tadesse, S. A. *BMC Complement. Altern. Med*. **2017**, *17*, 21- 28.
7. Abera, B.; Adane, L.; Mamo, F. *J. Pharmacogn. Phytochem*. **2018**, *7*, 3104 – 3111.
8. Ezenyi, I. C.; Mbamalu, O. N.; Balogun, L.; Omorogbe, L.; Ameh, F. S.; Salawu, O. A. *J. Phytopharmacol*. **2016**, *5*, 150-156.
9. Kristanti, A. N.; Aung, E. A.; Aminah, N. S.; Takaya, Y.; Ramadhan, R. *Open Chem. J*. **2020**, *18*, 1256–1281.
10. Pieme, C. A.; Ngoupayo, J.; Nkoulou, C. H.; Moukette, B. M.; Nono, B. L.; Moor, V. J. *Antioxidants*. **2014**, *3*, 618–635.
11. Tadesse, A. S.; Wubneh, Z. B. *BMC Complement. Altern. Med*. **2017**, *17*, 1–7.
12. Okhale, S. E.; Buba, C. I.; Oladosu, P.; Ugbabe, G. E.; Ibrahim, J. A.; Egharevba, H. O.; Kunle, O. F. *IJPPR*. **2018**, *10*, 341-349.
13. British pharmacopoeia II. HM, stationary office, London, **1980**, 109.
14. Adams, R. P. in *Identification of essential oil components by gas chromatography and mass spectrometry*. Allured publ. corp., Carol Stream, IL. USA. **2012**, 78 – 109.
15. Jennings, W.; Shibamoto, T. in: *Qualitative analysis of flavour volatiles by gas capillary chromatography*. Academic press, New York, **1980**; 68–109.
16. Joulain, D.; Koenig, W. A. in: *The atlas of spectra data of sesquiterpene hydrocarbon*. E. B. Verlay Hamburg, Germany, **1998**, 112–153.
17. Usman, L. A.; Agboola, T. A.; AbdulWaheed, J. O.; Ismaeel, R. O.; Ogundele, V. A.; Ibrahim, A. *NJPAS*. **2016**, *29*, 2968–2976.
18. Ilhami, G. *Chem-Biol. Interact.* **2009**, *179*, 71-80.
19. Chalchat, J.; Noudogbessi, J.; Sohounhloue, D. C. K.; Yedomonhan, P., Figueredo, G. *Rec. Nat. Prod.* **2008**, *2*, 33-38.
20. Trapp, S. C.; Croteau, R. B. *Genetics*. **2001**, *158*, 811–832.
21. Degenhardt, J.; Ko¨llner, T. G.; Gershenzon, J. *Phytochem*. **2009**, *70*, 1621–1637.
22. Usman, L. A.; Watti, O. I.; Ismaeel, R. O.; Ojumoola, A. O. *JOTCSA.* **2016**, *3*, 1–18.
23. Iijima, Y.; Davidovich-Rikanati, R.; Fridman, E.; Gang, D. R. *Plant Physiol*. **2004**, *136*, 3724–3736.
24. Mkaddem, M. G.; Romdhane, M.; Ibrahim, H.; Enn-ajar, M.; Lebrihi, A.; Mathieu, F.; Bouajila, J. *J. Med. Food*. **2010**, *13*, 1500–1504.
25. Paolini, J.; El Ouariachi, E.; Bouyanza, A.; Tomi, P.; Hammouti, B.; Salghi, R.; Majidi, L.; Costa J. *J. Med. Plants Res*. **2011**, *5*, 5773–5778.
26. Hussein, A. I.; Anwar, F.; Sherazi, S. T. H.; Pryzbylski, R. *Food Chem*. **2008**, *108*, 986-995.
27. Boligon, A. A.; Piana, M.; Brum, T. F.; Froeder, A. L. F.; Belke, B. V.; Schwanz, T. G.; Mario, D. N.; Alves, S. H. Athayde, M. L. *An. Acad. Bras. Cienc*. **2014**, *86*, 1463-1469.
28. Mehta, A. A.; Shah, B. B. *Asian J. Pharm. Pharmacol*. **2018**, *4*, 883–887.
29. Hou, C.; Chen, Y.: Wang, C. *Int. J. Food Prop.* **2019**. *22*, 230–238.

Article

J. Mex. Chem. Soc. **2024**, *68*(2)
Regular Issue

ISSN-e 2594-0317

Aliskiren Copper(II) Complex. Synthesis and Antioxidant Activity

Nadir Jori[1], María Soledad Islas[1,2*], Evelina Gloria Ferrer[1], Patricia Ana María Williams[1*]

[1]Centro de Química Inorgánica (CEQUINOR-CONICET-CICPBA-UNLP), Facultad de Ciencias Exactas, Universidad Nacional de La Plata, Boulevard 120 Nº 1465, C.C.962- (B1900AVV) -1900 La Plata, Argentina.
[2]Departamento de Química y Bioquímica, Facultad de Ciencias Exactas y Naturales, Universidad Nacional de Mar del Plata, Funes 3350, 7600 Mar del Plata, Argentina.

***Corresponding author:** María Soledad Islas, email: msislas@mdp.edu.ar, Tel. +54(0223)475-2200; Patricia Ana María Williams, email: williams@quimica.unlp.edu.ar, Tel. +54(0221)445-4393.

Received Febrarury 22nd, 2023; Accepted May 20th, 2023.

DOI: http://dx.doi.org/10.29356/jmcs.v68i2.1981

Abstract. Aliskiren (Alk) is a highly selective competitive inhibitor of renin used for the treatment of hypertension and related cardiovascular diseases. With the aim of improving its biological properties by the strategy of the induction of favorable conformational changes, we designed a metal-based drug. In this work we report the synthesis of a solid copper(II) complex with aliskiren, **CuAlk**, and its characterization in solution and solid-state. Moreover, and based on the association of hypertension with elevated levels of reactive oxygen species (ROS), the antioxidant properties of **CuAlk** were studied measuring the activities against 2,2-diphenyl-1-picrilhidrazil (DPPH•), hydroxyl (OH•) and peroxyl (ROO•) radicals, in addition to its superoxide dismutase (SOD) simil activity. Both the ligand and the complex were able to scavenge hydroxyl radicals, but upon complexation, the SOD mimetic activity of the ligand is enhanced.
Keywords: N-ligands, copper, antioxidants, EPR, superoxide dismutase.

Resumen. El Aliskiren (Alk) es un inhibidor por competencia altamente selectivo de la renina que se utiliza en el tratamiento de la hipertensión y enfermedades cardiovasculares relacionadas. Se diseñó un metalofármaco con la idea de mejorar las propiedades biológicas mediante la inducción de cambios conformacionales favorables. En este trabajo se reporta la síntesis de un complejo sólido de cobre(II) con aliskiren, **CuAlk**, junto con su caracterización en fase sólida y en solución. Además, de acuerdo con la relación que existe entre la hipertensión y los niveles elevados de especies reactivas de oxígeno (ROS), se estudian las propiedades antioxidantes del **CuAlk** frente a los radicales 2,2-difenil-1-picrilhidracilo (DPPH•), hidroxilo (OH•) y peroxilo (ROO•), además de la actividad superóxido dismutasa símil (SOD). Tanto el ligando, como el complejo fueron capaces de secuestrar radicales hidroxilos, pero, luego de la complejación, se mejoró la actividad SOD símil del ligando.
Palabras clave: N-ligandos, cobre, antioxidantes, EPR, superóxido dismutasa.

Introduction

Aliskiren (Alk) was the first reported compound in a novel class of renin inhibitors with the potential for treatment of hypertension and related cardiovascular diseases [1]. Being a highly selective competitive inhibitor of renin, it is able to block effectively the conversion of angiotensinogen to angiotensin I, as well as the later production of angiotensin II (Ang II). When Ang II levels are inhibited, the feedback loop is suppressed,

J. Mex. Chem. Soc. **2024**, *68*(2)
Regular Issue

ISSN-e 2594-0317

resulting in further reduction in plasma renin concentrations [2]. The drug is commercially available as aliskiren hemifumarate (Fig. 1).

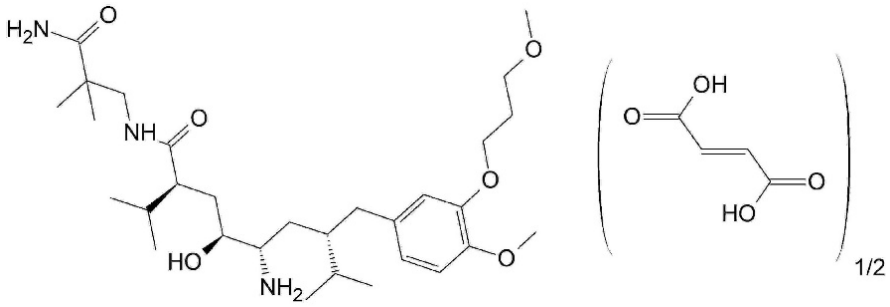

Fig. 1. Aliskiren hemifumarate (commercial drug).

In addition, it has been shown that Alk has a protective role against cisplatin induced nephrotoxicity in rats [3] and this could be associated to its antioxidant activity. It has been reported that Alk can decrease the Reactive Oxygen Species (ROS) produced by the Renin Angiotensin Aldosterone System (RAAS) at doses independent of decreasing blood pressure [4].

Copper(II) plays a critical role in the antioxidant defense of organisms, particularly in Cu/Zn-SOD, and in cardiovascular disease, as the heart and blood vessels are particularly susceptible to Cu deficiency [5]. Due to this, numerous copper(II) complexes with antihypertensive drugs, including β-blockers, vasodilators, ACE inhibitors, diuretics [6], and sartans, have been synthesized, some of which have improved the efficacy of the parent drug [7]. The action of these complexes is based on the ability of metal-based drugs to enhance the pharmacological effects of the original drug through various mechanisms, such as acting as a prodrug, improving targeting strategies, enhancing the lipophilic nature [8], and other mechanisms [9].

Taking this into account, we propose in this study to investigate a coordination complex containing copper(II) and Alk. In a first step, the aliskiren base (Alk base) was isolated from the hemifumarate anion. Then, a copper complex (**CuAlk**) was synthesized and characterized in both solid and solution states. This is, to our knowledge, the first metal coordination complex reported with Alk.

With the aim of studying how the *in vitro* antioxidant activity of the ligand is affected by complexation, we have performed several experiments that can be divided in three general groups: i) those based on the scavenging activity of a previously generated radical, such as 2,2-diphenyl-1-picrilhidrazil (DPPH$^{\bullet}$) or hydroxyl (OH$^{\bullet}$) radicals; ii) assays based in the mimetic activity of an antioxidant enzyme, like superoxidedismutase (SOD), in which the capacity of a compound to favor the dismutation of the generated superoxide radical is studied; iii) The third group involves the competitive methods, which use a reference compound as a probe, like the present method for the scavenge of the peroxyl (ROO$^{\bullet}$) radical, that follows the decay in the absorbance of pyranine (probe) by UV-vis spectrometry. To sum up, herein we report the synthesis and characterization of a copper(II) complex with Alk and the measurement of its antioxidant activity against different radicals.

Experimental

General section

All chemicals were used without further purification. Copper(II) nitrate hexahydrate was purchased from Biopack, and pure commercial samples of aliskiren hemifumarate (Jinlan Pharm-Drugs Technology Co., Ltd (China)). Elemental analysis for carbon, nitrogen and hydrogen were performed using a Carlo Erba EA 1108 analyzer. FTIR spectra of powdered samples (as pressed KBr pellets) were measured with an Equinox 55 FTIR-spectrophotometer from 4000 to 400 cm^{-1}. Thermogravimetric analysis (TGA) and differential thermal

J. Mex. Chem. Soc. **2024**, *68*(2)
Regular Issue

ISSN-e 2594-0317

analysis (DTA) were performed on a Shimadzu system (model TG-50 and DTA-50 respectively) working in an oxygen flow (50 mL min^{-1}) at a heating rate of 10 ^oC min^{-1}. Sample quantities ranged from 5 to 10 mg. Al_2O_3 was used as a differential thermal analysis standard. UV-vis in solution and diffuse reflectance spectra were collected from 185 to 900 nm with a spectrophotometer Shimadzu UV-vis 2600, equipped with halogen and deuterium lamps. For diffuse reflectance measurements MgO was used as an internal standard. A X-band EPR spectrometer (Bruker Elexsys E500T-A) was used to record the electron paramagnetic resonance (EPR) spectra of the complexes at room temperature and 120 K (with liquid air) in solid state and at room temperature in ethanolic solution. A computer simulation of the EPR spectra was performed using the program Easyspin 5.2.28 in Matlab 2014. NMR experiments were carried out using NMR tubes adapted with J-Young valves. NMR spectra were recorded on a Bruker 400 MHz spectrometer. NMR chemical shifts are reported in ppm with d_6-DMSO as internal reference. MS experiments were performed on an LTQ Orbitrap FTMS instrument (LTQ Orbitrap Elite FTMS, Thermo Scientific, Bremen, Germany) operated in positive mode, coupled with a robotic chip-based nano-ESI source (TriVersa Nanomate, Advion Biosciences, Ithaca, NY, U.S.A.). A standard data acquisition and instrument control system were utilized (Thermo Scientific), while the ion source was controlled by Chipsoft 8.3.1 software (Advion BioScience). Samples were loaded onto a 96-well plate (Eppendorf, Hamburg, Germany) with an injection volume of 5 µL. The experimental conditions for the ionization voltage were +1.4 kV, and the gas pressure was set at 0.30 psi. The temperature of the ion transfer capillary was 120 °C. FTMS spectra were obtained in the 80-1000 m/z range in the reduced profile mode, with a resolution set to 120,000. In all spectra, one microscan was acquired with a maximum injection time value of 1000 ms.

Aliskiren free base

0.25 g of the aliskiren hemifumarate (0.4 mmol) were dissolved in 15 mL H_2O and 1.5 mL NH_4OH were added, obtaining a cloudy suspension. The free base ($C_{30}H_{53}N_3O_6$) was obtained by two subsequent extractions with ethyl acetate (7.0 mL each). The organic phase was washed with 5 mL of distilled water and then all the volatiles were removed using a rotavapor, obtaining a colorless gel. A colorless solid can be collected by cooling the gel formed in the previous step. (0.167 g, 67 % yield). The absence of the fumarate bands [10] at 1565 cm^{-1} ($\nu_{as\ COO-}$) and 1635 cm^{-1} ($\nu_{s\ COO-}$) in the FTIR spectrum confirms its separation of the aliskiren base (Fig. S1). UV (EtOH) λ_{max} (log ε) 227 (3.998) nm (shoulder); 280 (3.468) nm; IR (KBr) ν_{max} 3408, 3355, 2958, 2931, 2873, 1663, 1650, 1608, 1591, 1515, 1469, 1443, 1425, 1386, 1369, 1260 1236, 1191, 1161, 1138, 1122, 1052, 1028, 807, 767, 607, 552, 435 cm^{-1}; ^{1}H NMR ($(CD_3)_2SO$, 400 MHz) δ 6.84 (1H, t), 6.54 (1H, s), 6.09 (2H, d), 6.0 (1H, s), 5.95 (1H, d), 2.96 (4H, s), 2.74 (3H, t), 2.50 (3H, s), 1.81 (3H, s), 1.70 (1H, m), 1.62 (2H, m), 1.40 (1H, t), 1.20 (2H, t), 0.90 (4H, m), 0.56 (1H, t), 0.43 (2H, m), 0.32 (6H, s), 0.10 (6H, t), 0.03 (6H, t); ^{13}C NMR ($(CD_3)_2SO$, 100 MHz) δ 166.60, 151.3, 113.8, 111.7, 71.4, 68.4, 65.1, 57.7, 55.3, 49.4, 46.2, 42.4, 33.3, 32.9, 30.1, 28.6, 23.1, 20.5, 19.8, 19.4, 16.9.

$[Cu(Alk)_2(H_2O)_2](NO_3)_2$ (CuAlk)

An ethanolic solution of $Cu(NO_3)_2$ (2 mmol, 2mL) was added dropwise to an ethanolic aliskiren base solution (1 mmol, 5 mL). This excess of copper(II) was added to favour the formation of the complex. Afterwards, the pH was adjusted to 12 with 1 M NaOH, leading to the precipitation of the excess of Cu(II) as a light blue solid ($Cu(OH)_2$, confirmed by FTIR spectroscopy) and the formation of a purple solution. After removing the solid by filtration, the purple solution was acidified with HNO_3 (0.1 mol/L) until pH 7 were the colour changes to blue. Then, the solution was slowly evaporated until 1 mL and afterwards, 3 mL of water were added, after an oily solid was obtained. The blue solid was separated from the solution and dried in oven at 60 °C (0.87 g, 70 % yield). Amorphous powder: UV-vis (EtOH) λ_{max} (log ε) 644 (1.504) nm; Diffuse reflectance λ_{max} 646 nm (Fig. S2), IR (KBr) ν_{max} 3431, 3335, 2959, 2832, 2873, 1665, 1658, 1650, 1608, 1591, 1515, 1468, 1443, 1425, 1384, 1260, 1235, 1191, 1161, 1138, 1121, 1052, 1029, 807, 768, 631 cm^{-1}; ^{1}H NMR ($(CD_3)_2SO$, 400 MHz) δ 6.80, 6.60, 3.90, 3.72, 3.44, 3.24, 2.50, 1.90, 1.02, 0.80 (very broad peaks); ^{13}C NMR ($(CD_3)_2SO$, 100 MHz) δ 147.0, 146.4, 111.2, 67.8, 64.7, 57.1, 54.8, 28.3; FTMS *m/z* (rel. int.) 1165.7 [M^+, $CuAlk_2^+$](26.1), 1164.7 [M H-1$^+$] (37.5), 1166.7 [MH^+] (25.0), 1842.0 (2.3), 1841 (1.7), 1718 (4.9), 1717.1 (5.4), 1716.1 (5.0), 1286 (1.0), 1188.7 (2.2), 676.2 (1.3) (Fig. S3 and S4); Anal. C 54.2 %, H 8.4%, N 8.3 %, calc. for $CuC_{60}H_{110}N_8O_{20}$ (Mw 1325.5 g/mol), C 54.3 %, H 8.2 %, N 8.4 %; Thermogravimetric analysis (TGA) range 50-100 °C (Calc. loss: 2.1 %, Exp. loss: 1.7 %, two labile water molecules per copper atom) with a broad endothermic peak, around 100 °C, DTA, At 800 °C the

J. Mex. Chem. Soc. **2024**, *68*(2)
Regular Issue

ISSN-e 2594-0317

weight loss (94.0 %, calc.; 94.1 %, exp.) represents the formation of CuO that was characterized by FTIR spectroscopy. No suitable crystals for X-ray structural determinations were obtained.

Spectrophotometric titration

Prior to determining the stoichiometry of the complex (CuAlk) in solution, it was necessary to remove fumarate anion from Alk hemifumarate. To accomplish this, 0.1218 g of Alk hemifumarate (0.1 mmol fumarate, 0.2 mmol Alk) were dissolved in 10 ml of 96 % ethanol. Next, 0.0242 g of $Cu(NO_3)_2.3H_2O$ (0.1 mmol) were added to the solution. The resulting mixture formed a light blue solid (copper fumarate by FTIR), which was then filtered and washed three times with 96 % ethanol. The remaining ethanolic solution and the washed solution (Alk base) were transferred quantitatively to a graduated flask and made up to 25 mL (8 mM). Subsequently, the molar ratio method was applied by adding varying quantities of ethanolic solution of $Cu(NO_3)_2.3H_2O$ (0.01 M) in a ligand-to-metal ratio ranging from 10 to 0.7. pH values were adjusted to 7.5 using 0.1 M NaOH solution in 96 % ethanol (Fig. S5).

Antioxidant properties

In these experiments the compounds were dissolved in the minimum quantity of ethanol (EtOH) to avoid their precipitation and were then added to the aqueous buffer and substrate solutions. The basal measurements were performed using the same proportion of EtOH. The final concentration of EtOH in each test achieved a maximum of 2 % in the final reaction mixtures. Due to the required conditions for each study, the maximum concentration tested for each compound can differ among experiments.

Scavenging of the hydroxyl radical ($OH^{\bullet}$)

Hydroxyl radicals were generated by the ascorbate–iron–H_2O_2 system. The reaction mixture was prepared by the addition of all the reagents up to the following concentrations: 3.75 mM 2-deoxyribose, 2.0 mM H_2O_2, 0.1 mM Fe^{+3}-EDTA and the test compound in 20 mM KH_2PO_4–KOH buffer (pH 7.4). The reaction was initiated by the addition of 0.1 mM of sodium ascorbate, followed by incubation (heating and shaking at 37 °C for 30 min). The extent of deoxyribose degradation was measured by the thiobarbituric acid method [11,12]. The solutions of $FeCl_3$, ascorbate, and H_2O_2 were prepared in distilled water immediately before use.

Scavenging of the 1,1-diphenyl-2-picrylhydrazyl radical ($DPPH^{\bullet}$)

A methanolic solution of $DPPH^{\bullet}$ was added to the compound solutions (final concentration of each compound 50, 100, 250 and 500 μM) dissolved in 0.1 M tris(hydroxymethyl)aminomethane-HCl buffer (pH 7.1) at 25 °C. The absorbance at 517 nm was measured after 60 min of the initiation of the reaction in the dark and compared with the absorbance of the control (Fig. S6).

Inhibition of the peroxyl radical ($ROO^{\bullet}$)

The decrease in pyranine (probe) intensity at 454 nm was followed by UV-vis spectrophotometry. Peroxyl radicals were generated by the thermal decomposition of AAPH (2,2-azobis(2-amidinopropane) dihydrochloride) [13], which can generate free radicals at a steady rate for extended periods of time (half-life of 175 h). Reaction mixtures of 3.0 mL contained 50 mM of AAPH, 0.05 mM of pyranine and different concentrations in the range 0.1-0.5 mM of the compounds to be studied. The absorbance spectra were measured with a thermostated cell at 37 °C. The delay of pyranine consumption (lag phase) was calculated as the time before the consumption of pyranine started (Fig. S7).

Superoxide dismutase assay

The superoxide dismutase (SOD) activity was examined indirectly using the nitroblue tetrazolium (NBT) assay. The ability of the compounds to inhibit the reduction of NBT by the superoxide anion generated by the phenazine methosulfate (PMS) and reduced nicotinamide adenine dinucleotide (NADH) system was determined. The system contained 0.5 mL of the sample, 0.5 mL of 1.40 mM NADH, and 0.5 mL of 300 μM NBT, in 0.1 M KH_2PO_4-NaOH buffer (pH 7.4). After incubation at 25 °C for 15 min, the reaction was started by the addition of 0.5 mL of 120 μM PMS [14]. Then, the reaction mixture was incubated for 5 min, and the absorbance of the band at 560 nm was measured. Each experiment was performed in triplicate and at least three

J. Mex. Chem. Soc. **2024**, *68*(2)
Regular Issue

ISSN-e 2594-0317

independent experiments were performed in each case. The SOD activity is expressed as the concentration of the tested compounds that produces the 50 % inhibition of the NBT reduction by superoxide produced in the system (IC_{50} values) and was evaluated from the absorbance decrease at 560 nm in comparison with the blank (the reaction mixture without the addition of the different compounds) (Fig. S8).

Results and discussion

Characterization of the structure of the complex

CuAlk was characterized by FTMS, FTIR, EPR, NMR and diffuse reflectance spectroscopies. The room temperature EPR spectra (Fig. 2) of solid-state showed an elongated octahedral geometry, $g_{//} > g_{\perp}$, $d_{x^2-y^2}$ ground state. The g values of $g_{//} = 2.221$; $g_{\perp} = 2.052$ and $A_{//} = 196 \times 10^{-4}$ cm^{-1}; $A_{\perp} = 23 \times 10^{-4}$ cm^{-1} are in agreement with a coordination environment of two nitrogen and two oxygen atoms in the equatorial plane, CuN_2O_2 [15-17]. Values of $G = (g_{//} - 2) / (g_{\perp} - 2) = 4.25$ (higher than 4) show that no significant magnetic exchange is present. Furthermore, low-temperature EPR measurement at 120 K has been performed but no super hyperfine coupling constant for nitrogen has been observed (Fig. S9). In addition, the diffuse reflectance spectrum (Fig. S2) showed a very broad band at 646 nm, consistent with a tetragonal distortion (Jahn-Teller effect) where more than one d-d transition is allowed [17,18], as was also suggested by EPR spectroscopy.

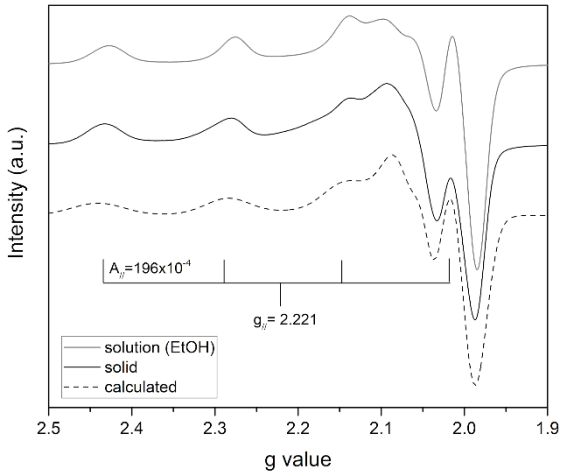

Fig. 2. Experimental (solid lines) and calculated (dotted lines) room temperature Band-X EPR of **CuAlk**. Solid complex in black and ethanolic solution (0.025M) in gray. Calculated values of $g_{//}$ and $A_{//}$ are also shown in the Figure.

Alk molecule (Fig. 1) contains a primary aliphatic amine, a hydroxyl group, and primary and secondary amide groups. Although there have been reports of copper complexes with deprotonated amide groups at neutral pH [19,20], Alk also possesses an amine and hydroxyl groups with higher basicity (the amine group in the free base exhibits a pKa value of 9.49 [1]). Consequently, we propose that the interaction between Alk and Cu(II) occurs through its aliphatic amine and hydroxyl groups. Therefore, only small changes are expected in FTIR spectrum of Alk, according to a previous report by Aydoğmuş et al. [21], since several absorption bands for stretching of O-H and N-H bonds are in the same region, and only a few of them are modified by metal complexation. However, clearer changes have been observed in the EPR and NMR spectra. The FTIR spectral changes are shown in Fig. S1 and listed in Table 1. In the 3500-3000 cm^{-1} region, only a change in the pattern of the broad band is observed due to the modification of the stretching frequencies of O-H and N-H (amine) involved in the coordination and the presence of coordinated water molecules in the metal complex. In the 1700-1600 cm^{-1} region, no changes in amide band [22] have been observed. The sharp band in 1384 cm^{-1} in

J. Mex. Chem. Soc. **2024**, *68*(2)
Regular Issue

ISSN-e 2594-0317

CuAlk is assigned to an ionic nitrate (non-coordinated) stretching mode [23]. The decrease of intensity of the band at 1138 cm^{-1}, assigned to the deformation N-H and rocking NH_2 modes [24], and the increase of intensity of the band due to the C-N stretching plus NH_2 torsion in 1050 cm^{-1}, present as a small shoulder next to the strong band in 1095 cm^{-1} are the main changes observed due to coordination of Alk to Cu(II).

Table 1. Tentative assignment of the main bands observed in FTIR spectra. Values are expressed in cm^{-1}.

Assignment	Alk base	CuAlk
ν N-H (amine and amide) + ν O-H (Alk) + ν O-H (water)	3355 (br,s) 3408 (br)	3335 (br, s) 3431 (br)
ν C=O (amide) + δ (N-H)	1663 (vs) 1650 (sh) 1608 (sh) 1591 (sh)	1665 (vs) 1658 (s) 1650 (sh) 1608 (sh) 1591 (sh)
ν N-O (nitrate)	-	1384 (vs)
δ (N-H) + γ NH_2	1138 (m)	1138 (m/w)
ν C-N aliphatic amine + τ NH_2	1052 (sh, w)	1052 (m)

Abbreviations: vs: very strong, s: strong, br: broad, sh: shoulder, m: medium, w: weak.

The measured ^{1}H NMR and ^{13}C NMR spectra of the free ligand, Alk, are in agreement with the reported values (Fig. S10 and S11) [25]. On the other hand, the ^{1}H NMR spectrum of a solution of **CuAlk** in d_6-DMSO showed broad resonances, as expected for the coordination to a paramagnetic Cu(II) center. The ^{13}C NMR spectrum suggests the coordination to the Cu(II) center, which may result in a reduced number of resonances and a broader range of chemical shifts.

Even though it is difficult to establish differences between the vibrational modes of the three N-containing groups, the tentative assignment presented here is supported by the higher basicity of a primary amine in comparison with primary and secondary amides [21], and the formation of a 5-member ring with Cu(II), and the EPR, NMR and FTMS spectral information. Based on these findings, we propose that **CuAlk** has a structure in which a Cu(II) center is tetragonally coordinated by two nitrogen and two oxygen atoms from the ligand in the equatorial plane (Fig. 3).

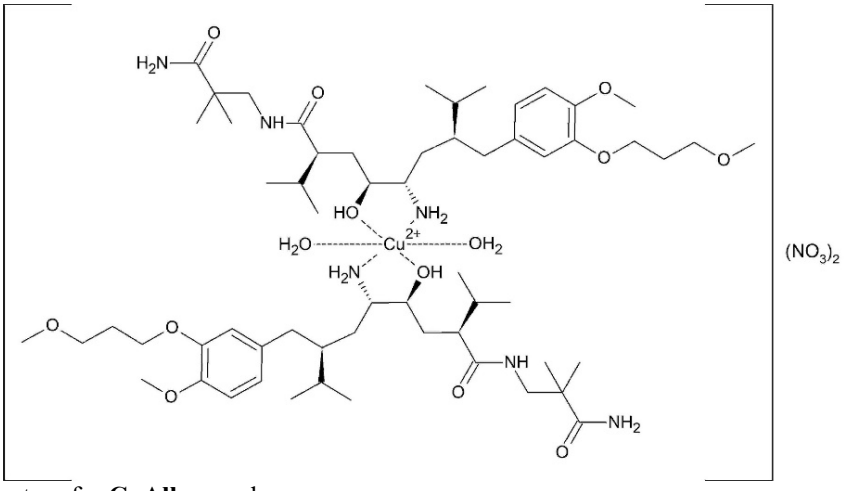

Fig. 3. Proposed structure for **CuAlk** complex.

J. Mex. Chem. Soc. **2024**, *68*(2)
Regular Issue

ISSN-e 2594-0317

The stability of **CuAlk** in ethanolic solution was determined using UV-vis spectroscopy. The observed UV-vis transition with a maximum at λ=644 nm and an ε= 31.9 M^{-1} cm^{-1} corresponds to d-d transitions, and therefore metal-centered, no band for Alk base has been observed in this region. No changes were observed up to 2 h, and the spectral patterns observed were similar to those of the blue solid obtained by diffuse reflectance spectroscopy (Fig. S2). Hence, we propose that the structure of the solid was retained upon dissolution and the complex remained stable at least during 2 h. Furthermore, a spectrophotometric titration of Alk:Cu (Fig. S5) was conducted using various ligand-to-metal molar ratios in ethanolic solutions ranging from L:M 10 to 0.7 at pH 7.5. The results indicated a final stoichiometry of 2:1 (L:M), which is consistent with the structural determination of the solid complex. The recorded FTMS spectrum in EtOH solution shows a complex with two ligands per Cu center as the most abundant species in the solution, indicating also, that the stoichiometry of the complex is retained in solution. The spectrum also shows the presence of different fragments, such as the free ligand and other Cu:L complexes with lower intensities (Fig. S3 and S4).

Antioxidant activities

The antioxidant properties of the free ligand and **CuAlk** were studied by different techniques: the scavenging power of the $DPPH^{\bullet}$, the scavenging of $OH^{\bullet}$ radical, the inhibition of the production of peroxyl radical ($ROO^{\bullet}$, lag phase) and the ability of mimic the SOD activity according to previously reported methods [26].

Neither Alk or **CuAlk** have shown significant scavenging activities on $DPPH^{\bullet}$ or on $ROO^{\bullet}$ radicals at concentrations up to 500 μM (Figs. S6, S7). Even though Cu(II) did not show any scavenging activity on $OH^{\bullet}$ radical in the range of concentrations studied, Alk and **CuAlk** exhibited a significant scavenging activity of this radical (Fig. 4). The statistical analysis of the data shows no difference between them, with an inhibition close to 40 % at the maximum concentration tested (100 μM).

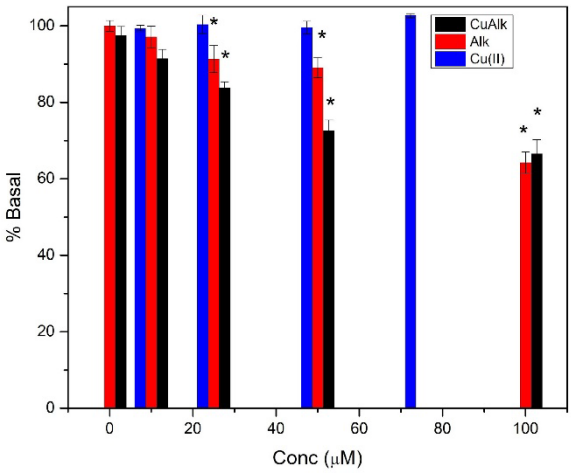

Fig. 4. Scavenging of hydroxyl radical ($OH^{\bullet}$) for **CuAlk** (black), Alk (red) and copper(II) salt (blue). * Significant values in comparison with the control ($p < 0.05$).

For **CuAlk**, the measured SOD activity (IC_{50} = 0.69 μM) (Table 2) is significantly lower than the corresponding value obtained for the metallic cation and comparable to the activity reported for the bovine enzyme (IC_{50}=0.21 μM) [26]. Alk base has not shown significant activity since at the maximum concentration tested (100 μM), an inhibition of only the 65 % of the NBT reduction was observed. In general terms, at neutral pH the value of the rate constant for the second order spontaneous dismutation of the native enzyme is about 2 x 10^7 M^{-1} s^{-1} [27]. From the obtained IC_{50} values, we have compared the activities from the calculation of the k_{McCF} (McCord-Fridovich) constant that standardizes the values and is independent of both detector concentration and nature [28]. The constant is calculated from the equation: $K_{McCF} = k_{detector}$·[detector]/IC_{50}, where k_{NBT} (pH = 7.8) = 5.94 × 10^4 mol^{-1} L s^{-1} and [detector]= NBT concentration in the mixture. Again, a SOD

J. Mex. Chem. Soc. **2024**, *68*(2)
Regular Issue

ISSN-e 2594-0317

mimetic value in the order of the value of the native enzyme was obtained for the complex. Based on these results, it is possible to conclude that the complexation of Cu(II) by Alk enhanced considerably its SOD mimetic behaviour. Just a few reported complexes exhibited such an enhancement in the SOD mimetic activity [29].

Table 2. IC_{50} values and kinetic constants of **CuAlk**, Cu(II) salt and bovine erythrocyte superoxide dismutase.

	IC_{50} (µM)	**K_{McCF} ($mol^{-1}L\ s^{-1}$)**
Cu(II)	3.20[a]	1.3 x 10^6
Alk	100 [b]	ND[c]
CuAlk	0.69	6.4 x 10^6
SOD	0.21[a]	2.1 x 10^7

[a] according to [26], [b] corresponds to 65 % inhibition, [c] not determined

It was suggested that the SOD mimicking ability depends on the coordination geometry around the metal center and the ligand system used, which affects its redox potentials [29]. For example, in copper(II) complexes with peptides and amide groups, a higher SOD-like activity is observed when the complex has a specific nitrogen donor set forming the metal binding site, and the Cu(II) center is weakly coordinated to solvent molecules in the axial position [30]. In this case, the improvement of **CuAlk** in comparison to Alk, could be due to the complexation of copper(II) with N and O donor atoms, according to the previous suggestions.

Conclusions

In this work, a new copper(II) complex $[Cu(Alk)_2(H_2O)_2](NO_3)_2$, **CuAlk** was synthesized by the addition of cupric nitrate to an ethanolic solution of aliskiren. In this new compund, the renin inhibitor aliskiren is acting as a bidentate ligand. The complex is stable in solution at physiological pH value. Neither the complex, nor the ligand were able to scavenge the $DPPH^{\bullet}$ and $ROO^{\bullet}$ radicals. On the other hand, both compounds have shown activity against $OH^{\bullet}$ radical. Furthermore, the complexation of Cu(II) with aliskiren has shown an increase in the SOD mimetic activity, considerably improving the antioxidant properties of the metal center.

Acknowledgements

This work was supported by UNLP (X/871), CICPBA, and ANPCyT (PICT 2019-0945), UNMdP (EXA 1022/21), Argentina. N.J. is Doctoral assistant/Ph.D. student at EPFL, Switzerland, M.S.I. is research fellow of UNMdP and CONICET, E.G.F, is research fellow of CONICET. P.A.M.W. is a research fellow of CICPBA, Argentina.

References

1. Wood, J. M.; Maibaum, J.; Rahuel, J.; Grütter, M. G.; Cohen, N. C.; Rasetti, V.; Rüger, H.; Göschke, R.; Stutz, S.; Fuhrer, W.; Schilling, W.; Rigollier, P.; Yamaguchi, Y.; Cumin, F.; Baum, H. P.; Schnell, C. R.; Herold, P.; Mah, R.; Jensen, C.; O'Brien, E.; Stanton, A.; Bedigian, M. P. *Biochem. Biophys. Res. Commun.* **2003**, *308*, 698–705. DOI: https://doi.org/10.1016/s0006-291x(03)01451-7.

J. Mex. Chem. Soc. **2024**, *68*(2)
Regular Issue

ISSN-e 2594-0317

2. Cromer, J.; Peker, S. *Pharm. Ther.* **2008**, *33*, 92–96.
3. Alshahrani, S.; Tripathi, P.; Ashafaq, M.; Sultan, M. H.; Moni, S. S.; Tripathi, R.; Siddiqui, A. H.; Rashid, H.; Malhan, A. M. *Toxin Rev.* **2022**, *41*, 175–185. DOI: https://doi.org/10.1080/15569543.2020.1857772.
4. Alshahrani, S. *Chem. Biol. Interact.* **2020**, *326*, 109145. DOI: https://doi.org/10.1016/j.cbi.2020.109145.
5. Uriu-Adams, J.Y.; Keen, C.L. *Mol Aspects Med.* **2005**, 26, 268-98. DOI: http://doi.org/10.1016/j.mam.2005.07.015.
6. Bontchev, P.R.; Pantcheva, I.N. *Trans. Met. Chem.* **2002**, 27, 1–21. DOI: https://doi.org/10.1023/A:1013466529495.
7. Islas, M.S.; Luengo, A.; Franca, C.A. Griera Merino, M.; Calleros, L.; Rodriguez-Puyol, M.; Lezama, L.; Ferrer, E.G.; Williams, P.A.M. *J. Biol. Inorg. Chem.* **2016**, 21, 851–863. DOI: https://doi.org/10.1007/s00775-016-1384-5
8. Claudel, M.; Schwarte, J.V.; Fromm, K.M. *Chemistry,* **2020**, 2, 849-899. DOI: https://doi.org/10.3390/chemistry2040056
9. Van Rijt, S.H., Sadler P.J. *Drug Discov. Today* **2009**, 14, 1089-1097. DOI: https://doi.org/10.1016/j.drudis.2009.09.003
10. Baddiel, C. B.; Cavendish, C. D.; George, W. O. *J. Mol. Struct.* **1970**, *5*, 263–274. DOI: https://doi.org/10.1016/0022-2860(70)80029-1
11. Halliwell, B.; Gutteridge, J. M. C.; Aruoma, O. I. *Anal. Biochem.* **1987**, *165*, 215–219. DOI: https://doi.org/10.1016/0003-2697(87)90222-3.
12. Zhong, Z.; Ji, X.; Xing, R.; Liu, S.; Guo, Z. *Bioorg. Med. Chem.* **2007**, *15*, 3775–3782. DOI: https://doi.org/10.1016/j.bmc.2007.03.036.
13. Huang, W. Y.; Majumder, K.; Wu, J. *Food Chem.* **2010**, *123*, 635–641. DOI: https://doi.org/10.1016/j.foodchem.2010.04.083.
14. Islas, M. S.; Luengo, A.; Franca, C. A.; Merino, M. G.; Calleros, L.; Rodriguez-Puyol, M.; Lezama, L.; Ferrer, E. G.; Williams, P. A. M. *J. Biol. Inorg. Chem.* **2016**, *21*. DOI: https://doi.org/10.1007/s00775-016-1384-5.
15. Tabbì, G.; Giuffrida, A.; Bonomo, R. P. *J. Inorg. Biochem.* **2013**, *128*, 137–145. DOI: https://doi.org/10.1016/j.jinorgbio.2013.07.035.
16. Peisach, J.; Blumberg, W. E. *Arch. Biochem. Biophys.* **1974**, *165*, 691–708. DOI: https://doi.org/10.1016/0003-9861(74)90298-7.
17. Castinñeiras, A.; Balboa, S.; Carballo, R.; Niclós, J. *Zeitschrift für Anorg. und Allg. Chemie* **2002**, *628*, 2353–2359. DOI: https://doi.org/10.1002/1521-3749(200211)628:11%3C2353::AID-ZAAC2353%3E3.0.CO;2-5.
18. Lever, A. B. P. *Inorganic Electronic Spectroscopy*, Second Edi.; Elsevier: Toronto, Canada, **1984**.
19. Miyamoto, T.; Kamino, S. Odani, A.; Hiromura, M.; Enomoto, S. *Chem. Lett.* **2013**, *42*, 1099-1101. DOI: https://doi.org/10.1246/cl.130405.
20. Hureau, C.; Eury, H.; Guillot, R.; Bijani, C.; Sayen, S.; Solari, P.L.; Guillon, E.; Faller, P.; Dorlet, P. *Chem. A Eur. J.* **2011**, *17*, 10151–10160. DOI: http://doi.org/10.1002/chem.201100751.
21. Aydoğmuş, Z.; Sari, F.; Ulu, S. T. *J. Fluoresc.* **2012**, *22*, 549–556. DOI: https://doi.org/10.1007/s10895-011-0988-y.
22. Kong, J.; Yu, S. *Acta Biochim. Biophys. Sin. (Shanghai).* **2007**, *39*, 549–559. DOI: https://doi.org/10.1111/j.1745-7270.2007.00320.x.
23. Nakamoto, K. *Infrared and Raman Spectra of Inorganic and Coordination Compounds Part A*; Wiley, **2009**.
24. Cacela, C.; Duarte, M. L.; Fausto, R. *Spectrochim. Acta Part A Mol. Biomol. Spectrosc.* **2000**, *56*, 1051–1064. DOI: https://doi.org/10.1016/S1386-1425(99)00203-6.
25. Matsoukas, M. T.; Zoumpoulakis, P.; Tselios, T. *J. Chem. Inf. Model.* **2011**, *51*, 2386–2397. DOI: https://doi.org/10.1021/ci200130m.

J. Mex. Chem. Soc. **2024**, *68*(2)
Regular Issue

ISSN-e 2594-0317

26. Islas, M. S.; Lezama, L.; Griera, M.; Cortes, M. A.; Rodriguez, M.; Ferrer, E. G.; Williams, P.A.M. *J. Inorg. Biochem.* **2013**, *123*, 23–33. DOI: https://doi.org/10.1016/j.jinorgbio.2013.02.005.
27. McCord, J. M.; Fridovich, I. *J. Biol. Chem.* **1969**, *244*, 6049–6055.
28. Durot, S.; Policar, C.; Cisnetti, F.; Lambert, F.; Renault, J.; Pelosi, G.; Blain, G.; Korri-Youssoufi, H.; Mahy, J.-P. *Eur. J. Inorg. Chem.* **2005**, *2005*, 3513–3523. DOI: https://doi.org/10.1002/ejic.200400835.
29. Khalid, H.; Hanif, M.; Hashmi, M.; Mahmood, T.; Ayub, K.; Monim-ul-Mehboob, M. *Mini-Reviews Med. Chem.* **2013**, *13*, 1944–1956. DOI: https://doi.org/10.2174/13895575113136660092.
30. Szyrwiel, L.; Shimura, M.; Setner, B.; Szewczuk, Z.; Malec, K.; Malinka, W.; Brasun, J.; Pap, J. S. *Int. J. Pept. Res. Ther.* **2019**, *25*, 711–717. DOI: https://doi.org/10.1007/s10989-018-9717-6.

Article

J. Mex. Chem. Soc. **2024**, *68*(2)
Regular Issue

ISSN-e 2594-0317

Phytochemistry, Mineral Estimation, Nutritional, and the *In Vitro* Anti-Sickling Potentials of Oil Extracted from the Seeds of *Mucuna Flagellipes*

Emmanuel U. Ejiofor[1*α], Alwell C. Ako[1α], Maxwell T. Kube[2], Ernest C. Agwamba[3], Chinweuba Alala[1], Kelvin Maduabuchi[1], Maureen Ejiofor[4]

[1]Department of Chemical Sciences, Faculty of Science, Clifford University, Owerrinta, Abia State, Nigeria.
[2]Department of Biochemistry, Usmanu Danfodiyo University, Sokoto, Nigeria.
[3]Department of Chemistry, College of Science and Technology, Covenant University, Ota, Ogun State, Nigeria.
[4]Department of Biochemistry, College of Natural Sciences, Michael Okpara University of Agriculture, Umudike, Abia State, Nigeria.

***Corresponding author:** Emmanuel Ejiofor, email: ejioforemmanuelbiz@gmail.com; Phone: +234 7036250103.

[α]Equal contribution and are both first authors.

Received November 5th, 2022; Accepted May 21st, 2023.

DOI: http://dx.doi.org/10.29356/jmcs.v68i2.1898

Abstract. Sickle cell disease is an inherited blood disorder indicative of red blood cells becoming sickle-shaped. The study investigated the *in vitro* anti-sickling potentials of the seed oil of *M. flagellipes*. The phytochemistry (fatty acids, vitamins, and minerals) was also determined using standard protocols. Finally, nutritional calculations on the oil were performed to determine its suitability for nutritional purposes. The result showed high zinc content (780 ± 2.50 µg/ 100 mg), while low iron content was observed (170 ± 1.30 µg/ 100 mg). Vitamin analysis showed the presence of vitamins A, E and K with values of 220 ± 1.60, 370 ± 2.20, and 197 ± 0.23 µg/100 mg respectively. The fatty acid profile revealed oleic (31.87 %) and linoleic (18.30 %) fatty acids as the major unsaturated fat in the oil, while palmitic fatty acid (5.91 %) was the major saturated fatty acid. Nutritional calculations showed high PUFA/SFA (2.07), MUFA/SFA (3.62), and UI (68.47). However, the index of thrombogenicity (0.07) and atherogenicity (0.11) was low in the seed oil. Finally, the *in vitro* anti-sickling potentials of the seed oil showed the oil inhibited and reversed sickling in a dose-dependent manner. Hbs polymerization was also inhibited and Fe^{2+}/Fe^{3+} was upregulated following treatment with the seed oil. Collectively, the oil showed good anti-sickling potentials, which can be labelled to the presence of zinc, vitamins and unsaturated fat. The nutritional calculations suggest that the seed oil is cardio-friendly and does not pose any nutritional threat.
Keywords: Anti-sickling, *M. flagellipes*, zinc, vitamins, unsaturated fats, polymerization.

Resumen. La anemia falciforme es un trastorno hereditario de la sangre que indica que los glóbulos rojos adquieren forma de hoz. Este estudio investigó los potenciales de evitar la malformación de células falciformes (anti-*sickling*) in vitro por el aceite de la semilla de *Macuna. flagellipes*. La fitoquímica (ácidos grasos, vitaminas y minerales) se determinó utilizando protocolos estándar. Finalmente, se realizaron cálculos nutricionales del aceite para determinar su idoneidad para fines nutricionales. El resultado mostró alto contenido de zinc (780 2,50 µg/100mg), mientras que se observó bajo contenido de hierro (170 1,30 µg/100mg). El análisis vitamínico mostró presencia de vitamina A, E y K con valores de 220 ± 1.60, 370 ± 2.20 y 197 ± 0.23 µg/100 mg, respectivamente. El perfil de ácidos grasos reveló ácidos oleicos (31.87 %) y linoleico (18.30 %) como las principales grasas insaturadas del aceite, mientras que el ácido palmítico (5.91 %) fue el principal ácido graso saturado. Los cálculos nutricionales mostraron un alto PUFA/SFA (2.07), MUFA/SFA (3.62), UI (68.47). Sin embargo, el índice de trombogenicidad (0.07) y aterogénesis (0.11) fue bajo en el aceite de semilla. Por último, los potenciales para evitar la malformación de células falciformes

J. Mex. Chem. Soc. **2024**, *68*(2)
Regular Issue

ISSN-e 2594-0317

in vitro por aceite de semilla mostraron que el aceite inhibió y revirtió la enfermedad de una manera dependiente de la dosis. La polimerización de Hbs también fue inhibida y Fe^{2+}/Fe^{3+} fue sobreregulada después del tratamiento con el aceite de la semilla. Colectivamente, el aceite mostró un buen potencial evitar la malformación de células falciformes, que puede ser atribuido a la presencia de zinc, vitaminas y grasa insaturada. Los cálculos nutricionales sugieren que el aceite de semilla es cardio-amigable y no representa ninguna amenaza nutricional.
Palabras clave: Anti-sickling; M. flagellipes; zinc; vitaminas, grasas insaturadas; polimerización.

Abbreviations

Gas chromatograph-mass spectroscopy	GC-MS
Hemoglobin	HB
Hypercholesterolemic	HYPER
Hypocholesterolemic	HYPO
Index of atherogenicity	IA
Index of thrombogenicity	IT
M. flagellipes seed oil	MFSO
Methemoglobin	MHb
Molecular weight	MW
Monounsaturated fatty acid	MUFA
National Institute of Standards and Technology	NIST
Oxidizability	Oxi
Polyunsaturated fatty acids	PUFA
Recommended dietary allowance	RDA
Retention time	RT
Saturated fatty acid	SFA
Sickle cell anemia	HbSS

Introduction

Sickle cell disease is an inherited blood disorder characterized by the production of erythrocytes that are sickled or shaped like crescents. In sickle cell disease, the body produces hemoglobin S, which is considered abnormal and affects the transport of oxygen around the body. Generally, it is caused by a mutation in the amino acid located at position 6 of the β-globin gene [1]. The amino acid valine replaces glutamic acid in the 6^{th} position of the β-globin chain located on chromosome 11. These series of events lead to the formation of the abnormal red blood cell with hemoglobin S, which displays a sickled shape [2]. This abnormality reduces the efficiency of the sickled hemoglobin to transport oxygen around the body, decreasing the solubility of blood in the deoxygenated form. Moreso, when the partial pressure of oxygen decreases, the abnormal hemoglobin becomes less soluble, forming polymers with other sickle hemoglobin [3]. The inefficiency of abnormal hemoglobin (hemoglobin S) to transport oxygen around the body, coupled with its ability to form polymers that can block blood flow routes, leads to the development of secondary conditions such as oxidative stress, inflammation, pain, cardiovascular diseases, vaso-occlusive crises, organ malfunctioning, and bone degeneration accompanying this disease [4].

This disease condition currently has no known cure, but medications are available to manage the condition and also alleviate the symptoms of the secondary complications associated with it. Furthermore, the use of nutrients such as vitamins, amino acids, and fatty acids in diets for managing the disease condition has long been documented in the literature [5-9]. Several drugs used in the management of this disease condition, such as hydroxyurea, piracetam, calcium antagonists, and several painkillers, are not without side effects and toxicities to body organs, which are attributed to their long-term use [3,10]. These drugs when available in developing countries are very expensive to afford, driving the search for alternatives from plants, which are widely available, relatively safe, and cheap [4].

J. Mex. Chem. Soc. **2024**, *68*(2)
Regular Issue

ISSN-e 2594-0317

Numerous studies have reported the application of plant materials for the management of sickle cell disease [4,11]. The plant *M. flagellipes,* which belongs to the family Leguminosae, is a plant localized mainly in Africa but present in other parts of the world [12]. The high nutritional profile and minerals of the leaves of *Mucuna flagellipes* have been reported by Ihedioha and Okoye [13]. The phytochemistry profile and mineral estimation of the seeds have shown a high content of flavonoids, vitamin C, zinc, and iron [14]. Furthermore, Uchegbu et al. [15] reported the presence of 9-octadecenoic acid, ethyl ester linoleic acid, ethyl ester, 9-octadecanoic acid, hexadecanoic acid, ethyl hexadecanoate, ethyl octadecenoate, eicosanoic acid, ethyl icosanoate, 3-hydroxypropyl-9-oate, and 9-methylbicyclo (3,3,1) nonane in the plant extract. Ajayi et al. [16] reported the presence of stearic, palmitic, linoleic, and oleic as major fatty acids in the seed oil of *M. flagellipes*. Recently, animal studies by Abireh et al. [17] reported the potential of *M. flagellipes* leaf extract to alleviate the bone marrow suppression, anemia, and leukemia effects following cyclophosphamide treatment of malignancies. The extract significantly improved packed cell volume, white blood cell counts, and the number of proliferating cells in the bone marrow. The ethanol extract of the seeds has been reported to possess anti-hypertensive potentials in salt-induced hypertension in rats *via* its ability to reduce blood pressure parameters [18]. In traditional systems in Eastern Nigeria, plant material is widely employed for the treatment of various ailments by traditional medical practitioners, specifically for the reduction of hypertension and blood-related issues.

Interest is growing in the use of seed oils rich in polyunsaturated and omega-3 fatty acids for managing sickle cell disease [19]. Polyunsaturated and omega-3 fatty acids have been reported to possess antioxidant activities and membrane protection potentials, which are strongly required in sickle cell disease fatty acids and omega-3 fatty acids for managing various diseases [9,20]. Furthermore, the identification of new sources of zinc in the diet of sickle cell patients is a new focus in managing the abnormalities associated with the disease.

Currently, there is no information on the *in vitro* anti-sickling potential of the seed oil extract of *M. flagellipes*. Therefore, the study aimed to assess the *in vitro* anti-sickling potentials of *M. flagellipes* seed oil (MFSO) by looking at its effects on inhibition and reversal of sickling, inhibition of hemoglobin polymerization, and the Fe^{2+}/Fe^{3+} ratio. The minerals (zinc and iron), vitamins (A, E, and K), and fatty acid profile were determined using spectrophotometric techniques. Nutritional calculations were employed to determine the safety potential of consuming the seed oil.

Experimental

Methods

Chemicals used

All chemicals used for this study were of analytical grade and were obtained from Merck, Germany.

Plant material procurement

The seeds of *M. flagellipes* were purchased in July 2021 from Orie Ntigha market in Isiala Ngwa North Local Government Area of Abia State, Nigeria. A sample of the seed was identified as *M. flagellipes* seed by Dr. Magnus C. Nwoko, a taxonomist at the Department of Biology, Federal University of Technology, Owerri, Imo State, Nigeria. A voucher specimen was assigned to the plant material (AEE/21/0155), and the specimen was deposited in the herbarium of the Department of Biology, Federal University of Technology, Owerri, Imo State, Nigeria.

Plant materials preparation and oil extraction

The casing of the seeds was cracked open to obtain the seed cotyledons. The seed cotyledons were washed in running tap water to remove sand and debris and then dried under shade for two weeks to attain an unformed weight. The dried seeds were milled into powder form with a mechanical blender and then stored in an airtight container. Extraction was performed using a Soxhlet extractor and n-hexane as a solvent. Briefly, 50 g of seeds of *M. flagellipes* powder were extracted and soaked in 500 mL of n-hexane (1:10 w/v) with the temperature set at 35 ºC throughout the extraction process. To ensure complete extraction of oil in the sample, the set-up was allowed to reflux continuously till a clear liquid was seen [21]. The extract was evaporated using a rotary evaporator and stored in a sterile brown and amber bottle in the dark prior to further analysis.

J. Mex. Chem. Soc. **2024**, *68*(2)
Regular Issue

ISSN-e 2594-0317

Phytochemical profile

GC-MS profiling and fatty acid analysis of seed oil extract

GC-MS analysis was performed using the method described by Ariyike et al. [22] at the University of Lagos, Lagos State, Nigeria. The composition of *M. flagellipes* seed oil (MFSO) was analyzed using a gas chromatograph coupled with a mass spectrometer GC-MS-QP 2010 Plus Shimadzu system. Operating condition of the GC-MS was Column Elite-1 fused silica capillary column (30 m × 0.25 mm 1D × µl df, composed of 100 % dimethyl polysiloxane). The carrier gas was ultra-pure helium (99.999 %) at a flow rate of 1.0 mL/min and an injection volume of 2 µL was employed (split ratio of 10:1). The injector temperature was set at 250 °C, ion source temperature 280 °C. The oven temperature was programmed 110°C (Isothermal for 2 min) with an increase of 10 °C /min to 200 °C then 5 °C/min to 280 °C/min, ending with a 9 min isothermal at 280 °C. Mass spectra were taken at 70 eV; a scan interval of 0.5 s and fragments from 40 to 550 Da. Total GC running time was 22 min and the compounds were identified by direct comparison of the retention times (RT) and mass fragmentation pattern with those from the National Institute of Standards and Technology (NIST) Library [23-24].

Vitamin estimation of MFSO

Vitamin A and E concentrations were determined in the oil sample using spectrophotometric methods as described by De'Leenheer et al. [25]. Briefly, exactly 0.1 g of the sample was dissolved in an acetone/hexane mixture (70:30 v/v), and the total carotenoid and vitamin E determinations were carried out by measuring absorbance at 470 nm and 270 nm, respectively, against a blank sample (solvent). Vitamin K was determined spectrophotometrically, as described by Gul et al. [26].

Mineral estimation of MFSO

The estimation of iron and zinc was performed using the wet digestion method described by AOAC [27]. Briefly, 0.5 g of the oil sample was boiled at 100 °C with 5 mL of concentrated nitric acid and 5 mL of a 30 % hydrogen peroxide solution for about 2 hours in an electric heating mantle until a clear solution was obtained. The solution was cooled and filtered through the Whatman No. 45 filter paper and then through 0.45 Millipore filter paper. The obtained filtrate was made up to 25 mL of the volumetric flask with distilled water and then analyzed for the individual minerals using an atomic absorption spectrophotometer (Bulk Scientific AAS model 210, equipped with a single slot burner and an air acetylene flame). Working standard solutions of zinc and iron were prepared, and the calibration and measurement of absorbance against a blank were performed using an AAS. The absorbance of each element in the filtrate was read at its wavelength from the spectrophotometer, and its concentration in the sample was extrapolated from the standard curve produced from the absorbance of the standard elements.

Nutritional indices of oil sample (MFSO)

Fatty acids ratios

The ratio between polyunsaturated fatty acid (PUFA) and saturated fatty acid (SFA) [PUFA/SFA] also regarded as the polyene index was estimated as described by Chen and Liu [28] and Eke et al. [29]. The ratios between monounsaturated fatty acids (MUFA) and SFA [MUFA/SFA], PUFA and MUFA [PUFA/MUFA], and [(PUFA+MUFA)/SFA] were calculated to indicate the nutritional potentials of SOPA.

Oxidizability

The oxidative stability which is also regarded as the oxidizability was determined using the formula described by McCormick et al. [30]

$$Oxidizability = [\frac{0.02(\%\ oleic) + \%\ linoleic}{100}] \quad (1)$$

Index of atherogenicity (IA)

The index of atherogenicity was calculated as described by Chen and Liu [28].

$$[C12{:}0 + (4\ x\ C14{:}0) + C16{:}0]/UFA \quad (2)$$

J. Mex. Chem. Soc. **2024**, *68*(2)
Regular Issue

ISSN-e 2594-0317

where C12:0 is lauric fatty acid; C14:0 is myristic fatty acid and C16:0 is palmitic fatty acids. UFA is summation of unsaturated fatty acids in oil samples.

Index of thrombogenicity (IT)

The thrombogenicity index was calculated as Chen and Liu described [28].

$$IT = (C14{:}0+C16{:}0+C18{:}0)/[0.5\ x\ MUFA + 0.5\ x\ n{-}6\ PUFA + 3\ x\ n{-}3\ PUFA{+}n{-}3{\div}n{-}6] \quad (3)$$

where C18:0 is stearic fatty acid; C14:0 is myristic fatty acid and C16:0 is palmitic fatty acids. MUFA is summation of monounsaturated fatty acids in oil samples.

Hypocholesterolemic/ hypercholesterolemic ratio

The hypocholesterolemic/ hypercholesterolemic ratio was calculated as described by Chen and Liu [28]

$$(cis - C18{:}1 + PUFA)/(C12{:}0 + C14{:}0 + C16{:}0) \quad (4)$$

Unsaturation index (UI)

The UI which shows the level of unsaturation in oils was determined as described by Chen and Liu [28]

$$UI = 1\ x(\%\ monoenoics) + 2\ x\ (\%\ dienoics) + 3\ x\ (\%\ trienoics) + 4\ x\ (tetraenoics) + 5\ x\ (\%\ pentaenoics) + 6\ x\ (\%\ hexaenoics) \quad (5)$$

***In vitro* anti-sickling assay**

Collection of blood sample and ethical approval

Sickle cell patients attending the Clifford University Medical Centre, Ihie, Isiala Ngwa North LGA, Abia State, Nigeria, provided blood samples for the research after getting their consent and approval. Ethical clearance for the study was obtained from the Clifford University Research Ethics Committee, and ethical clearance number CLU/ETC/21/103 was assigned. Six milliliters (6 mL) of blood were used the same day for analyses.

Sickling inhibition test

The *in vitro* sickling inhibition assay was performed using the method described by Egba et al. [31]. Briefly, 2 drops of HbSS blood, 2 drops of freshly prepared 2 % sodium metabisulphite and 2 drops of MFSO were mixed and covered. The solution was incubated for 30 mins at 37 °C and with the aid of a pipette, a drop was put on a slide, covered with a cover slip, and then viewed using a microscope at x 10 and x 40 magnifications. One hundred (100) cells were counted each from three randomly selected fields to evaluate the effect of MFSO on the HbSS erythrocytes. The test was performed in replicate, and the average reading was taking. The sickling inhibition (%) was determined using the equation below:

$$\text{Percentage inhibition} = \frac{number\ of\ cells\ unsickled}{Total\ number\ of\ cells\ counted} \times 100 \quad (6)$$

The control experiment was set up and did not contain MFSO, while *p*-hydroxybenzoic acid (5 % PABA) was used as standard agent.

Sickling reversal test

The sickling reversal test was performed as described by Ekeke et al. [32]. Briefly, 2 drops of HbSS blood were mixed with 2 drops of freshly prepared sodium metabisulphite and the mixture was covered. The mixture was incubated for 30 min during which sickling was induced. This was followed by the addition of 2 drops of buffered extract and the

J. Mex. Chem. Soc. **2024**, *68*(2)
Regular Issue

ISSN-e 2594-0317

resulting mixture was incubated for another 30 min. Buffer was used in place of the extract for the control, and a drop of each was placed on a slide and viewed at × 40 magnification. The percentage reversal was calculated as:

$$\text{Percentage reversal} = \frac{number\ of\ cells\ unsickled}{Total\ number\ of\ cells\ counted} \times 100 \quad (7)$$

Polymerization studies

The polymerization study was performed as described by Noguchi and Schechter [33]. Briefly, 0.25 cm^3 of normal saline (0.9 % w/v) was added to each test tubes containing 0.5 cm^3 of various dilutions of the MFSO respectively. Freshly prepared aqueous sodium metabisulphite (2.2 cm^3) and HbSS erythrocytes (0.05 cm^3) were added into the test tubes simultaneously. The contents were mixed, and the absorbance taken at 700 nm using a spectrophotometer after standardizing it with distilled water as blank. Readings were taken at 5- min interval for a period of 35 min and appropriate control experiment was set up without the extracts.

Determination of the Fe^{2+}/Fe^{3+} ratio in sickle cell blood

The method of Tietz [34] was adopted for the determination of Fe^{2+}/Fe^{3+} ratio in sickle cell blood. This method works on the principle that hemoglobin and methemoglobin absorbs light at 540 nm and 630 nm respectively. Exactly 5.0 cm^3 distilled water and 0.02 cm^3 sickle cell blood was placed in a test-tube. Exactly 0.02 cm^3 saline solution was introduced into the test tube and this served as the control. The test tube was kept for an hour at an ambient temperature and a spectrophotometer was used to determine its absorbance at 540 nm and 630 nm wavelengths. To determine the effect of MFSO on Fe^{2+}/Fe^{3+} ratio, the process described above was repeated replacing saline solution with different dilutions of the extract. The percentage hemoglobin and methemoglobin were determined thus:

$$\text{Percentage hemoglobin } (Fe^{2+}) = \frac{(A540)^2}{(A540)^2 + (A540)^2} \times 100 \quad (8)$$

The ratio of Fe^{2+}/Fe^{3+} was determined by dividing the values of each % Hb with the corresponding values of % MHb (before approximation).

Statistical analysis

The results were expressed as mean ± standard deviation. Data were analyzed using one way analysis of variance (ANOVA) and grouping information by Tukey pairwise comparison method with the Minitab 17 software, USA. Values were with $p < 0.05$ were considered as being significant.

Results

Quantification of MFSO fatty acids and phytocompounds

Table 1. Identified compounds present in *M. flagellipes* seed oil (MFSO).

Peak No.	Name of Compound	MW (g)	Fatty acid class	RT (min)	Molecular formular	Concentration (%)
1	2-hexanamine, 4-methyl	115.22	-	6.54	$C_7H_{17}N$	0.52
2	Resorcinol	110.11	-	7.73	$C_6H_6O_2$	1.37
3	Cathinone	149.19	-	8.83	$C_9H_{11}NO$	1.33
4	Guanidine, N,N-dimethyl	87.12	-	11.84	$C_3H_9N_3$	4.00

J. Mex. Chem. Soc. **2024**, *68*(2)
Regular Issue

ISSN-e 2594-0317

6	Pentadecanoic acid** (pentadecyclic acid)	242.39	SFA	14.55	$C_{15}H_{30}O_2$	1.04
7	n-Hexadecanoic acid** (palmitic fatty acid)	256.40	SFA	14.82	$C_{16}H_{32}O_2$	5.91
8	9,12-Octadecadienoic acid** (linoleic fatty acid)	280.44	PUFA-6	15.92	$C_{18}H_{32}O_2$	18.30
9	9-Octadecenoic acid** (oleic acid)	282.47	MUFA	15.99	$C_{18}H_{34}O_2$	31.87
12	Octadecanoic acid** (stearic acid)	284.48	SFA	16.46	$C_{18}H_{36}O_2$	1.85
13	Phenylephrine	167.20	-	17.76	$C_9H_{13}NO_2$	1.87
14	I-Guanidinosuccinimide	141.13	-	17.96	$C_5H_7N_3O_2$	0.69
16	Propanamide	73.09	-	19.13	C_3H_7NO	1.03
17	N-Desmethyltapentadol	207.31	-	19.58	$C_{13}H_{21}NO$	0.79
19	Alanyl-beta-alanine	344.40	-	20.03	$C_6H_{12}N_2O_3$	1.65
20	1,8-Octanediamine, *N,N′*-dimethyl-	172.31	-	20.09	$C_{10}H_{24}N_2$	1.85
21	3-Propoxamphetamine	193.28	-	20.21	$C_{12}H_{19}N_0$	0.94
22	1-Phenanthrene carboxylic acid	222.24	-	20.29	$C_{15}H_{10}O_2$	10.61
24	2-Heptenoic acid, 4-cyclopropyl-5-methylene-, methyl ester, (E)-	194.27	-	20.43	$C_{12}H_{18}O_2$	9.22
25	3-Keto-isosteviol	332.40	-	20.59	$C_{20}H_{28}O_4$	4.42

RT: Retention time (min); MW: Molecular weight (g); ** indicates fatty acids; SFA: Saturated fatty acids; PUFA: Polyunsaturated fatty acids; MUFA: Monounsaturated fatty acids

Vitamin and mineral content of MFSO

Table 2. The vitamin and mineral content of MFSO.

Vitamin	Concentration (µg/100mg)	RDA (mg/adult/day)
A	220 ± 1.60 (2.2 mg/kg)	0.9
E	370 ± 2.20 (3.7 mg/kg)	15
K	197 ± 0.23 (1.9 mg/kg)	0.12

J. Mex. Chem. Soc. **2024**, *68*(2)
Regular Issue

ISSN-e 2594-0317

Minerals		
Fe	170 ± 1.30 (1.7 mg/kg)	8
Zn	780 ± 2.50 (7.8 mg/kg)	7-9

Data are mean ± SD, n = 3; MFSO- *M. flagellipes* seed oil; RDA: recommended dietary allowance

Nutritional indices of MFSO

Table 3. The nutritional indices of the MFSO oils.

Sample	PUFA/ SFA	MUFA/ SFA	PUFA/ MUFA	(PUFA+ MUFA)/ SFA	IA	IT	HYPO/ HYPER	UI	OXI
MFSO	2.07	3.62	0.57	5.70	0.11	0.07	3.09	68.47	0.18

MFSO- oil of *M. flagellipes* seeds; Oxi- oxidiziability; HYPO- Hypocholesterolemic; HYPER- Hypercholesterolemic

Effects of MFSO extracts on sickling inhibition

The MFSO significantly ($p < 0.05$) decreased sickling in human erythrocytes when compared to the negative control (normal saline) at all concentrations tested in which sodium metabisulphite was used to exacerbate sickling. The highest inhibition (52.66 ± 0.18) was observed at the highest concentration, 100 %. However, this activity was low compared to the standard agent used p-hydroxybenzoic acid (PABA) used as the positive control.

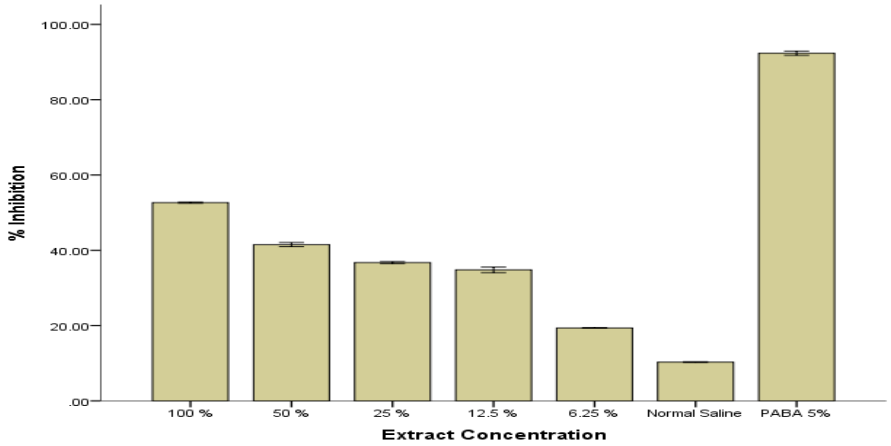

Fig. 1. % sickling inhibition of MFSO.

Effect of MFSO on sickling reversal

The MFSO significantly *($p < 0.05$)* reversed sickling in human erythrocytes when compared to the negative control (normal saline) at all concentrations tested in which sodium metabisulphite was used to exacerbate sickling. The highest inhibition (91.76 ± 0.65) was observed at the highest concentration, 100 %. However, this activity was low compared to the standard agent used *p*-hydroxybenzoic acid (PABA) used as the positive control.

J. Mex. Chem. Soc. **2024**, *68*(2)
Regular Issue

ISSN-e 2594-0317

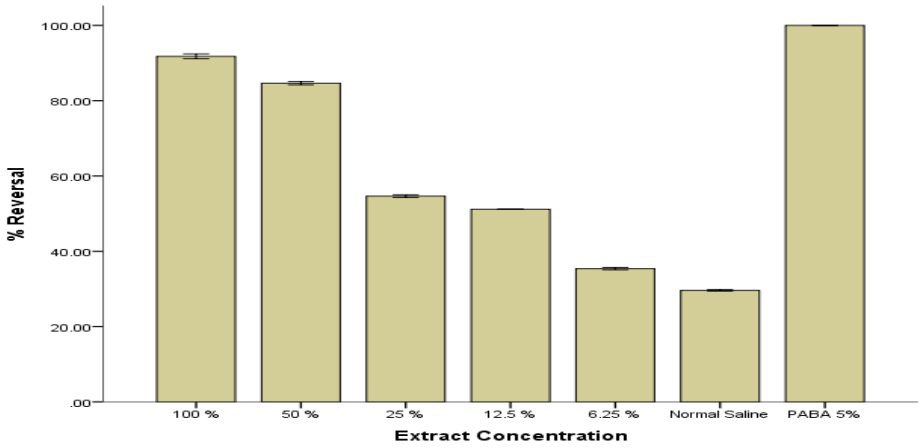

Fig. 2. % sickling reversal of MFSO.

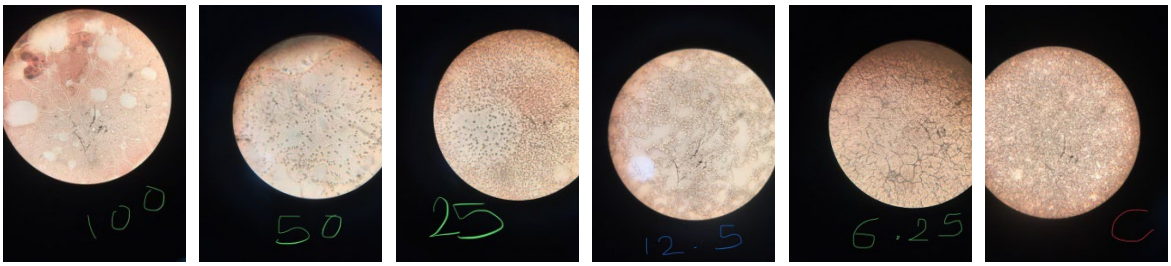

Fig. 3. The normalization of sickle cells treated n-hexane seed extracts of *M. flagellipes* at different concentrations.

Effect of MFSO on polymerization of sickle cell blood

The MFSO which shows a dose dependent activity, significantly decreased *($p < 0.05$)* polymerization of sickle cell at all studied concentration compared to negative control (normal saline). The observed activity for MFSO was however lower than the standard agent used. This indicates the ability of MFSO to inhibit polymer formation.

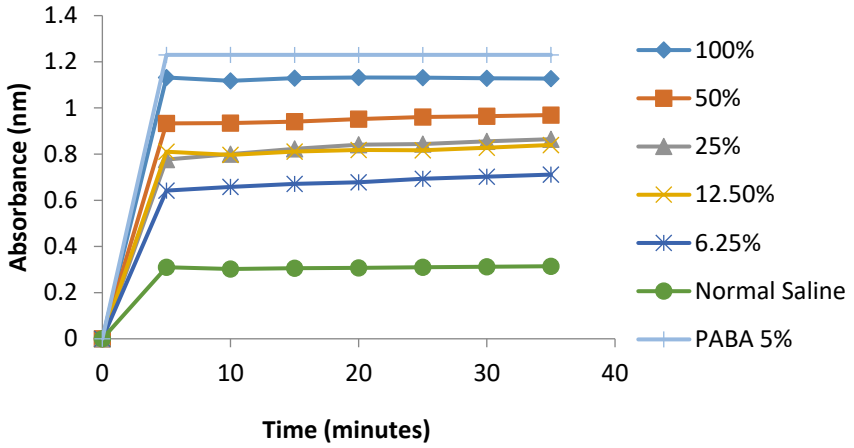

Fig. 3. Polymerization of sickle cell blood treated with MFSO at different concentration.

J. Mex. Chem. Soc. **2024**, *68*(2)
Regular Issue

ISSN-e 2594-0317

Effect of MFSO on % Hb, % MHb and Fe^{2+}/Fe^{3+} ratio in sickle cell blood

The MFSO inhibited the formation of methemoglobin formation, and this activity was dose dependent. At the highest concentration, the percentage methemoglobin formation has the lowest value of 10.8 ± 2.3 % and the ratio of Fe^{2+}/Fe^{3+} is 8.2. This activity was however lower than the standard agent used.

Table 5. Showing percentage hemoglobin, percentage methemoglobin and Fe^{2+}/Fe^{3+} ratio in sickled blood treated with MFSO.

Conc. (%)	%Hb	%MHb	Fe^{2+}/Fe^{3+} ratio
100	89.2±2.3	10.8±2.3	8.2
50	88.2±0.7	11.8±0.7	7.5
25	76.6±1.9	23.4±1.9	3.3
12.5	67.9±1.2	32.1±1.2	2.1
6.25 5% PABA	65.4±0.5 95.0±0.08	34.6±0.5 4.0±0.32	1.9 23.8
NS	64.3±1.4	35.7±1.4	1.8

Discussion

The use of natural products of plant origin in managing and treating disease is on the rise. More specifically, plant materials are strongly employed in managing sickle cell disease, especially in traditional systems in underdeveloped and developing countries. GC-MS quantification of fatty acids in the seed oil presented in Table 1 showed the presence of five (5) fatty acids, such as pentadecyclic acid (1.04 %), palmitic acid (5.91 %), linoleic acid (18.30 %), oleic acid (31.87 %), and stearic acid (1.85 %). The major saturated fatty acid was palmitic acid, while oleic fatty acid was detected as the major unsaturated fatty acid in the seed oil. The result for fatty acid analysis agrees with the report of Ajayi et al. [16], who reported the presence of oleic, linoleic, palmitic, and stearic acids as the major fatty acids in *M. flagellipes* seed oil (MFSO). Furthermore, the concentration of oleic acid in this study was similar to the value obtained by Ajayi et al. [16] for the seed oil of *M. flagellipes*. The application of essential fatty acids in managing pain and other abnormalities associated with sickle cell disease has been properly documented [5,9,20]. These fatty acids are also known to promote cell membrane activity and prevent vaso-occlusive crises. The high amount of oleic acid and linoleic acid, which are known polyunsaturated fatty acids, in the oil sample may contribute to phospholipid requirements in sickle cell disease to keep membrane integrity intact. The fatty acid n-hexadecenoic acid (palmitic fatty acid) has been reported to exert its action on sickle red blood cells *via* stabilization of the sickle cell membrane against hemolysis and formation of HbSS polymers [35]. Furthermore, linoleic acid has been linked to analgesic, antibacterial, antioxidant, antipyretic, antispasmodic, and sedative activities. These activities are highly needed in the sickle cell disease crisis. Thus, this suggests that the seed oil of *M. flagellipes* may offer many therapeutic potentials in sickle cell disease [3]. Fratianni et al. [36] also reported that oleic acid has antioxidant activity. In sickle cell disease, where abnormal hemoglobin thrives, the hemoglobin stabilizing capacity is negatively affected, thereby making the red blood cells more susceptible to damage from oxidative stress. This may overwhelm the antioxidant defense system. It has been shown that sickle red blood cells produce more quantities of superoxide radicals, hydrogen peroxide (H_2O_2), and hydroxyl radicals than normal erythrocytes [37].

The result for vitamins and minerals is presented in Table 2. The results showed a great number of fat-soluble vitamins; vitamin A (220 ± 1.60 µg/100mg), vitamin E (370 ± 2.20 µg/100mg) and vitamin K (197 ± 0.23 µg/100mg), which was within the RDA for the vitamins. The values reported for vitamin A and E in the seed oil

J. Mex. Chem. Soc. **2024**, *68*(2)
Regular Issue

ISSN-e 2594-0317

were lower than the values reported by Nwajagu et al. [38] in the processed and unprocessed seeds of *M. flagellipes* and its flour product. Deficiencies of antioxidant vitamins such as vitamin A and E have been reported in anemic conditions [39], and due to the nature of sickled cells, there is a constant need to furnish them with minerals and vitamins so as to keep them stable. Vitamins A and E, which are strong antioxidant vitamins detected in the seed oil, could contribute to the overall antioxidant status of the sick patient, and reduce symptoms. These antioxidant vitamins also play a role in the fight against infection, fight oxidative stress, and enhance iron absorption [7]. Vitamin K, a soluble vitamin, is useful in preventing excessive bleeding, which can lead to iron deficiency anemia. Mineral estimation showed an appreciable concentration of Fe (170 ± 1.30 µg/100 mg) and Zn (780 ± 2.50 µg/100 mg) in the seed oil. Interesting, the concentration of zinc was higher than iron in the sample and was within the recommended dietary allowance. The result reported for zinc and iron in the seed oil for this study was lower than the value reported for these minerals in the seed flour of *M. flagellipes* (32.60 ± 0.14 and 6.40 ± 0.03 mg/100g respectively) [40] and leaves (57.08 ± 8.44 and 5.83 ± 3.14 respectively) as reported by Ihedioha and Okoye [13]. This difference can be attributed to various factors ranging from the source of minerals to planting season, soil type, climate, and genetic and environmental factors [41-42]. Sickle cell anemia has been linked with zinc deficiency, making zinc supplementation in the diet helpful to manage or prevent some clinical manifestations [43]. Similarly, Datta et al. [8] reported the ability of zinc to prevent infection in sickle cell anemia, and reduced zinc bioavailability in sickle cell patients has been reported to lead to the development of several complications, ranging from wound healing problems to delayed or slow growth and vaso-occlusive crises [44]. The activity of zinc in reversing the functional state of sickle erythrocytes to their original biconcave structure, coupled with increasing their oxygen affinity, is established. Considering the value obtained for zinc in the seed oil, this plant material can contribute to the zinc bioavailability of sickle cell patients when consumed. Iron overload has been reported in patients with sickle cell anemia [45-46]. Therefore, it is important that iron supplementation be minimal for sickle cell patients, unless there is a proven case of iron deficiency. The result obtained for iron in this study, which was small compared to zinc, further justifies the use of seed oil in managing anemic conditions as it may not contribute to the overall iron burden of the sickle cell patient.

Sickle cell anemia is an inherited genetic disorder characterized by the inability of the red blood cells (erythrocytes) to carry enough oxygen around the body, leading to anemia and occlusion of small blood vessels. This series of activities leads to the development of excruciating body pains, crises, complications, and other manifestations [47]. The percentage activity of the seed oil on sickling inhibition and reversal is presented in figures 1 and 2. The seed oil at all studied concentrations significantly inhibited sickling and promoted reversal. This activity was however lower compared to 5 % *p*-hydroxybenzoic acid (PABA), the standard agent used. The anti-sickling potential observed in this study by the seed oil can be linked to the presence of zinc and some key vitamins present in the sample. The mechanism employed by zinc in inhibiting and reversing sickling has been reported [48]. Zinc binding to hemoglobin in sickle cells increases oxygen affinity and increases cell membrane filterability [49]. Zinc also decreases the quantity of hemoglobin linked with the red blood cell membrane, reducing the calcium effect in causing hemoglobin retention by the membrane and thus reducing the clumping that is observed in sickle cells. Zinc inhibits the role played by oxidative stress and proteins involved in inflammation (cytokines) in promoting sickle cell disease, and this is facilitated by its ability to promote and increase anti-inflammatory proteins [50].

The seed oil of *M. flagellipes* significantly inhibited HbS polymerization compared to the negative control, as seen in figure 3. The ability to inhibit HbS polymerization is a key area when looking for compounds with anti-anemic potential. The role played by minerals and vitamins in the prevention of HbS polymerization has been properly documented [6]. Zinc has been reported to stimulate the synthesis of metallothionein, a protein that binds and traps copper within the intestinal cells, inhibiting copper absorption [51]. The ability to keep copper trapped and not released is a key mechanism employed by zinc in inhibiting HbS polymerization. Copper has been reported to increase HbS polymerization by 33.13 % [6]. The high zinc content of the seed oil of *M. flagellipes* may contribute to this effect, as seen in this study. A key mechanism for inhibiting HbS polymerization is to increase oxygen affinity. Zinc plays a major role in increasing oxygen affinity in HbS conditions [52]. Experimental data has shown that the effect of oxygen on the inhibition of polymerization could be likened to the 2-state allosteric MWC (Monod-Wyman-Changeux) model of enzymes [53-54]. This suggests that an equilibrium exists between the low oxygen affinity of fully deoxygenated hemoglobin, which is labeled the T quaternary structure, and the high affinity arrangement of fully oxygenated hemoglobin, called the R quaternary structure. Increased oxygen affinity effectively controls polymerization *via* a shift from the T-R equilibrium towards the R

J. Mex. Chem. Soc. **2024**, *68*(2)
Regular Issue

ISSN-e 2594-0317

equilibrium and is considered an effective treatment approach in anemic conditions [55]. Also, the treatment of sickled blood cells with plant extracts has been suggested to inhibit the Ca^{2+}-activated K^+ channel [56]. The inhibition of this channel prevents the loss of water and potassium ions from sickled blood cells, preventing dehydration. This facilitates a decrease in the intracellular concentration of hemoglobin S and further prevents polymerization and sickling of erythrocytes. This could therefore have been another mechanism employed by the seed oil of *M. flagellipes* in preventing polymer formation, as seen in this study. The inhibition of HbS polymerization in this study can also be attributed to the presence of vitamins A and E and zinc, as recorded in this study. Studies by Djote et al. [19] attributed the anti-sickling potentials of Azadirachta indica seed oil to the presence of linoleic fatty acids and vitamin E.

The result for the effect of the seed on % Hb, % MHb, and the Fe^{2+}/Fe^{3+} ratio is presented in Table 4. The oil extracted from the seeds of *M. flagellipes* showed potential to increase the Fe^{2+}/Fe^{3+} ratio. This occurs by decreasing the methamoglobin (MHb) concentration that is produced from the conversion of the iron of deoxy-hemoglobin (Fe^{2+}, reduced state) to the ferric state (Fe^{3+}, oxidized state) [57]. The ratio of ferrous and ferric iron indicates the level of oxygen affinity for red blood cell hemoglobin [58]. The high Fe^{2+}/Fe^{3+} ratio observed in this study, as shown by the seed oil-treated group, corroborates the activity of the extract in improving oxygen affinity in sickled erythrocytes, which can be attributed to the presence of zinc, antioxidant vitamins, and polyunsaturated fatty acids present in the sample. Furthermore, the increased Fe^{2+}/Fe^{3+} ratio as revealed by the seed oil confirms the sickling reversal, indicating the seed oil's ability to convert deoxy-HbS to oxy-Hbs.

The nutritional index values of the oil extracted from *M. flagellipes* are presented in Table 3. Nutritional indices of oils are strongly employed to determine how fit an oil sample is for consumption. The PUFA/SFA ratio, also called the polyene index [29], is used to ascertain the impact of edible oils on the cardiovascular system. Saturated fatty acids (SFA) have been reported to promote high serum cholesterol levels, while polyunsaturated fatty acids (PUFAs) are established to reduce cholesterol levels. This has made the PUFA/SFA ratio a useful guide to determining if an oil sample will have positive effects on the body. Generally, a high PUFA/SFA ratio indicates a positive effect of the oil sample on overall cardiovascular health [28]. In this study, the PUFA/SFA ratio for MFSO was 2.07. This value was lower compared to the value report for soya bean seed oil (3.03-3.76) [59]. This suggests a great nutritional potential of MFSO, which is strongly linked to the high amount of PUFAs in the oil sample. The MUFA/SFA, PUFA/MUFA, and (PUFA+MUFA)/SFA values were 3.62, 0.57, and 5.70, respectively, and this corroborated the polyene index of MFSO and can be attributed to the rich amount of unsaturated fats in the oil sample. Consumption of oil rich in unsaturated fats suggests a low potential to develop cardiovascular diseases. The oxidizability value of the oil was 0.18, and this value was lower than the value reported for soya bean seed oil (7.51-7.63) [59]. Generally, oil samples with low oxidizability values are known to be more stable than their counterparts. The index of atherogenicity (IA) and index of thrombogenicity (IT) are employed to characterize the atherogenicity and thrombogenicity potentials of oil samples. While the IA shows the link between SFAs and the sum of unsaturated fats, the IT suggests the potential of the oil sample to form clots in blood vessels. The consumption of fats with low IT and IA has been linked to reducing cholesterol levels and contributing significantly to improved cardiovascular health. The IA value of 0.11 in this study was similar to the value reported for sunflower oil (0.09–0.11) [60]. The low value of IA in this study further suggests a good nutritional property of MFSO. The values reported for IT (0.07) in this study suggest the ability of the oil to prevent or not initiate thrombogenesis. In this study, we ascertained the hypocholesterolemic/hypercholesterolemic (HH) [61] ratio to determine the effect of the oil on the composition of cholesterol. It shows the relationship between hypocholesterolemic fatty acids (cis-C18:1 and PUFA) and hypercholesterolemic FA. A high HH value indicates a reasonable nutritional index of the oil sample. As seen in this study, the HH value was 3.09, which is low compared to Camelina oil (11.2–15.0) [60]. The UI value shown in this study (68.47) was low when compared to soybean oil (148–155) [62]. Oils with high UI values have been reported to maintain membrane fluidity under stress-associated conditions [63].

Conclusions

Despite the myriad uses of this plant in traditional systems, its seed oil's anti-sickling properties have not been investigated. The results obtained from this study have shown that the seed oil has great potential to

J. Mex. Chem. Soc. **2024**, *68*(2)
Regular Issue

ISSN-e 2594-0317

serve as an anti-sickling agent. The high zinc and vitamin content of the seed oil suggests it can replenish nutrients lost in sickle cell disease. The fatty acid profile of the seed oil shows a high level of unsaturated fatty acids, which are cardio-friendly and thus may not pose a threat when consumed. Further studies will be required to isolate and identify the specific anti-sickling agents in the seed oil. Furthermore, studies to determine the best way of processing and preserving the seed oil are warranted.

References

1. Strouse, J. *Handbook of Clin. Neurol.* **2016**, 138, 311-324.
2. Yenon, A. A.; Sangare, B.; Ndraman, D.; Sawadogo, D.; Yapi, H. F.; Nguessan, J. D.; Djaman, A. J. *The Pharma. Chem. J.* **2016**, 3, 351-358.
3. Mpiana, P. T.; Mudogu, V.; Tshibagu, D. S. T.; Kitwa, E. K.; Kanagila, A. B.; Lumbu, J. B. S.; Ngbolua, K. N.; Atibu, E. K.; Kakuli, M. K. *J. Ethnopharmacol.* **2008,** 120, I413-418.
4. Mohammed, R. H.; Sulaiman, S. K. *Int. J. Appl. Sci. Res.* **2021**, 4, 1-12.
5. Okpala, I.; Ibegbulam, O.; Duru, A.; Ocheni, S.; Emodi, I.; Ikefuna, A.; Umar, G.; Asinobi, I.; Madu, A.; Okoye, A.; Nwagha, T.; Oguonu, U.; Uamai, I.; Agwu, O.; Nonyelu, C.; Anike, U.; Agu, K.; Anigbo, C.; Chukwura, A.; Ugwu, O.; Herrada, S. *Acta Pathologica, Microbiologica, et Immunologica Scandinavica* **2011**, 119, 442–448.
6. Puppalwar, P. V.; Adole, P.; Dhok, A.; Bhatkulkar, P. *Int. J. Therapeutic Appl.* **2015**, 25, 1-6
7. Pullar, J. M.; Carr, A. C.; Vissers, M. C. M. *Nutrients* **2018,** 9, 866.
8. Datta, D.; Namazzi, R.; Conroy, A. L.; Cusick, S. E.; Hume, H. A.; Tagoola, A.; Ware, R. E.; Opoka, R. O.; John, C. C. *Trials* **2019,** 20, 460.
9. Khan, S.; Damanhouri, G.; Ahmed, T. J.; Halawani, S.; Ali, A.; Makki, A.; Khan, S. *J. King Saud Univ. – Sci*. **2022,** 34.
10. Ibrahim, N. K.; Ahmed, J. H.; Hassan, M. K. *Singapore Med. J.* **2010,** 51, 230-234.
11. Moody, J. O.; Ojo, O. O.; Omotade, O. O.; Adeyemo, A. A.; Olumese, P. E.; Ogundipe, O. O. *Phytother. Res.* **2003,** 17, 1173–1176.
12. Nwokocha, L. M; Williams, P. A. *Food Hydrocolloids* **2009,** 23, 1394-1397.
13. Ihedioha, J. N.; Okoye, C. O. *Am. J. of Plant Nutr. Fertilization Tech.* **2011,** 1, 55-63.
14. Okwu, D. E.; Okoro, E. *Med. Aromatic Plant Sci. Biotech.* **2007,** 1, 103- 106.
15. Uchegbu, *R.* I.; Ngozi-Olehi, L. C.; Mbadiugha, C. N.; Ahuchogu, A. A., Ogbuagu, O. E. *J. Nat. Sci. Res*. **2015,** 5, 12.
16. Ajayi, I. A.; Oderinde, R. A.; Kajogbola, D.; Uponi, J. I. *Food Chemistry*, **2006,** 99, 1, 115-120.
17. Abireh, I.; Ozioko, O.; Ikemefuna, O. *J. Exp. Res*. **2020,** 8, 1.
18. Jovita, E. E.; Ani, C. O.; Uzoma, I. C.; Pamela, A. S.; Onwuka, C. K.; Ayowumi, A. M.; Daniel, N. C. *Afr. J. Pharmacy Pharmacol*. **2016,** 11, 582- 592.
19. Djote W. N.; Kotue, T. C.; Mafogang, B.; Ngo, S. F.; Pieme, A. C. *J. Nutr. Food Lipid Sci.* **2020**, 1: 86-93.
20. Daak, A. A.; Lopez-Toledano, M. A.; Heeney, M. M. *Compl. Therapies in Med.* **2020**, 52, 102482.
21. Chukwu, C. N.; Onyedikachi, U. B.; Ejiofor, E. *CMU J. Nat. Sci.* **2022**, 21, e2022010.
22. Ariyike, O. A.; Hezekiah, A. G.; Obajimi, A. O.; Olusola, O. O. *GSC Biol. Pharmaceut. Sci.* **2019**, 7, 77–92.
23. Onyedikachi, U. B., Awah, F. M.; Chukwu, C. N.; Ejiofor, E. *Acta Universitatis Cibiniensis. Series E: Food Tech.* **2021,** 25, 1-14.
24. Onyedikachi, B.; Ejiofor, E.; Njoku, C.; Ejiofor, M.; Kanu, M. *J. Mex. Chem. Soc.* **2022**, 66, 433- 443
25. De' Leenheer, A. P.; Nelis, H. J.; Lambert, W. E.; Bauwens, R. M. *J. Chromatography A* **1988**, 29, 13-58.
26. Gul, W.; Anwar, Z.; Qadeer, K.; Perveen, S.; Ahmad, I. *J. Pharmacy Pharmaceut. Sci.* **2015**, 3, 14-22

J. Mex. Chem. Soc. **2024**, *68*(2)
Regular Issue

ISSN-e 2594-0317

27. AOAC, *Official method of Analysis.* **2005,** 18th Edition 935.14 and 992.24.
28. Chen, J.; Liu, H. *Int. J. Mol. Sci.* **2020**, 21, 5695.
29. Eke, R.; Ejiofor, E.; Oyedemi, S.; Onoja, S.; Omeh, N. *J. Food Biochem.* **2021**, e13763.
30. McCormick, R. L.; Ratcliff, M.; Moens, L.; Lawrence, R. *Fuel Processing Tech.* **2007**, 88, 651–657.
31. Egba, S. I.; Emmanuel, N. T.; Ogugua, N. V.; Ndohnui, N. N. *Int. J. Biochem. Biotech.* **2012**, 1, 226–229.
32. Ekeke, G. I.; Uwakwe, A. A.; Nwaoguikpe, R. N. *Nig. J. Biochem. Mol. Biol.* **2000**, 16, 45–47.
33. Noguchi, C. T.; Schechter, A. N. *Annual Rev.* **1985**, 4:239-245.
34. Tietz, N. W. *Fundamentals* of *clinical chemistry*, 2nd edn. W. B. Saunders Company, Philadelphia, **1976**, 34-40.
35. Chikezie, P. C.; Uwakwe, A. A. *Pharmacognosy Mag.* **2011,** 7, 121-125.
36. Fratianni, F.; d'Acierno, A.; Ombra, M. N.; Amato, G.; De Feo, V.; Ayala-Zavala, J. F.; Coppola, R.; Nazzaro, F. *Frontiers in Nutr.* **2021**, 8, 775751.
37. Hebbel, R. P.; Eaton, J. W.; Balasingam, M.; Steinber, M. H. *J. Clin. Investig.* **1982**, 70, 1253-1259.
38. Nwajagu, I. U.; Garba, A.; Nzelibe, H. C.; Chukwuekezie, N. E.; Abah, C. R.; Umar, A. T.; Anarado, C. S.; Kahu, J. C.; Olagunju, A.; Oladejo, A. A.; Bashiru I. *Am. J. Food and Nutr.* **2021**, 9, 49-59.
39. Ray, D.; Deshmukh, P.; Goswami, K.; Garg, N. *The Nat. Med. J. India*, **2007**, 20, 11–13.
40. Obi, C. D.; Okoye, J. I. *Int. J. Innovative Food*, *Nutr. Sustainable Agric.* **2017**, 5, 18-24.
41. Oyedemi, S. O.; Eze, K.; Aiyegoro, A. O.; Ibeh, R. C., Ikechukwu, G. C., Swain, S. S.; Ejiofor, E.; Oyedemi, B.O. *J. Biomolecular Struct. Dynamics* **2021**, 40: 9948- 9961.
42. Ejiofor, E. U.; Oyedemi, S. O.; Onoja, S. O.; SO, Omeh, N. Y. *South Afr. J. Bot.* **2022**, 146, 213-221.
43. Temiye, E. O.; Duke, E. S.; Owolabi, M. A.; Renner, J. K. *Anemia*, **2011**, 698586, 7.
44. Miranda, C. T.; Vermeulen-Serpa, K. M.; Pedro, A. C.; Brandão-Neto, J.; Vale, S. H.; Figueiredo, M. S. J. *Trace Elements in Med. Biol.* **2022**, 72, 126980.
45. Coates, T. D.; Wood, J. C. *British. J. Haematology*, **2017**, 177, 703 -716.
46. Sani, M. A.; Adewuyi, J. O.; Babatunde, A. S.; Olawumi, H. O.; Shittu, R. O. *Advances in Hematology*, **2015**, 386451, 5.
47. Rees, D. C.; Williams, T. N.; Gladwin, M. T. *Lancet,* **2010**, 376, 2018–2031.
48. Dash, S.; Brewer, G.; Oelshlegel, F. *Nature* **1974**, 250, 251–25.
49. Eaton, J. W.; Skelton, T. D., Swofford, H. S.; Kolpin, C. E.; Jacob, H. S. *Nature*, **1973**, 246, 105.
50. Bao, B.; Prasad, A. S.; Beck, F. W. *Translational Res.* **2008**, 152, 67–80.
51. Natta, C. L.; Tatum, V. L.; Chow, C. K. *Annals New York Acad. Sci*. **1992**, 669, 365-367.
52. Rifkind, J. M.; Heim, J. M. *Biochem.* **1997**, 16, 4438–4443.
53. Monod, J.; Wyman, J.; Changeux, J. P. *J. Mol. Biol.* **1965**, 12, 88-118.
54. Eaton, W. A.; Henry, E. R., Hofrichter, J.; Mozzarelli, A. *Nat. Struct. Biol*. **1999**, 6, 351-358.
55. Eaton, W. A.; Bunn, H. F. *Blood* **2017**, 12, 2719–2726.
56. Dennis, D.; Roberts, A. in: *Trease and Evans Pharmacognosy,* The Alden Press, Oxford, Great Britain. 1990, 832.
57. Murray, R. K.; Granner, D. K.; Mayes, P. A.; Rodwell, V. W. in: *Harper's Illustrated Biochemistry*, 27th edn. McGraw Hill Companies, New York. 2006
58. Osuagwu, C. G. *Nig. J. Biochem. Mol. Biol.* **2010,** 25, 68–71.
59. Szpunar-Krok, E.; Wondołowska-Grabowska, A. *Foods (Basel, Switzerland)*, **2022,** 11, 762.
60. Ratusz, K.; Symoniuk, E.; Wroniak, M.; Rudzi ´nska, M. *Appl. Sci.* **2018,** 8, 2606.
61. Santos-Silva, J.; Bessa, R.; Santos-Silva, F. *Livest. Prod. Sci.* **2002,** 77, 187–194.
62. Ghassemi-Golezani, K.; Farhangi-Abriz, S. *Russ. J. Plant Physiol*. **2018,** 65, 229–236.
63. Colombo, M. L.; Rise, P.; Giavarini, F.; De Angelis, L.; Galli, C.; Bolis, C. L. *Plant Foods Hum. Nutr*, **2006,** 61, 64–69.

Article

J. Mex. Chem. Soc. **2024**, *68*(2)
Regular Issue

ISSN-e 2594-0317

Fe_3O_4@NH_2@Oxalic Acid: A Convenient Catalyst for Synthesis of Pyrrolinone Derivatives

Seyran Esmaeilzadeh, Davood Setamdideh*, Fatemeh Ghanbary

Department of Chemistry, Mahabad Branch, Islamic Azad University, Mahabad, Iran.

***Corresponding author:** Davood Setamdideh, email: d.setamdideh@iau-mahabad.ac.ir; davood.setamdideh@gmail.com

Received November 11th, 2022; Accepted May 29th, 2023.

DOI: http://dx.doi.org/10.29356/jmcs.v68i2.1910

Abstract. In this context, an amine-functionalized magnetite nanoparticle was synthesized from $FeCl_3$•$6H_2O$ and 1, 2-ethylenediamine at 110 °C in ethylene glycol within 6 hours. Then, the obtained corresponding Fe_3O_4@NH_2 was used for the preparation of Fe_3O_4@NH_2@oxalic acid as organoacid-magnetic nanoparticles under ultrasonic irradiation at 60 °C within 4 hours. Its chemical structure was characterized by FT-IR, XRD, SEM, VSM, and EDAX spectra. The Fe_3O_4@NH_2@oxalic acid nanoparticles were successfully used for the synthesis of pyrrolinones derivatives in excellent yields of the products (90-95 %) within 6-10 hours at room temperature in ethanol.
Keywords: Ethylenediamine, amino-functionalization, nano-magnetite, pyrrolinones, green chemistry.

Resumen. Se sintetizó una nanopartícula de magnetita funcionalizada con aminas a partir de $FeCl_3$•$6H_2O$ y 1,2-etilendiamina a 110 °C en etilenglicol durante 6 horas. Posteriormente, el Fe_3O_4@NH_2 que se obtuvo se utilizó para la preparación de nanopartículas magnéticas organoácidas de Fe_3O_4@NH_2@ácido oxálico por irradiación ultrasónica a 60 °C durante 4 horas. Su estructura química se caracterizó por sus espectros de FT-IR, XRD, SEM, VSM, y EDAX. Las nanopartículas de Fe_3O_4@NH_2@ácido oxálico se utilizaron existosamente para sintetizar derivados de pirrolinonas con rendimientos excelentes (90-95%), en 6-10 horas de reacción a temperatura ambiente en etanol.
Palabras clave: Etilendiamina, funcionalización amino, nanomagnetita, pirrolinonas, química verde.

Introduction

The functionalization of the magnetic nanoparticles (the F-MNPs) is crucial for chemical processes, and they have many applications in medical and biological research. Meanwhile, the amine-functionalized magnetite nanoparticles (the AF-MNPs) have received more attention because of their properties such as excellent magnetism, tunable sizes, good crystallinity, and facile dispersion in water [1-13].

The AF-MNPs and their derivatives have been used for different fields in organic chemistry such as bio-conjugated to biological molecules (proteins, nucleic acids, and peptides) [1], for cellulase immobilization to prevent wastage of cellulosic resources [2], to prepare cis-pinane [3], catalyst for Heck reaction [4], synthesis of xanthenes [5], selective separation of catecholamines in urine [6], hydrogenation and Heck reactions by Pd immobilized on the AF-MNPs [7], for attachment of polyacrylic acid [8], for the treatment of gastric, colon, and pancreatic cancers in near future [9], for the synthesis of carbamates [10], for degradation of the methyl orange and *p*-nitrophenol reduction in aqueous media [11], enhanced photocytotoxicity [12], and removal of carmoisine dye from aqueous solutions [13].

J. Mex. Chem. Soc. **2024**, *68*(2)
Regular Issue

ISSN-e 2594-0317

On the other hand, pyrrolin-2-one skeleton has biological activity in some synthetic drugs and natural products, for example: *Cotinine* [14], *Doxapram hydrochloride* [15], *Ethosuximide* [16], *Rolipram* [17], *Lactacystin* [18], *Salinosporamide* [19], *(−)-Azaspirene* [20] *and Pesticides* [21] (Scheme 1).

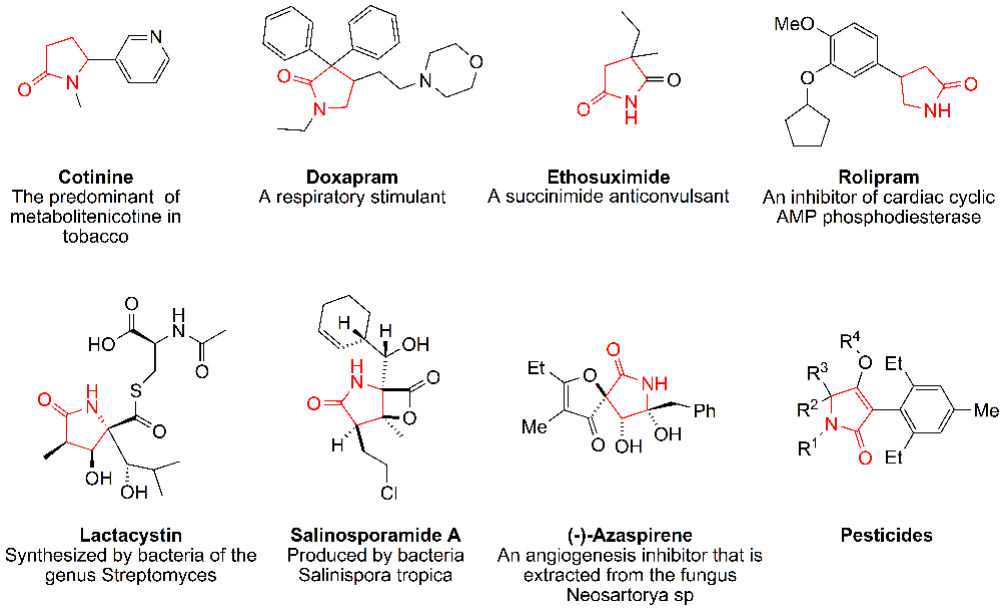

Scheme 1. The chemical structure of some natural products and drugs with pyrrolinone moiety.

Some procedures have been reported for the synthesis of pyrrolin-2-ones [22-27]. However, a coupling of arylamines and aromatic aldehydes with acetylenedicarboxylates is an important synthetic method for the synthesis of this class of compounds. This method has been studied by several protocols such as using of nano-TiO_2 [28], in water as a green solvent [29], by *p*-toluensulfonic acid [30], under ultrasound irradiation [31], or microwave irradiation [32], by ionic liquids [33], in the presence of nano-magnetic particles [34], and AmberChrom as a polymer catalyst [35]. For improving the obtained result as a part of the synthetic project we turned attention to the synthesis of a more stable and convenient catalyst for this procedure. Thus, we decided to link oxalic acid on magnetite nanoparticles by a covalent bond. Our survey showed using of amine-functionalized magnetite nanoparticles (the AF-MNPs) is a good approach for this subject. Thus, pyrrolin-2-ones were synthesized by a new methodology from aldehydes, anilines and dimethyl acetylenedicarboxylate by Fe_3O_4@NH_2@oxalic acid as a reusable nano-magnetic catalyst at room temperature (Scheme 2).

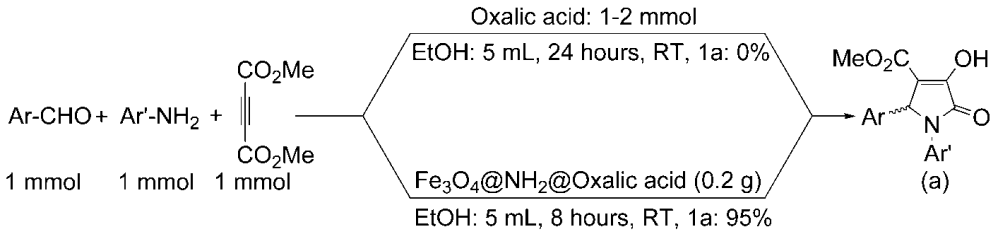

1a: Ar(Ph)Ar'(Ph)(8 h, 95%); **2a**: Ar(Ph)Ar'(4-MeOPh)(6 h, 90%); **3a**: Ar(3-ClPh)Ar'(4-MeOPh)(6 h, 95%); **4a**: Ar(4-BrPh)Ar'(4-BrPh)(10 h, 93%); **5a**: Ar(3-NO_2Ph)Ar'(4-BrPh)(10 h, 91%); **6a**: Ar(Ph)Ar'(4-BrPh)(10 h, 94%); **7a**: Ar(2-ClPh)Ar'(4-MeOPh)(6 h, 90%); **8a**: Ar(2-MeOPh)Ar'(4-MePh)(8 h, 92%)

Scheme 2. The synthesis of 1,5-diaryl-3-hydroxy-4-methoxycarbonyl-3-pyrrolin-2-ones by Fe_3O_4@NH_2@oxalic acid as a catalyst.

J. Mex. Chem. Soc. **2024**, *68*(2)
Regular Issue

ISSN-e 2594-0317

Experimental

Materials

All reagents were purchased from Sigma-Aldrich Company. FT-IR spectra were recorded on a Bruker spectrometer. XRD patterns were recorded using a Holland Philips (model: PW1730) (radiation, λ= 0.154056 nm, CuK), Step size 0.05°, time per step 1 second (2θ=5°-80°). SEM images were performed on a Model FESEM: TESCAN company (model: MIRA III) manufactured by Czech. EDX (Energy Dispersive X-Ray Analysis) was taken by FESEM: model: MIRA II from TESCAN company manufactured by Czech (Detector: SAMX, France). VSM analysis was taken by model MDKB manufactured by Kavir Kashan Magnet Company (Iran). TGA analysis was recorded by Model Q600; TA company manufactured by the USA. IR and ^{1}H NMR spectra were recorded on PerkinElmer FT-IR RXI and 300 MHz Bruker spectrometers, respectively. Pyrrolinone derivatives were characterized by their ^{1}H-NMR, FT-IR spectra. All yields referred to isolated pure products. TLC was applied for reaction monitoring over silica gel 60 F_{254} aluminum sheet.

Synthesis of Fe_3O_4@NH_2 nanoparticles

The magnetic amine-functionalized nanoparticles (Fe_3O_4@NH_2) were prepared *via* solvothermal reaction with major modification [1]. $FeCl_3.6H_2O$ (1.5 gr), 1, 2-ethylenediamine (3 g), and sodium acetate anhydrous (12 g) were dissolved in ethylene glycol (45 mL) *via* vigorous mechanical stirring. Then, the reaction was heated at 110°C for 6 hours under the Ar atmosphere. The obtained magnetic nanoparticles were isolated by a powerful magnet, and washed with distilled H_2O, and EtOH several times. Then, the product was dried at 60 °C for 2 hours.

Preparation of Fe_3O_4@NH_2@Oxalic acid nanoparticles

Fe_3O_4@NH_2 nanoparticles (0.25 g) were dispersed in ethanol (15 mL) by ultrasonic bath for 30 minutes. Then, a solution of oxalic acid (0.4 g) in ethanol-water (20mL/10mL) was prepared and was charged in the above solution. The obtained mixture was irradiated by ultrasonic irradiation for 4 hours at 60 °C under the Ar atmosphere. The obtained magnetic nanoparticles (i.e Fe_3O_4@NH_2@Oxalic acid) were isolated by a powerful magnet, washed with ethanol, and distilled water several times to remove all organic impurities. Then, the product was dried at 60 °C for 2 hours.

The synthesis of 1,5-diphenyl-3-hydroxy-4-methoxycarbonyl-3-pyrrolin-2-one (1a) by Fe_3O_4@NH_2@oxalic acid; A typical procedure

A mixture of benzaldehyde (0.106 g, 1 mmol), aniline (0.093 g, 1 mmol), and Fe_3O_4@NH_2@oxalic acid (0.2 g) in 5 mL of ethanol was prepared in a round-bottomed flask (25 mL) equipped with a magnetic stirrer and was strongly stirred at room temperature for 40 min. Then to the mixture dimethyl acetylenedicarboxylate (0.14 gr, 1 mmol) was added. The reaction was completed within 8 hours. The reaction was monitored over silica gel 60 F_{254} aluminum sheet (eluent: ethyl acetate/*n*-hexane: 1/1). The catalyst was separated by using a strong magnet. The separated catalyst was washed with acetone and ethanol two times then dried in an oven (50 °C) and reused for further reactions. The solvent has been evaporated by a rotary instrument and further residue was recrystallized from methanol. The white solid achieved an excellent yield of 0.295 g (95 %) with a melting point of 182–183 °C [30]. The product was characterized by ^{1}H-NMR, ^{13}C-NMR, FT-IR and C, H, N elemental analysis.

FT- IR (KBr)(cm^{-1}): 3260 (OH), 2958, 1702 (C=O), 1680 (C=O), 1498, 1382, 1232, 1002; ^{1}H NMR ($CDCl_3$): δ 3.60 (s, 3H, CH_3), 6.10 (s, 1H, CH), 7.07–7.62 (m, 10 H, Ar and br s, 1H, OH); ^{13}C NMR ($CDCl_3$): δ 50.55, 61.05, 112.35, 122.96, 125.80, 128.13, 128.38, 128.73, 129.13, 136.74, 137.00, 153.14, 162.96 (C=O), 164.49 (C=O). Anal. Calcd for $C_{18}H_{15}NO_4$: C, 69.89; H, 4.89; N, 4.53. Found: C, 69.92; H, 4.81; N, 4.48.

Results and discussion

A literature survey showed that the preparation of the AF-MNPs by direct coupling of amino agents to magnetite nanoparticles has been carried out by different chemical procedures. The chemical conditions for these methods have been summarized in table 1 for more consideration.

J. Mex. Chem. Soc. **2024**, *68*(2)
Regular Issue

ISSN-e 2594-0317

Table 1. Synthesis of the AF-MNPs by different protocols.

Entry	Magnetite source	Amino agent	Steps	Size, nm
1[1-3, 7-8, 40, 44-46, 48, 50, 52-53]	$FeCl_3$•$6H_2O$	1,6-hexadiamine	1	1.95-200
2[5]	$FeCl_3$•$6H_2O$ & $FeCl_2$•$4H_2O$	1,6-hexadiamine	1	20
3[6, 38, 49]	$FeCl_3$•$6H_2O$ & $FeCl_2$•$4H_2O$	$H_2N(CH_2)_3Si(OCH_3)_3$	2	13-150
4[36a]	$FeCl_3$•$6H_2O$	$H_2N(CH_2)_3Si(OCH_3)_3$	2	250
5[36]	$FeCl_3$•$6H_2O$ & $FeSO_4$•$7H_2O$	$H_2N(CH_2)_3Si(OCH_3)_3$	2	10
6[42, 45]	$Fe(NO_3)_3$•$9H_2O$	$H_2N(CH_2)_3Si(OCH_3)_3$	2	20-40
7[4, 39, 41]	$FeCl_3$•$6H_2O$	triethylenetetramine	1	70-100
8[37]	$FeCl_3$•$6H_2O$ & $FeCl_2$•$4H_2O$	$(CH_3O)_3Si(CH_2)_3NH(CH_2)_2NH(CH_2)_2NH_2$	2	20-100
9[43]	$FeCl_3.6H_2O$	poly(propyleneglycol)bis (2-aminopropyl ether)	1	20
10[47]	$FeCl_3$•$6H_2O$	2,2'-(ethylenedioxy)-bis-(ethylamine)	1	6
11[51]	$FeCl_3$•$6H_2O$	2-aminoterephthalic acid	2	4
12[6]	$FeCl_3$•$6H_2O$ & $FeSO_4$•$7H_2O$	$H_2N(CH_2)_3Si(OEt)_3$	2	none

In continuous of these procedures (table 1), Fe_3O_4@NH_2 was synthesized by a new protocol. The magnetite nanoparticles were prepared from $FeCl_3$•$6H_2O$. Also, 1, 2-ethylenediamine was used as an amino agent. As shown in table 2, some experiments were carried out for optimizing the best ratio of the reagents, temperature, and reaction time. All reactions were performed by a one-pot reaction of $FeCl_3$•$6H_2O$ and 1, 2-ethylenediamine in the ratio (1:10) in ethylene glycol at different temperatures & times under an inert atmosphere.

J. Mex. Chem. Soc. **2024**, *68*(2)
Regular Issue

ISSN-e 2594-0317

Table 2. Optimization reaction conditions for the synthesis of Fe_3O_4@NH_2 (product) from $FeCl_3$•$6H_2O$ (A), 1, 2-ethylenediamine (B), and sodium acetate anhydrous (C) in ethylene glycol (45 mL).

Entry	A/g	B/g	C/g	*θ*/° C	*t*/*h*	Product
1	1.5	2	3	150-190	3 and 6	impure
2	1.5	3	6	200	3 and 6	impure
3	1.5	2	12	200	6	impure
4	1.5	3	6	110	3	poor quality
5	1.5	3	12	110	6	good quality
6	1.5	3	6	110	12	poor quality

The quality of the obtained AF-MNPs was determined by comparing FT-IR spectra as shown in Fig. 1**(a-c)**. In Fig. 1**(a)**, the band at 645 cm^{-1} assigned to the impurity some amount of maghemite [36b] when the reactions were carried out at 200 °C (table 2, entry 2-3). The same results were achieved at 150-190 °C (table 2, entry 1). Due to the absorbance bands at 3428 cm^{-1} (NH stretching vibration) and 2934 and 2862 cm^{-1} (asymmetric stretching vibration and symmetric stretching vibration of CH_2), 1, 2-ethylenediamine was coated better at 110 °C within 6 hours (Fig. 1**(c)**) (Table 2, entry 5), while the coating was reduced in fewer time of reaction (3 hours, Fig. 1**(b)**) (Table 2, entry 4).

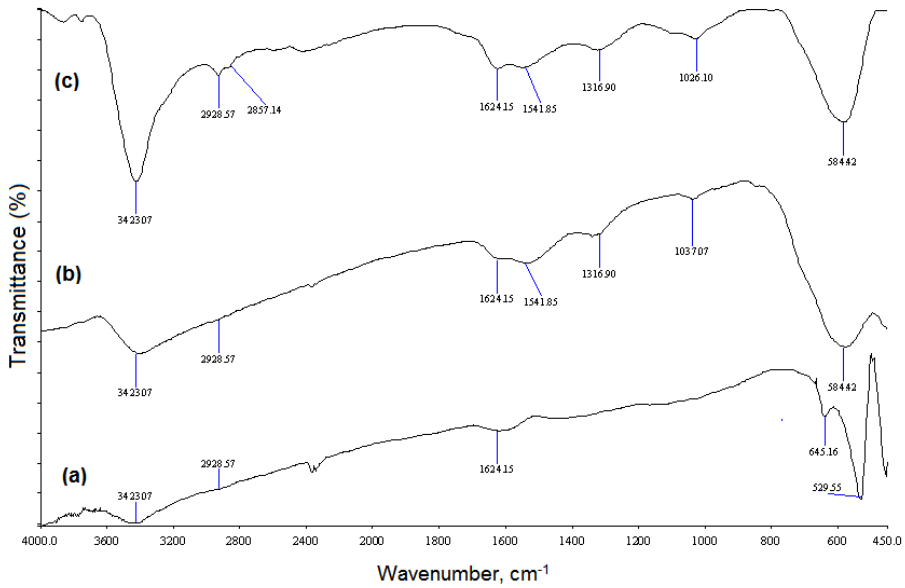

Fig. 1. (a) FT-IR spectrum of synthesized of Fe_3O_4-CH_2CH_2-NH_2 at 200 °C within 6 hours (Table 2, entry 3). **(b)** FT-IR spectrum of synthesized of Fe_3O_4-CH_2CH_2-NH_2 at 110 °C within 3 hours (Table 2, entry 4). **(c)** FT-IR spectrum of synthesized of Fe_3O_4-CH_2CH_2-NH_2 at 110 °C within 6 hours (Table 2, entry 5).

Thus, the results (Table 2, entry 5) showed that a one-pot reaction of $FeCl_3$•$6H_2O$ and 1, 2-ethylenediamine in the ratio (1:10) at 110 °C within 6 hours in ethylene glycol gave the best quality and quantity

J. Mex. Chem. Soc. **2024**, *68*(2)
Regular Issue

ISSN-e 2594-0317

of Fe_3O_4-CH_2CH_2-NH_2 (Fe_3O_4@NH_2) as shown in Scheme 1. The chemical structure of Fe_3O_4@NH_2 was characterized by FT-IR and VSM spectra.

A one-pot reaction of $FeCl_3.6H_2O$ and 1, 2-ethylenediamine in the ratio (1:10) at 110 °C within 6 hours in ethylene glycol gave the best quality and quantity of Fe_3O_4-CH_2CH_2-NH_2 (Fe_3O_4@NH_2) as shown in Scheme 3.

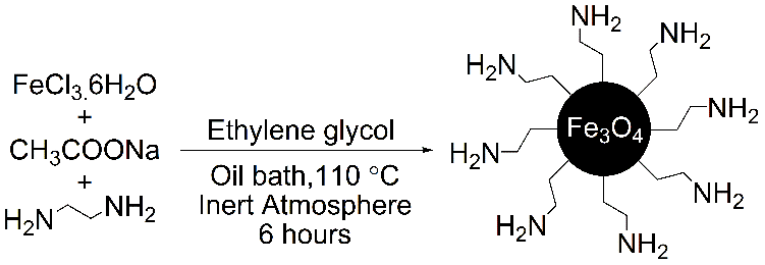

Scheme 3. The synthesis of Fe_3O_4@NH_2 nanoparticles.

Then, oxalic acid as an organic acid was linked to surface of Fe_3O_4@NH_2 nanoparticles. The best reaction conditions were obtained by performing some reactions in different conditions as shown in Table 3.

Table 3. Optimization reaction conditions for the synthesis of Fe_3O_4@NH_2@oxalic acid (product) from Fe_3O_4@NH_2 (1 g) under the Ar atmosphere.

Entry	$m_{\text{oxalic acid}}$ / g	Conditions	θ / °C	t / h	Product[1]
1	0.4	-	RT	2 or 4	no
2	0.4	ultrasonic	RT	2 or 4	no
3	0.8	ultrasonic	40	2 or 4	no
4	1.2	ultrasonic	40	2 or 4	no
5	1.2	ultrasonic	60	2	no
6	1.2	ultrasonic	60	4	yes
7	1.2	-	60	4	no
8[2]	1.6	ultrasonic	60	4	yes
9[2]	1.2	ultrasonic	60	8	yes

[1]The formation of the product (Fe_3O_4@NH_2@oxalic acid) was characterized by FT-IR spectrum.
[2]The obtained results from entries 8 and 9 are similar to entry 6. These results showed that more amounts of oxalic acid and more reaction time for the preparation of the product are not required.

The results showed (Table 3, entry 6) that oxalic acid can be linked by using ultrasonic irradiation at 60 °C within 4 hours under the Ar atmosphere. Thus, the Fe_3O_4-CH_2CH_2NH-CO-CO_2H (Fe_3O_4@NH_2@oxalic acid) nanoparticles were successfully synthesized, as shown in Scheme 4. The chemical structure of the Fe_3O_4@NH_2@oxalic acid was characterized by FT-IR, XRD, SEM, VSM, and EDAX spectra.

J. Mex. Chem. Soc. **2024**, *68*(2)
Regular Issue

ISSN-e 2594-0317

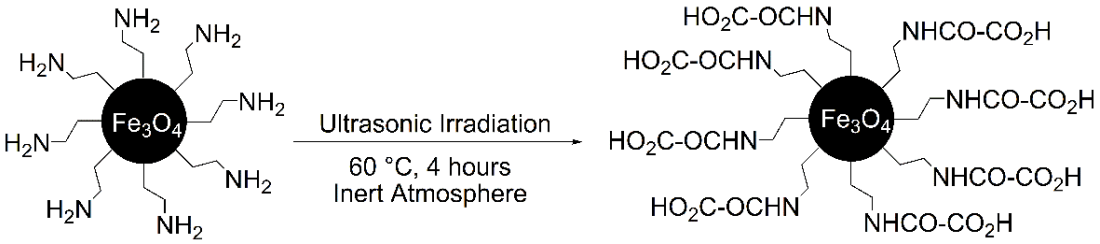

Scheme 4. The synthesis of Fe_3O_4@NH_2@oxalic acid nanoparticles from Fe_3O_4@NH_2 nanoparticles under ultrasonic irradiations.

The FT-IR spectrum of Fe_3O_4-CH_2CH_2-NH_2 (Fe_3O_4@NH_2) is shown in Fig. 2**(a)**. The band at 3428 cm^{-1} was assigned to NH stretching vibration which was combined with OH stretching vibration of the absorbed water on Fe_3O_4. The bands at 2934 cm^{-1} and 2862 cm^{-1} were assigned to asymmetric stretching vibration and symmetric stretching vibration of CH_2. The band at 1626 cm^{-1} was assigned to OH bending vibration of the absorbed water on Fe_3O_4. The band at 1547 cm^{-1} was assigned to NH bending vibration. The band at 1316 cm^{-1} was assigned to C–C stretching of vibration. The band at 1023 cm^{-1} was assigned to C–N stretching vibration and the band at 583 cm^{-1} was assigned to the Fe–O bending vibration [34b].

The FT-IR spectrum of Fe_3O_4-CH_2CH_2NH-CO-CO_2H (Fe_3O_4@NH_2@oxalic acid) has been shown in Fig. 2**(b)**. The band at 3394 cm^{-1} was assigned to OH stretching vibration of the COOH group. The band at 1684 cm^{-1} and 1673 cm^{-1} were assigned to C=O bond stretching vibrations of the COOH and CO-NH groups, respectively. The band at 1397 cm^{-1} was assigned to OH bending vibration of the COOH group. The band at 1267 cm^{-1} was assigned to C–O stretching vibration. The band at 1037 cm^{-1} was assigned to C–N stretching vibration. The band at 787 cm^{-1} was assigned to OH bending vibration of the COOH group, and 567 cm^{-1} was assigned to the Fe–O bending vibration.

A comparison of the FT-IR spectra of Fe_3O_4@NH_2 in Fig. 2**(a)** and Fe_3O_4@NH_2@oxalic acid in Fig. 2**(b)** shows that a band at 1626 cm^{-1} in Fig. 1**(a)** does not appear in the FT-IR spectrum of Fe_3O_4@NH_2@oxalic acid Fig. 2**(b)**. Because this band was replaced by a doublet band at 1684 cm^{-1} (acidic C=O) and 1673 cm^{-1} (amide C=O). This result that was indicated the successful attachment of oxalic acid to Fe_3O_4@NH_2 nanoparticles.

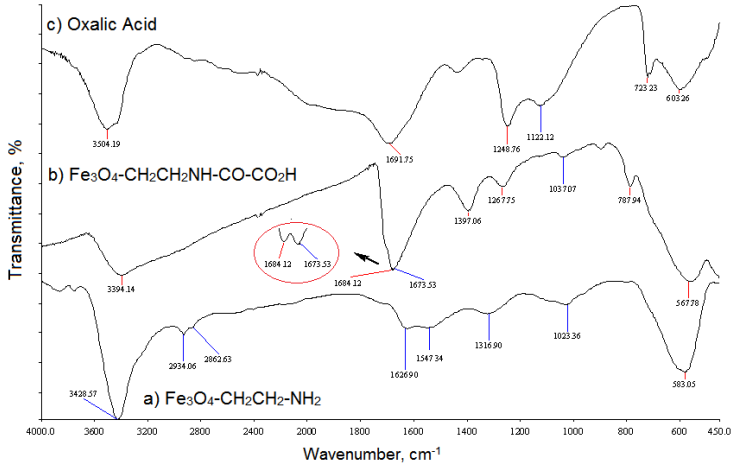

Fig. 2. The FT-IR spectra of **(a)** Fe_3O_4-CH_2CH_2-NH_2 (Fe_3O_4@NH_2), **(b)** Fe_3O_4-CH_2CH_2NH-CO-CO_2H, (Fe_3O_4@NH_2@oxalic acid) **(c)** oxalic acid.

J. Mex. Chem. Soc. **2024**, *68*(2)
Regular Issue

ISSN-e 2594-0317

The VSM spectrum was used to evaluate the magnetic measurement of magnetite nanoparticles at room temperature as shown in Fig. 3**(a)**. Due to the lack of magnetic remanence and coercivity, the room-temperature magnetization curve of the Fe_3O_4@NH_2 and Fe_3O_4@NH_2@oxalic acid nanoparticles suggests a paramagnetic state of the nanoparticles. The magnetization curves indicate the saturation magnetization of Fe_3O_4@NH_2@oxalic acid and Fe_3O_4@NH_2 nanoparticles, which were diminished to 10.50 emu/g from 12.90 emu/g. These results are significantly smaller than reported values for bulk Fe_3O_4 (92 emu/g and 100 emu/g) [54]. In the Fe_3O_4@NH_2 and Fe_3O_4@NH_2@oxalic acid adsorbed water, amine agent, and oxalic acid reduce the measured magnetic strength because magnetic nanoparticles are diluted with diamagnetic physically.

The SEM images of nano-Fe_3O_4@NH_2@oxalic acid (Fig. 3**(b)**) show the presence of spheric nanoparticles with 81 nm of average diameter.

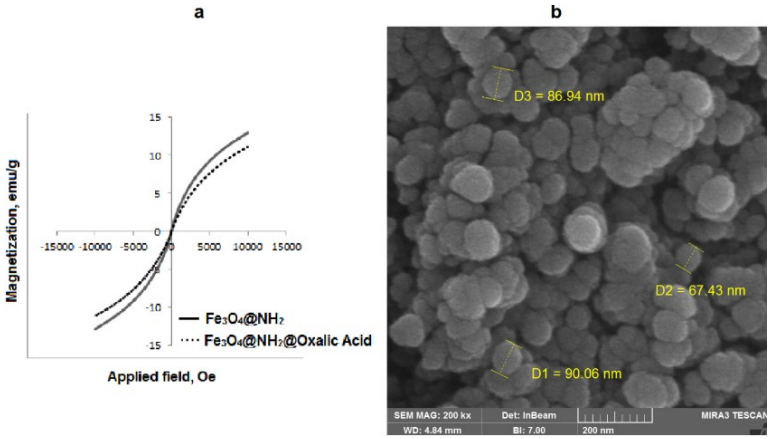

Fig 3. a) The room-temperature magnetization curve of the Fe_3O_4@NH_2 and Fe_3O_4@NH_2@oxalic acid nanoparticles. b) The SEM spectra of Fe_3O_4@NH_2@oxalic acid.

The XRD patterns of the Fe_3O_4@NH_2@oxalic acid nanoparticles are presented in Fig. 4. The peak positions are indexed as (111), (220), (331), (400), (422), (511), (440), (620), (533) and (444) in the 2θ range of 20–80°. These results reveal the existence of a Fe_3O_4 core in the Fe_3O_4@NH_2@oxalic acid which is in good agreement with the literature [54-55]. Fig. 5 shows EDAX analysis of Fe_3O_4@NH_2@oxalic acid nanoparticles. The sample peaks are observed for carbon, oxygen, iron, and nitrogen. It reveals that carbon was from 1, 2-ethylenediamine and oxalic acid, oxygen from oxalic acid and Fe_3O_4, iron from Fe_3O_4, and nitrogen from 1, 2-ethylenediamine. These results shows that surface of Fe_3O_4 was coated more than 93 % by organic materials (1, 2-ethylenediamine, and oxalic acid).

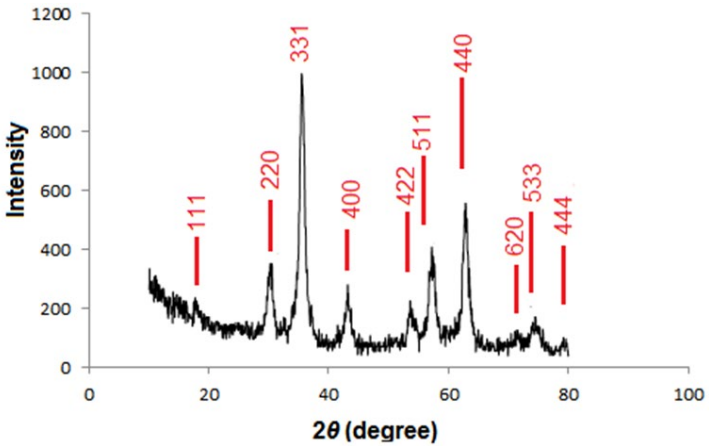

Fig 4. The XRD patterns of Fe_3O_4@NH_2@oxalic acid nanoparticles.

J. Mex. Chem. Soc. **2024**, *68*(2)
Regular Issue

ISSN-e 2594-0317

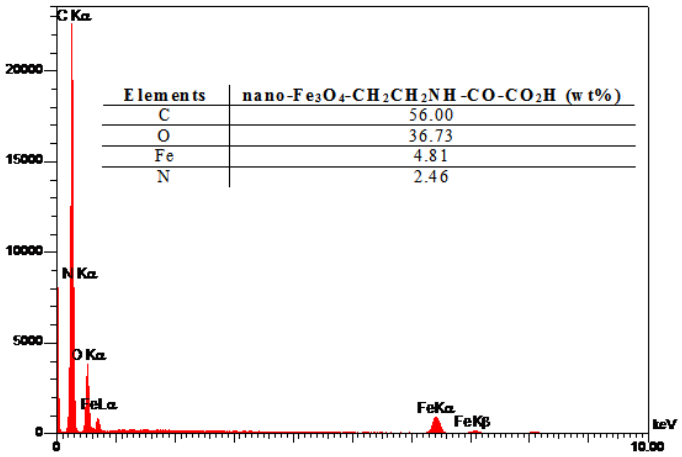

Fig 5. EDAX analysis of Fe_3O_4@NH_2@oxalic acid nanoparticles.

The synthesized Fe_3O_4@NH_2@oxalic acid nanoparticles were used for the synthesis of pyrrolin-2-one derivatives after optimum reaction conditions as shown in Table 4. It was best to combine benzaldehyde (1 mmol), aniline (1 mmol), and 0.2 g Fe_3O_4@NH_2@oxalic acid nanoparticles as the catalyst in ethanol. The reaction was completed after 8 hours to give the corresponding pyrrolin-2-ones in 95 % yields as shown in Scheme 2.

Table 4. Optimization reaction conditions for the synthesis of 1,5-diphenyl-3-hydroxy-4-methoxycarbonyl-3-pyrrolin-2-one in the presence of Fe3O4@NH2@oxalic acid nanoparticles as catalyst at room temperature.[a]

Entry	Catalyst	Amounts (g)	Solvent	*t*/h	Yields, %[b]
1	Fe_3O_4@NH_2@oxalic acid	0.1	EtOH	12	35
2	Fe_3O_4@NH_2@oxalic acid	0.15	EtOH	12	60
3	Fe_3O_4@NH_2@oxalic acid	0.2	EtOH	8	95
4	Fe_3O_4@NH_2@oxalic acid	0.5	EtOH	6	93
5	Fe_3O_4@NH_2@oxalic acid	1	EtOH	6	90
6	Fe_3O_4@NH_2@oxalic acid	0.2	MeOH	2	90
7	Fe_3O_4@NH_2@oxalic acid	0.2	EtOAc	24	75
8	Fe_3O_4@NH_2@oxalic acid	0.2	H_2O	24	0
9	Fe_3O_4@NH_2@oxalic acid	0.2	THF	24	47

[a]benzaldehye (1 mmol), aniline (1 mmol), DAMD (1 mmol). [b]The yields were referred to as isolated products.

For more proofing, the reaction of a variety of anilines and aromatic aldehydes was performed under optimized reaction conditions. All the reactions were completed within 6-10 hours in the excellent yields of pure products (1-8a) (90-95 %) as shown in scheme 2. All products were characterized by FT-IR, ^{1}H-NMR, ^{13}C-NMR and C. H, N elemental analysis. In the ^{1}H-NMR spectrum, the chemical shifts of the CH group in the

J. Mex. Chem. Soc. **2024**, *68*(2)
Regular Issue

ISSN-e 2594-0317

heterocyclic ring appear around 5.62-6.41 ppm, as a single signal. In the FT-IR spectrum, the C=O stretching frequency of the products appears around 1675-1693 cm^{-1}. The melting points of the products were measured and compared with the literature [30-35].

Due to the chemical structure of Fe_3O_4@NH_2@oxalic acid, CO_2H groups can provide an acidic surface with good polarity. All moieties in this reaction are polar. Thus, they can react and condensate more easily on Fe_3O_4@NH_2@oxalic acid surface by dipolar-dipolar interactions. Fe_3O_4@NH_2@oxalic acid nanoparticles activate the aldehyde functional group for reaction with aniline. Thus, an imine as an intermediate (step (I), Scheme 3) is produced. Then, the obtained H_2O molecules from this condensation reaction, react with DMAD and produce a 1,3-dipolar intermediate (step (II), Scheme 3) [30], which would undergo the addition to the imine (step (III & IV), Scheme 3). Then, an intramolecular attack of the amino group on one of the esters results in the formation of the five-membered ring as pyrrolin-2-one skeleton (a, step (V), Scheme 3).

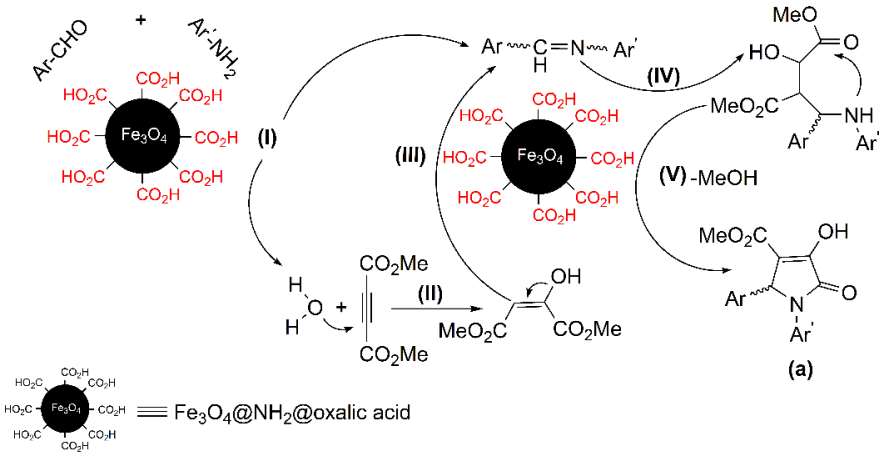

Scheme 3. The schematic and the tentatively proposed mechanism for the synthesis of pyrrolin-2-one derivatives by Fe_3O_4@NH_2@oxalic acid as catalyst.

Table 5. Comparison of synthesis of 1,5-diphenyl-3-hydroxy-4-methoxycarbonyl-3-pyrrolin-2-one by Fe3O4@NH2@oxalic acid with the different protocols.

Entry	Protocol	Yield	t/*h*	Green Profile	Availability	Reusable Catalyst	Reference
1	Fe_3O_4@NH_2@oxalic acid/EtOH/RT	95	8	yes	yes	yes	current
2	EtOH/H_2O/RT	87	15	yes	yes	no	29
3	*P*-TsOH/EtOH/RT	62	48	no	yes	no	30
4	Citric Acid/US/ EtOH/RT	90	0.3	yes	no	no	31
5	*P*-TsOH/MW/EtOH/RT	96	0.1	no	no	no	32
6	TiO_2 admicelle/H_2O/RT	75	18	yes	no	no	28
7	[bmim]BF_4/PEG-400/RT	89	1	yes	no	yes	33a
8	MW/[BBSI]Cl/Ethylene glycol/RT	90	0.1	yes	no	yes	33b

J. Mex. Chem. Soc. **2024**, *68*(2)
Regular Issue

ISSN-e 2594-0317

9	[BBSI]Cl/ball milling/RT	90	0.5	yes	no	yes	33c
10	[BBSI]HSO_4/ball milling/RT	87	0.4	yes	no	yes	33c
11	Fe_3O_4@SiO_2@Propyl–ANDSA/EtOH/RT	87	8	yes	no	yes	34
12	Fe_3O_4@PEG-400@oxalic acid/MeOH/RT	90	24	yes	no	yes	35
13	LEDs/Rose Benga /CH_3CN-H_2O	94	0.8	yes	no	yes	56
14	AmberChrom/brine/ EtOH/RT	95	6	yes	yes	yes	35

The reusability of Fe_3O_4@NH_2@oxalic acid catalyst was examined. The recycled catalyst can be used three more times. For example, the second and third rounds yields of the product (Scheme 2, 1a) were 92 % and 93 % respectively. For more consideration, the efficiency of Fe_3O_4@NH_2@oxalic acid nano-magnetic catalyst for the synthesis of 1,5-diphenyl-3-hydroxy-4-methoxycarbonyl-3-pyrrolin-2-one (Sheme 2, 1a) has been compared with other reported protocols as shown in Table 5. The comparison shows Fe_3O_4@NH_2@oxalic acid catalyst has a good potential for the synthesis of pyrrolin-2-one derivatives.

Conclusions

In this research, the Fe_3O_4@NH_2 nanoparticle was synthesized from $FeCl_3$•$6H_2O$ and 1, 2-ethylenediamine. Then, Fe_3O_4@NH_2@oxalic acid as an organoacid-magnetic nanoparticle was synthesized by coupling of Fe_3O_4@NH_2 nanoparticle and oxalic acid under ultrasonic irradiations. Also, the nano-Fe_3O_4@NH_2@oxalic acid was used for preparation of a variety of pyrrolin-2-ones. The reactions were performed in ethanol in the excellent of yields at room temperature. The recovered and regenerated catalyst can be useful for reaction with loss of activity. Thus, easy work-up, mild reaction conditions, recyclability, recovery, non-toxicity, economically affordable, and high efficiency are valuable characteristics that make this new method noteworthy.

Acknowledgements

The authors gratefully acknowledge the financial support of this work by the Research Council of the Islamic Azad University, Mahabad Branch, Mahabad, Iran. DOI:

References

1. Wang, L.; Bao, J.; Wang, L.; Zhang, F.; Li, Y. *Chem. Eur. J.* **2012**, *12*, 6341- 6343. DOI: https://doi.org/10.1002/chem.200501334.
2. Hana, J.; Wang, L.; Wang, Y.; Dong, J.; Tang, X.; Ni, L.; Wang, L. *Biochem. Eng. J.* **2018**, *130*, 90-98. DOI: https://doi.org/10.1016/j.bej.2017.11.008.

J. Mex. Chem. Soc. **2024**, *68*(2)
Regular Issue

ISSN-e 2594-0317

3. Liua, Y.; Lib, L.; Liub, S.; Xiea, C.; Yub, S. *J. Mol. Catal. A. Chem.* **2016**, *424*, 269-275. DOI: https://doi.org/10.1016/j.molcata.2016.09.007.
4. Ma, M.; Zhang, Q.; Yin, D.; Dou, J.; Zhang, H.; Xu, H. *Catal. Commun.* **2012**, *17*, 168-172. DOI: https://doi.org/10.1016/j.catcom.2011.10.015.
5. Naeimi, H.; Ansarian, Z. *J. Taiwan Inst. Chem. Eng.* **2018**, *85*, 265-272. DOI: https://doi.org/10.1016/j.jtice.2018.01.047.
6. Han, Q.; Wu, X.; Cao, Y.; Zhang, H.; Zhao, Y.; Kang, X.; Zhu, H. *Separations* **2021**, *8*, 196 https://doi.org/10.3390/separations8110196.
7. Zhang, F.; Jin, J.; Zhong, X.; Li, S.; Niu, J.; Li, R.; Ma, J. *Green Chem.* **2011**, *13*, 1238-1243. DOI: https://doi.org/10.1039/C0GC00854K.
8. Xu, Y. Y.; Zhou, M.; Geng, H. J.; Hao, J. J.; Ou, Q. Q. *Appl. Surf. Sci.* **2012**, *258*, 3897-3902. DOI: https://doi.org/10.1016/j.apsusc.2011.12.054
9. Wang, X.; Almoallim, H. S.; Cui, Q.; Alharbi, S. A.; Yang, H. *Int. J. Biol. Macromol* **2021**, *171*, 198-207. DOI: https://doi.org/10.1016/j.ijbiomac.2020.12.037.
10. Sharma, K.; Dutta, S.; Sharma, S. *Dalton Trans.* **2015**, *44*, 1303-1316. DOI: https://doi.org/10.1039/C4DT03236E.
11. Snoussi, Y.; Bastide, S.; Abderrabba, M.; Chehimi, M. M. *Ultrason. Sonochem.* **2018**, *41*, 551-561. DOI: https://doi.org/10.1016/j.ultsonch.2017.10.021.
12. Zhang, Z.; Zhu, Y.; Dai, R.; Zhang, Y.; Wang, H.; Li, J. *Photodiagnosis Photodyn. Ther.* **2018**, *23*, 50-54. DOI: https://doi.org/10.1016/j.pdpdt.2018.06.002.
13. Gemeay, A. H.; Keshta, B. E.; El-Sharkawy, R. G.; Zaki, A. B. *Environ. Sci. Pollut. Res.* **2020**, *27*, 32341-32358. DOI: https://doi.org/10.1007/s11356-019-06530-y.
14. Dwoskin, P.; Teng, L.; Buxton, S. T.; Crooks, P. A. *J. Pharmacol. Exp. Ther*. **1999**, *288*, 905-911. DOI:https://jpet.aspetjournals.org/content/288/3/905.short.
15. Singh, P.; Dimitriou, V.; Mahajan, R. P.; Crossley, A. W. *Br. J. Anaesth*. **1993**, *71*, 685-688. DOI: https://doi.org/10.1093/bja/71.5.685.
16. Patsalos, P. N. *Epilepsia* **2005**, *46*, 140-148. DOI: https://doi.org/10.1111/j.1528-1167.2005.00326.x.
17. Lampe, J. W.; Chou, Y.; Hanna, R. G.; Di Meo, S. V.; Erhardt, P. W.; Hagedorn, A. A.; Ingebretsen, W. R.; Cantor, E. *J. Med. Chem.* **1993**, *36*, 1041-1047. DOI: https://doi.org/10.1021/jm00060a012.
18. Omura, S.; Fujimoto, T.; Otoguro, K.; Matsuzaki, K.; Moriguchi, R.; Tanaka, H.; Sasaki, Y. *J. Antibiot.* **1991**, *44*, 113-116. DOI: https://doi.org/10.7164/antibiotics.44.113.
19. Feling, R. H.; Buchanan, G. O.; Mincer, T. J.; Kauffman, C. A.; Jensen, P. R.; Fenical, W. *Angew. Chem. Int. Ed.* **2003**, *42*, 355-357. DOI: https://doi.org/10.1002/anie.200390115.
20. Asami, Y.; Kakeya, H.; Onose, R.; Yoshida, A.; Matsuzaki, H.; Osada, H. *Org. Lett.* **2002**, *4*, 2845-2848. DOI: https://doi.org/10.1021/ol020104+.
21. Fischer, R.; Lehr, S.; Drewes, M. W.; Feucht, D.; Malsam, O.; Bojack, G.; Arnold, C.; Auler, T.; Hills, M.; Kehne, H. German Patent DE 102004053191 2006.
22. Franco, M. S. F.; Casagrande, G. A.; Raminelli, C.; Moura, S.; Rossatto, M.; Quina, F. H.; Pereira, C. M. P.; Flores, A. F. C.; Pizzuti, L. *Synth. Commun.* **2015**, *45*, 692-701. DOI: https://doi.org/10.1080/00397911.2014.978504.
23. Andana, M.; Hashimoto, S. I. Tetrahedron *Lett.* **1998**, *39*, 79-82. DOI: https://doi.org/10.1016/S0040-4039(97)10493-2.
24. Choi, D. R.; Lee, K. Y.; Chung, Y. S.; Joo, J. E.; Kim, Y. H.; Oh, Ch. Y.; Lee, Y. S.; Ham, W. H. *Arch. Pharm. Res.* **2005**, *28*, 151-158. DOI: https://doi.org/10.1007/bf02977706.
25. Burgess, L. E.; Meyers, A. I.; *J. Org. Chem.* **1992**, *57*, 1656-1662. DOI: https://doi.org/10.1021/jo00032a012.
26. Overman, L. E.; Remarchuk, T. P.; *J. Am. Chem. Soc*. **2002**, *124*, 12-13. DOI: https://doi.org/10.1021/ja017198n.

J. Mex. Chem. Soc. **2024**, *68*(2)
Regular Issue

ISSN-e 2594-0317

27. Singh, V.; Saxena, R.; Batra, S. *J. Org. Chem.* **2005**, *70*, 353-356. DOI: https://doi.org/10.1021/jo048411b.
28. Sarkar, R.; Mukhopadhyay, C. *Tetrahedron Lett.* 2013, 54, 3706-3711. DOI: https://doi.org/10.1016/j.tetlet.2013.05.017.
29. Zonouz, A. M.; Eskandari, I.; Notash, B. *Synth. Commun.* **2015**, *45,* 2115-2121. DOI: https://doi.org/10.1080/00397911.2015.1065506.
30. Sun, J.; Wu, Q.; Xia, E.Y.; Yan, C. G. *Eur. J. Org. Chem.* **2011**, 2981-2986. DOI: https://doi.org/10.1002/ejoc.201100008.
31. Ahankar, H.; Ramazani, A.; Slepokura, K.; Lis, T.; Joo, S. W. *Green Chem*. **2016**, *18*, 3582-3593. DOI: https://doi.org/10.1039/c6gc00157b.
32. Marapala, K. S.; Venkatesh, N.; Swapna, M.; Venkateswar, P. R. *Int. J. ChemTech Res.* **2020**, *13*, 227-231. DOI: https://doi.org/10.20902/ijctr.2019.130128.
33. a) Pervaram, S.; Ashok, D.; Venkata Ramana Reddy, C.; Sarasija, M.; Ganesh, A. *Chem. Data Collect.* **2020**, 29, 100508. DOI: https://doi.org/10.1016/j.cdc.2020.100508. b) Ghaffari Khaligh, N.; Mihankhah, T.; Rafie Johan, M.; Titinchi, S. J. J. *Green Process Synth*. **2019**, 8, 373-381. DOI: https://doi.org/10.1515/gps-2019-0004. c) Ghaffari Khaligh, N.; Mihankhah, T.; Rafie Johan, M.; *Synth. Commun.* **2019**, *49*, 1334-1342. DOI: https://doi.org/10.1080/00397911.2019.1601225.
34. a) Ghorbani-Vaghei, R.; Sarmast, N.; Mahmoodi, J. *Appl. Organomet. Chem*. **2017**, *31*, e3681. DOI: https://doi.org/10.1002/aoc.3681. b) Esmaeilzadeh, S.; Setamdideh, D. *J. Serb. Chem. Soc.* **2021**, *86*, 1039-1056. DOI: https://doi.org/10.2298/JSC210521059E.
35. Hamdi Mohamadabad, P.; Setamdideh, D. *Org. Prep. Proced. Int.* **2023**, *55*, 265-275. DOI: https://doi.org/10.1080/00304948.2022.2141044.
36. a) Kim, H. K.; Park, J. W.; *J. Environ. Sci. Health. A.* **2019**, *54*, 648-656. DOI: https://doi.org/10.1080/10934529.2019.1579535. b) Burakevich, J. V.; Lore, A. M.; Volpp, G. P. *J. Org. Chem*. **1971**, *36*, 1-4. DOI: https://doi.org/10.1021/jo00800a001.
37. Chan, C. C. P.; Gallard, H.; Majewski, P. *J. Nanopart. Res.* **2012**, *14*, 828. DOI: https://doi.org/10.1007/s11051-012-0828-2.
38. Ebrahimi-Tazangi, F.; Hekmatara, S. H.; Yazdi, J. S. *J. Alloys Compd.* **2019**, *809*, 151779. DOI: https://doi.org/10.1016/j.jallcom.2019.151779.
39. Zhang, C. L.; Cheng, H. D.; Ren, S. Y.; Zhang, W. P.; Chen, Z.; Wang, Y.; MA, J. H.; Zhang, C. S.; Guo, Z. Y. *IOP Conf. Ser.: Earth Environ. Sci.* **2018**, *199,* 052042. DOI: https://doi.org/10.1088/1755-1315/199/5/052042.
40. Fan, G.; Rena, Y.; Jiangb, W.; Wang, C.; Xub, B.; Liu, F. *Catal. Commun.* **2014**, *52*, 22. DOI: https://doi.org/10.1016/j.catcom.2014.04.006.
41. Gao, J.; He, Y.; Zhao, X.; Ran, X.; Wuc, Y.; Su, Y.; Dai, J. *J. Colloid Interface. Sci.* **2016**, *481***,** 220-228. DOI: https://doi.org/10.1016/j.jcis.2016.07.057.
42. Chu, C.; Lu, C.; Yuan, J.; Xing, C. *Sci. Nutr.* **2020**, *8*, 3673-3681. DOI: https://doi.org/10.1002/fsn3.1651.
43. Guan, N.; Xu, J.; Wang, L.; Sun, D. *Colloid Surf. A-Phsicochem. Eng. Asp.* **2009**, *346*, 221-228. DOI: https://doi.org/10.1016/j.colsurfa.2009.06.022.
44. He, X.; Yang, W.; Li, S.; Liu, Y.; Hu, B.; Wang, T.; Hou, X. *Microchim. Acta.* **2018**, *185*, 125. DOI: https://doi.org/10.1007/s00604-018-2672-2.
45. Jafarnejad, M.; Daghighi Asli, M.; Afshar Taromi, F.; Manoochehri, M. *Int. J. Biol. Macromol.* **2020**, *148*, 201-217. DOI: https://doi.org/10.1016/j.ijbiomac.2020.01.017.
46. Lin, S.; Hua, X.; Yang, Y.; Liu, L.; Lin, K. *Water Sci. Technol.* **2017**, *76*, 452-458. DOI: https://doi.org/10.2166/wst.2017.225.
47. Das, M.; Dhak, P.; Gupta, S.; Mishra, D.; Maiti, T. K.; Basak, A.; Pramanik, P. *Nanotechnology* **2010**, *21*, 125103. DOI: https://doi.org/10.1088/0957-4484/21/12/125103.

J. Mex. Chem. Soc. **2024**, *68*(2)
Regular Issue

ISSN-e 2594-0317

48. Baghani, A. N.; Mahvi, A. H.; Gholami, M.; Delikhoon, N. R. M. *J. Environ. Health Sci. Eng.* **2016**, *14*, 11. DOI: https://doi.org/10.1186/s40201-016-0252-0.
49. Pazouki, M.; Zabihi, M.; Shayegan, J.; Fatehi, M. H. *J. Chem. Eng.* **2018**, *35*, 671-683. DOI: https://doi.org/10.1007/s11814-017-0293-9.
50. Han, L.; Li, Q.; Chen, S.; Xie, W.; Bao, W.; Chang, L.; Wang, J. *Sci. Rep.* **2017**, *7*, 7448. DOI: https://doi.org/10.1038/s41598-017-07802-8.
51. Li, Y.; Xie, Q.; Hu, Q.; Li, C.; Huang, Z.; Yang, X.; Guo, H. *Sci. Rep.* **2016**, *6,* 30651. DOI:https://doi.org/10.1038/srep30651.
52. Xiong, S.; Wang, M.; Cai, D.; Li, Y.; Gu, N.; Wu, Z.; *Anal. Lett.* **2013**, *46*, 912-922. DOI: https://doi.org/10.1080/00032719.2012.747094.
53. Tang, Z.; Li, F. *J. Comput. Theor. Nanosci.* **2016**, *13,* 772-776. DOI: https://doi.org/10.1166/jctn.2016.4873.
54. Cornell, R. M.; Schwertmann, U. U. in: *The Iron Oxides: Structure Properties, Reactions, Occurrences and Uses*, 2nd ed.; Completely Revised and Extended Edition; Wiley-VCH: Weinheim, Germany, 2003.
55. Loh, K. S.; Lee, Y. H.; Musa, A.; Salmah, A. A.; Zamri, I. *Sensors.* **2008**, *8*, 5775. DOI: https://doi.org/10.3390/s8095775.
56. Dutta, A.; Rohman, M. A.; Nongrum, R.; Thongni, A.; Mitra, S.; Nongkhlaw, R. *New J. Chem.* **2021**, *45*, 8136 -8148. DOI: https://doi.org/10.1039/D1NJ00343G.

Article

J. Mex. Chem. Soc. **2024**, *68*(2)
Regular Issue

ISSN-e 2594-0317

Morphological and Nutritional Characterization of Wild Edible Blackberries (*Rubus* spp.) from Sinaloa, Mexico

Oscar Abel Sánchez-Velázquez[1], Masiel Rivera-Atondo[2], Jorge Milán-Carrillo[1,2], Julio Montes-Ávila[1], Saraid Mora-Rochín[1,2], Edith Oliva Cuevas-Rodríguez[1,2,*]

[1]Programa de Posgrado Integral en Biotecnología, Facultad de Ciencias Químico-Biológicas, Universidad Autónoma de Sinaloa. Culiacán Rosales, Sinaloa, México. CP 80060.
[2]Posgrado en Ciencia y Tecnología de Alimentos, Facultad de Ciencias Químico-Biológicas, Universidad Autónoma de Sinaloa. Culiacán Rosales, Sinaloa, México. CP 80060.

***Corresponding author:** Edith Oliva Cuevas-Rodríguez, email: edith.cuevas.r@uas.edu.mx

Received August 28th, 2022; Accepted May 30th, 2023.

DOI: http://dx.doi.org/10.29356/jmcs.v68i2.1868

Abstract. Wild blackberries (*Rubus*) are fruits that grow in inaccessible high mountain areas, which has made it difficult to study their chemical and nutritional composition. The objective of this research was to evaluate the nutritional composition and the macro- and micro-nutrient profile of wild species of fruits of the *Rubus* genus collected in Sinaloa, Mexico. Botanical samples of wild *Rubus* were identified and deposited in the Herbarium of the Institute of Biology of the UNAM. Subsequently, the chemical composition the profile of carbohydrates, lipids and minerals were evaluated. Wild *Rubus* species were identified as *R. liebmannii*, *R. coriifolius* and *R. palmeri*. In addition, it was found that *R. liebmannii* is the first time it has been recorded for the state of Sinaloa. Likewise, the results show that carbohydrates represent the largest proportion of the macro-components (85 %, glucose and fructose); they have a high content of fatty acids (such as linolenic acid) and are rich sources of minerals (such as K, Ca and Mg). The results of this research could be relevant to be used in the genetic improvement of commercial species that currently exist in the market.
Keywords: *Rubus*; wild blackberries; macro-nutrients; minerals; fatty acids.

Resumen. Las zarzamoras silvestres (*Rubus*) son frutos que se desarrollan en zonas de alta montaña poco accesibles, lo que ha dificultado el estudio de su composición química y nutricional. El objetivo de la presente investigación fue evaluar la composición nutricional y el perfil de macro y micronutrientes de especies silvestres de frutos del género *Rubus* colectadas en Sinaloa, México. Muestras botánicas de *Rubus* silvestres fueron identificadas y depositadas en el Herbario del Insituto de Biología de la UNAM. Posteriormente se les evaluó la composicón química, el perfil de perfil de carbohidratos, lípidos y minerales. Las especies silvestres de *Rubus* fueron identificadas como *Rubus liebmannii*, *Rubus coriifolius* y *Rubus palmeri.* Además, se encontró que *Rubus liebmannii*, es la primera vez que se registra para el estado de Sinaloa. Asimismo, los resultados muestran que los carbohidratos representan la mayor proporción de los macro-componentes (85 %, glucosa y fructosa); tiene un alto contenido de ácidos grasos (como ácido linolénico) y son fuentes ricas de minerales (como K, Ca y Mg). Los resultados de la presente investigación podrían ser de relevancia para ser utilizados en el mejoramiento genético de especies comerciales que actualmente existen en el mercado.
Palabras clave: *Rubus*; zarzamoras silvestres; macronutrientes; minerales; ácidos grasos.

J. Mex. Chem. Soc. **2024**, *68*(2)
Regular Issue

ISSN-e 2594-0317

Introduction

The genus *Rubus* L. is a large and complex group of plants in the family Rosaceae naturally distributed in fresh and tropical regions worldwide with an uncertain number of species since some studies estimate 250–330 species, but others up to 750 species [1-3]. In Mexico, Rzedowski and Calderón de Rzedowski [4] catalogued 61 *Rubus* species, but recently, Rodríguez-Bautista et al. [5] reported only 42 species of this genus using bioinformatic tools. The most studied *Rubus* species in Mexico are mainly located in the Trans-Mexican Volcanic Belt and the Sierra Madre del Sur [4-6], though some exploratory research for the Sierras Madre Occidental has provided new records of wild *Rubus* for Sinaloa and Durango and some of these species are underutilized as a seasonal food source by local human communities [7,8]. However, all these investigations mention the need for more studies on this group's systematics, taxonomy, evolution, and ecology for Mexico and the world.

Several authors mention that *Rubus* species, and other Rosaceae species, are difficult to delimitate because of their easily hybridization among *Rubus* species, frequent apomixis, phenotypic plasticity and the lack of a consensus on the morphology of the genus [9-11]. The morphology of the *Rubus* species is multifaceted and varied since they can be shrub or woody plants, prostrate or erect, with compound leaf blades and serrated-toothed margins [12,13], which are considered useful characters to generate taxonomic discriminations when distinguishing these from other Rosaceae species [14]. However, within *Rubus*, the most relevant criteria are those that show the least phenotypic variation, highlighting among their flowers and fruits, as well as some constant characteristics of leaves, stems and roots [6,10].

The high variability is not exclusive to anatomical structures in *Rubus* plants since this diversity is also found in the phytochemical profile of nutritional compounds and secondary metabolites of leaves, roots, and fruits [15-20]. The macro- and micronutrients reported in *Rubus* fruits are well known in some popular commercial-domesticated *Rubus*, such as *R. fruticosus* (common blackberry), *R. coreanus* (bokbunja or Korean berry) and *R. idaeus* (common raspberry), which include a large variety of amino acids, vitamins, carbohydrates, lipids, and minerals, as well as their phytochemical profile [16,20-22].

The chemical profile of bioactive compounds (including tannins, flavonoids, and phenolic acids) of wild *Rubus* species from the "Chara Pinta (Tufted-Jay) Sanctuary" in Sinaloa, Mexico, is well documented by previous works [18-20]. However, the composition of nutritional, macro- and micronutrients remains unexplored. This study aims to evaluate the nutritional composition and the macro- and micronutrient profiles of wild *Rubus* berries from Sinaloa, Mexico.

Experimental

Materials and methods

Plant material

A search for individuals of the genus *Rubus* L. was carried out in 3 sites with anthropogenic alterations within the "Chara Pinta Sanctuary" (23º48'48.4 " N, 105º50'15.1" W), in the ejido lands of El Palmito, Concordia, Sinaloa, Mexico, during the spring-summer 2015 season (June 29-30, 2015). The collection sites were the Cabins of the Chara Pinta Sanctuary (CP, 2172 m a.s.l.), the Road to El Mirador (CM, 2163 m a.s.l.) and kilometer 200 of Federal Highway 40 (CF, 2013 m a.s.l.) (Fig. 1). Specimens with fertile stems (which presented leaves and inflorescences with fruits in different degrees of maturity and apical flowers or buds) and sterile stems were collected, taking care that these came from the central part of the plant, since in this region it is where it presents less phenotypic variability of the same structures, as different previous studies have established [14]. The plant material was pressed and dried at 50 ºC for 72 h. The material was analyzed and herbarized with the support of the National Herbarium of the Institute of Biology of the National Autonomous University of Mexico (MEXU) staff. About 1.0 kg of only ripe fruits of two from three *Rubus* species was collected and immediately freeze-died at -80 °C. However, for one of them, the collected fruits were insufficient for the subsequent nutritional evaluation.

J. Mex. Chem. Soc. **2024**, *68*(2)
Regular Issue

ISSN-e 2594-0317

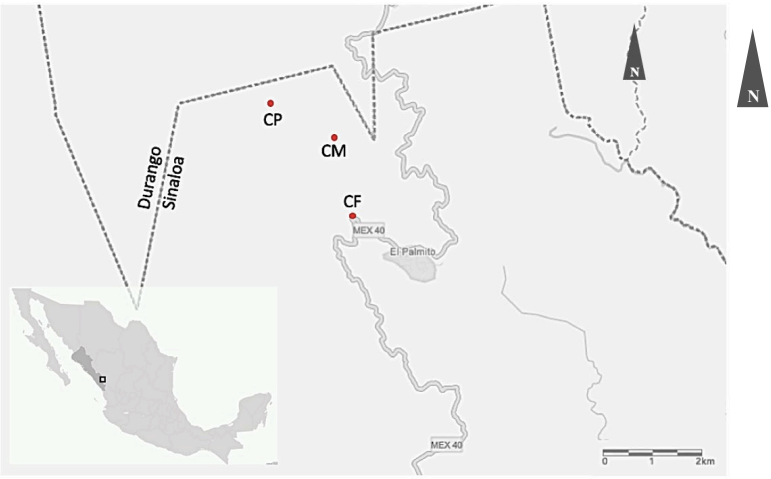

Fig. 1. Map of the wild blackberry collection sites in El Palmito, Sinaloa, Mexico. CP, Cabins of the Chara Pinta Sanctuary; CM, Road to El Mirador; CF, Federal Highway México 40.

Identification of wild blackberry species

The characters present in the exsiccates were compared with those of specimens previously identified and deposited in the MEXU, as well as with those described in the following floristic consultation sites: Tropicos (www.tropicos.org); KEW: World Checklist of Selected Plant Families (apps.kew.org); Catalog of Life (www.catalogueoflife.org); Global Biodiversity Information Facility (data.gbif.org); The New York Botanical Garden Virtual Herbarium (data.gbif.org); JSTOR Plant Science (plants.jstor.org); Encyclopedia of Life (www.eol.org); Biodiversity Heritage Library (www.biodiversitylibrary.org); and the Mesoamerican Flora project (http://www.tropicos.org/Project/FM).

Proximate composition of berries

Protein, moisture, fat, and ashes contents were determined on a dry basis according to the AOAC methods [23]. An amount of 0.2 g of freeze-dried fruits was digested with 1.625 g of catalyst (KSO_4:$CuSO_4$, 10:1, w/w) and 5 mL of H_2SO_4 for 6 h at 550 ºC. Then, 10 mL of distilled water was added, before adding 15 mL of H_3BO_3 and 3 drops of methyl red as an indicator. The colour of the mix was adjusted with 40 % NaOH and titrated with 0.08 N HCl. For moisture, 1.0 g of dried samples were held at 130 ºC for 1 h to remove remained moisture. The crude lipid content was estimated in 1.5 g of dried fruits in a Soxhlet system using petroleum ether and Whatman paper #1. Finally, ash content was measured in 1.0 g of freeze-dried fruits in a muffle at 550 ºC for 12 h. Carbohydrates were estimated by weight difference.

Extraction of macro-nutrients

Freeze-dried powder (360 g) of both *Rubus* fruits were mixed with 1 L of acidified methanol (80:0.3, MeOH:trichloroacetic acid, v/w) at 4 ºC for 24 h, then filtered with Whatman paper #1. These steps were repeated, and filtered fractions were collected together. Briefly, the MeOH was extracted by rotary evaporation in a Büchi equipment (Labortechnick AG., Switzerland). The aqueous part was exposed to ethyl acetate (1:1, v/v) and shacked vigorously for 2 min in a separatory funnel twice. The oily and watery phases were concentrated by rotary evaporation. The non-polar fraction (NPF) was kept at -20 ºC under its posterior evaluation. For carbohydrate isolation, the defatted samples were freeze-dried at -80 ºC, 5.0 g of this were resuspended in 100 mL of acidified water (0.3 % TCA), and exposed to 100 g of Amberlite XAD-7 adsorption resin (Sigma-Aldrich, St.-Louis, USA) for 30 min. A glass column of 300 × 25 mm was packed with the mix and washed with 500 mL of acidified water. The pH of the liquid was adjusted to 7.0 and freeze-died under its analysis.

J. Mex. Chem. Soc. **2024**, *68*(2)
Regular Issue

ISSN-e 2594-0317

Profile of carbohydrates

The carbohydrate-enriched fractions (CEF) were profiled according to the procedure reported by Xiang et al. [24], with some modifications. Briefly, 10 mg of CEF were solubilized with 50 µL of the derivatizing *N*,*O*-bis(trimethylsilyl)trifluoroacetamide **(**BSTFA, 33027, Sigma-Aldrich, St.-Louis, USA) and 50 µL of pyridine (27047, Sigma-Aldrich, St.-Louis, USA), sonicated for 5 min and heated at 70 ºC for 4 h. Afterwards, 1.5 mL of HPLC grade MeOH was used to resuspend the mix. A volume of 5 µL was injected in a GC-MS Agilent system (GC6890N-MS5973, Agilent Technologies, Inc., La Jolla, USA) and carried out with helium gas through a QUADREX 007-23 (30 m × 0.25 mm ID, 0.25 µm film thickness, Quadrex Corp., Woodbridge, USA). The injector temperature was 250 ºC, while the oven was at 60 ºC and the temperature gradient of 5 ºC/min until 200 ºC and heated up 10 ºC/min until 275 ºC, remaining constant at 275 ºC as far as 60.5 min. Mass detector was operated in the electron impact mode with 70 eV of energy. The temperatures for the detector and the quadrupole were 245 ºC and 150 ºC, respectively. The resulting data were compared with the NIST/EPA/NIH database Version 2.0 (NIST 08 Mass Spectral Library, Gaithersburg, USA). The obtained results were presented as relative percentages (%) of carbohydrates.

Profile of lipophilic compounds

The lipophilic profile was performed following the method described by Ahumada-Santos et al. [25]. About 5.0 mg of FEF were solubilized in 1 mL of hexane HPLC degree and injected in an Agilent GS-MS system (GC6890N-MS5973, Agilent Technologies, Inc., La Jolla, USA) through a QUADREX 007-23 (30 m × 0.25 mm ID, 0.25 µm film thickness, Quadrex Corp., Woodbridge, USA), using helium gas as a carrier. A volume of 5 µL was injected at 250 ºC of vaporizer temperature, the oven started at 60 ºC and the gradient was increased 5 ºC/min until 200 ºC and heated up 10 ºC/min until 275 ºC, remaining constant at 275 ºC as far as 60.5 min. The equipment mass detector was used in the electron impact mode with 70 eV of energy. Temperatures for the detector and the quadrupole were 245 ºC and 150 ºC, respectively. The results were compared with information compilated in the NIST/EPA/NIH database Version 2.0 (NIST 08 Mass Spectral Library, Gaithersburg, USA). Results were expressed as relative percentages (%) of the identified lipophilic compounds.

Profile of minerals

The mineral profiling was done following the procedure of Frías-Espericueta et al. [26], with slight adaptations. About 1.0 g of freeze-dried powder of both fruits was calcinated at 550 ºC for 2 h into a muffle. Ashes were solubilized in 5 mL of concentrated HNO_3 (trace metal grade) and kept at room temperature for 1 h. Then, the mix was filtered and made up to 50 mL with Milli-Q water. Finally, 1.0 mL of sample was injected in a Varian SpectrAA 220 atomic absorption spectrophotometry (Varian, Palo Alto, USA) and monitored with the Varian AA software version v3.10 (Varian, Palo Alto, USA). Analysis of certified reference material (DOLT-4, National Research Council Canada) gave recovery acceptable values of 95–115 % in all analyzed metals. Results were expressed as mg/100 g dw.

Statistical analysis

Data were analyzed by one-way analysis of variance using the Statgraphics Centurion XVI.I statistical package (Statgraphics Technologies, UK). Tukey's test was used to compare mean values +/- standard deviation under a statistical difference (p<0.05). All experiments were done in triplicate (n=3).

Results and discussion

Description of collected *Rubus*

The following *Rubus* species were described and identified in the Chara Pinta Sanctuary, Sinaloa (Fig. 2):

Rubus liebmannii Focke, Abh. Nat. Ver. Bremen 4: 158. 1874

TYPE: MEXICO, Oaxaca, Cerro de Zempoaltepec. 1842. Holotype: Liebmann s.n.; 1841-1843; Mexico (C).

J. Mex. Chem. Soc. **2024**, *68*(2)
Regular Issue

ISSN-e 2594-0317

Perennial stems, 2–3 m tall; shoots erect, terminal part arched, abruptly angulate, scarcely hairy and armed with some compact curved spines; trimeric, deciduous leaves **(**Fig. 2**(A.1)**); petioles hairy, prickly, 4–6 cm long; stipulate tiny, hoggy, 8–10 mm long; leaflets irregular, fine and pronouncedly serrated, green and pubescent on both sides, terminal leaflet oval or elliptic, acuminate, with 8–10 veins on each side, 7–10 cm long, its petiole 2–3 cm long; lateral leaflets 4–5.5 cm long, with petioles approximately 2 mm long (Fig. 2**(A.2)**); densely hairy and spiny flower stems, small, curved spines; terminal and axillary panicles, short, sloping; tomentose stems and pedicels with small glands; cinereo-tomentose calyx, glanduliferous; sepals extended or reflexed; oval, pink petals (Fig. 2**(A.3)**); fruits 1 cm long, black; numerous, tomentulous drupelets (Fig. 2**(A.4)**).

Material examined: IBUNAM: MEXU: 1417228. *Rubus liebmannii* Focke ROSACEAE Shrub 2.5 m; spiny, semi-woody, hairy, brown, semiglabre stems; alternate, trifoliate, spiny leaves, biserrulous margin; inflorescence in corymb: pink, pentameric, perfect flowers. El Palmito, Concordia, Sinaloa, Mexico. 23°35’22.5” N, 105°52’09.5” W, 2172 m a.s.l. 06/30/2015. Collector: Oscar Abel Sánchez-Velázquez. Determined: Biol. Gilda Ortíz-Calderón / Dr. Oscar Abel Sánchez-Velázquez.

This species had not been previously reported for the state of Sinaloa. This blackberry is also known as “tunita de cerro”, “zarza” and “zarzamora” in Spanish and “citun-zarza” and “tsitubi” in Purepecha. Its geographical distribution is reported in the forested areas of Michoacán, Hidalgo, Durango, Jalisco, and Guanajuato. Ecologically, like many *Rubus* species, they are important plants as colonizers of new sites for the development of other associated species of primary vegetation [4]. Some anatomical parts (leaves, stems and fruits) of this plant are used in traditional medicine for diarrhea, colds, dysentery, and insomnia [27]. This is a species of blackberry endemic to Mexico that is not under any category of protection under Mexican law and that had not been reported for the state of Sinaloa.

Rubus coriifolius Liebm. Vidensk. Meddel. 1852: 157. 1853.

TYPE: MEXICO, Veracruz, Mirador. 1853. Type: Liebmann s.n.; Sep; Mexico: Alpatlahua, 7000'(C).

Perennial stems, 1.5-2 m tall; subrepent buds, pubescent, rarely with small thorns; stems angled, with long, recurved and compact spines, puberulent at the base; leathery, persistent leaves, pentameric leaflets (sterile stems) (Fig. 2**(B.1)**); semibristled stipules, 4–5 mm long, pubescent; pubescent petioles, rarely with glands intermixed with villi, petioles and central vein spines, 5–7 cm long; leaflets elongated-ovate 5–10 cm long, obtuse at the base, accumulated at the apex, roughly biserrated, dark green, puberulent, underside densely pubescent, with prominent veins (Fig. 2**(B.2)**); petiole of the average follicle 3–4 cm long, those of the lateral leaves approximately 2.5 cm long and those smaller than 4–6 mm long; alternate floral branch leaves; leaflets 5–7 cm long, 2.5-3 cm wide; petiole of the middle leaflet 12–16 mm long, those of the lateral leaflets 2–5 mm long; terminal and axillary panicles, the main frequently 30 cm long; scattered, tomentose branches, often with interspersed glandular villi; lanceolate, sharp bracts; sepals thick, ovate, acuminating or acute, tri-veined, tomentose, at the end reflexed; petals obovate, longer than sepals, pink or white (Fig. 2**(B.3)**); small fruits, red or black when approaching maturity, glabrous; 8–20 drupelets, ovoid, glabrous, gradually fall apart (Fig. 2**(B.4)**).

Material examined: IBUNAM: MEXU: 1417229. *Rubus coriifolius* Liemb. ROSACEAE Shrub 3 m; climbing branches; spiny, semi-woody and herbaceous stems, hairy, glandular; alternate leaves, tri or pentafoliate, spined, biserrulous margin; hairy-glandular inflorescence, corymb: perfect white, pentameric flowers. El Palmito, Concordia, Sinaloa. 23°34’09.7” N, or 105°50’57.1” W. 2013 m a.s.l. 06/30/2015. Collector: Dr. Oscar Abel Sánchez-Velázquez. Determined: Biol. Gilda Ortíz-Calderón / Dr. Oscar Abel Sánchez-Velázquez.

Rubus coriifolius is a plant distributed in the mountainous systems of highlands forestry coverage in Mexico and even in Central America and Venezuela [28]. Stems, leaves and fruits are used in traditional herbalism for antimicrobial and antiparasitic purposes [29].

Rubus palmeri Rydberg, sp. Nov.

TYPE: MEXICO, Durango, San Ramón. 1906. Isotype: T: Edward Palmer - 78. (MO/BC: MO-197903/A: 1927515). Perennial stems, reclining on bushes or walls, 2–4 m long, angled, hairy, tomentose or glabrous, the oldest, armed with strong recurved spines 5–8 mm long; pentafoliated or trifoliate leaves (Fig.

J. Mex. Chem. Soc. **2024**, *68*(2)
Regular Issue

ISSN-e 2594-0317

2**(C.1)**); petioles, petioles and central veins hairy and heavily armed with curved spines; subulated stipules; 8–10 mm long; leaflets rounded-oval or obovate, abruptly short and acuminate at the apex, rounded or bordered at the base, 5–10 cm long, light green, burr and irregularly serrated, with oval teeth, sparsely hairy in the upper part, rather dense villi on the underside; about 10 lateral veins on each side (Fig. 2**(C.2)**); inflorescences with many flowers, frequent foliaceous, villous-tomentose bracts, some glands and armed with recurved stingers; sepals are ovate, apiculate, tomentose on both sides, about 7 mm long; white, obovate petals, 12–15 mm long (Fig. 2**(C.3)**); dark purple fruits, large, juicy; glabrous drupelets, 20–35; fall, 3 mm long, strongly reticulated (Fig. 2**(C.4)**).

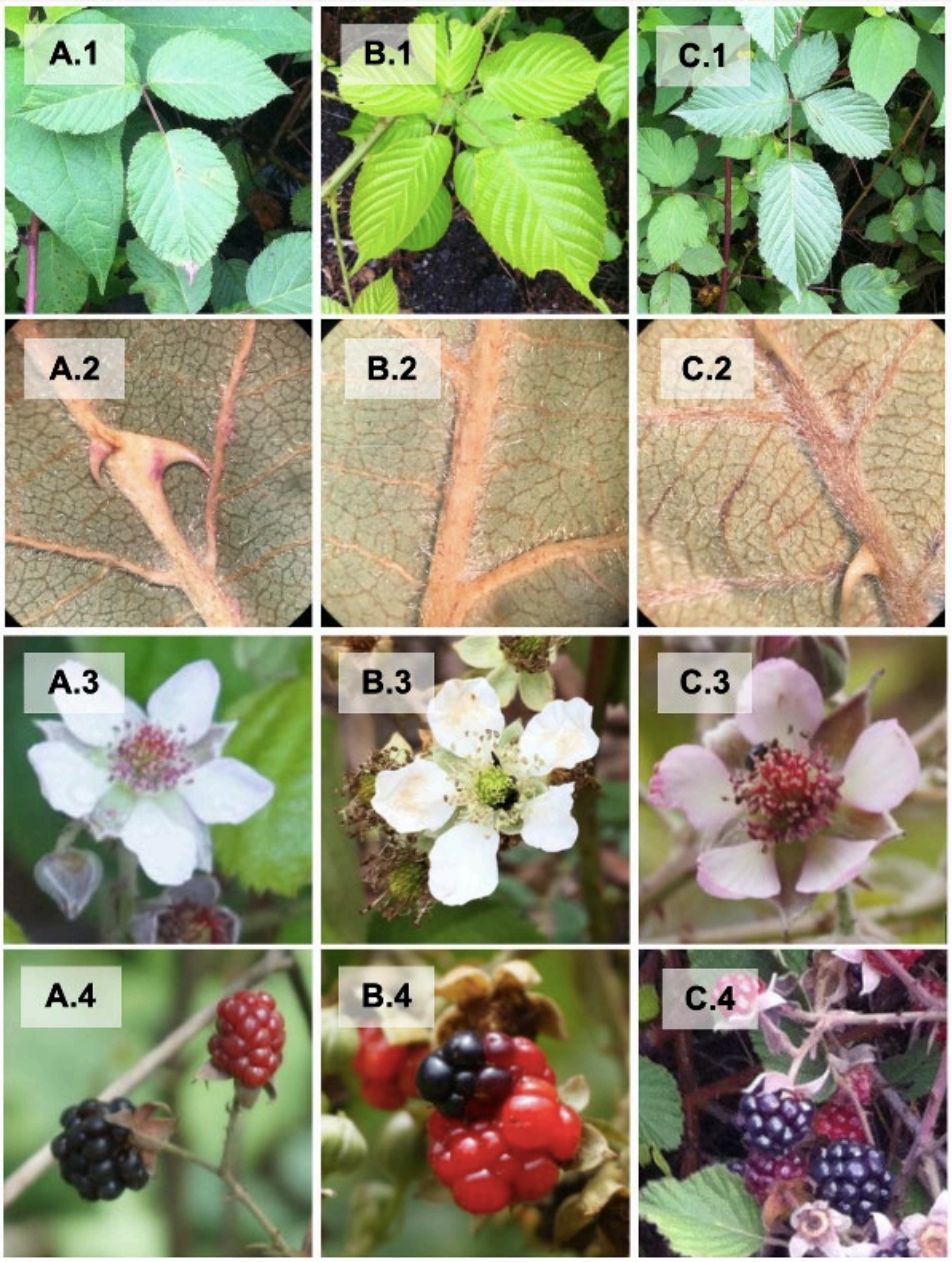

Fig. 2. Illustration of some anatomical parts used for the identification of wild blackberries from the Chara Pinta Sanctuary. A. *R. liebmannii*; B. *R. coriifolius*; C. *R. palmeri*; leaves **(1)**; underside of leaflets **(2)**; flowers **(3)**; fruits **(4)**.

J. Mex. Chem. Soc. **2024**, *68*(2)
Regular Issue

ISSN-e 2594-0317

Material examined: IBUNAM: MEXU: 1417230. *Rubus palmeri* Rybd. ROSACEAE Shrub 2 m; hanging and creeping branches; spiny, semi-woody, hairy stems; alternate leaves, tri or pentafoliate, spined, biserrulous margin; hairy inflorescence, corymb: white, pentameric, perfect flowers. El Palmito, Concordia, Sinaloa. 23°34'55.7" N, or 105°51'21.4" W. 2163 m a.s.l. 06/29/2015. Collector: Dr. Oscar Abel Sánchez-Velázquez. Determined: Biol. Gilda Ortíz-Calderón / Dr. Oscar Abel Sánchez-Velázquez.

Rubus palmeri is a species native to northwestern Mexico and other states such as Chiapas, San Luis Potosí, Tamaulipas, and Veracruz, in addition to being distributed in Guatemala [28]. Fruits of this species are used to make jams, tamales, and sweets, while their leaves are used as medicines for parasitic diseases and gastrointestinal system pain [4].

Despite their morphological peculiarities, these three species are evolutionarily related to each other [5]. *Rubus liebmannii* and *Rubus coriifolius* belong to the *Floribundi* subgenus, while *Rubus palmeri* is classified as part of *Sapidi*. The criteria for this robust grouping are more related to the characteristics of inflorescences, such as the number and arrangement of flowers, as well as the presence and abundance of glandular trichomes and spines [30]. Other related subgenres are *Adenotrichi* and *Duri*, in which most of the tropical species described in the American continent are found [31].

The El Palmito Sanctuary region has a temperate sub-humid (Cwa) climate with a marked rainy season between July and September. Peaks of more than 2,000 m a.s.l dominate the relief. And deep ravines that converge in perennial water flows. That is why the vegetation is intimately linked to a high mountain orography, typical of the Sierra Madre Occidental, where botanical communities such as mountain mesophyll forest, pine forest and mixed oak-pine forest stand out, and to a lesser extent it can be found riparian and gallery vegetation [32]. The dominant plant species belong to the genera *Pinus* and *Quercus*; however, it is also frequent to find individuals from other genera such as *Salix*, *Abies*, *Juniperus*, and *Cupressus*. While secondary vegetation is made up of species of *Datura*, *Argemone*, *Salvia*, *Ipomoea*, *Lopezia*, *Castilleja*, *Geranium*, *Sida*, *Oxalis*, among many others, including *Rubus coriifolius* and *Rubus palmeri* [7,32]. Human economic activities have modified the local ecosystems during the last one hundred years, generating environmental conditions for foreign and exotic flora, like *Hypoestes phyllostachya*, *Ricinus cummunis*, *Ipomoea quamoclit*, *Taraxacum officinale*, *Trifolium repens*, and *Melinis repens*, which indicates that there is a flow of species from other latitudes to these sites, either deliberately or accidentally [8].

Therefore, the collection sites have some representative characteristics of the different types of vegetation in the Chara Pinta Sanctuary. The Cabins site (CP) is a deforested area of approximately 5 ha of gentle inclination and bordered by a canopy of Nearctic affinity (*Pinus herrerai*, *Pinus engelmannii*, *Pinus lumholtzii* and *Pinus douglasiana*). Human influence in CP is high due to the change in land use for recreational purposes, whose occupation is restricted to no more than 50 people, but this figure is rarely reached. *Rubus liebmannii* individuals were found at this site, forming corridors, at least 30 m long, on the margin of a low-traffic dirt road. Additionally, a *Rubus coriifolius* specimen was identified at this location.

The path to the viewpoint (CM) is a crossing point to the Mirador, located between the cabins and the community of El Palmito (Table 1). In this place are present individuals of *Pinus engelmannii* and *Pinus douglasiana*, as well as *Quercus urbanii*, *Arbutus xalapensis* and *Conostegia xalapensis*. Mixed and dispersed individuals of *Rubus liebmannii* and *Rubus palmeri* (RP) were observed at this site. Deforestation of plants with a diameter greater than 1.5 m is still active here. Secondary vegetation is also made up of some introduced grasses and herbaceous plants.

The last site consists of a point of convergence between Federal Highway Mexico 40 and a constant flow (CF) waterfall. The flora present here corresponds to gallery vegetation and orographic shade, with species such as *Alnus glabrata*, *Dendropanax arborens*, *Arbutus madrensis*, *Casimiroa edulis*, *Clethra hartwegii*, etc. In addition, you can find minor species of *Cuphea*, *Castilleja*, *Cosmos*, *Adiantum*, by others, as well as introduced species such as *Leonotis nepetifolia*, *Lysamachia arvensis* and *Melinis repens* [8]. Individuals of RC and RP were found in interspersed communities on the roadside at a distance of no more than 10 m between the convergence of the highway and the stream.

The reproductive season of wild *Rubus* in tropical ecosystems generally occurs a few weeks before the rainy season. The simultaneous co-fructification of one or more species facilitates zoochory by sharing dispersers in common with each other [33]. This phenomenon favors plant succession with native flora and the recruitment of invasive or non-native species and, due to the characteristics of *Rubus* fruits, it is

J. Mex. Chem. Soc. **2024**, *68*(2)
Regular Issue

ISSN-e 2594-0317

one of the genera that has increased its distribution to new lands around the world and has caused different impacts on colonized ecosystems [33].

The ease with which wild *Rubus* species can colonize new pristine and degraded ecosystems, the morphological plasticity of some taxonomic characters, apomixis, and interspecific hybridization makes it difficult to keep floristic listings for *Rubus* up to date. Maintaining constant and consecutive studies of the genus in the Chara Pinta Sanctuary can be useful to know the ecological relevance of these species to maintain the quality of the ecosystem, as well as compile characteristics with possible agronomic interest that allow us to enhance the knowledge of these fruits could increase their interest for human nutrition purposes.

Table 1. Presence of *Rubus* species at collection site.

Site	**Geographical Location**	**Species**		
		RL	**RC**	**RP**
CP	N 23°35'22.5", W 105°52'09.5"	X	X	
CM	N 23°34'55.7", W 105°51'21.4".	X		X
CF	N 23°34'09.7", W 105°50'57.1"		X	X

RL, *Rubus liebmannii*; RC, *Rubus coriifolius*, RP, *Rubus palmeri*; CP, Cabins Chara Pinta; CM, Road to El Mirador; CF, Federal Highway México 40.

Proximate composition

Results from the chemical composition analysis of raw dried fruits of *R. liebmannii* and *R. palmeri* are displayed in Table 2. The protein content for *R. liebmannii* was 5,402 mg/100 g dw, while for *R. palmeri* it was 5,019 mg/100 g dw. It is known that the proteins and polypeptides in *Rubus* fruits are present in low amounts, but with a rich profile of amino acids [34], additionally, the nitrogenous content decreases with the maturity level of fruits [35]. In some grown *Rubus* berries, such as *R. coreanus*, *R. ideaus* or *R. fruticosus* [16,36], the protein content is about 5–7 % dw, while in wild *Rubus* species from upper latitudes showed protein proportions of 3.3–4.4 % dw, like *R. ellipticus* and *R. niveus* [37], although, for berries of the wild *R. amabilis*, proteins can represent up to >10 % dw [38]. However, tropical blackberries such as *R. adenotrichus* and *R. ulmifolius* presented values of 5.9 % and 6.56 % dw in ripe fruits [37]. It means that wild tropical and cultivated blackberries could have similar protein content.

Table 2. Proximate composition and mineral profile of *R. liebmannii* and *R. palmeri* fruits.

Macro-nutrients	**Composition (mg/100 g dw)**	
	Rubus liebmannii	***Rubus palmeri***
Protein	5,402 ± 424[a]	5,019 ± 537[a]
Lipids	6,433 ± 398[b]	7,239 ± 520[a]
Ashes	2,503 ± 211[b]	2,929 ± 110[a]
Carbohydrates	85,749 ± 738[a]	84,892 ± 615[a]

J. Mex. Chem. Soc. **2024**, *68*(2)
Regular Issue

ISSN-e 2594-0317

Micro-nutrients			
Minerals	**RDA (mg/day)**		
Potassium (K)	3,500	592.8 ± 31.9[a]	480.0 ± 33.9[b]
Calcium (Ca)	1,200	188.9 ± 7.1[b]	205.1 ± 9.5[a]
Magnesium (Mg)	350	104.6 ± 3.8[b]	165.4 ± 19.7[a]
Sodium (Na)	2,000	61.4 ± 2.5[b]	83.8 ± 8.5[a]
Manganese (Mn)	75	10.7 ± 1.0[a]	7.3 ± 0.6[b]
Iron (Fe)	15	4.4 ± 0.3[a]	4.2 ± 0.3[a]
Zinc (Zn)	10	1.8 ± 0.1[b]	2.4 ± 0.1[a]
Copper (Cu)	2	0.7 ± 0.0[a]	0.8 ± 0.1[a]

RDA, recommended daily allowance minerals in adults (RDI, 2006). Mean ± S.D. Similar letters at same line indicate non statistical differences (p<0.05). n=3.

For *R. liebmannii* the lipid compounds represented 6,433 mg/100 g dw and for *R. palmeri* 7,239 mg/100 g dw, with differences (p<0.05) between them. Most of the oily portion of *Rubus* berries is found in the dermis and seed [21,34]. Therefore, *R. palmeri* could have a greater quantity of lipids because it has more oily structures in the fruitlessness (around >30 drupeols/drupelet) compared to fruits of *R. liebmannii* (<25 drupeols/drupelet). Our results indicate that *R. liebmannii* and *R. palmeri* have a higher content of lipids compared to other *Rubus* berries, such as wild *R. ellipticus*, *R. ulmifolius*, and *R. niveus* with 1.1–4.7 % dw [37]; wild genotypes of raspberry (*R. idaeus*) with 2.1–3.47 % dw; and grown raspberries and blackberries with 3.3–4.2 % dw [16,21,39]. The presence of a number of oily anatomical structures in our *Rubus* fruits could contribute to the superior content of lipids in these. However, also external circumstances may affect their synthesis and concentration to protect the fruits against biotic and abiotic environmental conditions.

Ash content was 2,503 and 2,929 g/100 g dw correspondingly for *R. liebmannii* and *R. palmeri*, with statistical differences (p<0.05) between them. Ashes represent the minerals contained within fruit structures and may contribute to fruit nutraceutical properties [16]. These results are within the range reported for wild *R. amabilis* [37,38] from fresh highlands, but lower than tropical wild or grown *Rubus* with ash contents of 3.0–4.4 % dw [35,40]. This phenomenon is a natural process determined by factors such as mineral availability in soil, diversity of micro- and macro-elements, or the metabolism of fruits during the ripening process [35,41]. Thus, *Rubus* fruits are an excellent source of microelements that could contribute to reaching the required daily dose of minerals [16,37]. Individual minerals will be discussed in more detail in the next section.

The total carbohydrates contents were estimated at 85,749 and 84,982 mg/100 g dw for *R. liebmannii* and *R. palmeri*, respectively, without statistical differences (p<0.05) between them. It is known that the carbohydrates represent the major macro-compounds in *Rubus* berries (>80 % dw), so our results coincide with the reported for wild blackberries genotypes, such as *R. imperialis*, *R. ellipticus* or *R. idaeus* [37,38], but are lower than the >90 % dw reported in some grown *Rubus* genotypes [16]. The carbohydrates represent the sum of free carbohydrates, fiber, and starch [35,42], and their structural and metabolic role is crucial for the maturity process, synthesis of secondary metabolites, and sensory properties for the dispersing animals, but also carbohydrates represent 40–80 % of total energy requirement in humans [43].

Mineral composition

In both *Rubus* species, the blackberries presented the following mineral distribution: K<Ca<Mg<Na<Mn<Fe<Zn<Cu. However, their contents were not the same in these berries (Table 2).

J. Mex. Chem. Soc. **2024**, *68*(2)
Regular Issue

ISSN-e 2594-0317

Potassium (K) was the major mineral in both fruits, since in *R. liebmannii* its content was 592.9 mg/100 g dw, while for *R. palmeri* was 480.0 mg/100 g dw, being this last statistically low (p<0.05). The potassium content in our fruits was lower than that reported for *R. ellipticus*, *R. niveus* and *R. ulmifolius* fruits (680–920 mg/100 g dw) [37], but higher than amounts reported for raspberry cultivars (103–152 mg/100 g dw) [44,45], as well as fruits of *R. amabilis* (113.3 mg/100 g dw) [38]. The recommended daily dose of K is 2500 mg per day, so the intake of 100 g of dry fruit of *R. liebmannii* or *R. palmeri* could contribute with the 16.9 % and 13.7 % of the K required in adults.

Table 3. Lipid and carbohydrate profiles of wild *Rubus* fruits.

Profile	**RT (min)**	***Rubus liebmannii***	***Rubus palmeri***
Lipid compounds		**Proportion in NPF (%)**	
C16:0, palmitic acid	30.6	10.3 ± 0.4^{b}	15.2 ± 0.3^{a}
C18:0, stearic acid	41.1	0.9 ± 0.1^{a}	0.6 ± 0.0^{b}
C18:1, oleic acid	39.0	25.6 ± 1.2^{b}	30.7 ± 1.5^{a}
C18:2, linoleic acid	39.8	15.1 ± 1.4^{a}	6.3 ± 0.8^{b}
C18:3, linolenic acid	38.9	28.0 ± 0.1^{b}	30.2 ± 0.1^{a}
α-tocopherol	52.6	12.5 ± 1.1^{a}	9.0 ± 1.8^{b}
β-sitosterol	53.9	6.5 ± 0.5^{b}	8.0 ± 0.3^{a}
Carbohydrates		**Proportion in CEF (%)**	
D-fructose	30.31	48.7 ± 0.5^{b}	49.7 ± 0.5^{a}
D-altrose	31.74	7.2 ± 1.7^{a}	6.8 ± 0.4^{a}
D-galactose	34.40	18.0 ± 0.6^{a}	17.8 ± 1.0^{a}
D-xylose	34.51	6.7 ± 0.9^{a}	5.5 ± 0.4^{b}
D-glucose	39.96	19.8 ± 0.7^{a}	21.0 ± 0.7^{a}

RT, retention time; NPF, non-polar fraction; CFE, carbohydrate enriched fraction. Mean ± S.D. Similar letters at same line indicate non statistical differences (p<0.05). n=3.

Calcium (Ca) content in *R. liebmannii* and *R. palmeri* were 188.9 and 205.1 mg/100 g dw, respectively, having differences (p<0.05) between them. The calcium concentration in *R. palmeri* was closer to the highest values reported by Castilho Moro et al [45] for raspberry cultivars in tropical cultivars (162–175 mg/100 g dw), similar to *R. imperialis* (190–202 mg/100 g dw) [39], but our two fruits had less Ca than the reported for *R. idaeus* from cold latitudes, *R. ellipticus*, *R. ulmifolius* and *R. niveus*, ranged around 243–620.5 mg/100 g dw [37]. For adults, 100 g of dried berries of *R. liebmannii* and *R. palmeri* could represent 15.7 % and 17.1 %, respectively, of the recommended daily allowance (RDA) of Ca [46].

Magnesium (Mg) was the third majority element in both species with values of 104.6 and 165.4 mg/100 g dw, respectively for *R. liebmannii* and *R. palmeri* being statistically different (p<0.05). *R. liebmannii* presented Ca amounts lower than subgenus *Ideaobatus* cultivars and wild species (119–162 mg/100 g dw) [37,45]. On the other hand, the Mg content of *R. palmeri* is higher than raspberries and *R.*

J. Mex. Chem. Soc. **2024**, *68*(2)
Regular Issue

ISSN-e 2594-0317

ulmifolius (149–162 mg/100 g dw), but inferior to the reported for *R. niveous* (179 mg/100 g dw) [37,45]. In adults is necessary to consume around 300 mg of Mg/day, so 100 g of our dried fruits may represent 29.9 % and 47.3 % of the Mg recommended daily dose.

Sodium (Na) concentrations in *R. liebmannii* and *R. palmeri* were 61.4 and 83.8 mg/100 g dw, respectively, being different (p<0.05). Our values are included in the ranged Na content of 56.3-89.4 mg/100 g dw reported for several *Rubus* fruits [37]. The Na requirement is around 2,000 mg/day, so 100 g of dried fruits of *R. liebmannii* and *R. palmeri* could represent only 3.1 % and 4.2 %, respectively.

Manganese (Mn) content was 10.7 and 7.3 mg/100 g dw for *R. liebmannii* and *R. palmeri*, respectively, having differences (p<0.05). This microelement values were higher in our fruits compared to other *Rubus* fruits, that ranged in 1.4–2.4 mg/100 g dw [37]. The Mn contents from *R. liebmannii* could represent 14.3 %, while *R. palmeri* may be the 9.7 % of this mineral RDA consuming 100 g dry fruits.

Iron (Fe) contents for *R. liebmannii* and *R. palmeri* were 4.4 and 4.2 mg/100 g dw. This trace element has values between 1.0 and 4.2 mg/100 g dw [37,39,45,47]. In contrast to other microelements, Fe content increase with the fruit ripening process [47]. In cultured blackberries, the Fe content represents only 8 % of the RDA [16], but 100 g of dried *R. liebmannii* and *R. palmeri* could represent more than 29.3 % and 30 % of the RDA, respectively. Iron is an essential mineral for human health and plays a key role in a wide variety of metabolic processes, such as the transport of oxygen, hormones, and connective tissue production, among others [48].

Zinc (Zn) content was 1.8 and 2.4 mg/100 g dw for *R. liebmannii* and *R. palmeri*, respectively, with differences (p<0.05). Zn concentration in these fruits resulted lower than species such as *R. ellipticus*, *R. ulmifolius* or *R. niveus* (8.1–17.6 mg/100 g dw), but the concentration of Zn in *R. palmeri* is ranged from 2.1–3.0 mg/100 g dw of species as *R. amabilis* and *R. idaeus* [37,38,45]. A portion of 100 g of dried *R. liebmannii* or *R. palmeri* could represent 18 % and 24 % of the Zn RDA, respectively.

Lastly, the copper (Cu) amount in *R. liebmannii* was 0.7 mg/100 g dw and 0.8 mg/100 g dw for *R. palmeri*. This trace element is reported in other *Rubus* berries in ranges of 0.1–0.6 mg/100 dw [37,39,45], the reason why the Cu of our fruits is within the usual concentrations for the *Rubus* berries. The RDA of Cu is relatively low (2 mg/day), thus, consuming 100 g dw of *R. liebmannii* or *R. palmeri*, could contribute to the 35 % and 40 %, respectively, necessary for an adult.

Lipid compounds

The profile of lipid compounds is resumed in Table 3. Five long-chain fatty acids (LCFA) were found in both *Rubus* fruits, including two saturated fatty acids (C16:0, C18:0), one monounsaturated (C18:1), and two polyunsaturated fatty acids (C18:2, C18:3). Palmitic or hexadecenoic acid (C16:0) was reported at 10.3 % and 15.2 % of the NPF for *R. liebmannii* and *R. palmeri*, respectively, having differences (p<0.05) between them. Bushman et al. [34] reported in seeds of five *Rubus* genotypes, proportions of 1.9–3.5 % of palmitic acid; Caidan et al. [38] reported in *R. amabilis* 0.27 % for hexadecenoic acid of the total oil content; and in raspberry varieties Celik & Ercisli [21] found proportions of 4.9–8.3 % for this saturated fatty acid. It means that our fruits had, at least, 0.2–1.8 times more proportions of C16:0. This is the most abundant saturated fatty acid in foods and the human body, and it could be synthesized endogenously via *de novo* lipogenesis [49]. Palmitic acid plays a key role in many physiological processes, but it should also be noted that it can also have adverse health effects, especially when combined with other risk factors such as heart disease and a high predisposition to cancer development [49–51].

Stearic or octadecanoic acid (C18:0) for *R. liebmannii* was 0.9 %, while for *R. palmeri* was statistically lower (p<0.05) being only 0.6 % of the NPF. In both species, this was the minor fatty acid. In *R. idaeus*, some genotypes presented non-detectable levels of C18:0, but in those who managed to be identified they did not show quantities of stearic acid >1.2 % [21]; in seed-subproducts from five *R. fruticosus* cultivars, the range of octadecanoic acid was 0.8–3.3 % [34]; and in *R. amabilis* this fatty acid showed values of 0.15 % of total oil content [38]. Stearic acid is known to be less abundant than other saturated LCFA in foods, like palmitic acid [49], and we confirmed this fact in *R. liebmannii* and *R. palmeri* NPF.

Oleic acid (C18:1) is an omega-9 fatty acid, monounsaturated and observed in *R. liebmannii* 25.6 % of the NPF, while for *R. palmeri* it was 30.7 %. This fatty acid represents the major fatty compound in *R. palmeri* and the second most abundant in berries of *R. liebmannii*, agreeing with other *Rubus* berries. Therefore, fruits of a Tibetan blackberry showed a C18:1 content of 8.61 % of the total fatty fraction, while

J. Mex. Chem. Soc. **2024**, *68*(2)
Regular Issue

ISSN-e 2594-0317

in seed oils from cultured blackberries and raspberries, Dimića et al. [52] and Radocaj et al. [53] reported proportions of 3.43–3.53 %, and Bushman et al. [34] recorded percentages of 10.4–17.3 in seed from five varieties of caneberries (*Rubus* spp.). According to the last, *R. liebmannii* and *R. palmeri* presented higher proportions of this vital fatty acid. In the human body, oleic acid has modulatory effects on health and chronic degenerative diseases [54], thus the regular consumption of these fruits could provide a valuable amount of omega-9 fatty acids.

Linoleic acid (C18:2) is an omega-6 fatty acid, polyunsaturated with a content of 15.1 % in the NPF for *R. liebmannii*, while for *R. palmeri* it was statistically lower (p<0.05), representing 6.3 %. The C18:2 had values of 42.2–52.6 % of oily proportion in cultured raspberries [21], whereas, for varieties of cranberry this fatty acid was determined in concentrations of 53.1–63.7 % of oily content in seeds. Having said this, we can see that our fruit has very low levels of C18:2 compared to the grown genotypes of some *Rubus* berries. This content has beneficial effects for medical and nutritional purposes, including neuro and cardioprotection, antimicrobial activity, and anticarcinogenic effects. It aids in the synthesis of beneficial lipoproteins while reducing high-density lipoprotein levels [55].

The last fatty acid identified was a-linolenic acid (C18:3), an omega-3 fatty acid polyunsaturated that represented 28.0 % of the NPF of *R. liebmannii*, and 30.2 % of *R. palmeri*. This omega-3 was the main oily compound in *R. liebmannii* and the second most abundant in *R. palmeri*, having statistical differences (p<0.05) between them. Hence, our fruits have linolenic acid levels in the range reported for grown *Rubus* fruits, which reach the 15.2–31.2 % of the total oily portion [21,34,38]. a-Linolenic acid is an essential fatty acid for humans and other animals, and it is fundamental to many cellular functions [56]. Together with linoleic acid, this is the main fatty acid in plants and other *Rubus* berries [21,53], but in our case, oleic and linolenic acids represented >58 % of the oil content.

In addition to fatty acids, two lipid phytocompounds were identified in *R. liebmannii* and *R. palmeri* NPF (Table 3). A type of vitamin E, α-tocopherol, was identified in *R. liebmannii* in a proportion of 12.5 % of the FNP, meanwhile, in *R. palmeri* it was statistically lower (p<0.05) with values of 9.0 %. α-tocopherol is also reported in other *Rubus* berries, such as some cultivars of *R. fruticosus* in proportions of 0.8–1.3 mg/100 g of fruit pomace [16] and 1.6-12.6 % for cranberry seeds [34]. It is because in our fruits, the α-tocopherol has relatively high levels of the potent lipid antioxidant [57]. α-tocopherol is considered a homologous of vitamin E and exhibits antioxidant activity in the human body protecting polyunsaturated fatty acids against free radicals [58]. This lipophilic compound is absorbed from several food sources, and accumulated in cell membranes before scavenging radicals *via* delivering an H^+ to quench free oxygen and other radicals, but the interactions "O-H" has been shown, at least, 10 % weaker than other antioxidant phytochemicals. However, the tocopheryl radical produced is less reactive than the products of polyphenols [59]. It is for all the above that *R. liebmannii* and *R. palmeri* may be considered good sources of this priceless dietary component.

β-sitosterol was also detected in NPF of *R. liebmannii* and *R. palmeri* of 6.5 % and 8.0 %, respectively, having statistical differences (p<0.05). β-sitosterol is a phytosterol that occurs naturally in *Rubus* fruits and other plants with important roles related to cellular structures and membrane functionality [60,61]. Blackberry pomaces made from grown varieties presented three types of sterols (campesterol, stigmasterol and β-sitosterol), of which, β-sitosterol is the majoritarian (0.43 g/100 g dw) [53]. But also, have been reported in other berries, such as *R. suavissimus* [59], *R. glaucus* [60] and *R. idaeus* [60]. This phytosterol has shown antineoplastic activities, improves the permeability of the skin barrier, reduces cholesterol levels, and promotes the synthesis of hyaluronic acid [62,63].

Carbohydrate profile

The carbohydrate profile was formed by a mix of an aldopentose, a ketohexose, and some aldohexoses (Table 3). D-fructose was the main carbohydrate in the CEF from *R. liebmannii* and *R. palmeri* with proportions of 48.7 % and 49.7 %, respectively, having differences (p<0.05) among them. During fruit ripening Acosta-Montoya et al. [35] and Lefèvre et al. [44] reported concentrations of fructose between 2.5–10.4 g/100 g dw in *R. adenotrichus* and 18.3 mg/100 g dw in *R. idaeus*, respectively. Compared to these wild and commercial *Rubus* genotypes, our fruits seem to show, at least, twice as much fructose. This ketohexose is the major and most important carbohydrate in the human diet, only after glucose [43]. Interestingly, the fructose content is not only favored by the ripening stage but also is influenced by the fruit size, since berries

J. Mex. Chem. Soc. **2024**, *68*(2)
Regular Issue

ISSN-e 2594-0317

of *R. hirsutus* showed statistical differences (p<0.05) comparing large fruits with medium or small [35,42]. The berries from *R. palmeri* are 0.5–1.0 cm bigger than *R. liebmannii* fruits, and this size difference could be one of the possible reasons for the D-fructose in these.

D-altrose was at proportions of 7.2 % and 6.8 % in the CEF from *R. liebmannii* and *R. palmeri*, respectively. The altrose is an uncommon aldohexose not reported previously in fruits of this genus. But Tako et al. [64] reported this unusual sugar as deoxy shape in some mushrooms with folk medical properties. But also, the altrose could be wrongly identified as an isomer of other aldohexoses such as D-glucose, D-mannose, or D-galactose, which have been recorded in *Rubus* fruits [42]. More studies are required on this compound to confirm its presence in these fruits.

D-galactose was found to be 18.0 % and 17.8 % of the CEF for *R. liebmannii* and *R. palmeri*, respectively. D-galactose was also identified in *R. idaeus* as part of hetero-polysaccharides or in form of D-galacturonic acid [43]. Galactose is an important compound of cell walls in fruits and other plant anatomical structures, but in nutraceutical terms, this plays an important role as part of anthocyanin moieties [40]. The linked galactose to anthocyanidins influences the bioavailability, metabolism and bioactivity in the human body [65].

D-xylose represented the lowest proportion of individual carbohydrates in *R. liebmannii* with 6.7 %, and 5.5 % for *R. palmeri*, with statistical differences (p<0.05) between them. This aldopentose has been recorded in other *Rubus*, such as grown *R. idaeus* [43]. However, it has not been previously quantified in other *Rubus* berries. Xylose is present in *Rubus* fruits glucosiding or acyling aglycones like cyanidin or delphinidin [66]. Furthermore, the xylosyl, an acyl group linking a hexose and an aglycone, allows holding the stability of anthocyanins through the intestine biotransformation before joining the bloodstream [67].

Finally, the D-glucose occupied 19.8 % of the CEF from *R. liebmannii*, while for *R. palmeri* it represented 21.0 %, as far as this aldohexose was the second most frequent in these fruits. This aldohexose was reported in fruits of wild *R. adenotrichus* as the main individual at contents about 117 mg/g of dw [35]. Though, as Pentelidis et al. [68] claim in their work, the fructose content is predominant in *Rubus* berries, and it is refuted by Lefèvre et al. [44] in Russian-grown raspberries. Glucose is the most abundant monosaccharide in nature, with many important functions in plants: most of the organoleptic attributes of *Rubus* fruits are due to this aldohexose, since the sweetness, odor, or flavor is favored for this, and the main sugar in anthocyanins of these red fruits [42,43,69]. Glucose stands out in the nutritious properties of *Rubus* berries because it is the primary source of fuel for body metabolism, but their antioxidant effects are less known as working in synergy with natural antioxidants such as α-tocopherol, tannins and flavonoids [18,69].

Conclusions

Specimens of *Rubus liebmannii*, *Rubus coriifolius*, and *Rubus palmeri* were well identified by their anatomical attributes in the forested lands of the Chara Pinta Sanctuary, Sinaloa, Mexico. *Rubus liebmannii* was recorded in Sinaloa for the first time. The proximate composition of two wild blackberries (*R. liebmannii* and *R. palmeri*) was described for the first time. The protein content in these fruits was higher than other popular *Rubus* berries. The carbohydrates represented the major macro-compounds (>85 % dw) made up of >50 % fructose and glucose but also reported altrose for the first time for *Rubus* berries. Ashes in both species resulted similarly to the reported for highland *Rubus* berries. The mineral profile showed a similar trend in both fruits (K<Ca<Mg<Na<Mn<Fe<Zn<Cu). Potassium and calcium content in 100 g dw of our *Rubus* fruits may contribute to the >15 % of the RDI, but for Mg, Fe or Cu represented at least 29 % of the RDI. Two saturated, monounsaturated and two polyunsaturated fatty acids were identified in these fruits, a-linolenic acid being the majority in the two berries. Also, the α-tocopherol and β-sitosterol were identified. The studied *R. liebmannii* and *R. palmeri* fruits showed a quite rich profile and quantity of nutrients, which, in some cases, were greater than those reported in the popular blackberries or raspberries. The attractive characteristics of these fruits could be considered for the genetic improvement of existing crops or for exploiting these berries as new cultivars in the forestlands of Sinaloa.

J. Mex. Chem. Soc. **2024**, *68*(2)
Regular Issue

ISSN-e 2594-0317

References

1. Ling-ti, L.; Boufford, D. E. *Flora of China*. **2003**, *9*, 195–285.
2. Huang, J. Y.; Hu, J. M. *Taiwania*. **2009**, *54*, 285–310.
3. https://doi.org/10.15468/c3kkgh, accessed in April 2020.
4. Rzedowski, J.; Calderón de Rzedoswki, G. *Flora del Bajío y de Regiones Adyacentes*, Familia Rosaceae. Instituto de Ecología A. C. Centro Regional del Bajío Pátzcuaro, Morelia, Michoacán. **2005**, *135*, 163.
5. Rodríguez-Bautista, G.; Segura-Ledezma, S. D.; Cruz-Izquierdo, S.; López-Medina, J.; Cruz-Huerta, N.; Valenzuela-Núñez, L. M. *Polibotánica*, **2021**, *52*, 103-116. DOI: https://doi.org/10.18387/polibotanica.52.8.
6. Rodriguez-Bautista, G.; Segura Ledesma, S. D.; Cruz-Izquierdo, S.; López-Medina, J.; Gutiérrez-Esponisa, A.; Cruz-Huerta, N.; Carrillo-Salazar, J.; Valenzuela Núñez, L. M. *Biotecnia*. **2018**, *21*, 97-105.
7. González-Elizondo, M. S.; González-Elizondo, M.; Tena-Flores J.; Ruacho-González L.; López-Enríquez I. *Acta Bot. Mex.* **2012**, *100*, 351-403.
8. Ávila-González, H.; González-Gallegos, J. G.; López-Enríquez, I. L.; Ruacho-González, L.; Rubio-Cardoza, J.; Castro-Castro, A. *Bot. Sci.* **2019**, *97*, 789-820. DOI: https://doi.org/10.17129/botsci.2356.
9. Piedra-Malagón, E. M.; Albarrán-Lara, A. L.; Rull, J., Piñero, D.; Sosa, V. *System. Biod*. **2016**, *14*, 244-260. DOI: https://doi.org/10.1080/14772000.2015.1117027.
10. Moreno-Medina, B.L.; F. Casierra-Posad; S. Albesiano. *Rev. Bras. Frutic*. **2020**, *42*, e-542. DOI: https://doi.org/10.1590/0100-29452020542.
11. Moreno-Medina, B.; Casierra-Posada, F. *Rev. Bras. Frutic*. **2021**, *43*, e-713. DOI: https://doi.org/10.1590/0100-29452021713.
12. Clark, J. R.; Stafne, E. T.; Hall, H. K.; Finn, C. E. Janick J. (ed), John Wiley & Sons, Inc., New Jersey, **2007**, *29*, 19-144.
13. Espinosa B.; Ligarreto N.; Barrero M.G.A.; Medina C.C.I. *Rev. Col. Cien. Hort.* **2016**, *10*, 211. DOI: http://dx.doi.org/10.17584/rcch.2016v10i2.4755.
14. Focke, W. O. *Bibliotheca Botanica*. **1914**, *17*, 1–274.
15. Cuevas-Rodríguez, E.O.; Yousef, G.G.; García-Saucedo, P.A.; Medina-García, J.; Paredes-López, O.; Lila, M.A. *J. Agric. Food Chem*. **2010**, *58*, 7458–7464. DOI: https://doi.org/10.1021/jf101485r.
16. Zia-Ul-Haq, M.; Riaz, M.; De Feo, V.; Jaafar, H.Z.E.; Moga, M. *Molecules*. **2014**, *19*, 10998-11029. DOI: https://doi.org/10.3390/molecules190810998.
17. Schädler, V.; Dergatschewa, S. *Nat. J. Physiol., Pharm. Pharmacol.* **2017**, *7*, 501-508. DOI: https://doi.org/10.5455/njppp.2017.7.1234224012017.
18. Sánchez-Velázquez, O. A.; Montes-Ávila, J.; Milán-Carrillo, J.; Reyes-Moreno, C.; Mora-Rochin, S.; Cuevas-Rodríguez, E. O. *J. Food Measur. Charac.* **2019**, *13*, 2265-2274. DOI: https://doi.org/10.1007/s11694-019-00146-z.
19. Sánchez-Velázquez, O. A.; Cuevas-Rodríguez, E. O.; Reyes-Moreno, C.; Ríos-Iribe, E. Y.; Hernández-Álvarez, A. J.; León-López, L.; Milán-Carrillo, J. *J. Food Sci. Technol.* **2021**, *58*, 4654–4665. DOI: https://doi.org/10.1007/s13197-020-04953-x.
20. Sánchez-Velázquez, O. A.; Mulero, M.; Cuevas-Rodríguez, E. O.; Mondor, M.; Arcand, Y.; Hernández-Álvarez, A. J. *Food Func.* **2021**, *12*, 7358-7378. DOI: https://doi.org/10.1039/d1fo00986a.
21. Celik, F.; Ercisli, S. *J. Med. Plants Res*. **2009**, *3*, 583-585.
22. Lee, J.; Dossett, M.; Finn, C. E. *J. Funct. Foods,* **2013**, *5*, 1985–1990. DOI: https://doi.org/10.3748/wjg.14.4280.

J. Mex. Chem. Soc. **2024**, *68*(2)
Regular Issue

ISSN-e 2594-0317

23. AOAC International. Official Methods of Analysis, 20th edn. **2016**, AOAC International, Saint Paul, MN, USA.
24. Xiang, Z.; Cai, K.; Geng Z.; Zhang J.; Zhou, S. *Anal. Lett.* **2013**, *46*, 640-650. DOI: https://doi.org/10.1080/00032719.2012.730594.
25. Ahumada-Santos, Y. P.; Montes-Ávila, J.; Uribe-Beltrán, M. J.; Díaz-Camacho, S. P.; López-Anguloa, G.; Veja-Aviña R.; López-Valenzuela, J. A.; Heredia, J. B.; Delgado-Vargas F. *Indust. Crops Prod*. **2013**, *49*, 143-149. DOI: https://doi.org/10.1016/j.indcrop.2013.04.050.
26. Frías-Espericueta, M. G.; Cardenas-Nava, N. G.; Márquez-Farías, J. F.; Osuna, López, J. I.; Muy-Rangel, M. D.; Rubio-Carrasco, W. Voltolina D. *Bull. Environ. Contam. Toxicol*. **2014**, *93*. DOI: https://doi.org/10.1007/s00128-014-1360-0.
27. Aguilar-Contreras, A.; Camacho-Pulido, J. R.; Chino-Vargas, S.; Jácquez-Ríos, P.; López-Villafranco, M. A. in: *Plantas Medicinales del Herbario del IMSS: Su Distribución por Enfermedades*. Editorial IMSS-Roche Syntex, Ciudad de México, México, 1ra Edición. **1994**.
28. www.datosabiertos.unam.mx, accessed in January 2022.
29. www.congresos.cio.mx, accesed in January 2020.
30. Kirchoff, B.K.; Claßen-Bockhoff, R. *Annal. Bot*. **2013**, *112*,1471-1476. DOI: https://doi.org/10.1093/aob/mct267.
31. New York Botanical Garden (NYBG). **1963**. North American Flora. New York Botanical Garden 22. 1-102.
32. www.conabio.mx, accesed February 2020.
33. Rejmãnek, M. *Guay. Bot.* **2015**, *72*, 27-33. DOI: http://dx.doi.org/10.4067/S0717-66432015000100004.
34. Bushman, B. S.; Phillips, B.; Isbell, T.; Ou, B.; Crane, J. M.; Steven, A.; Knapp, J. *J. Agric. Food Chem*. **2004**, *52*, 7982−7987. DOI: https://doi.org/10.1021/jf049149a.
35. Acosta-Montoya, Ó.; Vaillant, F.; Cozzano, S.; Mertz, C.; Pérez, A. M.; Castro, M. V. *Food Chem*. **2010**, *119*, 1497–1501. DOI: https://doi.org/10.1016/j.foodchem.2009.09.032.
36. Kim, S. J.; Lee, H. J.; Kim, B. S.; Lee, D.; Lee, S. J.; Yoo, S. H.; Chang, H. I. *J. Agric. Food Chem*. **2011**, *59*, 11786-11793. DOI: https://doi.org/10.1021/jf104192a.
37. Ahmad, M.; Masood, S.; Sultana, S.; Hadda, T. B.; Bader, A.; Zafar, M. *J. Pharm. Sci.* **2015**, *28*, 241-247.
38. Caidan, R.; Cairang, L.; Liu, B.; Suo, Y. *J. Food Comp. Anal*. **2014**, *33*, 26-31. DOI: https://doi.org/10.1016/j.jfca.2013.09.009.
39. Schmeda-Hirschmann, G.; Feresin, G.; Tapia, A.; Hilgert, N.; Theoduloz, C. *Sci. Food Agric.* **2005**, *85*, 1357–1364. DOI: https://doi.org/10.1002/jsfa.2098.
40. Liu, Y.; Song, X., Zhang, D.; Zhou, F.; Wang, D.; Wei, Y.; Gao, F.; Xie, L.; Jia, G.; Wu, W.; Ji, B. *Brit. J. Nut.* **2012**,*108*, 16-27. DOI: https://doi.org/10.1017/S000711451100523X.
41. Marles, R.J. *J. Food Comp. Anal*. **2017**, *56,* 93-103. DOI: https://doi.org/10.1016/j.jfca.2016.11.012.
42. Fu, Y.; Zhou, X.; Chen, S.: Sun, Y.; Shen, Y.; Ye, X. *LWT - Food Sci. Technol*. **2015**, *60*, 1262e-1268e. DOI: https://doi.org/10.1016/j.lwt.2014.09.002.
43. Yu, Z.; Liu, L.; Xu, Y.; Wang, L.; Teng, X.; Li, X.; Dai, J. *Carbohyd. Polym*. **2015**, *132*, 180–186. DOI: https://doi.org/10.1016/j.carbpol.2015.06.068.
44. Lefèvre, I.; Ziebel, J.; Guignard, C.; Sorokin, A.; Tikhonova, O.; Dolganova, N.; Hoffmann, L.; Eyzaguirre, P.; Hausman, J-F. *J. Berry Res*. **2011**, *1*, 159–167.
45. Castilho Maro, L. A.; Pio, R.; Santos Guedes, M. N.; Patto De Abreu, C. M.; Nogueira Curi, P. *Fruits*. **2013**, *68*, 209-217. DOI: https://doi.org/10.1051/fruits/2013068.
46. Dietary Reference Intakes Essential Guide Nutrient Requirements (RDI). Edited by: Otten J.J., Hellwig J.P., Meyers L.D. The National Academies Press, Washington, DC. **2006**.

J. Mex. Chem. Soc. **2024**, *68*(2)
Regular Issue

ISSN-e 2594-0317

47. Surya, M. I.; Suhartati, S.; Ismaini, L.; Lusini, Y.; Dian Anggraeni, D.; Normasiwi, S.; Asni, N.; Abu, M.; Sidiq, B. *J. Trop. Life Sci.* **2018**, *8*, 75-80.
48. http://ndb.nal.usda.gov/, accessed in March 2020.
49. Carta, G.; Murru, E.; Banni, S.; Manca, C. *Front. Physiol.* **2017**, *8*, 902. DOI: https://doi.org/10.3389/fphys.2017.00902.
50. Fernandes, E.; Lopes, C. M.; Lúcio, M. Chapter 15–Bioactive lipids: Pharmaceutical, nutraceutical, and cosmeceutical applications. In: *Bioactive Lipids*, Academic Press. **2023**, 349-409.
51. Fattore, E.; Fanelli, R. *Int. J. Food Sci Nut.* **2013**, *64*, 648-659. DOI: https://doi.org/10.3109/09637486.2013.768213.
52. Dimića, E. B.; Vujasinovićb, V. B.; Radočajc, O. F.; Pastor, O. P. *Acta Period. Techn*. **2012**, 43, 1–9. DOI: https://doi.org/10.2298/APT1243001D.
53. Radocaj, O.; Vujasinovic, V.; Dimic, E.; Basi, Z. *Eur. J. Lipid Sci. Technol.* **2014**, *116*, 1–10. DOI: https://doi.org/10.1002/ejlt.201400014.
54. Sales-Campos, H., Reis de Souza, P., Crema Peghini, B., Santana da Silva, J., Ribeiro *Mini-Rev. Med. Chem.* **2013***, 13*. DOI: https://doi.org/10.2174/138955713804805193.
55. Kelly, G. S. *Altern. Med. Rev*. **2001**, *6*, 367-82.
56. Schönfeld, P.; Wojtczak, L. *J. Lipid Res.* **2016**, *57*, 943-954. DOI: https://doi.org/10.1194/jlr.R067629.
57. Oomah, B. D.; Ladet, S.; Godfrey, D. V.; Liang, J.; Girard, B. *Food Chem*. **2000**, *69*, 187-193. DOI: https://doi.org/10.1016/S0308-8146(99)00260-5.
58. Suárez-Jiménez, G. M.; López-Saiz, C. M.; Ramírez-Guerra, H. E.; Ezquerra-Brauer, J. M.; Ruiz-Cruz, S.; Torres-Arreola, W. *Int. J. Mol. Sci.* **2016**, *17*, 1968. DOI: https://doi.org/10.3390/ijms17121968.
59. Traver, M. G.; Stevens, J. F. *Free Rad. Biol. Med*. **2011**, *51*, 1000-1013. DOI: https://doi.org/10.1016/j.freeradbiomed.2011.05.017.
60. Piironen, V.; Toivo, J.; Puupponen-Pimia, R.; Lampi, A. M. *J. Sci. Food Agric*. **2003**, *83*, 330–337. DOI: https://doi.org/10.1002/jsfa.131.
61. Chaturvedula, V. S. P.; Prakash, I. *Int. Curr. Pharm. J.* **2012**, *1*, 239-242.
62. Pantoja-Chamorro, A. L.; Hurtado-Benavides, A. M.; Martínez-Correa, H. A. *Inf. Tecnol.* **2017**, *28*, 35-46. DOI: http://dx.doi.org/10.4067/S0718-07642017000100005.
63. Yu, H.; Xueqing, S.; Dan, L; Minhua, H; Yanhua, L. *Anais Acad. Brasil. Ciênc*. **2019**, *91*, e20181088. DOI: https://doi.org/10.1590/0001-3765201920181088.
64. Tako, M.; Shimabukuro, J.; Jiang, W.; Yamada, M.; Ishida, H.; Kiso, M. Rare. *Biochem. Comp.* **2013**, *1*, 1-6.
65. Kamiloglu, S.; Capanoglu, E.; Grootaert, C.; Van, Camp, J. *Int. J. Mol. Sci.* **2015**, *16*, 21555–21574. DOI: https://doi.org/10.3390/ijms160921555.
66. Fan-Chiang, H.-J.; Wrolstad, R. E. *J. Food Sci.* **2005**, *70*. DOI: https://doi.org/10.1111/j.1365-2621.2005.tb07125.x.
67. Fang, J. *Drug Metab. Rev.* **2014**, *46*, 508–520. DOI: https://doi.org/10.3109/03602532.2014.978080.
68. Pantelidis, G. E.; Vasilakakis, M.; Manganaris, G. A.; Diamantidis, G. R. *Food Chem.* **2007**, *102*, 777–783. DOI: https://doi.org/10.1016/j.foodchem.2006.06.021.
69. Zaitoun, M.; Ghanem, M.; Harphoush, S. *Int. J. Pub. Health Res*. **2018**, *6*, 93-99.

Article

J. Mex. Chem. Soc. **2024**, *68*(2)
Regular Issue

ISSN-e 2594-0317

Synthesis of Functionalized Flexible and Rigid Polyurethane for Oil Spill Treatment

Hadi S. Al-Lami[1*], Abdullah A. Al-Khalaf[2], Abbas F. Abbas[1]

[1]Department of Chemistry, College of Science, University of Basrah, Basrah, Iraq.
[2]State Company for Iron and Steel, Ministry of Industry and Modified Minerals, Basrah, Iraq.

***Corresponding author:** Hadi S. Al-Lami, email: hadi.abbas@uobasrah.edu.iq

Received April 13th, 2023; Accepted June 1st, 2023.

DOI: http://dx.doi.org/10.29356/jmcs.v68i2.2046

Abstract. To improve the oleophilic and hydrophobic properties of two different types of polyurethane sponge (flexible, FPU, and rigid, RPU) for oil spill cleanup, acrylamido phenyl chalcone palamitamid, a recently synthesized monomer with long chains of linear alkyl groups, was in situ crosslinked with divinylbenzene. Grafted PU cubes were characterized by Fourier transform infrared spectroscopy (FTIR) and scanning electron microscopy (SEM). The water sorption of ungrafted FPU and RPU decreased from 18.05 and 15.66 to 7.31 and 7.06 for grafted FPU and RPU, respectively. The effect of oil type on the sorption capacity testing was explored and compared using crude oil, diesel fuel, and water-oil systems. It was found that the crude oil and diesel fuel sorption of grafted FPU and RPU cubes was increased compared with ungrafted FPU and RPU cubes, and the maximum values for adsorption were recorded using crude oil. These results can be explained by increasing the adherent forces between the adsorbent and the oil surface with increasing oil viscosity, and consequently, the oil adsorption increases. The high oil absorption capacity is mainly attributed to the high porosity of the sponges. The modified FPU and RPU cubes can be effectively used in oil and water spill cleanup.
Keywords: Oil spill; polyurethane; grafting; crude oil; diesel fuel.

Resumen. Para mejorar las propiedades oleófilica e hidrofóbica de dos tipos diferentes de esponjas de poliuretano (flexible, FPU y rígida, RPU) para la limpieza de derrames de petróleo, se llevó a cabo una reacción de entrecruzamiento *in situ* con divinilbenceno a partir de acrilamido fenil chalcona palamitamida, un monómero recientemente sintetizado y que contiene cadenas largas de grupos alquilo lineales. Los cubos de PU injertados se caracterizaron mediante espectroscopía infrarroja por transformada de Fourier (FTIR) y microscopía electrónica de barrido (SEM). La sorción de agua de FPU y RPU no injertadas disminuyó desde 18,05 y 15,66 hasta 7,31 y 7,06 para FPU y RPU injertados, respectivamente. Se exploró y comparó el efecto del tipo de petróleo en las pruebas de capacidad de sorción, utilizando petróleo crudo, combustible diesel y mezcla agua-petróleo. Se encontró que la sorción de petróleo crudo y combustible diesel de los cubos de FPU y RPU injertados aumentó en comparación con los cubos de FPU y RPU no injertados, obteniéndose los valores máximos de adsorción para el caso de petróleo crudo. Estos resultados pueden explicarse en base al aumento de las fuerzas de adherencia entre el adsorbente y la superficie del aceite al aumentar la viscosidad del aceite, y como consecuencia la adsorción del aceite aumenta. La alta capacidad de absorción de aceite se atribuye principalmente a la alta porosidad de las esponjas. Los cubos FPU y RPU modificados se pueden utilizar eficazmente en la limpieza de derrames de petróleo y agua.
Palabras clave: Derrame de petróleo; poliuretano; injerto; petróleo crudo; combustible diesel.

J. Mex. Chem. Soc. **2024**, *68*(2)
Regular Issue

ISSN-e 2594-0317

Introduction

Due to the oil industry's rapid expansion, which includes oil extraction and the creation of its derivatives, as well as the industrial sector's rapid growth, there is now a considerable increase in the volume of oily wastewater. Many activities, such as industrial effluent release, offshore and onshore petroleum industries, and accidental spills, cause petroleum hydrocarbon contamination in water [1,2]. Petroleum hydrocarbons (crude oil, diesel oil, engine oil, etc.) cause many toxic compounds that are potent immunotoxicants and carcinogenic to human beings [3]. Many technologies, such as booms, skimmers, dispersants, bioremediation, in situ burning, and sorbents, were utilized to prevent further environmental damage from oil spills [4-7]. Among the methods mentioned above, adsorption has provoked considerable interest because of its facile operation, low cost, and flexible design [8,9].

In recent years, great attention has been given to the fabrication of highly hydrophobic materials to separate oil and water [10]. Polymers with hydrophobic–oleophilic properties could be used as low-surface-energy materials for the surfaces of oil sorbents. Up to now, some of them, such as polypropylene (PP) and polyurethane (PU), have already been commercialized [11]. Among the typical and extensively used polymers, polyurethane (PU) is one of the front runners in synthetic polymer materials with excellent mechanical strength, high abrasion resistance, toughness, low-temperature flexibility, corrosion resistance, processability, etc., and is applied in coatings, adhesives, fibers, synthetic leather, and several other novel fields. In addition, PU contains alternating hard and soft segments, which are easily "tailored-made" to gain desired performance by altering the types and quantities of isocyanate, polyol, surfactants, catalysts, fillers, and matrices during the manufacturing process or via advanced characterization techniques [12-14]**.**

Recently, commercial sponge adsorbents, including polyurethane (PU) sponges, have attracted great attention for oil-water separation due to their low cost, good flexibility, three-dimensional structure, and facile design [15]. Given their outstanding properties, sponge adsorbents have been developed as alternative adsorbing materials. However, both PU sponges are naturally amphipathic, limiting oil removal from oil-water mixtures [16]. As a result, recent research has focused on modifying the surface of PU sponges to convert the hydrophilic surface to a hydrophobic surface. Such a surface would make the sponge have a high oil adsorption capacity and good water repellency in the separation process of oil and water. To this end, various materials have been selected to decorate the commercial sponges, including, hydrophobic polymers [9], hydrophobic nanoparticles [17,18], carbon materials [19-21], and so on. These modification materials could successfully switch the hydrophilic sponge surface to hydrophobic, making the sponge materials promising candidates for oil spill cleanup. To address oil spill cleanup in specific situations, sponge adsorbents with additional properties such as magnetic property, stimuli-responsiveness, and excellent durability under harsh conditions have recently been investigated**.**

It is essential to create a quick and effective approach for changing the hydrophilic sponge surface to a hydrophobic one to satisfy the application requirement in oil spill remediation [22–24]. Herein, we explore the chemical surface modification of two types of polyurethane (PU) surfaces: flexible polyurethane foam (FPU) and rigid polyurethane foam (RPU) to compare their activity in cleaning oil spills. Utilize graft polymerization to modify polyurethane (PU) surfaces with additional long-chain monomer molecules in the presence of cross-linkers to improve the hydrophobic/oleophilic nature of the surfaces and, as a result, the performance of the surfaces as oil-cleaning sorbents. The sorption capacities of both grafted PU foams were evaluated in water, crude oil, and diesel fuel, and the capacities were compared between the two types of grafted polyurethane (PU).

Experimental

Materials

All three Sigma-Aldrich, Merck, and Fluka companies supplied all the chemicals and solvents used in this study. Arix S.p.A., an Italian company, provided the flexible polyurethane (FPU) sponge for commercial use, and rigid polyurethane foam (RPU) was created following the published method [25], and rigid

J. Mex. Chem. Soc. **2024**, *68*(2)
Regular Issue

ISSN-e 2594-0317

polyurethane foam (RPU) was prepared as reported in the literature [25]. Both foams were cut to 1 cm^3 before being used. The Zubair Field Operation Division Company (ZFOD) supplied the Iraqi crude oil and diesel fuel.

Hydrophobic/oleophilic compound

The new pre-prepared hydrophobic/oleophilic acrylamide phenyl chalcone palamitamid monomer [26] was used to be crosslinked by divinylbenzene and *in situ* grafting polymerization on the FPU and RPU foam cubes. Its structure is exhibited in Fig. 1.

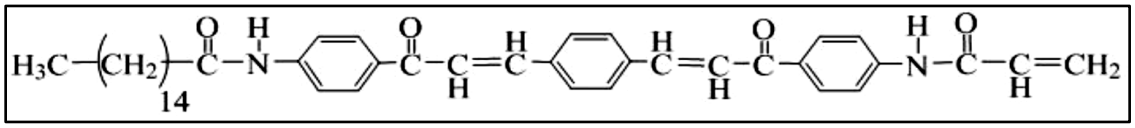

Fig. 1. The chemical structure of the prepared acrylamido phenyl chalcone palamitamid.

Grafting copolymerization

The *in situ* grafting reaction was performed in a 100-ml three-necked round-bottom flask equipped with a thermometer, nitrogen gas inlet, and reflux condenser. The flask was filled with 0.01 g of the initiator benzoyl peroxide (BPO) dissolved in 50 ml of toluene solvent. 0.2 g of ungrafted flexible polyurethane (FPU) sponge or rigid polyurethane (RPU) foam cubes were immersed in the stirred reactive solution for 20 min at 80 °C. The flask was then filled with a mixture containing 0.3 g of each acrylamide phenyl chalcone palamitamid and 0.003 g of the cross-linker divinylbenzene (DVB). After 6 hours of interaction under stirring (500 rpm) and a nitrogen gas atmosphere at 80 °C, the cubes were washed with ethanol and deionized water several times, then dried at 60 °C under vacuum for 48 hours [25,26]. Schemes 1 and 2 show the grafting reactions of acrylamido phenyl chalcone palamitamid-crosslinked-divinylbenzene onto FPU and RPU, respectively.

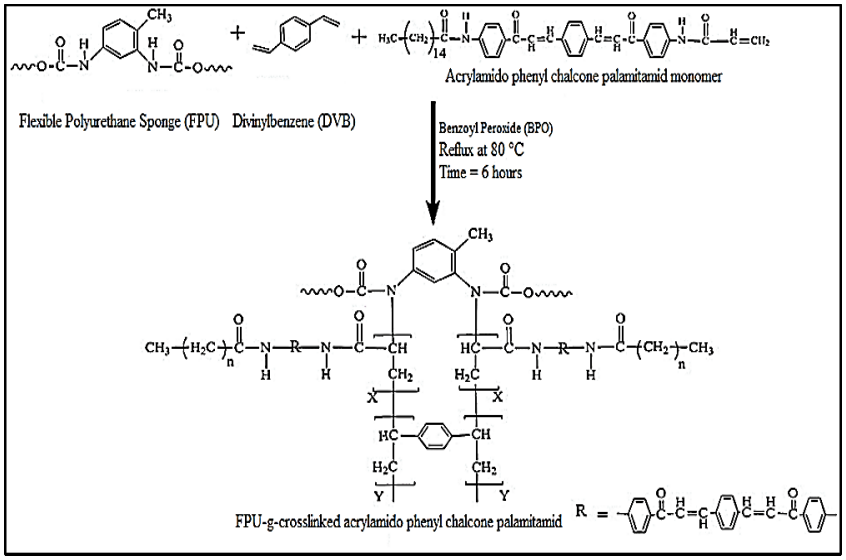

Scheme 1. *In situ* grafting polymerization of the prepared crosslinked monomer onto the FPU surface.

J. Mex. Chem. Soc. **2024**, *68*(2)
Regular Issue

ISSN-e 2594-0317

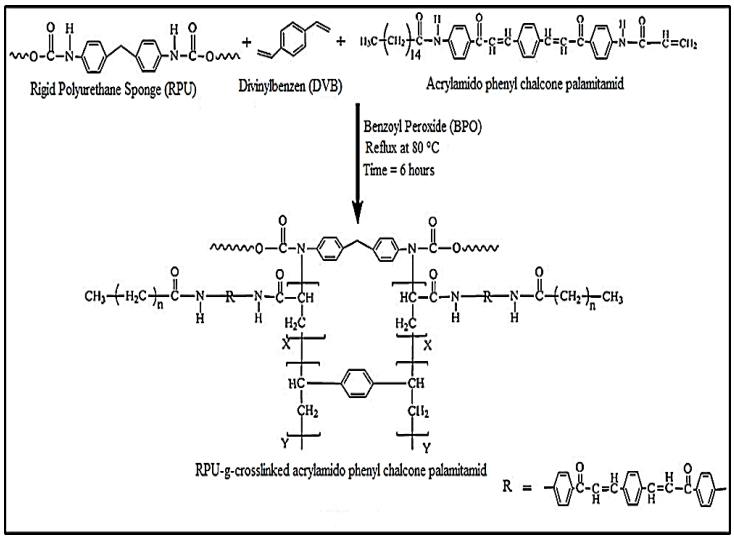

Scheme 2. *In situ* grafting polymerization of the prepared crosslinked monomer onto the RPU surface.

Sorption capacity tests

The method improved for the measurement of the oil sorption capacity of the sorbent was based on ASTM F726 2017 Standard Test Method for Sorbent Performance of Adsorbents for use on crude oil and related spills [27,28].

Water sorption tests

In these tests, the sorbent (FPU or RPU) cubes were initially weighed and then placed into a 100-ml Erlenmeyer flask that contained 50 ml of deionized water. The closed Erlenmeyer flask was then put in a shaker (150 rpm) and shaken for 15 minutes. The contents of the flask were allowed to settle for 2 minutes. The sorbent was removed and allowed to drain for 30 seconds before being immediately transferred to a preweighed Erlenmeyer flask and weighed. The water sorption was calculated using the following equation (1):

$$Water\ sorption\ \left(\frac{g}{g}\right) = \frac{(S_{wt} - S_o)}{S_o} \tag{1}$$

where S_o is the initial dry weight of the sorbent and S_{wt} is the wet weight of the sorbent (after water sorption).

Oil sorption test

For oil sorption tests, crude oil, or diesel fuel (50 ml) was decanted into a 100 ml beaker. The sorbent (FPU or RPU) cubes were weighed, and their value recorded, then they were immersed in crude oil or diesel fuel. In general, after 20 minutes of inundation, the sorbent (FPU or RPU) cubes were removed and allowed to drain for 30 seconds. The saturated sorbent was then immediately transferred to a pre-weighed weighing bottle and weighed. On a weight basis, the oil sorption of sorbent (FPU) cubes was calculated as follows using equation (2):

$$Oil\ sorption\ (g/g) = \frac{(S_t - S_o)}{S_o} \tag{2}$$

where S_o is the initial dry weight of a sorbent and S_t is the weight of the sorbent with oil absorbed. Solvent sorption capacity measurements were carried out similarly.

Oil-water system sorption test

In water–oil system sorption tests, 4.0 g of crude oil or diesel fuel was decanted into a 100 mL Erlenmeyer flask that was filled with 50 mL of deionized water, and the thickness of the oil layer was 2–3 mm.

J. Mex. Chem. Soc. **2024**, *68*(2)
Regular Issue

ISSN-e 2594-0317

The sorbent (FPU or RPU) cubes were initially weighed and put into the Erlenmeyer flask. The closed Erlenmeyer flask was then put in a shaker (150 rpm) and shaken for 30 minutes. The contents of the closed Erlenmeyer flask were allowed to settle for 2 minutes. The sorbent (FPU or RPU) cubes were then transferred to an Erlenmeyer flask and extracted several times with petroleum ether (boiling range 30–60 °C); the sorbent was then removed and squeezed to extract the absorbed petroleum ether. Anhydrous sodium sulfate was added to the petroleum ether solution until there was no agglomeration, and then the Erlenmeyer flask was sealed for 30 minutes to dehydrate [27,28]. The oil–water system sorption capacities were obtained using equation (3).

$$Oil - water\ sorption\ (g/g) = \frac{(M_t - M_o)}{S_o} \tag{3}$$

where M_o is the constant weight beaker, Mt is the weight of the constant weight beaker with absorbed oil, and S_o is the initial dry weight of the sorbent.

Results and discussion

To develop the oleophilic and hydrophobic properties of PU foams, *in situ* grafting polymerization with acrylamido phenyl chalcone palamitamid monomer crosslinked with divinylbenzene was used to modify two types of polyurethane (PU): flexible polyurethane (FPU) and rigid polyurethane (RPU). Fourier transform infrared (Shimadzu FTIR-8400/Japan) and scanning electron microscopy (MIRA3 LMU TESCAN/Czech Republic) were employed to analyze the polyurethane. The testing used crude oil and diesel fuel as oil samples, and the sorption properties of the ungrafted and grafted PU cubes in water, pure oil phase, and water-oil systems were fully investigated and compared. The experiment's data was an average of three experiments.

FTIR characterization

FTIR analysis confirmed the grafting polymerization of FPU and RPU foams with prepared crosslinked grafted monomers. The reduction in the peak of the isocyanate group of the urethane at 2368 cm^{-1} in the FTIR spectra implied the correctness of the grafting process. When comparing the infrared spectra of both grafted polyurethane foams (Figures 3 and 5) to the infrared spectra of an ungrafted polyurethane (Figures 2 and 4) we observe a decrease in the strength of the NCO peak that appears at 2250 cm^{-1}. In addition to an increase in the intensity of each of the (CH_2) aliphatic peaks at (2866–2970) cm^{-1}, the carbonyl group (C=O) exhibits a shift from 1712 cm-1 to 1720 cm^{-1}, as well as an increase in its intensity. These values agreed very well with the results reported in the literature [29,30].

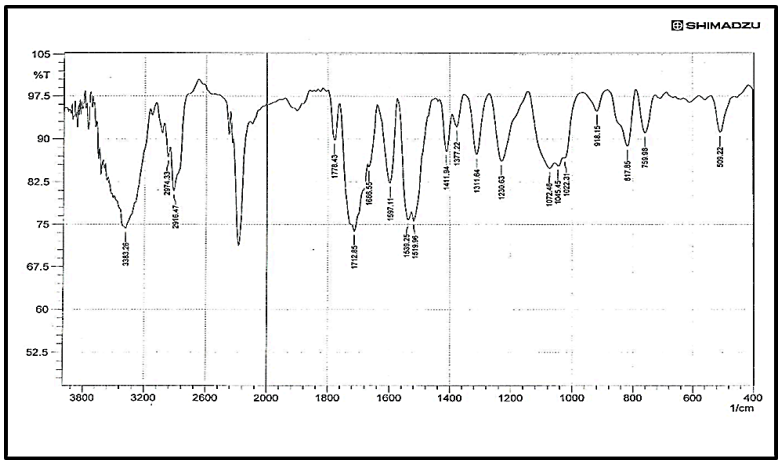

Fig. 2. FTIR spectrum of ungrafted RPU foam.

J. Mex. Chem. Soc. **2024**, *68*(2)
Regular Issue

ISSN-e 2594-0317

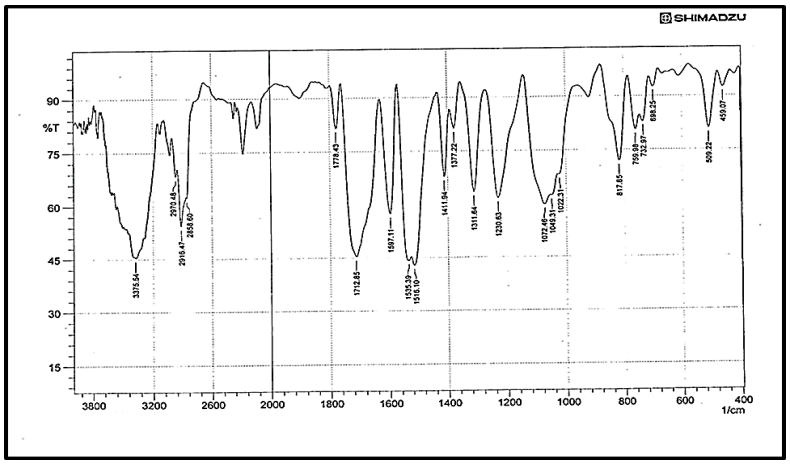

Fig. 3. FTIR spectrum of grafted RPU foam.

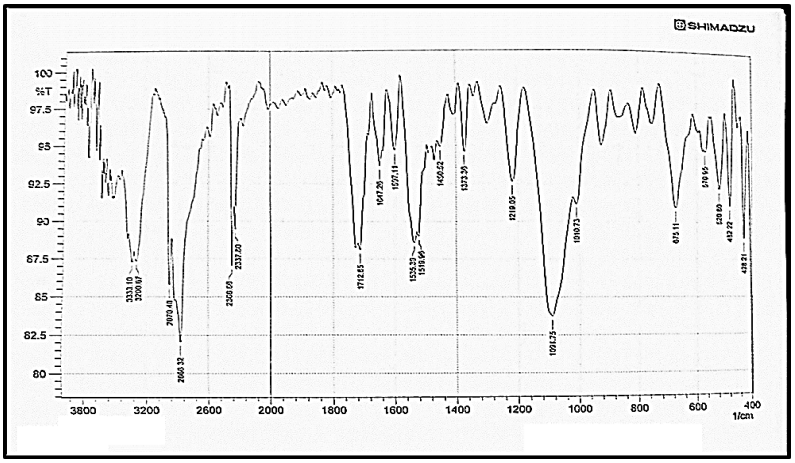

Fig. 4. FTIR spectrum of ungrafted FPU foam.

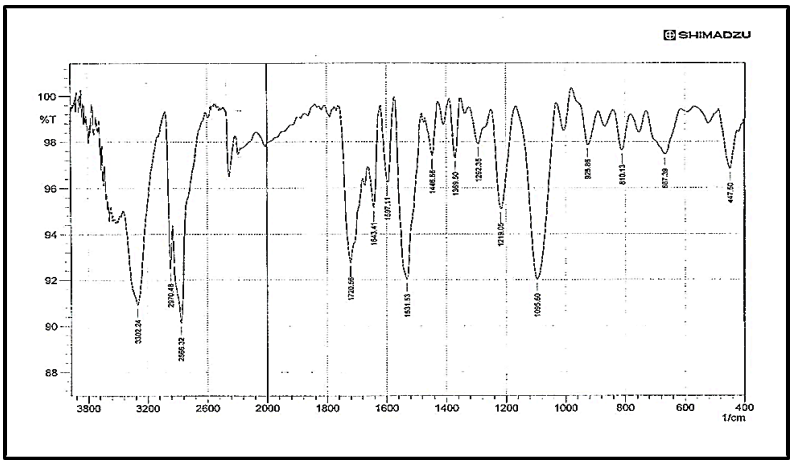

Fig. 5. FTIR spectrum of grafted FPU foam.

J. Mex. Chem. Soc. **2024**, *68*(2)
Regular Issue

ISSN-e 2594-0317

SEM characterization

Scanning electron microscopy (SEM) was used to analyze and study the morphological aspects of the ungrafted PU surface and the modified PU surface. From the SEM micrographs of the ungrafted flexible and rigid PU cubes and the grafted flexible and rigid PU cubes shown, the pentagonal cell structure of the ungrafted PU cubes was not ideal.

Fig. 6 shows different magnification ratios of the SEM images of the PU sponges before and after being grafted [31]. The surfaces of the untreated RPU sponges were smooth and flat (Fig. 6**(a–c)**), and there was no destruction in the RPU cubes. Furthermore, Fig. 7 shows that the *in-situ* crosslinking grafting polymerization destroyed the cell structure and backbone of the PU cubes [28]. The micrographs also show the presence of thin cellular wall films within the foams, which may enhance their surface area, possibly further aiding oil sorption.

There were no obvious micro-scale protrusions or spherical structures distributed on the surfaces at the high magnification shown in Figures 6**(a)** and 7**(a)**, as well as at low magnification in Figures 6 **(b)**, **(c)** and 7 **(b)**, **(c)**. The high-magnification SEM picture also showed that numerous microscopic spherical particles were dispersed on the sponge [32]. The SEM images demonstrated that grafting with the new monomers resulted in the formation of spherical particles on the surface. The spherical particles were very important to the hydrophobicity of the sponges, just like surface protrusions were to the hydrophobicity of lotus leaves [33].

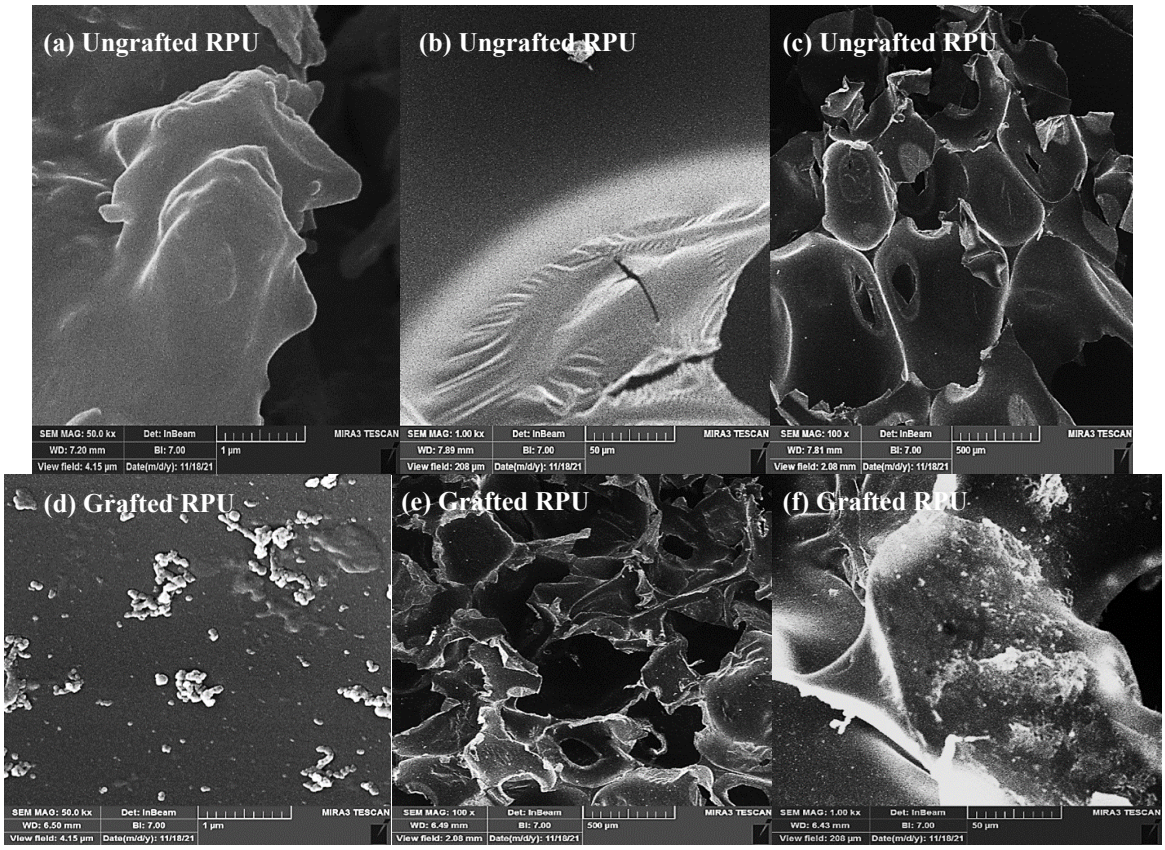

Fig. 6. SEM photographs of the ungrafted RPU cubes **(a-c)**, and grafted RPU **(d-f)**.

J. Mex. Chem. Soc. **2024**, *68*(2)
Regular Issue

ISSN-e 2594-0317

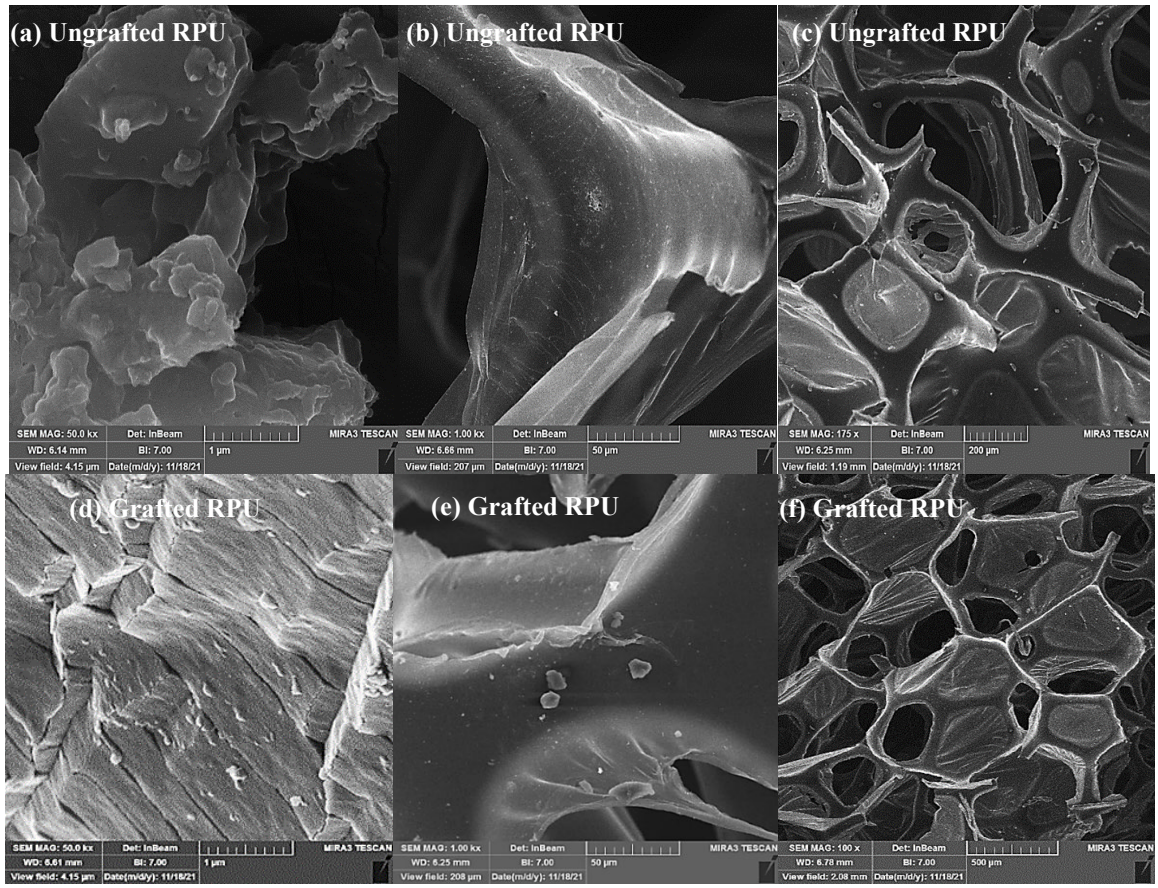

Fig. 7. SEM photographs of the ungrafted FPU cubes **(a-c)**, and grafted FPU **(d-f)**.

Water sorption capacity

In water sorption tests, the water sorption was calculated using Equation 1. The results obtained for the water sorption capacity of ungrafted FPU, grafted FPU, ungrafted RPU, and grafted RPU cubes are listed in Table 1 and shown in Fig. 8. The water sorption capacity is found to be higher for ungrafted FPU and RPU cubes compared to the grafted FPU and RPU cubes, where it decreased by about 60 % after the grafting process for the grafted FPU and by about 55 % for the grafted RPU, as shown in Fig. 8. This may be attributed to the long alkyl chains of the crosslinked grafted monomer, which exhibit more oleophilic and less hydrophobic properties simultaneously [34]. This implies that PU cubes grafted with the newly prepared crosslinked monomer were more hydrophobic than ungrafted FPU and RPU cubes. The increase in the hydrophobic properties of the grafted PU cubes may be attributed to the decrease in polarity due to the presence of more non-polar methylene groups in the grafted crosslinked monomer [35].

It was also observed that for both ungrafted and grafted samples, the FPU's absorption capacity is marginally greater than that of the RPU when comparing the two types of polyurethane. This is because flexible polyurethane has heterogeneous pore geometry and pore distribution in contrast to rigid polyurethane, which has rather homogeneous pore geometry and pore distribution [36]. These outcomes match those of the SEM depicted in Figures 6 and 7. When compared to the uneven and poorly dispersed pores of RPU, the pores of FPU are homogeneous and well-distributed. Therefore, samples of FPU grafted and ungrafted will absorb water more than those of RPU grafted and ungrafted.

J. Mex. Chem. Soc. **2024**, *68*(2)
Regular Issue

ISSN-e 2594-0317

Table 1. The water sorption capacity of the ungrafted and grafted FPU and RPU cubes.

Cube Type	S_o (g)	S_{wt} (g)	Water Sorption Capacity (g/g)	Capacity Ratio (%)
Ungrafted FPU	0.1033	1.9674	18.05	59.50
Grafted FPU	0.1085	0.9012	7.31	
Ungrafted RPU	0.0881	1.4674	15.66	54.92
Grafted RPU	0.0914	0.73592	7.06	

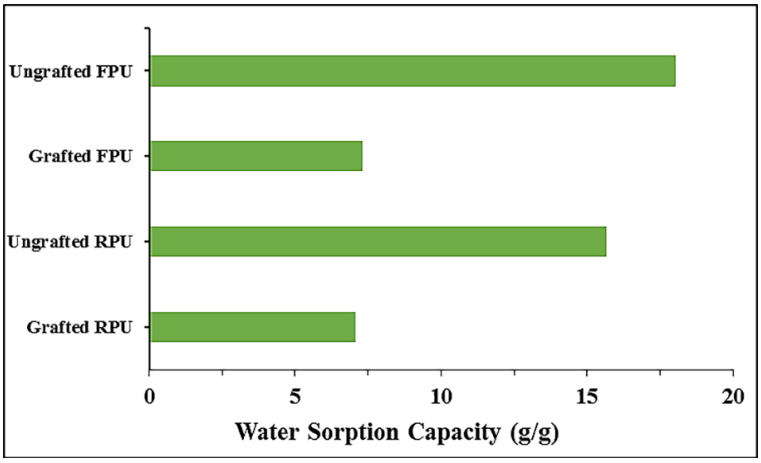

Fig. 8. The water sorption capacity of the ungrafted and grafted FPU and RPU cubes.

Crude oil sorption capacity

The crude oil sorption of both grafted and ungrafted polyurethane foam was calculated using Equation 2. The results of the crude oil absorption capacity of ungrafted FPU and RPU cubes and grafted FPU and RPU cubes obtained are shown in Table 2 and Fig. 9.

The results revealed that *in situ* crosslinking polymerization of the prepared monomer would increase the oleophilicity of both types of tested PU, i.e., RPU and FPU. This effect may be attributed to the effect of the alkyl chain length of the grafted monomer on the porosity of the grafted RPU and FPU, as seen by SEM on the changed PU foam surfaces. The micrographs also show the presence of thin cellular wall films within the foams, which may enhance their surface area, possibly further aiding oil sorption. The particles were generally spherical. However, it can be said that the size distribution for all samples is rather wide. It can be seen that the PU has a porous network structure. This indicates that the crosslinked alkyl chain length of the compounds plays an important role in the capacity of the grafted RPU and FPU foam for crude oil absorbency. Increasing the number of CH_2 groups in the alkyl chain length resulted in better crude oil sorption capacity due to the increasing hydrophobicity properties [37].

J. Mex. Chem. Soc. **2024**, *68*(2)
Regular Issue

ISSN-e 2594-0317

Table 2. The crude oil sorption capacity of the ungrafted and grafted FPU and RPU cubes.

Cube Type	S_o (g)	S_{co} (g)	Crude Oil Sorption Capacity (g/g)	Capacity Ratio (%)
Ungrafted FPU	0.0916	2.7536	29.06	40.46
Grafted FPU	0.1055	5.255	48.81	
Ungrafted RPU	0.1360	3.1587	22.23	46.10
Grafted RPU	0.1062	4.4861	41.24	

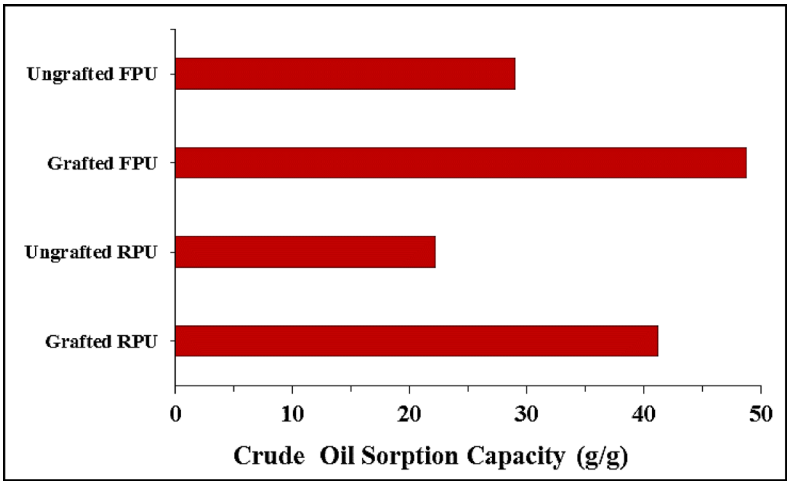

Fig. 9. The crude oil sorption capacity of the ungrafted and grafted FPU and RPU cubes.

Diesel fuel sorption capacity

The diesel fuel sorption capacities of ungrafted FPU and RPU cubes and grafted FPU and RPU cubes are calculated using equation 2 and shown in Table 3 and Fig. 10. As expected, grafted (FPU or RPU) cubes showed enhanced performance in absorbing crude oil and diesel fuel, as shown in Figures 2 and 3, in contrast with ungrafted (FPU or RPU) cubes. Comparing the two Tables (2 and 3), perhaps a difference was observed in the absorption ratio between the grafted FPU and RPU cubes for both crude oil and diesel fuel absorption, but it was much higher than the capacity of water absorption (Table 1).

Table 3. The diesel fuel sorption capacity of the ungrafted and grafted FPU and RPU cubes.

Cube Type	S_o (g)	S_{co} (g)	Crude Oil Sorption Capacity (g/g)	Capacity Ratio (%)
Ungrafted FPU	0.1082	3.0587	27.27	35.53
Grafted FPU	0.1055	4.7841	42.30	
Ungrafted RPU	0.1060	2.2587	20.31	45.36
Grafted RPU	0.0906	3.4861	837.4	

J. Mex. Chem. Soc. **2024**, *68*(2)
Regular Issue

ISSN-e 2594-0317

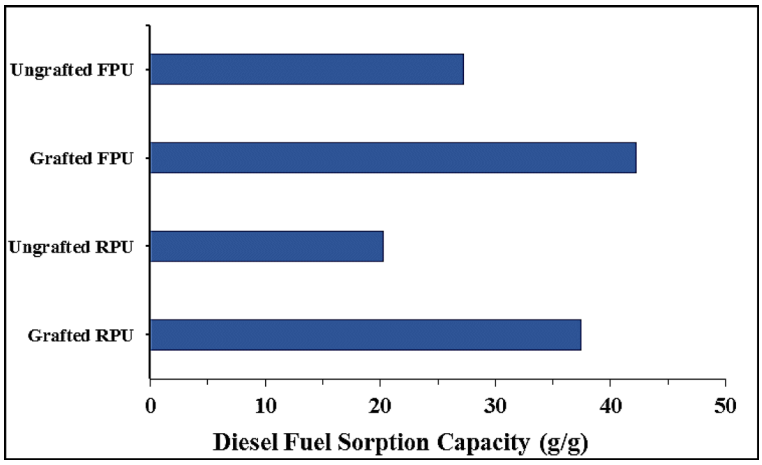

Fig. 10. The diesel fuel sorption capacity of the ungrafted and grafted FPU and RPU cubes.

Furthermore, the incorporation of long-chain crosslinked alkyl groups into the PU backbones improves the hydrophobic properties of the FPU or RPU cubes. In contrast, the sorption capacity of the grafted PU cubes for crude oil and diesel fuel increased in a higher manner than that of the ungrafted PU cubes due to the presence of long aliphatic non-polar groups (-CH_3 and -CH_2). These are hydrophobic groups in nature, and the enhanced oleophilic and hydrophobicity of grafted (FPU or RPU) cubes may be used to explain this [38]. This can be seen clearly in Table 4 and Fig. 12.

Table 4. The water, crude oil, and diesel sorption capacities of the ungrafted and grafted FPU and RPU cubes.

Cube Type	Water Sorption (g/g)	Crude Oil Sorption (g/g)	Diesel Fuel Sorption Capacity (g/g)
Ungrafted FPU	18.0454	29.0611	27.27
Grafted FPU	7.3059	48.8104	42.30
Ungrafted RPU	15.6560	22.2257	20.31
Grafted RPU	7.0516	41.2419	37.48

J. Mex. Chem. Soc. **2024**, *68*(2)
Regular Issue

ISSN-e 2594-0317

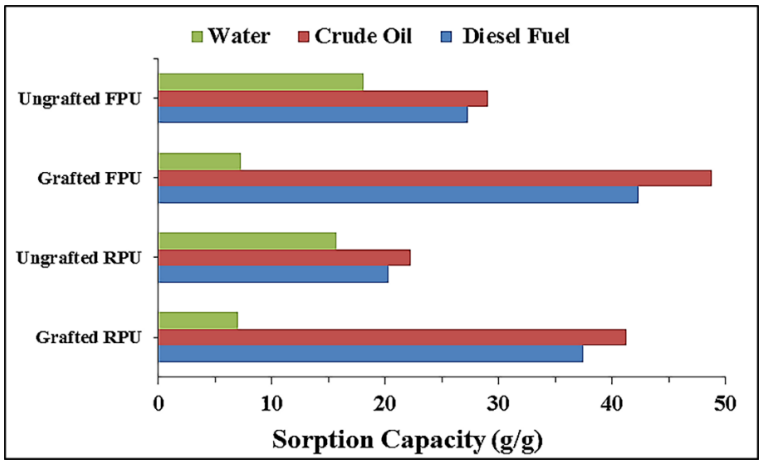

Fig. 11. Water, crude oil, and diesel fuel sorption capacities of the ungrafted and grafted FPU and RPU cubes.

Water-oil system sorption tests

To investigate their sorption capacity in water systems, crude oil, and diesel fuel were accidentally spilled on the water's surface. Grafted and ungrafted FPU and RPU cubes were simply placed on the surface of the oil-water mixture to allow for the collection of oils from the water's surface, which was quickly absorbed, and they were separated from the aqueous phase by removing the cube samples. Their oil sorption capacities in the water–crude oil system and the water–diesel fuel system were calculated using Equation 3.

The results obtained are shown in Table 5 and Fig. 12 and Table 6 and Fig. 13, respectively. The largest crude oil sorption capacity obtained with the grafted FPU was 46.65 g/g, which is greater than the grafted RPU of 38.78 g/g. The same method obtained with a water-diesel fuel system ranged from 36.35 to 34.49 g/g. These results imply that the grafted FPU and RPU were developed to show higher sorption capacities, as shown in the tables and figures above. On the other hand, the results revealed that the hydrophobic surfaces have less interaction with water because of the nonpolar functional groups at the surface. SEM analysis of these outcomes provided support. When crude oil and diesel fuel were cleaned from the water's surface using PU cubes as absorbent materials, they displayed great oil sorption capacity and selectivity by combining special wettability and high porosity.

Table 5. The Sorption of water–crude oil system tests the ungrafted and grafted FPU and RPU cubes in the water-crude oil sorption system.

Cube Type	S_o	M_o	M_t	Water-Crude Oil System Sorption Capacity (g/g)	Capacity Ratio (%)
Ungrafted FPU	0.1033	43.2935	46.1122	27.29	41.50
Grafted FPU	0.1096	43.2935	48.4064	46.65	
Ungrafted RPU	0.1051	43.2935	45.6561	22.48	42.03
Grafted RPU	0.136	43.2935	48.5675	38.78	

J. Mex. Chem. Soc. **2024**, *68*(2)
Regular Issue

ISSN-e 2594-0317

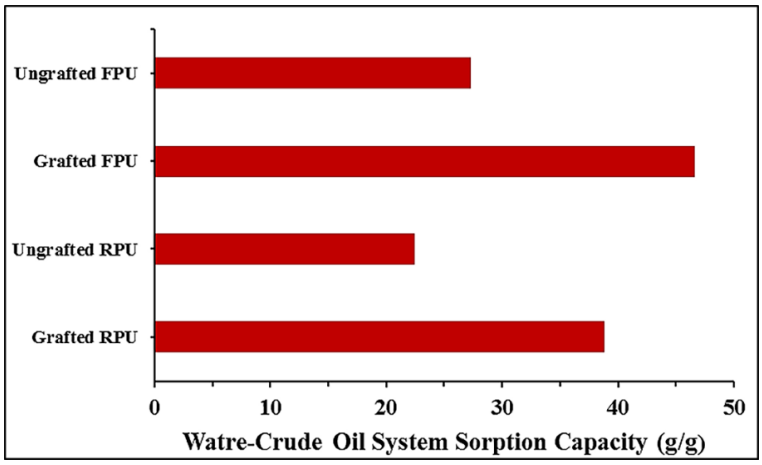

Fig. 12. The crude oil sorption capacity in the water–crude oil system of the ungrafted and grafted FPU and RPU cubes.

Table 6. The sorption of water–diesel fuel system capacities of the ungrafted and grafted FPU and RPU cubes in a water-diesel fuel sorption system.

Cube Type	S_o	M_o	M_t	Water-Diesel Fuel System Sorption Capacity (g/g)	Capacity Ratio (%)
Ungrafted FPU	0.1033	43.2935	45.5954	22.28	38.71
Grafted FPU	0.1096	43.2935	47.2776	36.35	
Ungrafted RPU	0.1023	43.2935	45.3643	20.24	41.32
Grafted RPU	0.109	43.2935	47.0530	34.49	

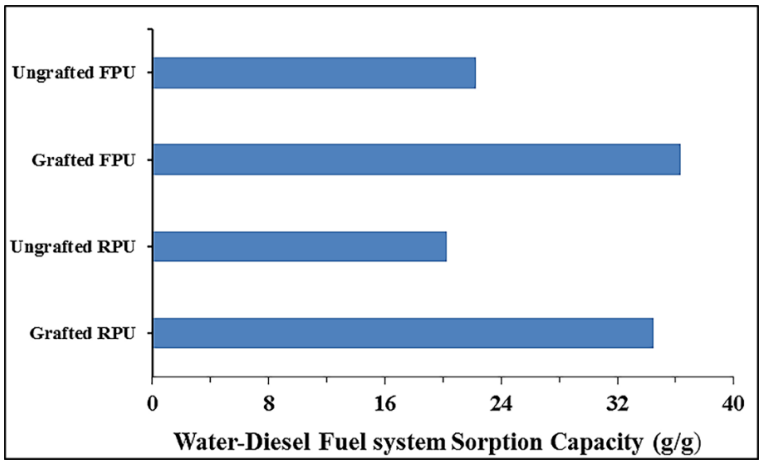

Fig. 13. The diesel fuel sorption capacity in water–diesel fuel system of the ungrafted and grafted FPU and RPU cubes.

J. Mex. Chem. Soc. **2024**, *68*(2)
Regular Issue

ISSN-e 2594-0317

Effect of the water-oil type on the sorption capacities

The effect of oil type on oil sorption capacity using water-crude oil and water-diesel fuel systems can be demonstrated in Table 6 and Fig. 14. Both crude oil and diesel fuel have maximum sorption capacities, with crude oil having the best value. Oil adsorption increases as oil viscosity increases because of the adhering forces between the adsorbent and the oil surface. The PU cube's excellent capacity to absorb oil is due to its high porosity. Oil was stored in the pores thanks to the attraction forces between the oil and the grafted FPU and RPU. The sponge was filled with many holes that let water pass through. The exceptional oil absorption capacity of the PU cubes is partly due to their high porosity.

Oil was able to be stored in the pores due to the forces of attraction between it and the grafted cubes. Therefore, oil was able to reach a greater level. The entire structure could be thought of as capillary walls, and these holes are roughly equivalent to capillaries. Because crude oil and diesel fuel have viscosities that are higher than the viscosity of water, there may be a differential in the sorption capacities of the two substances in their respective water systems. The competition between water and both crude oil and diesel fuel at the sponge's surface is heightened, which lowers the amount of each liquid that is absorbed compared to when each liquid is alone.

Table 6. The water-crude oil, and water-diesel sorption system capacities of the ungrafted and grafted FPU and RPU cubes.

Cube Type	Water-Crude Oil System Sorption Capacity (g/g)	Water-Diesel Fuel System Sorption Capacity (g/g)
Ungrafted FPU	29.0611	27.27
Grafted FPU	48.8104	42.30
Ungrafted RPU	22.2257	20.31
Grafted RPU	41.2419	37.48

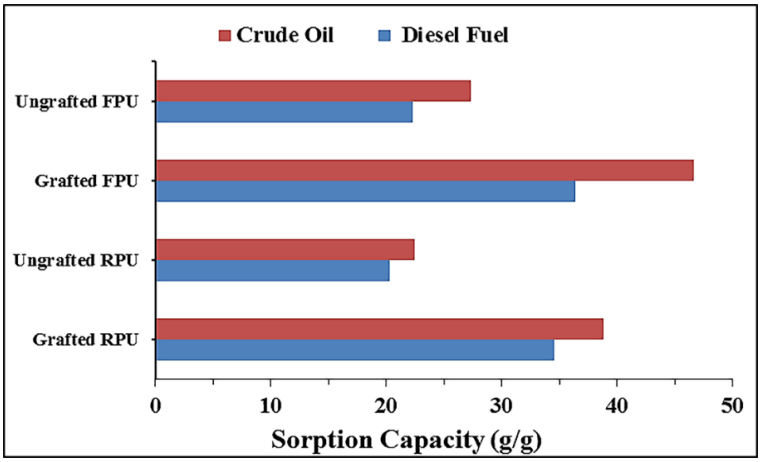

Fig. 14. The sorption of water-crude oil and water-diesel fuel systems of the ungrafted and grafted FPU and RPU cubes.

Conclusions

Commercial FPU and prepared RPU cubes were successfully grafted by in situ polymerization with an oleophilic/hydrophobic crosslinked monomer based on the prepared acrylamido phenyl chalcone

J. Mex. Chem. Soc. **2024**, *68*(2)
Regular Issue

ISSN-e 2594-0317

palamitamid. Oils were collected from the surface of the water by simply placing ungrafted and grafted (FPU and RPU) cubes on the surface of the crude oil-water mixture and the diesel fuel-water mixture. The oil sorption of modified FPU and RPU cubes was enhanced, especially in the water–oil system, meeting the challenge for environmental protection of marine systems and aqueous ecosystems. When compared to ungrafted FPU and RPU cubes, the grafting modification reduced the water sorption capacity by 60 % and 55 %, respectively. The crude oil sorption and diesel fuel sorption capacities of grafted FPU were increased from 29.06 to 48.81 g/g and from 27.27 to 42.30 g/g, respectively, compared to ungrafted FPU, while grafted RPU increased from 22.23 to 41.24 g/g and from 20.31 to 37.84 g/g for diesel fuel, respectively. in the water–crude oil system, compared with ungrafted FPU and RPU cubes of 27.29 g/g for FPU and 22.48 g/g. The hydrophobic polyurethane sponges described here might be a potential absorptive material for the cleanup of water-oil spills due to their simplicity of manufacture, good commercial availability of raw materials, and outstanding reusability.

Acknowledgements

The authors would like to thank the Department of Chemistry, College of Science, at the University of Basrah for their assistance. Without their exceptional assistance, this paper and the research results behind it would not have been possible.

References

1. Peterson, C. H.; Rice, S. D.; Short, J. W.; Esler, D.; Bodkin, J. L.; Ballachey, B. E.; Irons, D.B. *Science.* **2003**, *302*, 2082–2086. DOI: https://doi.org/10.1126/science.1084282.
2. Bidgoli, H.; Khodadadi, A.A.; Mortazavi, Y. *J. Environ. Chem. Eng.* **2019**, *7*, 103340. DOI: https://doi.org/10.1016/j.jece.2019.103340.
3. Liu, Y.; Wang, X.; Feng S. *Adv. Funct. Mater.* **2019**, *29*, 1902488. DOI: https://doi.org/10.1002/adfm.201902488.
4. Benner, S. W.; John, V. T.; Hall, C. K. *J. Phys. Chem.* **2015**, *119*, 6979-6990. DOI: https://doi.org/10.1021/acs.jpcb.5b01092.
5. Kim, H.; Zhang, G., Chung, T. M., Nam, C. *Adv. Sustainable Syst.* **2022**, *6*, 2100211. DOI: https://doi.org/10.1002/adsu.202100211.
6. Muriel, D. F.; Katz, J.; *Langmuir.* 2021, *37*, 1725-1742. DOI: https://doi.org/10.1021/acs.langmuir.0c02986.
7. Baharuddin, S. H.; Mustahil, N. A.; Reddy, A. V. B.; Abdullah, A.A.; Mutalib, M. I. A.; Moniruzzaman, M. *Chemosphere*. **2020**, *249*, 126125. DOI: https://doi.org/10.1016/j.chemosphere.2020.126125.
8. Lü, X.; Cui, Z.; Wei, W.; Xie, J.; Liang, J.; Huang, J.; Liu, J. *Chem. Eng. J.* **2016**, *284*, 478–486. DOI: https://doi.org/ 10.1016/j.cej.2015.09.002.
9. Peng, M.; Zhu, Y.; Li, H.; He, K.; Zeng, G.; Chen, A.; Chen, G. *Chem. Eng. J.* **2019**, *373*, 213-226. DOI: https://doi.org/10.1016/j.cej.2019.05.013.
10. Mao, M.; Xu, H.; Guo, K. -Y.; Zhang, J. -W.; Xia, Q. -Q.; Zhang, G. -D.; Zhao, L.; Gao, J. -F.; Tang, L. -C. *Appl. Sci. Manuf.* **2021**, *140*, 106191. DOI: https://doi.org/10.1016/j.compositesa.2020.106191.
11. Ge, J.; Zhao, H. Y.; Zhu, H.W.; Huang, J.; Shi, L. A.; Yu, S. H. *Adv. Mater.* **2016**, *28*, 10459-10490. DOI: https://doi.org/10.1002/adma.201601812.
12. Peponi, L.; Puglia, D.; Torre, L.; Valentini, L.; Kenny, J. M. *Mater. Sci. Eng. Reports.* **2014**, *85*, 1–46. DOI: https://dx.doi.org/10.1016/j. mser.2014.08.002.
13. Tian, S. *Polymers.* **2020**, *12*, 1996-2011. DOI: https://doi.org/10.3390/polym12091996.
14. Zhu, X.; Li, Q.; Wang, L.; Wang, W.; Liu, S.; Wang, C.; Qian, X. *Eur. Polym. J.* **2021**, *161*, 110837. DOI: https://doi.org/10.1016/j.eurpolymj.2021.110837.

J. Mex. Chem. Soc. **2024**, *68*(2)
Regular Issue

ISSN-e 2594-0317

15. Pham, V. H.; Dickerson, J. H. *ACS Appl. Mater. Interf.* **2014**, *6*, 14181–14188. DOI: https://doi.org/10.1021/am503503m.
16. Zhang, W.; Zhai, X.; Xiang, T.; Zhou, M.; Zang, D.; Gao, Z.; Wang, C. *J. Mater. Sci.* **2017**, *52*, 73–85. DOI: https://doi.org/10.1007/s10853-016-0235-7.
17. Lei, Z.; Zhang, G.; Ouyang, Y.; Liang, Y.; Deng, Y.; Wang, C. *Mater. Lett.* **2017**, *190*, 119–122. DOI: https://doi.org/10.1016/J.MATLET.2016.12.082.
18. Cho, E. C.; Chang-Jian, C. W.; Hsiao, Y.S.; Lee, K. C.; Huang, J. H. *J. Taiwan Inst. Chem. Eng.* **2016**, *67*, 476–483. DOI: https://doi.org/10.1016/j.jtice.2016.08.002.
19. He, K.; Chen, G.; Zeng, G.; Chen, A.; Huang, Z.; Shi, J.; Huang, T.; Peng, M.; Hu, L. *Appl. Catal.* **2018**, *228*, 19–28. DOI: https://doi.org/10.1016/j.apcatb.2018.01.061.
20. Shiu, R. F.; Lee, C. L.; Hsieh, P. Y.; Chen, C. S.; Kang, Y. Y.; Chin, W. C.; Tai, N. H. *Chemosphere.* **2018**, *207*, 110-117. DOI: https://doi.org/ 10.1016/j.chemosphere.2018.05.071
21. Bagoole, O.; Rahman, M. M.; Shah, S.; Hong, H.; Chen, H.; Ghaferi, A. A.; Younes, H. *Environ. Sci. Pollut. Res. Int.* **2018**, *25*, 23091–23105. DOI: https://doi.org/10.1007/s11356-018-2248-z.
22. Wang, H.; Zhang, C.; Zhou, B.; Zhang, Z.; Shen, J.; Du, A. *ACS Appl. Nano Mater.* **2020**, *3*, 1479–1488. DOI: https://doi.org/ 10.1021/acsanm.9b02303.
23. Khosravi, M.; Azizian, S. *ACS Appl. Mater. Interf.* **2015**, *7*, 25326. DOI: https://doi.org/10.1021/acsami.5b07504.
24. Oribayo, O.; Pan, Q.; Feng, X.; Rempel, G. L. *AIChE J.* **2017**, *63*, 4090–4102. DOI: https://doi.org/10.1002/aic.15767.
25. Borreguero, A. M.; Valverde, J. L.; Peijs, T.; Rodríguez, J. F.; Carmona, M. *J. Mater. Sci.* **2010**, *45*, 4462–4469. DOI: https://doi.org/10.1007/s10853-010-4529-x.
26. Al-Khalaf, A. A.; Abbas, A. F.; Al-Lami, H. S. Basrah *J. Sci.* **2022**, *40*, 437-464. DOI: https://doi.org/10.29072/basjs.20220214.
27. Bazargan, A.; Tan, J.; McKay, G. *J. Test. Evalu.* **2015**, *43*, 1271-1278. DOI: https://doi.org/10.1520/JTE20140227.
28. Li, H.; Liu, L.; Yang, F. *Mar. Pollut. Bull.* **2012**, *64*, 1648–1653. DOI: https://doi.org/10.1016/j.marpolbul.2012.05.039.
29. Wong, C. S.; Badri, K. H. *Mat. Sci. Appl.* **2012**, *3*, 78-86. DOI: https://doi.org/10.4236/msa.2012.32012.
30. Selvam, R.; Subramanian, K. *Adv. Polym. Technol.* **2018**, *37*, 724–731. DOI: https://doi.org/10.1002/adv.21714.
31. Peng, L.; Yuan, S.; Yan, G.; Yu, P.; Luo, Y. *J. Appl. Polym. Sci.* **2014**, *131*, 40886. DOI: https://doi.org/10.1002/app.40886.
32. Keshawy, M.; Farag, R. K.; Gaffer, A. *Egypt. J. Pet.* **2020**, *29*, 67-73. DOI: https://doi.org/10.1016/j.ejpe.2019.11.001.
33. Zhang, Y. L.; Xia, H.; Kim, E.; Sun, H. B. *Soft Matter*. **2012**, *8*, 11217-11231. DOI: https://doi.org/10.1039/c2sm26517f.
34. Zhu, J.; Wang, Z.; Ni, H.; Liu, X.; Ma, J.; Du, J. *J. Chem.* **2016**, *2016*, 1–7. DOI: https://doi.org/10.1155/2016/6095023.
35. Reichardt, C.; Welton, T. in: *Solvents and Solvent Effects in Organic Chemistry*, 4th ed. Wiley-Vch Verlag Gmbh & Co. Kgaa, Weinheim, **2010**. DOI: https://doi.org/10.1002/9783527632220.
36. Blazejczyk, A.; Wierzbicka, P. *Polimery-Warsaw*. **2018**, *63*, 685-693. DOI: https://doi.org/10.14314/polimery.2018.10.4.
37. Al-Khalaf, A. A.; Al-Lami, H. S.; Abbas, A. F. *Pet. Sci. Technol*. **2022**, 1-16. DOI: https://doi.org/10.1080/10916466.2022.2118774.
38. Visco, A.; Quattrocchi, A.; Nocita, D.; Montanini, R.; Pistone, A. *Nanomaterials.* **2021**, *11*, 735-749. DOI: https://doi.org/10.3390/nano11030735.

Article

J. Mex. Chem. Soc. **2024**, *68*(2)
Regular Issue

ISSN-e 2594-0317

Non-covalent Interactions in Dihalogenated Compounds $Ch(C_6H_4CH_2X)_2$ (Ch = O, S; X = Cl, Br, I). Synthesis, Crystal Structure, and Hirshfeld Surface Analysis

J. Viridiana García-González, José G. Alvarado-Rodríguez*, Noemí Andrade-López, Cristian G. Guerra-Poot

Área Académica de Química, Universidad Autónoma del Estado de Hidalgo, km. 4.5 Carretera Pachuca-Tulancingo, Col. Carboneras. C.P. 42184.Mineral de la Reforma, Hidalgo, México.

***Corresponding author:** José G. Alvarado-Rodríguez, email: jgar@uaeh.edu.mx

Received March 29th, 2023; Accepted June 6th, 2023.

DOI: http://dx.doi.org/10.29356/jmcs.v68i2.2036

Abstract. In this work, the synthesis and structural study by means of single-crystal X-ray diffraction of compounds of general formula **Ch**$(C_6H_4CH_2$**X**$)_2$ (**Ch** = O, S; **X** = Cl, Br, I) is reported. These compounds contain two flexible hydrocarbonated arms –CH_2–**X** in the *ortho* positions to the **Ch** heteroatom. These compounds were synthesized through a linear synthesis starting from diphenylether or diphenylsulfide. Based on the structural analysis, we describe the more relevant molecular features as well as the non-covalent interactions that the heavy halogen atoms display with other moieties that promote the cohesion of the crystal arrangement. The Hirshfeld analysis displayed that the **X**···π, **X**···**X**, and C–H···**X** interactions are quite significant in the crystal arrangement.
Keywords: Non-covalent interactions; dihalogenated compounds; Hirshfeld surfaces.

Resumen. En este trabajo, se describen la síntesis y el estudio estructural de difracción de rayos-X de monocristal de seis compuestos con fórmula general **Ch**$(C_6H_4CH_2$**X**$)_2$ (**Ch** = O, S; **X** = Cl, Br, I), que contienen dos brazos hidrocarbonados flexibles –CH_2–**X** en las posiciones *orto* al heteroátomo **Ch**. Estos compuestos fueron sintetizados a través de una síntesis lineal, partiendo de difeniléter o difeniltioéter. A través del análisis estructural se describen las características moleculares más relevantes, así como las interacciones no-covalentes que presentan los átomos de halógeno pesados con otros grupos funcionales para dar cohesión a la red cristalina. El estudio de las superficies de Hirshfeld mostró que las interacciones **X**···π, **X**···**X** y C–H···**X** son muy relevantes en esta cohesión.
Palabras clave: Interacciones no-covalentes; compuestos dihalogenados; superficies de Hirshfeld.

Introduction

In many aspects, the physicochemical properties and reactivity of halogenated organic compounds is strongly based on the nature of the **X** halogen substituent (**X** = F, Cl, Br, or I); for example, with an increase in the atomic number of the halogen, C–X bond energies decrease markedly, i.e., C–F > C–Cl > C–Br > C–I [1], and the order of reactivity can generally be predicted by the relative easiness with which the respective carbon–halogen bonds are broken. Other features such as the electron-withdrawing effect, atomic size, and polarizability of the halogen substituent also affect the reactivity of these halogenated compounds [2]. A typical reaction of these compounds is nucleophilic substitution of the halogen by electron-rich molecules or anions

J. Mex. Chem. Soc. **2024**, *68*(2)
Regular Issue

ISSN-e 2594-0317

such as ammonia, cyanide (a pseudohalide), hydroxide, alkoxides, or even another halogen [3]. In this vein, halogen-by-halogen exchange substitution provides a convenient route for synthesizing alkyl halides [4]. Other typical and very useful reaction of alkyl halides involves the formation of free radicals in the presence of very active alkaline or alkaline earth metals; subsequent reaction of these radicals can lead to the formation of organometallic compounds or coupling of the alkyl radicals to enlarge carbon chains [5].

On the other hand, the presence of a halogen atom makes possible the formation of either **Y**–**X**···**A** intra- or intermolecular non-covalent interactions; here, **Y**–**X** is the halogen bond donor such as I_2, Br_2, ICl, haloalkanes; haloarenes, haloimides, etc., meanwhile **A** represents the halogen bond acceptor that can be an atom with an electronic lone pair, a p system, or an anion [6,7]. Moreover, the halogen atom usually displays two regions; an electrophilic region diametrically opposed to the **Y**–**X** sigma bond (named as a σ-hole) and a nucleophilic region transversal to the stated bond (Fig. 1). Hence, due to the anisotropic distribution of the electron density, these two interactions have an important electrostatic component. [8]

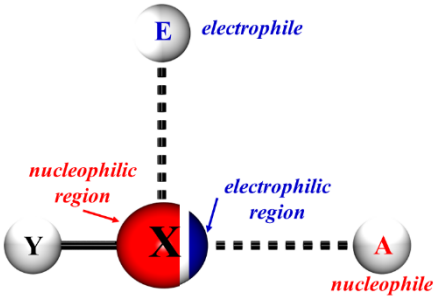

Fig. 1. Diagrammatic representation of an **X**···**A** halogen bond; also, is displayed a possible transversal **E**···**X** interaction.

A chief key to the formation halogen bonds is the polarizability of the halogen atom. Therefore, the strongest halogen bonds are formed by the most easily polarizable halogens, and the strength of the halogen bonds typically decreases in the order I > Br > Cl > F [9]. Several distinctive features of **X**···**A** halogen bond, such as the high directionality and strength tunability, prompted a plethora of applications in organocatalysis [10], crystal engineering [11]and drug design [12], and their influence on packing modes and the consequent orientation of organic molecules, are also considered important in conjunction with the practically ubiquitous both classical and no-classical hydrogen bond [13,14].

Thus, as a part of our studies in the reactivity of halogenated compounds [15], herein we report the structural analysis in crystalline state of two series of conformationally flexible di(2-halomethylphenyl)ethers (compounds **3a**, **4a**, and **5a**) and di(2-halomethylphenyl)thioethers (compounds **3b**, **4b**, and **5b**) of general formula **Ch**($C_6H_4CH_2$**X**)$_2$, where **Ch** is a chalcogen atom (oxygen or sulfur) and **X** = Cl, Br or I. To provide a structural context, in the 3D pie chart showed in Fig. 2 are presented the results of a delimited search in the Cambridge structural database for compounds containing at least one C_6–CH_2–**X** moiety.

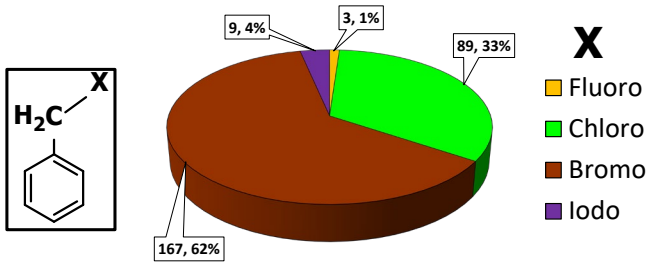

Fig. 2. Numerical and relative proportion of halocompounds containing at least one C_6–CH_2–**X** moiety. (268 hits; data retrieved from CSD version 5.43, updated to November 2022).

J. Mex. Chem. Soc. **2024**, *68*(2)
Regular Issue

ISSN-e 2594-0317

From these data, it is clear the dominance of the bromomethylenic compounds (167 compounds), and the scarceness of fluoro- and iodo- ones. In addition, we want to highlight two experimental facts: the first one is that the presence of two conformationally flexible –CH_2–**Br** arms in 1,4-dibromo-2,5-bis(bromomethyl)benzene allowed dimorphism, displaying Br···Br non-covalent interactions in solid crystalline state [16]. The second one is that there is just one compound with a slightly similar chemical environment to **3a-5a** and **3b-5b**, reported as a private communication (Ref. CSD code MUMQAO) [17].

In the title compounds, the presence of two –CH_2–**X** arms of different nature in both series prompted the formation of several **X**···p and **X**···**X** alongside to C–H···**X** interactions. A Hirshfeld surface analysis was carried out to describe the interactions present in the isostructural compounds.

Experimental

Instrumentation and software

Melting points were determined with a Mel–Temp II instrument. IR spectra were recorded in the 4,000–400 cm^{-1} range on a Perkin-Elmer System 2000 FT-IR spectrometer, as KBr pellets. ^1H and ^{13}C NMR spectra were recorded in $CDCl_3$ on a Bruker Avance III 400 MHz spectrometer (400.1 MHz for ^1H and 100.0 MHz for ^{13}C) at 23 °C and calibrated by using the residual proton resonance of $CDCl_3$. Chemical shifts (δ) are reported in ppm and coupling constants (*J*) are in Hz. For the assignment we used 2D correlation experiments such as COSY, HSQC and HMBC.

Suitable crystals for the X-ray diffraction analysis were obtained for compounds **3a**, **4a**, **5a**, **4b**, and **5b** by slow evaporation of CH_2Cl_2 solutions. Each single crystal was either glued on a tip of a thin glass fiber or mounted on a Nylon loop. Diffraction data were collected at 294 K in an Agilent Gemini diffractometer equipped with an Atlas CCD detector; we used graphite-monochromated Mo-Kα radiation (0.71073 Å). Absorption corrections were made by multi-scan methods using the CrysAlisPro software [18]. By using the Olex2 interface [19], the structures were solved by intrinsic phase methods using SHELXT [21] and all the non-hydrogen atoms were anisotropically refined by full-matrix least-squares on F^2 using SHELXL [22]. Hydrogen atoms were placed in their calculated positions and then refined using the riding model. Crystallographic data are listed in Table 1, and selected bond distances and angles are given in Table 2. The asymmetric unit of **3a** displayed just the half of the molecule (see gray moiety in Fig. 3); the other half is related by a two-fold axis, where the oxygen atom is placed on it (see green moiety in Fig. 3). The ORTEP views of the molecular structures are shown in Figures 3 and 4.

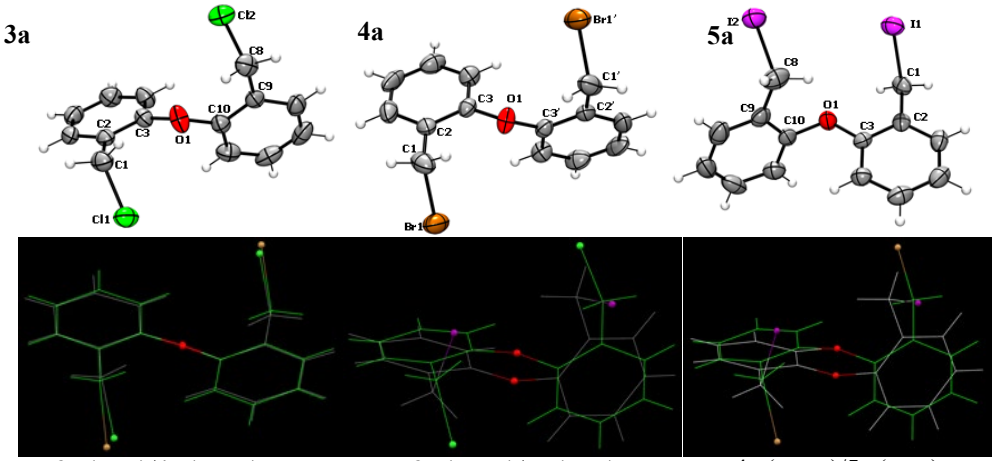

3a (gray)/**4a** (green) overlaying (RMSD = 0.154 Å; deviation$_{max}$ = 0.359 Å)

3a (green)/**5a** (gray) overlaying (RMSD = 1.172 Å; deviation$_{max}$ = 3.234 Å)

4a (green)/**5a** (gray) overlaying (RMSD = 1.281 Å; deviation$_{max}$ = 3.578 Å)

Fig. 3. Molecular structures of O($C_6H_4CH_2$**X**)$_2$ compounds (ORTEP at 50 %) and overlay results of the corresponding pairs.

J. Mex. Chem. Soc. **2024**, *68*(2)
Regular Issue

ISSN-e 2594-0317

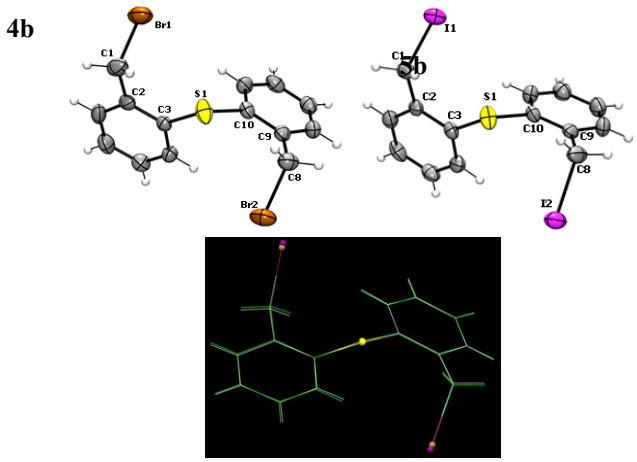

4b (gray)/**5b** (green) overlaying
(RMSD = 0.064 Å;
deviation$_{max}$ = 0.1544 Å)

Fig. 4. Molecular structures of $S(C_6H_4CH_2\mathbf{X})_2$ compounds (ORTEP at 50 %) and overlay results of the pair.

Table 1. Crystal data and refinement details.

	3a	**4a**	**5a**	**4b**	**5b**
Empirical formula	$C_{14}H_{12}Cl_2O$	$C_{14}H_{12}Br_2O$	$C_{14}H_{12}I_2O$	$C_{14}H_{12}Br_2S$	$C_{14}H_{12}I_2S$
Formula weight [g/mol]	267.14	356.06	450.04	372.12	466.10
Crystal system	triclinic	monoclinic	monoclinic	triclinic	triclinic
Space group	*P*–1	*I*2/a	$P2_1$	*P*–1	*P*–1
a [Å]	7.6808(4)	12.279(3)	8.2871(4)	8.2610(14)	8.2734(5)
b [Å]	7.9888(4)	9.2954(17)	4.6487(3)	9.2086(13)	9.5171(7)
c [Å]	10.7391(4)	11.972(3)	18.5371(12)	10.6912(17)	10.7511(9)
α [º]	87.075(4)	90	90	102.043(13)	103.115(7)
β [º]	79.474(4)	99.17(2)	90.603(5)	101.772(14)	101.149(6)
γ [º]	83.979(4)	90	90	113.586(15)	112.203(6)
V [Å^3]	643.95(5)	1349.1(5)	714.09(7)	690.4(2)	725.83(10)
Z	2	4	2	2	2
r_{calc} [g/cm^3]	1.378	1.753	2.093	1.790	2.133
Absorption coefficient [mm^{-1}]	0.484	5.990	4.386	5.996	4.453
F(000)	276	696.0	420.0	364.0	436.0

J. Mex. Chem. Soc. **2024**, *68*(2)
Regular Issue

ISSN-e 2594-0317

Crystal size [mm^3]	0.3 × 0.2 × 0.1	0.3 × 0.3 × 0.2	0.2 × 0.2 × 0.1	0.5 × 0.5 × 0.5	0.2 × 0.1 × 0.1
2Θ range data collection [º]	6.068 to 59.062	6.722 to 59.244	6.562 to 59.278	6.858 to 59.262	6.85 to 59.148
Measured reflections	23203	5234	18168	5913	5595
Data/restraints/parameters	3407/0/154	1678/0/78	3656/1/154	3262/0/154	3432/0/155
R_1; wR_2 [I>2□(I)]	0.0416, 0.0900	0.0442; 0.1146	0.0279; 0.0528	0.0458; 0.0795	0.0609; 0.0871
R_1; wR_2 [All data]	0.0680, 0.1026	0.0975; 0.1381	0.0417; 0.0578	0.1054; 0.1016	0.1339; 0.1079
Goodness-of-fit on F^2	1.031	1.040	1.039	0.995	1.031
Largest diff. peak / hole [$eÅ^{-3}$]	0.27/−0.30	0.63/−0.57	0.46/−0.52	0.33/−61	1.77/−1.32
Flack parameter	Not applicable	Not applicable	−0.019(16)	Not applicable	Not applicable
CCDC	2252394	2252390	2252392	2252393	2252391

Table 2. Selected bond lengths (Å) and angles (°) for **Ch**($C_6H_4CH_2$**X**)$_2$.

	3a	**4a**	**5a**	**4b**	**5b**
	(**Ch** = O **X** = Cl)	(**Ch** = O **X** = Br)	(**Ch** = O **X** = I)	(**Ch** = S **X** = Br)	(**Ch** = S **X** = I)
C–**X**	1.801(2); 1.802(2)	1.950(4)	2.180(6); 2.150(6)	1.971(4); 1.968(4)	2.170(5); 2.163(5)
C–**Ch**	1.383(2); 1.385(2)	1.381(4)	1.368(6); 1.408(6)	1.783(4); 1.794(3)	1.776(4); 1.769(4)
C–**Ch**–C	119.22(14)	118.5(4)	118.9(4)	101.03(17)	101.6(2)
C2–C3–**Ch**–C10	140.64(16)	138.6(4)	179.0(5)	134.9(3)	137.0(4)
C9–C10–**Ch**–C3	144.21(16)	138.6(4)	102.3(6)	127.3(3)	126.8(4)
$\|\Delta_{ta}\|$	3.57	0.0	76.7	7.6	10.2

$|\Delta_{ta}|$ is the difference of the C–C–**Ch**–C torsion angles; see text.

The atomic coordinates of all **3a**–**5a** diphenylether and **4b** and **5b** diphenylthioether compounds determined by X-ray crystallographic studies at 294 K were used to construct the molecular Hirshfeld surfaces based on the electron distribution calculated as the sum of spherical atomic electron densities (the promolecule), which dominates the corresponding sum over the crystal (the procrystal) yielding an implicit 0.5 value for the promolecule-to-procrystal ratio. The bond lengths involving hydrogen atoms were adjusted to values derived

J. Mex. Chem. Soc. **2024**, *68*(2)
Regular Issue

ISSN-e 2594-0317

from neutron diffraction [22]. The Hirshfeld surfaces mapped with d_{norm} and 2D fingerprint plots presented were generated using CrystalExplorer21 with a high standard surface resolution [23]. They were mapped using a fixed color scale, red-white-blue, where red highlights are for contacts shorter than van der Waals (vdW) radii sum, white for contacts around vdW separation, and blue is for contacts longer than the vdW sum.

The molecular electrostatic potential mapping (MEP) was calculated to characterize the close contacts by projecting the Hirshfeld surface with this MEP. We used the Tonto quantum modelling package [24] implemented in CrystalExplorer21 using the Becke three-parameter Lee–Yang–Parr (B3LYP) hybrid functionals [25] with the DGDZVP basis set [26,27].

General methods

All manipulations involving *n*-BuLi reagent were performed in a dry nitrogen atmosphere using standard Schlenk techniques. Solvents, *N,N,N′N′*-tetramethylethylenediamine (TMEDA), and *N,N*-dimethylformamide (DMF) were purchased from Sigma-Aldrich and dried by standard methods and distilled prior to use. The reagents used in the syntheses were purchased from Aldrich and used without purification. Merck Kiesel gel 60 (0.063–0.40 mm) was used for column chromatography.

The sequence of the reaction steps is summarized in Scheme 1. Dihalogenated compounds **3a**, **3b**, **4a**, **4b**, **5a** and **5b** were prepared by linear synthesis, starting from either diphenylether or diphenylthioether, respectively (the **a** letter refers to the compounds with **Ch** = oxygen and **b** to compounds with **Ch** = sulfur).

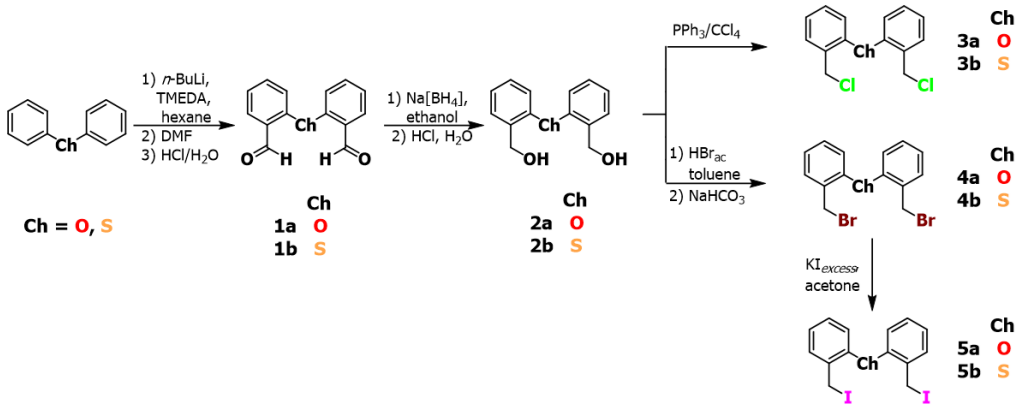

Scheme 1. Synthesis of dihalogenated compounds.

Synthesis of the dialdehyde $O(C_6H_4CHO)_2$ (1a)

Dialdehyde **1a** is known from the literature [28, 29]. Modification of this method allowed the desired product to be obtained in a much higher yield and without purification by column chromatography. Diphenylether (6.5 mL, 41 mmol) was dissolved in dry hexane (40 mL) under an inert nitrogen atmosphere, and TMEDA (13.5 mL, 90.2 mmol) was added at 25 °C. A solution of *n*-butyllithium in hexane (2.5 M, 36.1 mL, 90.2 mmol) was added dropwise to the stirred reaction mixture at 0 °C. This mixture was stirred at 0 °C for 22 h, turning into a beige one. Then, dry DMF (11.5 mL, 147.6 mmol) was poured dropwise into the reaction mixture. The white solution was stirred for 1 h at 70 °C. Aqueous hydrochloric acid (40 mL HCl in 60 mL of distilled water) was added, and the mixture was stirred for fifteen minutes. After, the compound was extracted with $CHCl_3$ (30 mL). The combined organic phases were dried with Na_2SO_4, and the volatiles were removed under reduced pressure to yield the title compound as a beige solid (8.8 g, 95 %).

mw = 226.22 g/mol. mp = 65 °C. IR (KBr, cm^{-1}): ν = 3071, 2856, 2755, 1685, 1599, 1472, 1455, 1394, 1276, 1224, 1097, 881, 827, 758. ^{1}H-RMN (400 MHz, $CDCl_3$, ppm) δ = 10.50 (s, 2H, H1), 7.99 (d, ^3J = 7.69 Hz, 2H, H7), 7.59 (t, ^3J = 7.69 Hz, 2H, H5), 7.30 (t, ^3J = 7.80 Hz, 2H, H6), 6.96 (d, ^3J = 8.32 Hz, 2H, H4). ^{13}C{^{1}H}-RMN (100 MHz, $CDCl_3$, ppm) δ = 188.7 (C1), 158.9 (C3), 136.1 (C5), 129.3 (C7), 127.3 (C2), 124.6 (C6), 119.2 (C4).

J. Mex. Chem. Soc. **2024**, *68*(2)
Regular Issue

ISSN-e 2594-0317

Synthesis of $O(C_6H_4CH_2OH)_2$ (2a)

The diol **2a** is known from the literature [30]; here is introduced an alternative procedure to obtain it in a much higher yield. Thus, to an ethanolic solution (60 mL) of **1a** (8.8 g, 38.9 mmol) was slowly added $Na[BH_4]$ (3.8 g, 97.4 mmol), and the resulting mixture was stirred for 1 h at 0 °C and three hours at room temperature. Then, it was acidified with diluted HCl (40 mL HCl in 60 mL of distilled water), followed by extraction with CH_2Cl_2 (60 mL). The combined organic phases were washed with brine (60 mL), dried (Na_2SO_4), and the volatiles were removed under reduced pressure. The product was obtained as a white solid (9.35 g, 99 %).

mw = 230.25 g/mol. mp = 86 °C. IR (KBr, cm^{-1}): ν = 3272 (OH), 3082, 3039, 2929, 2886, 1689, 1604, 1581, 1484, 1452, 1230, 1110, 1034, 880, 755. ^{1}H-RMN (400 MHz, $CDCl_3$, ppm) δ = 7.39 (d, ^3J = 7.19 Hz, 2H, H7), 7.25 (td, ^3J = 7.69 Hz, ^4J = 1.22 Hz, 2H, H5), 7.10 (td, ^3J = 7.44 Hz, ^4J = 0.69 Hz, 2H, H6), 6.82 (d, ^3J = 8.06 Hz, 2H, H4), 4.68 (s, 4H, H1). $^{13}C\{^1H\}$-RMN (100 MHz, $CDCl_3$, ppm) δ = 154.8 (C3), 131.4 (C7), 130.1 (C5), 129.3 (C2), 123.7 (C6), 117.9 (C4), 61.2 (C1).

Synthesis of the dichlorinated compound $[\{O(C_6H_4CH_2)_2\}Cl_2]$ (3a)

To a reaction flask, were added the diol **2a** (1.0 g, 4.3 mmol), carbon tetrachloride (20 mL), and triphenylphosphine (2.73 g, 10.4 mmol). The solution was heated at 65–70 °C for 24 h, and the reaction mixture was cooled and filtered. The yellow solution was chromatographed over a silica gel column with hexane/dichloromethane (1:1). The solution was evaporated to give a colorless crystalline solid (0.50 g, 43%).

mw = 267.14 g/mol. mp = 68 °C. IR (KBr, cm^{-1}): ν = 3036, 2922, 2851, 1581, 1483, 1452, 1239, 1193, 1104, 914, 748, 672. ^{1}H-RMN (400 MHz, $CDCl_3$, ppm) δ = 7.50 (dd, ^3J = 7.60 Hz, ^4J = 1.50 Hz, 2H, H7), 7.28 (td, ^3J = 7.60 Hz, ^4J = 1.5 Hz, 2H, H5), 7.14 (t, ^3J = 7.40 Hz, 2H, H6), 6.83 (d, ^3J = 8.00 Hz, 2H, H4), 4.73 (s, 4H, H1). $^{13}C\{^1H\}$-RMN (100 MHz, $CDCl_3$, ppm) δ = 154.9 (C3), 131.2 (C7), 130.3 (C5), 128.7 (C2), 124.1 (C6), 118.5 (C4), 41.2 (C1).

Synthesis of dibrominated compound $[\{O(C_6H_4CH_2)_2\}Br_2]$ (4a)

Dibrominated compound **4a** was synthesized according with the literature procedure [30]. To a toluene solution (30 mL) of **2a** (9.35 g, 40.6 mmol), was added dropwise HBr (15.3 mL, 142.1 mmol) dissolved in toluene (10 mL), and the resulting mixture was refluxed for 22 h. Then, saturated aqueous $NaHCO_3$ solution (20 mL) was carefully added, followed by extraction with CH_3Cl_3 (20 mL). The organic phase was separated, dried (Na_2SO_4), and evaporated to obtain a brown solid. The compound was purified by washing it with cold ethanol, to obtain a white crystalline solid (6.37 g, 44 %).

mw = 356.04 g/mol. mp = 92 °C. IR (KBr, cm^{-1}): ν = 3058, 3034, 2985, 1579, 1485, 1449, 1242, 1185, 899, 775, 605. ^{1}H-RMN (400 MHz, $CDCl_3$, ppm) δ = 7.49 (d, ^3J = 7.60 Hz, 2H, H7), 7.28 (t, ^3J = 8.00 Hz, 2H, H5), 7.13 (t, ^3J = 7.60 Hz, 2H, H6), 6.85 (d, ^3J = 9.20 Hz, 2H, H4), 4.66 (s, 4H, H1). $^{13}C\{^1H\}$-RMN (100 MHz, $CDCl_3$, ppm) δ = 154.9 (C3), 131.5 (C7), 130.3 (C5), 129.0 (C2), 124.1 (C6), 118.6 (C4), 28.2 (C1).

Synthesis of diiodo compound $[\{O(C_6H_4CH_2)_2\}I_2]$ (5a)

Preparation of **5a** was based on literature methods where the starting materials are also primary alcohols [31, 32]. Thus, KI (3.5 g, 21.0 mmol) was added to **4a** (3 g, 8.4 mmol) previously dissolved in acetone (40 mL). This mixture was refluxed for 22 h. Next, the solvent was removed in vacuo, and the residue was dispersed in CH_2Cl_2 (50 mL). The resulting precipitate was filtered off, and the solvent was removed in vacuo to yield **5a** as a brown solid (3.7 g, 97 %).

mw = 450.0 g/mol. mp = 96 °C. IR (KBr, cm^{-1}): ν = 3034, 2972, 1577, 1484, 1450, 1243, 1150, 894, 755. ^{1}H-RMN (400 MHz, $CDCl_3$, ppm) δ = 7.45 (dd, ^3J = 7.62 Hz, ^4J = 1.63 Hz, 2H, H7), 7.22 (td, ^3J = 7.69 Hz, ^4J = 1.68 Hz, 2H, H5), 7.07 (td, ^3J = 7.52 Hz, ^4J = 0.98 Hz, 2H, H6), 6.81 (d, ^3J = 8.18 Hz, 2H, H4), 4.60 (s, 4H, H1). $^{13}C\{^1H\}$-RMN (100 MHz, $CDCl_3$, ppm) δ = 154.27 (C3), 131.0 (C7), 130.4 (C5), 129.7 (C2), 124.1 (C6), 118.6 (C4), –0.03 (C1).

Synthesis of the dialdehyde $S(C_6H_4CHO)_2$ (1b)

1b was prepared in a similar way as **1a** [29]. For the formation of the dilithiated compound, we used diphenylsulfide (5.0 mL, 30 mmol), dry hexane (40 mL), TMEDA (10.4 mL, 69.0 mmol), and *n*-butyllithium in hexanes (2.5 M, 36.1 mL, 90.2 mmol). Then, this mixture was refluxed for 40 minutes forming an orange

J. Mex. Chem. Soc. **2024**, *68*(2)
Regular Issue

ISSN-e 2594-0317

solution. The reaction was cooled down to 25 °C before dry DMF (8.1 mL, 105 mmol) was poured dropwise into the reaction mixture. The white solution was stirred for 1 h. Aqueous hydrochloric acid (30 mL HCl in 60 mL of distilled water) was added, and the mixture was stirred for fifteen minutes, followed by extraction with CH_3Cl (30 mL). The combined organic phases were dried (Na_2SO_4), and the volatiles were removed under reduced pressure to yield the **1b** as a brown viscous liquid (6.5 g, 90 %).

mw = 242.29 g/mol. IR (KBr, cm^{-1}): ν = 3059, 2850, 2738, 1688, 1584, 1458, 1440, 1259, 1198, 1040, 845, 822, 747. ^{1}H-RMN (400 MHz, $CDCl_3$, ppm) δ = 10.34 (s, 2H, H1), 7.95 (d, ^3J = 7.42 Hz, 2H, H7), 7.47 (m, 4H, H5), 7.16 (d, ^3J = 7.68 Hz, 2H, H6). ^{13}C{^{1}H}-RMN (100 MHz, $CDCl_3$, ppm) δ = 191.7 (C1), 138.7 (C3), 135.1 (C2), 134.8 (C4), 132.7 (C7), 131.9 (C5), 128.0 (C6).

Synthesis of the diol $S(C_6H_4CH_2OH)_2$ (2b)

2b was prepared in a similar was as the **2a** compound. **1b** (6.5 g, 27 mmol), ethanol (40 mL), $Na[BH_4]$ (2.45 g, 64.8 mmol), diluted HCl (10 mL HCl in 20 mL of distilled water), CH_2Cl_2 (40 mL), brine (60 mL). The product was a yellow viscous liquid (6.6 g, 99 %).

mw = 246.32 g/mol. IR (KBr, cm^{-1}): ν = 3376, 3283, 3057, 2884, 1613, 1442, 1198, 1031, 747. ^{1}H-RMN (400 MHz, $CDCl_3$, ppm) δ = 7.45 (dd, ^3J = 7.50 Hz, ^4J = 0.82 Hz, 2H, H7), 7.27 (td, ^3J = 7.37 Hz, ^4J = 1.38 Hz, 2H, H6), 7.18 (td, ^3J = 7.30 Hz, ^4J = 1.54 Hz, 2H, H5), 7.12 (dd, ^3J = 7.73 Hz, ^4J = 1.28 Hz, 2H, H4), 4.72 (s, 4H, H1), 2.92 (s, 2H, O<u>H</u>). ^{13}C{^{1}H}-RMN (100 MHz, $CDCl_3$, ppm) δ = 141.3 (C3), 133.3 (C2), 132.2 (C4), 128.8 (C7), 128.6 (C5), 127.9 (C6), 63.4 (C1).

Synthesis of the dichlorinated compound [{$S(C_6H_4CH_2)_2$}Cl_2] (3b)

3b was prepared in a similar was as **3a**. **2b** (1.5 g, 6.2 mmol), carbon tetrachloride (20 mL), triphenylphosphine (3.6 g, 13.6 mmol). The yellow solution was chromatographed over a silica gel column with hexane/dichloromethane (1:1). The compound is a yellow liquid (0.77 g, 44 %).

mw = 267.14 g/mol. IR (KBr, cm^{-1}): ν = 3057, 2956, 2850, 1589, 1468, 1440, 1263, 1205, 1041, 821, 736, 666. ^{1}H-RMN (400 MHz, $CDCl_3$, ppm) δ = 7.51 (dd, ^3J = 7.50 Hz, ^4J = 1.10 Hz, 2H, H7), 7.30 (td, ^3J = 7.80 Hz, ^4J = 1.30 Hz, 2H, H6), 7.24 (td, ^3J = 7.40 Hz, ^4J = 1.30 Hz, 2H, H5), 7.16 (dd, ^3J = 7.71 Hz, ^4J = 0.90 Hz, 2H, H4), 4.79 (s, 4H, H1). ^{13}C{^{1}H}-RMN (100 MHz, $CDCl_3$, ppm) δ = 138.2 (C3), 135.0 (C2), 132.9 (C4), 130.7 (C7), 129.7 (C5), 128.2 (C6), 44.5 (C1)

Synthesis of dibrominated compound [{$S(C_6H_4CH_2)_2$}Br_2] (4b)

Dibrominated compound **4b** was synthesized according with the literature process [30]. To a toluene solution (20 mL) of diol **2b** (6.6 g, 26.79 mmol) was added dropwise HBr (10.8 mL, 93.76 mmol) dissolved in toluene (10 mL) and the resulting mixture was stirred for 22 h at reflux temperature. Then saturated aqueous $NaHCO_3$ solution (20 mL) was added carefully, followed by extraction with CH_3Cl (20 mL). The organic phase was separated, dried (Na_2SO_4) and evaporated to obtain a brown liquid. For the purification of the compound **4b**, a chromatographic column of the crude reaction is carried out, using silica as stationary phase and dichloromethane as eluent. From the purification a light-yellow viscous liquid was obtained, to crystallize the product were seeded crystals (2.5 g, 25 %).

mw = 372.11 g/mol. mp = 71 °C. IR (KBr, cm^{-1}): ν = 3051, 2973, 1563, 1469, 1440, 1218, 1038, 764, 730, 606. ^{1}H-RMN (400 MHz, $CDCl_3$, ppm) δ = 7.47 (dd, ^3J = 7.54 Hz, ^4J = 1.35 Hz, 2H, H7), 7.27 (td, ^3J = 7.07 Hz, ^4J = 1.55 Hz, 2H, H6), 7.22 (td, ^3J = 7.26 Hz, ^4J = 1.46 Hz, 2H, H5), 7.16 (dd, ^3J = 7.71 Hz, ^4J = 1.35 Hz, 2H, H4), 4.71 (s, 4H, H1). ^{13}C{^{1}H}-RMN (100 MHz, $CDCl_3$, ppm) δ = 138.5 (C3), 135.2 (C2), 133.1 (C4), 131.2 (C7), 129.7 (C5), 128.2 (C6), 31.8 (C1).

Synthesis of diiodo compound [{$S(C_6H_4CH_2)_2$}I_2] (5b)

Preparation of the title compounds was based on literature methods [31,32]. KI (1.12 g, 6.72 mmol) was added to **4b** (1.0 g, 2.69 mmol) dissolved in acetone (25 mL). This mixture was heated to reflux for 22 h. After the solvent was removed in vacuo, the residue was dispersed in CH_2Cl_2 (30 mL). The resulting precipitate was filtered off, and the solvent was removed in vacuo to yield the desired diiodo **5b** as a brown solid (1.23 g, 98 %).

mw = 466.10 g/mol. mp = 101 °C. IR (KBr, cm^{-1}): ν = 3043, 2929, 1557, 1470, 1437, 1206, 1151, 1030, 755. ^{1}H-RMN (400 MHz, $CDCl_3$, ppm) δ =7.45 (dd, ^3J = 7.56 Hz, ^4J = 1.51 Hz, 2H, H7), 7.22 (td, ^3J =

J. Mex. Chem. Soc. **2024**, *68*(2)
Regular Issue

ISSN-e 2594-0317

7.38 Hz, ^4J = 1.55 Hz, 2H, H6), 7.17 (td, ^3J = 7.49 Hz, ^4J = 1.56 Hz, 2H, H5), 7.11 (dd, ^3J = 7.70 Hz, ^4J =1.47 Hz, 2H, H4), 4.64 (s, 4H, H1). $^{13}C\{^1H\}$-RMN (100 MHz, $CDCl_3$, ppm) δ = 139.9 (C3), 134.3 (C2), 133.1 (C4), 130.7 (C7), 129.2 (C5), 128.3 (C6), 4.11 (C1).

Results and discussion

Synthesis

The overall linear synthesis of the respective diol compounds **Ch**$(C_6H_4CH_2$**OH**$)_2$ were based on a regioselective double-lithiation of the corresponding diphenyl(thio)ether, followed by a formylation reaction with DMF *in situ*; then a reduction of the resulting –CHO groups was carried out. Afterwards, the synthesis of the dichloro compounds **3a** and **3b** was carried out under Appel conditions, by using carbon tetrachloride and triphenylphosphine [33,34]. Dibrominated compounds **4a** and **4b** were obtained from a substitution reaction of the hydroxyl groups, by using Br^- as a nucleophile. Finally, the Br-by-I halide exchange to obtain **5a** and **5b** was achieved with an excess of potassium iodide in acetone, by using **4a** and **4b** as starting materials.

NMR analysis

NMR spectra of all compounds were recorded in $CDCl_3$ solutions at 25 °C; the assignment of the signals was carried out by the heteronuclear and homonuclear correlation of two-dimensional experiments (COSY, HSQC and HMBC). The signals of the aromatic protons of the ligand framework were observed as an ABCD pattern. In ^{13}C-NMR, six signals are observed for the different aromatic carbons; the signal found in higher frequency correspond to the carbons directly bonded to the heteroatom, due to the electron-withdrawing effect. This effect is more noticeable when **Ch** = O due to its higher electronegativity compared to the sulfur atom. On the other hand, the $–CH_2–$ signals for both series of compounds (**Ch** = O, S) were used to monitoring that the chemical transformations were successful. The changes of these signals are clearly noticeable on ^{13}C-NMR. Thus, when the carbon atom corresponds to the CHO functional group, the signal is around 190 ppm, and when the reduction reaction is carried out for its transformation into the $–CH_2–$OH group, the carbon signal shifts ca. 60 ppm low-frequency. Then, the carbon resonances for $–CH_2–$**X** were observed at 41.2, 28.2, 44.5, and 31.8 ppm for **3a**, **4a**, **3b**, and **4b**, respectively; when the halogen exchange occurs to obtain $–CH_2–$I, a considerable change in the displacement of these carbons towards frequencies close to 0 ppm was observed, this due to the electro-donating effect exerted by the iodine atom.

X-Ray single crystal analysis

Molecular structures of Ch$(C_6H_4CH_2X)_2$

There are some general features in the structural data of the **3a**–**5a** diphenylether and **4b** and **5b** diphenylthioether corresponding sets. In all compounds, the C_{sp2}–**Ch** and C_{sp3}–**X** bond distances are comparable to the covalent radii sum [$\Sigma r_{cov}(C_{sp2}, O)$ = 1.39 Å; $\Sigma r_{cov}(C_{sp2}, S)$ = 1.78 Å; $\Sigma r_{cov}(C_{sp3}, Cl)$ = 1.78 Å; $\Sigma r_{cov}(C_{sp3}, Br)$ = 1.96 Å; $\Sigma r_{cov}(C_{sp3}, I)$ = 2.15 Å][35]. Also, the C–**Ch**–C angles are practically equal in each set, being the C–O–C angle the wider one. The difference in C–**Ch**–C angles is the expected; this bond angle decreases as the atomic number of the chalcogen atom (**Ch**) increases, as has been discussed by Prof. Gillespie for several compounds of the ***p***-block, where the central atom has unshared lone pairs. [36] To analyze the conformations of the compounds in each set, we overlayed each pair of molecules (Figures 3 and 4). We used the Mercury 4.0 software [37] to calculate the root mean square deviation (RMSD) and the maximum deviation data in these superimpositions. Thus, we observed striking differences in the conformation of the diphenylether derivatives **3a**–**5a** in the solid state, despite the similitude of their skeletal structures. Firstly, the conformations of **3a** and **4a** are very similar (RMSD = 0.154 Å), regardless of their different crystalline systems and space groups (vide infra). The main conformational difference of this pair in comparison with **5a** lays on the direction of the C–**X** bonds; in **3a** (**X** = Cl) and **4a** (**X** = Br), the halogen atoms are pointed to opposite sides, while in the diiodo compound, the C–I bonds are oriented to the same side. For the diphenylthioethers **3b** and **4b**, the conformations are essentially the same (RMSD = 0.064 Å, with a maximum deviation of 0.154 Å, mainly due to the expected difference in C–**X** bond lengths). In these compounds, the halogen atoms are also pointed to opposite sides. We

J. Mex. Chem. Soc. **2024**, *68*(2)
Regular Issue

ISSN-e 2594-0317

also analyzed the C2–C3–**Ch**–C10 and C9–C10–**Ch**–C3 torsion angles. As a result, excepting the data for **5a**, the difference of these angles ($|\Delta_{ta}|$) is lesser than 10.3°, indicating a practically two-fold rotational symmetry (in fact, **4a** displays a perfect C_2 axis that bisects the C–O–C bond angle, with an obviously null difference in torsion angles). On the other hand, **5a** shows a difference of 76.7° that is consistent with an almost orthogonal arrangement of both phenyl rings around the C–O–C plane.

Crystal arrangement of Ch($C_6H_4CH_2X)_2$ derivatives

The chloro derivative **3a** crystallized in the triclinic system, while **4a** and **5a** pair crystallized in the monoclinic system, but in different space groups. On the other hand, both diphenylthioether compounds **4b** and **5b**, besides to be isostructural, they are also isomorphic, crystallizing in the centrosymmetric triclinic system, with a higher cell volume in **5b** due to the larger size of the iodine atoms. In all **Ch**($C_6H_4CH_2$**X**)$_2$ derivatives, notwithstanding the different nature of either **Ch** or **X** atoms, were observed non-classical C–H···**X** hydrogen bonding as well as p-interactions that contributes to the cohesion of the crystal (Fig. 5).

In the Fig. 5 we plotted a portion of the crystal structure where the molecules were related by their symmetry operators and, for the sake of comparison, we highlighted the C–H···**X** hydrogen bonding around the **X** atom in the asymmetric unit. In all plots, the asymmetric unit is displayed in gray color; the other colors are used for moieties related by other symmetry operation, such as inversion (in yellow) or, in the case of **4a**, rotation, rotation-inversion (both in green), and gliding (in magenta). The tagged distances of the intermolecular contacts and the symmetry operators for all compounds are summarized in Table 3. For **4a**, the asymmetric unit is just the half, with the oxygen atom positioned on a two-fold axis; the other half is generated by the corresponding two-fold rotation. As commented, **4b** and **5b** were isomorphic and, for conciseness, we just graph the structure of the iodo derivative. To build all the plots showed, we considered intermolecular H···**X** contacts smaller than 3.6 Å. From the plots, the number of contacts in the diphenylether derivatives decreases in the order **3a**>**4a**>**5a**; the magnitude of the distances must also decrease but in the inverse order because of the different atom sizes. On the other hand, the number of intermolecular interactions is the same in the diphenylthioethers **4b** and **5b**, as can be expected, because of their isomorphism.

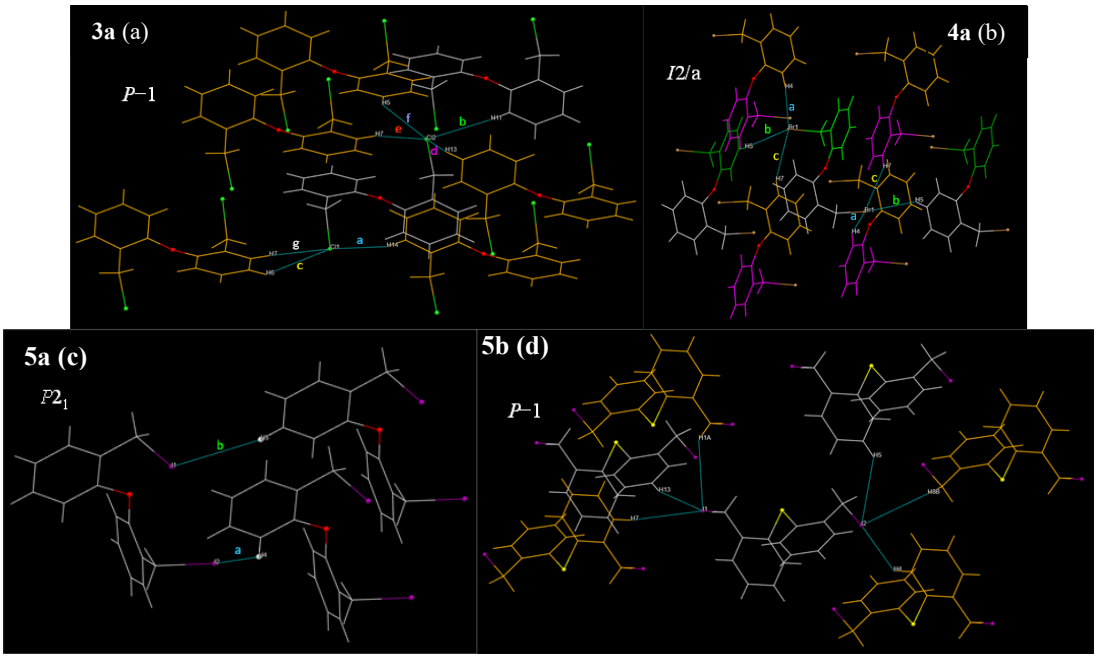

Fig. 5. C–H···**X** hydrogen bonding in **Ch**($C_6H_4CH_2$**X**)$_2$ derivatives (colours are used to highlight the symmetry operation involved in the generation of symmetry-related moieties; see text).

J. Mex. Chem. Soc. **2024**, *68*(2)
Regular Issue

ISSN-e 2594-0317

Table 3. Structural data of C–H···X hydrogen bonding in **Ch**($C_6H_4CH_2$**X**)$_2$ derivatives and symmetry operators.

tag	3a	4a	5a	4b	5b
a	2.918; C–H14···Cl1 1−x, 1−y, 1−z	3.047; C–H4···Br1 x, 1/2−y, −1/2+z	3.358; C–H4···I2 −1+x, y, z	3.160; C–H4···Br2 −1+x, y, z	3.239; C–H4···I2 1−x, 1−y, 1−z
b	3.106; C–H11···Cl2 −1+x, y, z	3.186; C–H5···Br1 −1/2+x, −1/2+y, −1/2+z	3.371; C–H5···I1 −1+x, 1+y, z	3.302; C–H13···Br1 x, y, −1+z	3.329; C–H13···I1 x, y, −1+z
c	3.108; C–H6···Cl1 2−x, 1−y, 2−z	3.207; C–H7···Br1 −1/2+x, 1−y, z	Not applicable	3.333; C–H5···Br2 x, y, −1+z	3.372; C–H5···I2 −1+x, y, z
d	3.130; C–H13···Cl2 1−x, −y, 1−z	Not applicable	Not applicable	3.374; C–H7···Br1 2−x, 2−y, −z	3.574; C–H7···I1 2−x, 2−y, −z
e	3.132; C–H7···Cl2 1−x, 1−y, 2−z	Not applicable	Not applicable	3.454; C–H8B···Br2 −x, 1−y, 1−z	3.582; C–H8B···I2 −x, 1−y, 1−z
f	3.181; C–H5···Cl2 1−x, −y, 2−z	Not applicable	Not applicable	3.469; C–H1A···Br1 1−x, 2−y, −z	3.499; C–H1A···I1 1−x, 2−y, −z
g	3.254; C–H7···Cl1 2−x, 1−y, 2−z	Not applicable	Not applicable	Not applicable	Not applicable

Hirshfeld surface analysis

The Hirshfeld surface (HS) encloses either a molecule or a cluster of molecules, and its corresponding 2D-fingerprint is unique for a given compound, therefore, the construction of this type of surfaces makes them a useful approach to compare crystal structures [23]. The surfaces based on the d_{norm} of all **Ch**($C_6H_4CH_2$**X**)$_2$ compounds clearly exhibit red spots in the vicinity of the **X** substituents, corresponding to the presence of close contacts due to C–H···**X** non-classical hydrogen bonding, i.e., contact distances that are shorter than the van der Waals radii sum [**3a**(1), **4a**(1), **5a**(1), **4b**(1), and **5b**(1) plots] in Fig. 6. The fragment patch plots are useful to calculate the number of molecules that interacts with a central one; also, the area data of these patches can be used to find the external major molecular fragments that are closer to a HS given. In Fig. 6 are plotted the corresponding fragment patches over the HS [**3a**(2), **4a**(2), **5a**(2), **4b**(2), and **5b**(2) plots]. In the O($C_6H_4CH_2$**X**)$_2$ compounds, the number of interacting molecules is 15, 20, and 16, for **3a**, **4a**, and **5a**, respectively (we considered a radius of 4.10 Å as an atom---atom distance, instead of the default value of 3.80 Å in CrystalExplorer). The four larger areas over the HS surface are 52.5, 43.0, 35.6, and 21.7 Å^2 for **3a** (52.5 % superficial area); 52.7, 51.6, 42.0, and 42.0 Å^2 for **4a** (63.0 % superficial area); and 63.6, 61.5, 29.9, and 20.3 Å^2 for **5a** (57.0 % superficial area). For the isomorphic **4b** and **5b** there are 16 molecules around the HS in each one; the larger areas are 52.5, 47.8, 44.5, and 44.1 Å^2 for **4b** (62.2 % superficial area); and 55.0, 48.4, 47.3, and 43.5 Å^2 for **5b** (61.7 % superficial area). Overall, four interacting molecules cover more than 52 % of each corresponding HS, despite their different surrounding number (see above).

J. Mex. Chem. Soc. **2024**, *68*(2)
Regular Issue

ISSN-e 2594-0317

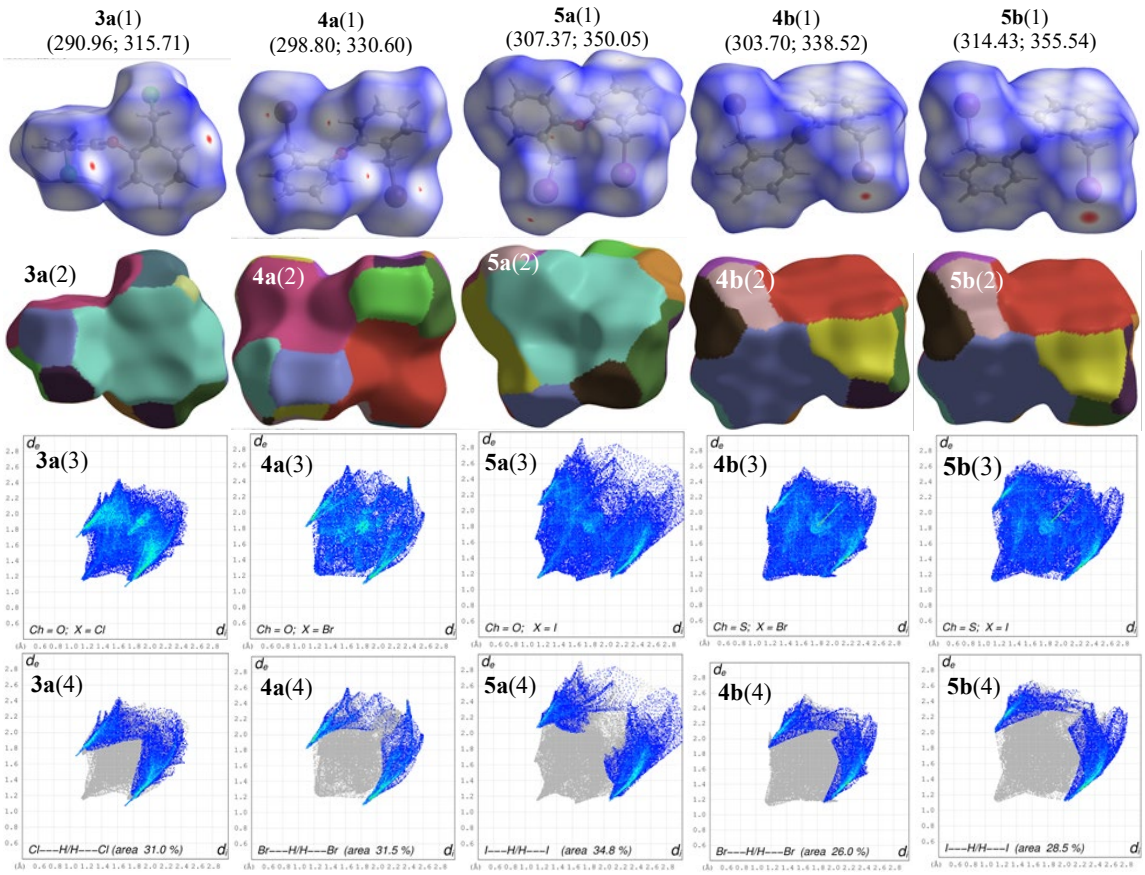

Fig. 6. Hirshfeld surfaces mapped over d_{norm}, fragment patches, and fingerprint plots for **Ch**($C_6H_4CH_2$**X**)$_2$ (**Ch** = O, S; **X** = Cl, Br, I) compounds (data in parentheses are superficial area in Å^2 and volume in Å^3).

To evaluate the contribution of the intermolecular contacts we plotted the 2D-fingerprints of the corresponding Hirshfeld surfaces [**3a**(3), **4a**(3), **5a**(3), **4b**(3), and **5b**(3) plots]. For the sake of comparison, we decomposed the corresponding overall 2D fingerprints plots in their **X**···H/H···**X** [**X** = Cl, Br, I; **3a**(4), **4a**(4), **5a**(4), **4b**(4), and **5b**(4) plots in Fig. 7] fingerprint plots for all compounds. We also plot the contribution of all contacts by means of a stacked bar chart, where we consider the reciprocal ones. The analysis of the intermolecular contact contributions for all compounds showed that H···H contacts are dominant, from 43.6 to 37.7 % contribution (Fig. 7). The next predominant non-covalent contributions are the **X**···H/H···**X** non-classic hydrogen bonding (green bars); we observed that compounds with **Ch** = O display higher values, probably due to the higher electronegativity of the oxygen atom in **3a**-**5a** when compared to the sulfur atom in **4b** and **5b**. To finish, the C···H/H···C (black bars) also display significant contributions due to the presence of the aromatic rings, which ones enhance C–H···pi as well as pi···pi interactions.

J. Mex. Chem. Soc. **2024**, *68*(2)
Regular Issue

ISSN-e 2594-0317

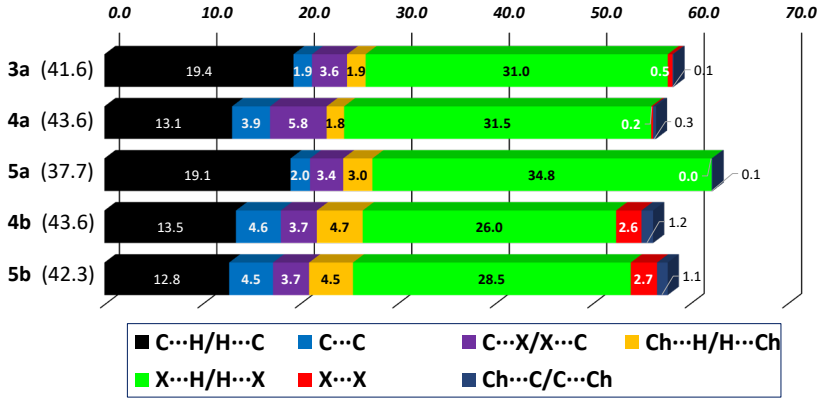

Fig. 7. Relative contributions in percentage of various intermolecular contacts of **Ch**($C_6H_4CH_2$**X**)$_2$ (**Ch** = O, S; **X** = Cl, Br, I) molecular crystals (H···H contacts are in parentheses).

A deeper analysis indicated that **4a** displayed a high C···Br/Br···C contribution (5.8 %, purple bar) in a centrosymmetric arrangement, and the isomorphic **4b**/**5b** pair displayed **X**···**X** notable contributions (red bars). In the first case, **4a** displayed C–Br···pi interactions alongside with other two C–H···Br interactions; the distance from this bromo atom to the centroid of the three C4, C5, and C6 aromatic atoms is 3.801 Å that is longer than the van der Waals radii sum [Σr_{vdW}(C, Br) = 3.55 Å]. The analysis of their Hirshfeld surfaces decorated with the molecular electrostatic potential (MEP) showed that the centrosymmetric arrangement of two molecules effectively displayed complementary interactions (see Fig. 8). The bromo atom in the C–Br bond display at its σ-hole position a positive potential (5.96 kcal/mol, in blue colour), while the three C(4), C(5), and C(6) aromatic atoms display a complementary negative potential (7.03 kcal/mol, in red colour) that is indicative of a C–Br···pi interaction of attractive nature. Something similar is observed for the C–H(4)···Br interaction, where the negative belt around the Br atom is displaying a negative potential (−15.06 kcal/mol, in red colour); as expected, the hydrogen atom in the C–H(4) bond has a positive potential (14.62 kcal/mol, in blue colour).

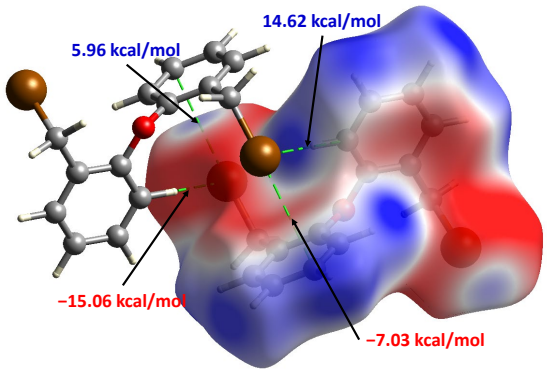

Fig. 8. Views of calculated electrostatic potential mapped on the Hirshfeld surface of **4a** showing the potential at the points of contact for Br···pi and C–H···Br noncovalent interactions.

Finally, as has been commented, the isomorphic **4b**/**5b** pair displayed **X**···**X** interactions (**X** = Br, I). In Fig. 9 we show the corresponding Hirshfeld surfaces decorated with the MEP to highlight just these interactions. In the front and rear plots, it is worth mentioning that there are differences in the positions of the head black arrow and the dashed lines that specify the shortest **X**···**X** interatomic distances intersecting the HS

J. Mex. Chem. Soc. **2024**, *68*(2)
Regular Issue

ISSN-e 2594-0317

decorated with the MEP. These positions are different because of we took the potential energy data from the intersection of the surface with the straight line coming from either outer or inner C–**X** bond, since in this position is where the s-hole is located. Each compound displays both complementary positive and negative potentials; the C–Br(1) and C–I(1) inner bonds display positive potentials of 7.53 and 11.61 kcal/mol for **4b** and **5b**, respectively (in blue color) while the matching negative potentials are −8.22 and −11.23 kcal/mol (in red color). Also, in the rear plots we show other positive potentials of 7.65 and 15.19 kcal/mol that match with the C(12) and C(13) benzenic carbons, similar to that observed in **4a**.

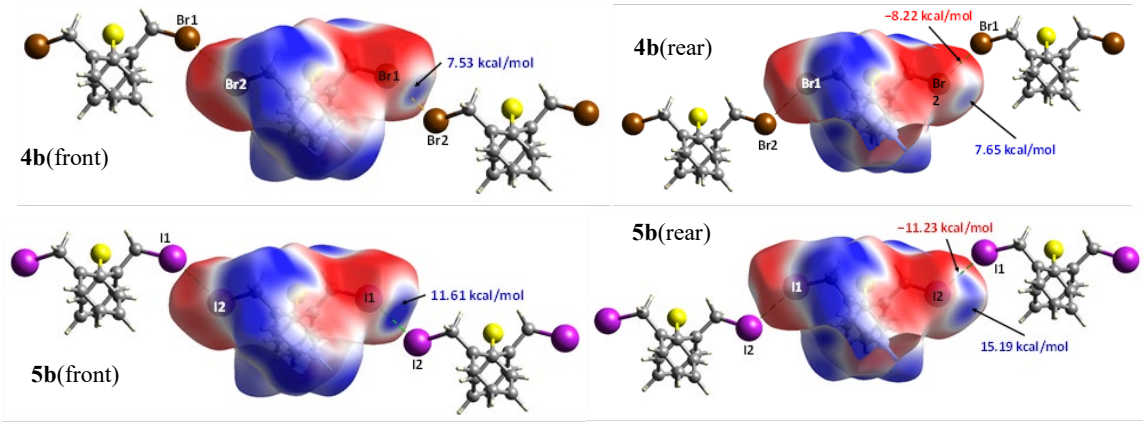

Fig. 9. Views of calculated electrostatic potential mapped on the Hirshfeld surface of **4b** and **5b** showing the potential at the points of contact for C–**X**···**X**–C (**X** = Br, I) noncovalent interactions.

Conclusions

Two series of dihalogenated compounds of general formula **Ch**($C_6H_4CH_2$**X**)$_2$ were synthetized by a linear approach from either cheap diphenylether or diphenylthioether used as starting materials. Despite the similitude in the skeletal structure, all compounds based on the ether framework displayed different interactions in the crystal arrangement. On the other hand, the thioether compounds were isostructural and isomorphic and, in these two cases we observed that the bromo- and iodo compounds were more susceptible to form **X**···**X** interactions and displayed little disposition to form **X**···H hydrogen bonding, due to the presence of the less electronegative sulfur atom as compared with the oxygen ones in the diphenylethers.

Acknowledgements

JVGG fully acknowledges the scholarship from CONACYT (ID 791450). This research was supported by project A1-S-12381 (CONACYT). CGGP acknowledges the financial assistant support from the same project (ID DIDI-DI- BECA-001).

References

1. Dean, J. A., in: *Lange's Handbook of Chemistry* (15th Edition), McGraw-Hill Education, New York, **1999**, 330.
2. Häggblom, M. M.; Bossert, I. D., in: *Halogenated Organic Compounds - A Global Perspective. In Dehalogenation.* Springer, Boston, MA, **2004**, 3-29. DOI: https://doi.org/10.1007/0-306-48011-5_1.

J. Mex. Chem. Soc. **2024**, *68*(2)
Regular Issue

ISSN-e 2594-0317

3. Patai S., Rappoport Z., in: *Halides, Pseudo-Halides and Azides*; *Part 1 and Part 2 in The Chemistry of Functional Groups*, John Wiley & Sons Ltd, **1983**, 1-223. DOI:10.1002/9780470771716.
4. Anderson B. M., Meyers R. A.; in: *Halogen Chemistry*. *In Encyclopedia of Physical Science and Technology* (Third Edition), Academic Press, Elsevier, **2003**, 197-222. DOI: https://doi.org/10.1016/B0-12-227410-5/00307-0.
5. Smolnikov, S.; Bin Shahari, M.; Dolzhenko, in: *Green sustainable process for chemical and environmental engineering and science: A. Sonochemical protocols for Grignard reactions*. Elsevier, **2020**, 243-255. DOI: 10.1016/B978-0-12-819540-6.00009-7.
6. Odd Hassel – Nobel Lecture. NobelPrize.org. Nobel Prize Outreach AB 2023. Sun. 19 Mar 2023. https://www.nobelprize.org/prizes/chemistry/1969/hassel/lecture/
7. Desiraju, G. R.; Ho, P. S.; Kloo, L. Legon, A. C.; Marquardt, R.; Metrangolo, P.; Politzer, P.; Resnati, G.; Rissanen, K. *Pure Appl. Chem.* **2013**, *85*, 1711–1713. DOI: http://dx.doi.org/10.1351/PAC-REC-12-05-10.
8. Cavallo, G.; Metrangolo, P.; Milani, R.: Pilati, T.; Priimagi, A.; Resnati, G. Terraneo, G. *Chem. Rev.* **2016**, *116*, 2478-2601. DOI: https://pubs.acs.org/doi/10.1021/acs.chemrev.5b00484.
9. Metrangolo, P.; Neukirch, H. Pilati, T.; Resnati, G. *J. Am. Chem. Soc.* **2005**, *38*, 386–395. DOI: https://doi.org/10.1021/ar0400995.
10. Sutar, R. L.; Huber, S. M. *J. Am. Chem. Soc.* **2019**, *9*, 9622–9639. DOI: https://doi.org/10.1021/acscatal.9b02894.
11. Ding, X., Tuikka, M.; Haukka, M., in: *Halogen Bonding in Crystal Engineering: Recent Advances in Crystallography*, IntechOpen, **2012**, 143-168. DOI: https://doi.org/10.5772/48592.
12. Nunzi, F.; Cesario, D.; Tarantelli, F.; Belpassi, L. *Chem. Phys. Lett*. **2021**, *771*, 138522. DOI: https://doi.org/10.1016/j.cplett.2021.138522.
13. Prasanna, M.D.; Guru Row, T.N. *Cryst. Eng.* **2000**, *3*, 135-154. DOI: https://doi.org/10.1016/S1463-0184(00)00035-6.
14. Zhao-Qi, G.; Shi-Hui, Q.; Huan-Hui, Y.; Shan-Chao, W.; Meng, Z.; Gui-Mei, T.; Yong-Tao, W.; Tao, A.; Seik-Weng N. *J. Mol. Struct.* **2022**, *1267*, 133606. DOI: https://doi.org/10.1016/j.molstruc.2022.133606.
15. Mejia-Rivera, F. J.; Alvarado-Rodríguez, J. G.; Andrade-López, N.; Cruz-Borbolla, J.; Jancik, V. *Inorg. Chem. Commun.* **2018**, *97*, 44-48. DOI: https://doi.org/10.1016/j.inoche.2018.09.006.
16. Nather, C.; Jess, I.; Kus, P.; Jones, P.G. *Cryst. Eng. Comm.* **2016**, *18*, 3142
17. Xu, X.; Strongin, R.M.; Fronczek, F.R. *CSD Communication (Private Communication),* **2015**.
18. Oxford Diffraction CrysAlis software system, version 1.171.37.35. Oxford Diffraction Ltd., Abingdon, UK (**2014**)
19. Dolomanov, O.V.; Bourhis, L.J.; Gildea, R.J.; Howard, J.A.K.; Puschmann H. J. *Appl. Cryst.* **2009**, *42*, 339–341.
20. Sheldrick, G.M. *Acta Cryst. A.* **2015***, 71*, 3–8.
21. Sheldrick, G.M. *Acta Cryst. C.* **2015**, *71*, 3–8.
22. Spackman, M.A.; Jayatilaka, D. *CrystEngComm*. **2009**, *11*, 19–32
23. Spackman, P.R.; Turner, M.J.; McKinnon, J.J.; Wolff, S.K.; Grimwood, D.J.; Jayatilaka, D.; Spackman, M.A. *J. Appl. Cryst.* **2021**, *54*,1006–1011.
24. Jayatilaka, D.; Grimwood D.J. *Comput. Sci. ICCS*, **2003**, *4*, 142–151.
25. Becke A.D. *J. Chem. Phys.* **1993**, *98*, 5648–5652
26. Godbout, N.; Salahub, D. R.; Andzelm J.; Wimmer Can, E. *J. Chem.* **1992**, *70*, 560–571.
27. Sosa, C.; Andzelm, J.; Elkin, B.C.; Wimmer, E.; Dobbs, K.D.; Dixon D.A. *J. Phys. Chem.* **1992**, *96*, 6630–6636.
28. Osuka, A.; Kobayashi, F.; Maruyama, K. *Bull. Chem. Soc. Jpn.* **1991***, 64*, 1213-1225. DOI: https://doi.org/10.1246/bcsj.64.1213.

J. Mex. Chem. Soc. **2024**, *68*(2)
Regular Issue

ISSN-e 2594-0317

29. Britovsek, G. J. P.; Gibson, V. C.; Hoarau, O. D.; Spitzmesser, S. K.; White, A. J. P.; Williams, D. J. *Inorg. Chem.* **2003**, *42*, 3454-3465. DOI: https://doi.org/10.1021/ic034040.
30. Martínez-Otero, D.; Alvarado-Rodríguez, J. G.; Cruz-Borbolla, J.; Andrade-López, N.; Pandiyan, T.; Moreno-Esparza, R.; Flores-Alamo, M.; Cantillo-Castillo J. *Polyhedron.* **2012**, *33*, 367-377. DOI: https://doi.org/10.1016/j.poly.2011.11.053.
31. Kida, T.; Kikuzawa, A.; Higashimoto, H.; Nakatsuji, Y.; Akashi, M. *Tetrahedron*. **2005**, *61*, 5763–5768. DOI: https://doi.org/10.1016/j.tet.2005.04.026.
32. McAdam, C.J.; Hanton, L.R.; Moratti, S.C.; Simpson*, J. Acta Crystallogr. E: Crystallogr. Commun*. **2015**, *71*, 1505-1509. DOI: 10.1107/S2056989015021295.
33. Appel, R. *Angew. Chem. Int. Ed. Engl.* **1975**, *14*, 801-811. DOI: https://doi.org/10.1002/anie.197508011.
34. Cristol, S. J.; Strom, R. M.; Stull, D. P., *J. Org. Chem*. **1978**, *43*, 1150. DOI: https://doi.org/10.1021/jo00400a027.
35. Cordero, B.; Gómez, V.; Platero-Prats, A. E.; Revés, M.; J. Echeverría, J., Cremades, E.; Barragán F.; Alvarez, S. *Dalton Trans*. **2008**, *21*, 2832-2838. DOI: https://doi.org/10.1039/B801115J.
36. Gillespie, R.J. Popelier, P.L.A., in: *Chemical Bonding and Molecular Geometry; From Lewis to Electron densities.* Oxford University Press, New York, **2001**, 84. DOI: 10.1021/ed080p31.
37. Macrae, C. F.; Sovago, I.; Cottrell, S. J.; Galek, P. T. A.; McCabe, P.; Pidcock, E.; Platings, M.; Shields, G. P.; Stevens, J. S.; Towler, M.; Wood, P. A. *J. Appl. Cryst.* **2020**, 53, 226-236. DOI: https://scripts.iucr.org/cgi-bin/paper?gj5232.

Article

J. Mex. Chem. Soc. **2024**, *68*(2)
Regular Issue

ISSN-e 2594-0317

Development of a Composite Cu(II)-Selective Potentiometric Sensor Based on a Thiourea Derivative Symmetric Schiff Base

Ozden Yildirim[1], Fatih Coldur[2]*, Cihan Topcu[3], Bulent Caglar[2]

[1]Graduate School of Natural and Applied Sciences, Erzincan Binali Yildirim University, 24100, Erzincan, Turkey.
[2]Department of Chemistry, Faculty of Arts and Sciences, Erzincan Binali Yildirim University, 24100 Erzincan, Turkey.
[3]Department of Biomedical Engineering, Faculty of Engineering, Samsun University, 55420 Ondokuzmayis, Samsun, Turkey.

***Corresponding author:** Fatih Coldur*, e-mail: fatihcoldur@hotmail.com

Received October 5th, 2022; Accepted July 5th, 2023.

DOI: http://dx.doi.org/10.29356/jmcs.v68i2.1884

Abstract. In the present study, initially, a thiourea derivative symmetric Schiff base, (1E,3E)-1,3-bis(5-bromo-2-hydroxybenzylidene)thiourea, was synthesized and characterized by FTIR and SEM-EDX analysis. In addition, an all-solid-state composite Cu(II)-selective potentiometric sensor based on this synthesized compound as an electroactive substance was constructed. Optimization studies indicated that the composition of the optimum sensing composite exhibiting the best potentiometric characteristics was 3.0% Schiff base, 5.0 % multi-walled carbon nanotube (MWCNT), 20.0 % paraffin oil and 72.0% graphite by mass. The proposed sensor displayed a linear response in the concentration range of 5.0×10^{-6}-1.0×10^{-1} M with a slope of 31.1 mV/decade and a detection limit of 5.0×10^{-7} M. The proposed sensor exhibited a fairly selective, stable (potential drift: 1.85 mV/h), and rapid (<10 s) response towards Cu(II) ions. Because of the magnitude of its potential drift, the sensor should be recalibrated along the analysis time at least half an hour apart. The sensor can employed safely in the samples with pHs in the range of 2.0-6.5. The lifetime of the fresh sensor surface was determined as 2 weeks. The most important advantage of the sensor is that the sensing composite surface is renewable (at least 10 times) and thus the sensor can be used many times for a long period of time. The analytical applications of the sensor were executed successfully by using the electrode in the potentiometric titration of Cu(II) ions with EDTA as an indicator electrode, in the direct determination of Cu(II) contents of spiked water samples, and in the determination of (w/w) Cu% content of a Turkish coin.
Keywords: Potentiometric sensor; copper(II)-selective electrode; all-solid-state sensor; copper(II) determination; symmetric Schiff base, thiourea derivative.

Resumen. En este estudio, inicialmente, se sintetizó una base de Schiff simétrica derivada de la tiourea, (1E,3E)-1,3-bis(5-bromo-2-hidroxibenciliden)tiourea, y se caracterizó mediante análisis FTIR y SEM-EDX. Además, se construyó un sensor potenciométrico selectivo de Cu(II) de estado sólido basado en este compuesto sintetizado como sustancia electroactiva. Los estudios de optimización indicaron que la composición del compuesto sensor óptimo que presentaba las mejores características potenciométricas fue con 3 % de base de Schiff, 5 % de nanotubos de carbono multipared (MWCNT), 20 % de aceite de parafina y 72 % de grafito en masa. El sensor propuesto mostró una respuesta lineal en el rango de concentración de 5×10-6 a 1×10-1 M con una pendiente de 31 mV/década y un límite de detección de 5×10-7 M. El sensor propuesto mostró una respuesta bastante selectiva, estable (deriva de potencial: 1.85 mV/h) y rápida (<10 s) hacia los iones Cu(II). Debido a la magnitud de su deriva de potencial, el sensor debe recalibrarse a lo largo del tiempo de análisis con un intervalo

J. Mex. Chem. Soc. **2024**, *68*(2)
Regular Issue

ISSN-e 2594-0317

de al menos media hora. El sensor puede emplearse con seguridad en las muestras con pH en el rango de 2.0 a 6.5. La vida útil de la superficie fresca del sensor se determinó en 2 semanas. La ventaja más importante del sensor es que la superficie del compuesto sensor es renovable (al menos 10 veces) y, por tanto, el sensor puede utilizarse muchas veces durante un largo periodo de tiempo. Las aplicaciones analíticas del sensor se llevaron a cabo con éxito, utilizando el electrodo en la valoración potenciométrica de iones Cu(II) con EDTA como electrodo indicador, en la determinación directa del contenido de Cu(II) de muestras de agua enriquecidas y en la determinación del contenido (p/p) de Cu% de una moneda turca.
Palabras clave: Sensor potenciométrico; electrodo selectivo de cobre(II); sensor de estado sólido; determinación de cobre(II); base de Schiff simétrica, derivado de tiourea

Introduction

One of the leading classes of environmental pollutants is heavy metals and they are major pollutants particularly in water pollution. Although several heavy metals at trace levels play essential roles in the survival of organisms, their excessive accumulation in living things has hazardous implications and is one of the primary reasons of the emergence of certain diseases, especially cancer [1].

Due to its high electrical conductivity, chemical stability, plasticity, and capacity to form alloys with numerous metals, copper is used extensively in industrial activities [2]. As a result of these activities, an increasing amount of copper has been discharged into the environment day by day and led to various environmental and health problems. The United States Environmental Protection Agency (EPA) and The World Health Organization (WHO) have set permitted levels for copper in ground water and drinking water at 3 mg/L and 2 mg/L, respectively [3]. The upper tolerable limit for copper in adults is reported as 10 mg per day [4]. High levels of copper exposure might create various health problems such as gastrointestinal distress, anemia, and disruption of liver and renal functions [5]. In particular, the exposure of individuals with Wilson's and Menke's disease to copper is more risky than healthy individuals [6].

Considering the toxic effects of copper, its determination is quite critical. There are a number of analytical techniques that have been reported for the determination of copper ions at very low concentration levels, including ion chromatography [7,8], UV-Vis Spectrophotometry [9,10], flame atomic absorption spectrometry (FAAS) [11,12], graphite-furnace atomic absorption spectrometry (GF AAS) [13], Colorimetry [14-16], fluorescence spectroscopy [17,18], ICP-MS [19], ICP-OES [20], ICP-AES [21], Capilarry Electrophoresis-UV [22], titrimetry [23], gravimetry [24], electrogravimetry [25] and electrochemical methods [26-30].

The majority of the above-mentioned techniques take a long time and need the use of environmentally hazardous solvents, complicated pretreatment procedures, special tools, skilled operators, and expensive reagents. Therefore, it is critical to develop a copper detection method that is more efficient, simple, economical, and reliable.

Ion-selective electrodes create an impression as an alternative method to the majority of the aforementioned detection methods for Cu^{2+} due to their outstanding features such as high precision and accuracy, broad linear operational range, relatively short analysis time, low limit of detection, adequate selectivity, simple design, cost effectiveness, not to damage the studied samples, mostly no requirement of preprocessing steps, and determinations in colored or turbid solutions [31]. In ionophore-based ISEs, the most critical element controlling the analytical selectivity of the sensor is the chemical substance employed as the ionophore. In the construction of ion-selective electrodes, Schiff bases [32,33], amide derivatives and oxamides [34], crown ethers [35,36], calixarenes [37,38], cryptants [39,40], porphyrins [41,42], metal chelates and ligands [43] are prevalently used as ionophore materials.

Schiff bases, reported first by Hugo Schiff [44], are compounds that bear the imine (-C=N–) functional group. These are condensation products formed by the nucleophilic addition reaction of primary amines with aldehydes and ketones. Schif bases have been resently used in various fields of application such as corrosion inhibitor [45,46], in the structure of dyestuffs and pigments [47], stabilizers increasing the stability of polymers and light stabilizer in thermoplastic resins [48], ion carriers in polymeric structures [49], in the production of

J. Mex. Chem. Soc. **2024**, *68*(2)
Regular Issue

ISSN-e 2594-0317

anticancer, antimicrobial, antifungal and antioxidant substances [50,51], in the developments of fungicide and insecticide in agriculture [52], in the production of cosmetics [53],in perfume [54] and pharmaceutical industry [55].

In recent years, potentiometric sensor technology has made extensive use of all-solid-state composite carbon paste type ion sensors because of their advantages over traditional PVC membrane ion-selective sensors, including the lack of an internal reference solution, robustness and durability, ease of preparation, long life span, renewability, and compatibility with miniaturization. It has also been reported in previous studies that extra improvements in electrochemical performance properties of sensors can be obtained by doping carbon-based nanomaterials (carbon nanotube graphene, etc.) into the sensing carbon paste composite [56,57]. In this study, initially, a novel Schiff base was synthesized and characterized. Later, a composite copper(II)-selective potentiometric sensor based on graphite, carbon nanotubes, paraffin oil, and a currently synthesized symmetric Schiff base as ionophore substance was constructed for the first time for Cu(II) determinations. The potentiometric performance characteristics and analytical applications of the designed sensor were revealed. We believe that the proposed sensor will make a significant contribution to the literature in this area due to its properties as follows: miniaturization, durability, renewability, and performance characteristics comparable to its counterparts.

Experimental

Material and reagents

All 5-bromo-salcilaldehyde (5-Br-SA), thiourea (TU), graphite, multi-walled carbon nanotubes (MWCNTs) and paraffin oil were obtained from Sigma-Aldrich (Germany). All the cation solutions used throughout the study were prepared from the nitrate salts of the relevant cations at analytical purity. Deionized water (18.3 MΩ) was used in the preparation of all the solutions.

Instruments

Potentiometric measurements were performed by a laboratory-made high input impedence computer-controlled potentiometric measurement system. A Gamry (USA) brand saturated Ag/AgCl electrode was used as reference electrode in all potential measurements. All pH measurements were performed with a desktop type Thermo Fisher Scientific (USA) Orion Star A215 pH/Conductivity meter. The FTIR spectra of the samples were attained by a Thermo Nicolet 6700 spectrophotometer in the region of 4000–400 cm^{-1} using the KBr technique. SEM/EDX data of the samples were obtained from field emission scanning electron microscopy (FE-SEM) (Quanta FEG 450-FEI). ICP-MS analysis were conducted by an Agilent 7700 Series ICP-MS system. The deionized water used along the study was supplied from the Human Corporation Zeener Power II (Korea) water purification system.

Potentiometric measurements

All potentiometric measurements were recorded at room temperature (20±2) °C. The utilized electrochemical cell assembly for the entire study was as follow:

Ag/AgCl Reference Electrode || Cu(II) solution | sensing carbon paste | Cu wire

The potentiometric data were collected while the indicator and reference electrodes were immersed in 25 mL of the test solutions, which were stirred at a constant speed. Between measurements, the reference and indicator electrodes were rinsed with deionized water and wiped with soft adsorbent tissue paper.

Synthesis of (1E,3E)-1,3-bis(5-bromo-2-hydroxybenzylidene)thiourea

The synthesis of thiourea derivative Schiff base (1E,3E)-1,3-bis(5-bromo-2-hydroxybenzylidene)thiourea used as an ionophore in the study was carried out by modifying the synthesis procedure followed by Xinde et al. [58]. For this, 5 mL solutions of thiourea (TU) (0.152 g, 2 mmol) and 5-

J. Mex. Chem. Soc. **2024**, *68*(2)
Regular Issue

ISSN-e 2594-0317

bromo-salcilaldehyde (5-Br-SA) (0.804 g, 4 mmol) were combined and mixed at room temperature with the aid of a magnetic stirrer until the final color of the solution turns yellow (72 hours). Later, the pH of the solution was adjusted to 8.0 by incorporating concentrated ammonia solution to the solution. The mixture was stirred again at room temperature for extra 24 hours until a yellow precipitate formed. After removing some of the solvent by distillation, the solution was left to cool. The obtained precipitate was separated by filtration and recrystallized in methanol. The resulting crystals were stored in a desiccator until used. The synthesis reaction of Schiff base is given in Scheme 1.

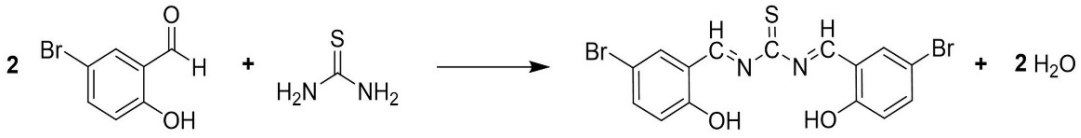

Scheme 1. The synthesis reaction of (1E,3E)-1,3-bis(5-bromo-2-hydroxybenzylidene)thiourea.

Fabrication of the sensors

The synthesized new Schiff base was used as an electroactive material in the production of all-solid-state composite ion-selective sensors. Potentiometric response of the electrode is created by the complexation reaction between Cu(II) ions and electroactive Schiff base compound present in the sensing composite. Sensing composite component of the sensors were prepared by incorporating graphite, MWCNT, Schiff base and paraffin oil components at different proportions and mixing them well. Then the obtained composites were filled into a teflon tube (inner diameter: 0,4 mm, length: 15 mm) with a conductive wire attached to the other end and pressed. The preparation and general structure of the electrodes are illustrated in Fig. 1. The sensors were conditioned by immersing into 10^{-2} M Cu^{2+} solution for 12 hours The constructed sensors were stored dry under laboratory conditions when not in use. Before starting each measurement process, the sensors were preconditioned in the conditioning solution for at least 1 hour. When the potentiometric behaviour of the sensor was deteriorated, a thin layer of 1mm was removed from the sensor surface with a scalpel and a fresh surface was obtained again. In this way, an electrode surface has the feature of being renewed by cutting 10 times. After the removal of the thin section, the electrode was made ready for measurements by following the same procedures as the newly prepared electrodes. The schematic representation of the potentiometric measurement cell utilized in the current study is as given below:

Ag/AgCl, KCl (3 M) || Cu^{2+} (Test solution) / sensitive composite/Cu wire

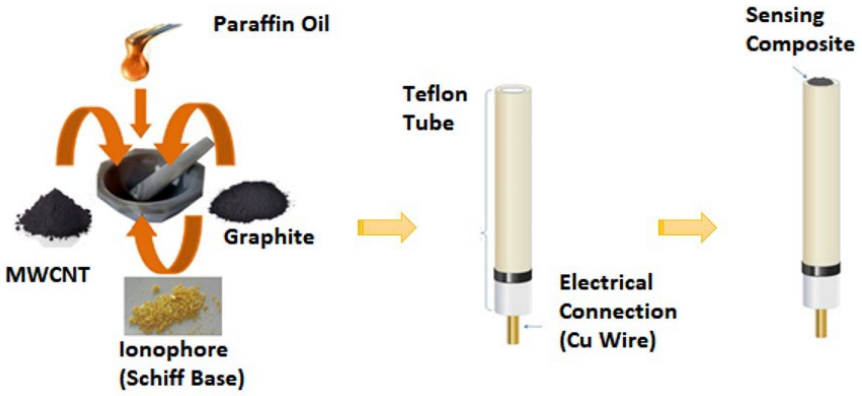

Fig. 1. The preparation and general structure of all solid-state composite potentiometric sensors**.**

J. Mex. Chem. Soc. **2024**, *68*(2)
Regular Issue

ISSN-e 2594-0317

Results and discussion

Characterizations of synthesized Schiff Base

The FTIR spectra for the starting materials 5-BrSA and TU, as well as the product (1E,3E)-1,3-bis(5-bromo-2-hydroxybenzylidene)thiourea compounds, are demonstrated in Fig. 2.

In the FTIR spectrum of pure 5-BrSA (Fig. 2**(a)**), O-H stretching at 3230 cm^{-1}, O-H bending at 1650 cm^{-1} and C-O stretching bands at 1270 cm^{-1} are observed. The C-H stretching bands of the aldehyde group on 5-BrSA at 2920, 2877 and 2741 cm^{-1}; and the bending band at 1374 cm^{-1} are observed. The carbonyl (C=O) stretching band of the aldehyde group is quite strong at 1672 cm^{-1}. In addition, the C-H stretching band at 3045, C=C stretching bands at 1609, 1560 and 1467 cm-1 and out-of-plane bending peaks below 1000 cm^{-1} which belong to the aromatic ring are observed.

When the FTIR spectrum of pure TU illustrated in Fig. 2**(b)** is examined, N-H bending band at 1620 cm^{-1}, N-H stretching bands at 3382, 3276 and 3179 cm^{-1} belonging to amine group are observed. C-N and C=S stretching vibrations also appear at 1412 cm^{-1} and 1090 cm^{-1}, respectively.

When the FTIR spectrum of (1E,3E)-1,3-bis(5-bromo-2-hydroxybenzylidene)thiourea (Fig. 2**(c)**) which is obtained by the reaction of TU and 5-BrSA at a ratio of 1:2 is examined in detail, the N-H stretching bands at 3382, 3276 and 3179 cm^{-1}, N-H bending band at 1620 cm^{-1} originated from TU amine group are disappeared after the synthesis reaction. Similarly, after the reaction, aldehyde C-H stretching bands at 2920, 2877 and 2741 cm^{-1}, C-H bending band at 1374 cm-1 and strong C=O stretching band at 1672 cm^{-1} emerged from 5-BrSA are also disappeared. On the other hand, a new C=N stretch band appeared at 1650 cm-1 in the synthesized compound. The appearance of a C=N stretching IR band and disappearances of N-H and C=O stretching IR bands confirm that TU and 5-BrSA combine to form (1E,3E)-1,3-bis(5-bromo-2-hydroxybenzylidene)thiourea Schiff base. Especially, disappearance of N-H stretching vibrations of $-NH_2$ groups in TU compound verifies that TU and 5-BrSA are combined in 1:2 stoichiometry (Scheme 1) as an expected chemical structure. In addition to these, the C=C stretch and C-H bending peaks of the aromatic ring in the newly synthesized compound are also observed.

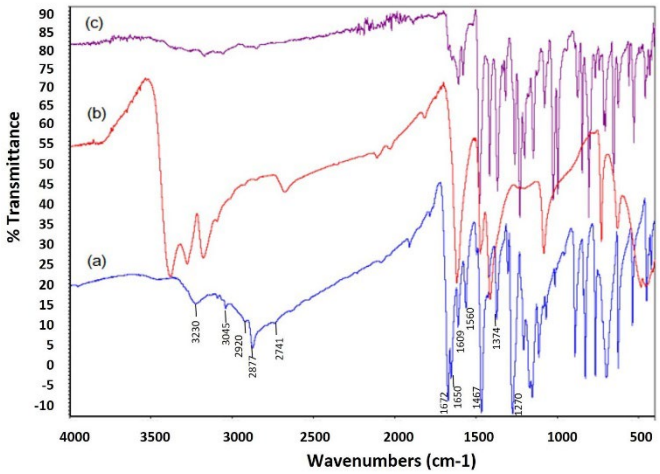

Fig. 2. FTIR spectra of **(a)** 5-BrSA **(b)** TU and **(c)** Schiff base.

SEM-EDX measurements were performed for further characterization of the synthesized compound and the related SEM-EDX data is depicted in Fig. 3.

J. Mex. Chem. Soc. **2024**, *68*(2)
Regular Issue

ISSN-e 2594-0317

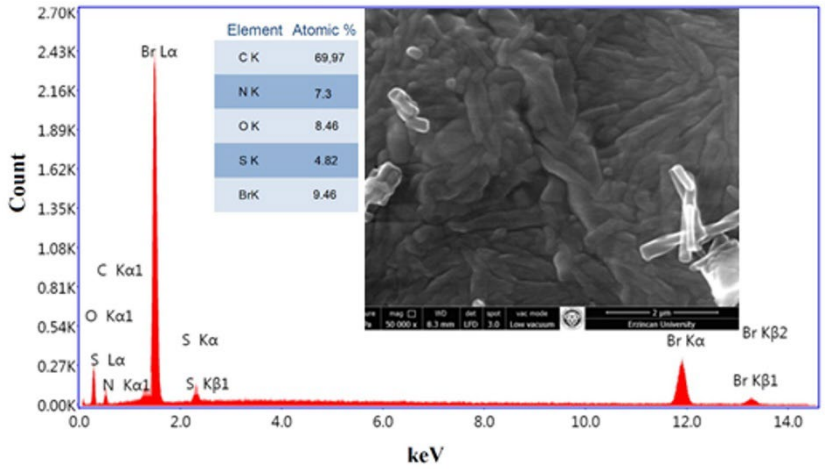

Fig. 3. SEM-EDX analysis of the synthesized Schiff base.

The theoretically calculated atomic percentage values of the C, N, O, S, and Br atoms in the structure of the compound are 68.18, 9.09, 9.09, 4.55, and 9.09, respectively. The values obtained by EDX measurements for the interested elements are 69.97, 7.3, 8.46, 4.82, and 9.46, respectively. According to EDX analyses, the atomic percentage values of N, O, and Br atoms are nearly two times greater than that of the S atom. Additionally, the atomic percentage value of the C atom is approximately 15 times greater than that of the S atom. These results endorse that the compound obtained in the synthesis reaction has the expected chemical structure.

Optimization of the sensor composition

In potentiometric ion selective sensors, it is familiar that the structural composition of the sensing unit tremendously influences the performance properties of the sensor. For this reason, composition of the composite sensing unit displaying the best performance properties was scrutinized by studying the different incorporation ratios of the components. The studied electrode compositions and a summary of some certain potentiometric performance characteristics belonging to them were provided in Table 1 and Table 2, respectively.

Initially, the influence of the paraffin oil ratio in the composite membrane structure on the potentiometric performance properties of the sensor was investigated. For this purpose, the sensors containing a fixed ionophore content of (w/w) 5.0 % were prepared using graphite and varying amounts of paraffin oil (Composition 1-4). The data in Table 2 indicate that the best potentiometric performance characteristics are obtained when (w/w) 20.0 % of paraffin oil is used in the composite structure (Composition 3). In addition, the effect of MWCNT ratio used in the membrane structure on the potentiometric behaviour of the sensor was investigated. Inevitably, the electrodes were produced by using the compositions containing graphite and MWCNT in various ratios by keeping the paraffin oil ratio constant at (w/w) 20.0% (Composition 1-4). The potentiometric performance characteristics of the sensors given in Table 2 show that the membrane with the best performance in terms of MWCNT ratio is the one containing (w/w) 5.0 % of MWCNT (Composition 7). In the following section of the optimization study, the influence of the ionophore percent by mass on the final performance properties of the sensor was investigated. To this end, a series of composites were prepared by using ionophore material at varying mass percentages by keeping the paraffin oil and the MWCNT ratio constant at (w/w) 20.0 % and (w/w) 5.0, respectively (Composition 7, 10-12). The calculated performance characteristics indicate that the composition containing (w/w) 3.0 % ionophore (Composition 10) exhibits the best potentiometric performance properties in terms of ionophore ratio. In the last part of the optimization studies, the influence of the ionic additive percentage on the sensor performance was examined. Therefore, a series of all-solid-state composite electrodes were

J. Mex. Chem. Soc. **2024**, *68*(2)
Regular Issue

ISSN-e 2594-0317

produced by adding ionic additives in the ratios varying between (w/w) 0.5-2.5 % to the composition of (w/w) 20.0 % paraffin oil, (w/w) 5.0 % MWCNT, and (w/w) 3.0 % ionophore (NaTPB) (Composition 13-17) and their performance characteristics were compared. The data given in Table 2 indicate that none of the studied compositions including ionic additive had any premptory effect on the electrode performances. All these membrane optimization studies indicate that the sensor composition exhibiting the best potentiometric performance properties among the studied membranes consists of (w/w) 3.0 % ionophore, (w/w) 5.0 % MWCNT, (w/w) 20.0 % paraffin oil and (w/w) 72.0 % graphite. The following section takes a closer look at the potentiometric performance characteristics of the sensor prepared on the bases of the optimum composition.

Table 1. The examined sensor compositions in the optimization study.

Compositions	**(w/w) %**				
	Ionophore	**Graphite**	**MWCNT**	**Paraffin Oil**	**Ionic Additive (NaTPB)**
1	5.0	65.0	-	30.0	-
2	5.0	70.0	-	25.0	-
3	5.0	75.0	-	20.0	-
4	5.0	80.0	-	15.0	-
5	5.0	74.0	1.0	20.0	-
6	5.0	72.0	3.0	20.0	-
7	5.0	70.0	5.0	20.0	-
8	5.0	65.0	10.0	20.0	--
9	10.0	65.0	5.0	20.0	-
10	3.0	72.0	5.0	20.0	
11	2.0	73.0	5.0	20.0	-
12	1.0	74.0	5.0	20.0	-
13	3.0	71.5	5.0	20.0	0.5
14	3.0	71.0	5.0	20.0	1.0
15	3.0	70.5	5.0	20.0	1.5
16	3.0	70.0	5.0	20.0	2.0
17	3.0	69.5	5.0	20.0	2.5

J. Mex. Chem. Soc. **2024**, *68*(2)
Regular Issue

ISSN-e 2594-0317

Table 2. Some of the performance characteristics of the sensors prepared in the investigated membrane compositions.

Compositions	Slope, mV/decade	Detection Limit, M	Linear Range, M	R^2
1	20.3	1.0×10^{-4}	1.0×10^{-3}-1.0×10^{-1}	0.9981
2	21.8	1.0×10^{-4}	5.0×10^{-4}-1.0×10^{-1}	0.9943
3	24.4	5.0×10^{-5}	1.0×10^{-4}-1.0×10^{-1}	0.9987
4	21.2	1.0×10^{-4}	5.0×10^{-4}-5.0×10^{-2}	0.9921
5	25.0	1.0×10^{-5}	3.0×10^{-5}-1.0×10^{-1}	0.9966
6	28.3	8.0×10^{-6}	1.0×10^{-5}-1.0×10^{-1}	0.9972
7	28.5	2.0×10^{-6}	1.0×10^{-5}-1.0×10^{-1}	0.9973
8	27.1	5.0×10^{-6}	1.0×10^{-5}-1.0×10^{-2}	0.9949
9	23.5	5.0×10^{-5}	1.0×10^{-4}-1.0×10^{-2}	0.9968
10	31.1	5.0×10^{-7}	5.0×10^{-6}-1.0×10^{-1}	0.9959
11	29.7	9.0×10^{-7}	7.0×10^{-6}-1.0×10^{-1}	0.9924
12	28.9	1.0×10^{-6}	8.0×10^{-6}-1.0×10^{-2}	0.9924
13	26.2	8.0×10^{-6}	1.0×10^{-5}-1.0×10^{-2}	0.9986
14	27.8	8.0×10^{-6}	2.0×10^{-5}-1.0×10^{-2}	0.9962
15	27.4	7.0×10^{-6}	2.0×10^{-5}-1.0×10^{-2}	0.9977
16	29.0	8.0×10^{-6}	1.0×10^{-5}-5.0×10^{-3}	0.9938
17	28.9	6.0×10^{-6}	1.0×10^{-5}-5.0×10^{-3}	0.9943

Potentiometric performance characteristics of the optimum sensor composition

In order to reveal the potentiometric performance characteristics of the developed Cu^{2+}-selective electrode in detail, a series of potentiometric measurements were taken in standard Cu^{2+} solutions in the concentration range of 1.0×10^{-1}–1.0×10^{-8} M. The obtained potentiometric response curve, calibration curve and linear calibration plot were created and depicted in Fig. 4. The potentiometric response of the electrode fits the mathematical equation of $E=31{,}136.\log[Cu^{2+}]+2769{,}2$. The electrode exhibits a linear response to Cu^{2+} ions in the concentration range of 5.0×10^{-6}-1.0×10^{-1} M with a slope of 31.1 mV/decade and a detection limit of 5.0×10^{-7} M calculated according to the IUPAC recommendations [59]. As could be seen, the suggested electrode exhibits a near-Nernstian response to Cu^{2+} ions.

J. Mex. Chem. Soc. **2024**, *68*(2)
Regular Issue

ISSN-e 2594-0317

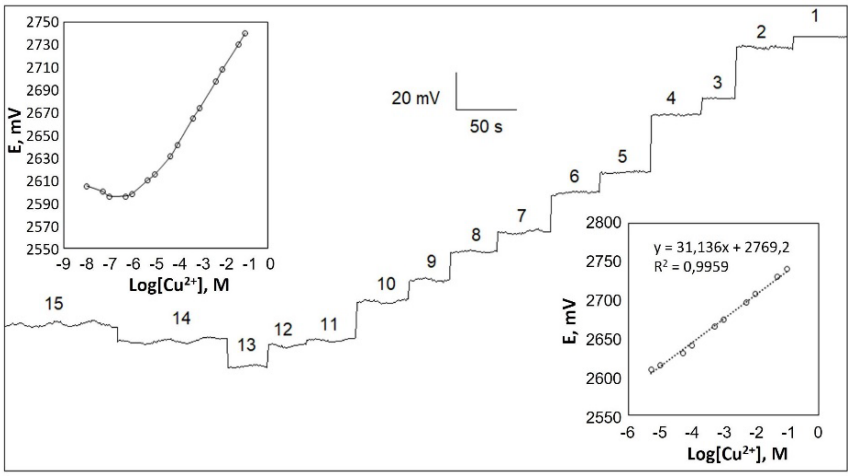

Fig. 4. The potentiometric responses of the sensor in Cu^{2+} solutions at different concentrations, the corresponding response curve (upper left inset), and the calibration graph (bottom right inset) in the linear operating range. (1: $1{,}0\times10^{-1}$ M, 2: $5{,}0\times10^{-2}$ M, 3: $1{,}0\times10^{-2}$ M, 4: $5{,}0\times10^{-3}$ M, 5: $1{,}0\times10^{-3}$ M, 6: $5{,}0\times10^{-4}$ M, 7: $1{,}0\times10^{-4}$ M, 8: $5{,}0\times10^{-5}$ M, 9: $1{,}0\times10^{-5}$ M, 10: $5{,}0\times10^{-6}$ M, 11: $1{,}0\times10^{-6}$ M, 12: $5{,}0\times10^{-7}$ M, 13: $1{,}0\times10^{-7}$ M, 14: $5{,}0\times10^{-8}$ M, 15: $1{,}0\times10^{-8}$ M).

Real-time measurements were taken from low concentration to high concentration and vice versa in standard Cu^{2+} solutions while the potentiometric system was continuously collecting data to determine the response time of the sensor. Fig. 5 depicts the time required for the sensor response to reach equilibrium during transitions between solutions at varying concentrations. The response time of the sensor was calculated as t_{95} for each concentration change, as recommended by IUPAC [59]. Taking the average of these calculated t_{95} values yielded the sensor's average response time. It is seen that the sensor responds quickly enough to the concentration changes of Cu^{2+} ions and reaches equilibrium in a short time. It was determined that the average response time of the sensor calculated at the studied concentrations was <10 s.

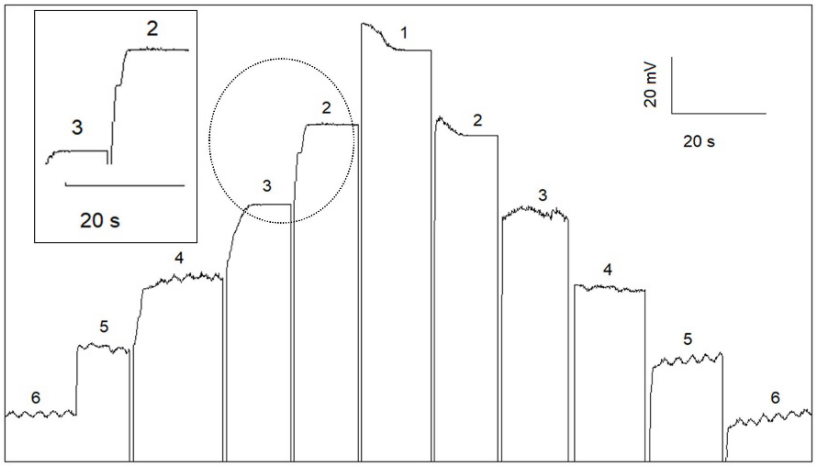

Fig. 5. Response time of the suggested Cu^{2+}-selective sensor. (1: 1.0×10^{-1} M 2: 1.0×10^{-2} M 3: 1.0×10^{-3} M 4: 1.0×10^{-4} M, 5: 1.0×10^{-5} M, 6: 1.0×10^{-6} M).

J. Mex. Chem. Soc. **2024**, *68*(2)
Regular Issue

ISSN-e 2594-0317

To have an idea about the repeatability of the sensor response, repeated measurements were taken in 1.0×10^{-5}, 1.0×10^{-4} and 1.0×10^{-3} M Cu^{2+} solutions (Fig. 6). The mean and standard deviations of the potential values obtained from the repeated measurements carried out in 1.0×10^{-5}, 1.0×10^{-4} and 1.0×10^{-3} M Cu^{2+} solutions were figured out as 2613.6 ± 2.5, 2641.3 ± 0.6 and 2670.6 ± 0.3 respectively. In addition to repeatability studies of the proposed electrode, the reproducibility of the electrode behavior depending on the surface regeneration was also investigated. Three fresh surfaces were created on the same electrode by removing 1 mm sections from its surface each time. After each new surface was obtained, the surfaces were conditioned by following the conditioning process of a new electrode and related calibration lines were created in standard copper(II) solutions (in the range of 5.0×10^{-6}-1.0×10^{-1} M). The calibration lines obtained for each fresh surface are illustrated in Fig. 7. As can be seen the slope values belonging to each fresh surface changed between 30.95 and 31.92 mV/decade which indicates that the potentiometric behaviour of the electrode remains nearly unchanged. However, it should be noted that although there is not much change in the slope of the electrode depending on surface renewal, there is a shift in the initial potentials of the calibration lines. Therefore, it seems imperative to recalibrate the electrode after each surface renewal.

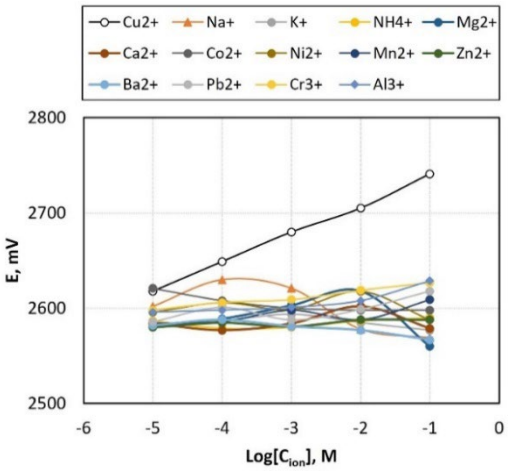

Fig. 6. Repeatability of the sensor in Cu^{2+} solutions at different concentrations.

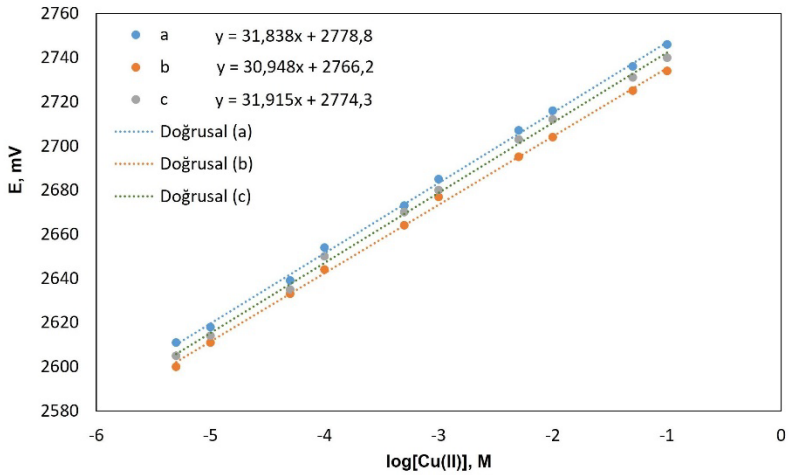

Fig. 7. Potentiometric response plots of the Cu^{2+}-selective electrode depending on surface renewal.

J. Mex. Chem. Soc. **2024**, *68*(2)
Regular Issue

ISSN-e 2594-0317

To expose the selective behaviour of the sensor toward Cu^{2+} in comparison to other ionic species, potentiometric signals in Cu^{2+} and other ionic species solutions at various concentrations were recorded. The potentiometric response curves attained against the concentrations of the solutions are shown in Fig. 8. When Fig. 8 is examined, it is noteworthy that the response of the sensor to Cu^{2+} distinguishes significantly from the response of the other studied ionic species. The selectivity coefficients for each examined ionic species were computed using the Separate Solution Method [60] and reported in Table 3 in order to quantitatively express the selectivity of the sensor.

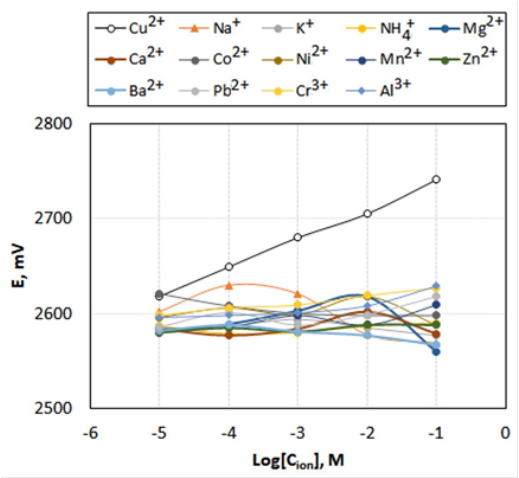

Fig. 8. The potentiometric response of the Cu^{2+}-selective sensor in solutions of different ions at different concentrations.

Table 3. Selectivity coefficients were calculated according to the Separate Solution Method (SSM) for some studied species.

Ion (X)	**log $K_{Cu(II),X}$**	**Ion (X)**	**log $K_{Cu(II),X}$**
Cu^{2+}	0.00	Ni^{2+}	-3.01
Na^{+}	-2.33	Mn^{2+}	-4.30
K^{+}	-2.10	Zn^{2+}	-4.00
NH_4^{+}	-3.93	Ba^{2+}	-4.36
Mg^{2+}	-3.01	Pb^{2+}	-4.01
Ca^{2+}	-3.54	Cr^{3+}	-4.04
Co^{2+}	-3.67	Al^{3+}	-3.98

Table 3 shows that K^{+}, Na^{+}, and Ni^{2+}, in that order, are the most significant ions that interfere with Cu^{2+} ions. Even when compared to the most interfering K^{+} ion, the electrode is more selective to Cu^{2+} ions more than 100 times.

In order to determine the useful pH operating range of the electrode, potential measurements were recorded in the standard solutions containing 1.0×10^{-3} and 1.0×10^{-4} M fixed Cu^{2+} and different H_3O^{+} ion

J. Mex. Chem. Soc. **2024**, *68*(2)
Regular Issue

ISSN-e 2594-0317

concentrations (pH=0.5-11.6). The pH of the solutions was adjusted by adding a few drops of concentrated HCl and NaOH solutions. The pH profile of the electrode was obtained by plotting the relevant potential values against the solution pHs (Fig. 9). The potential values of the sensor against Cu^{2+} ions in the pH range of 2.0-6.5 are strikingly unaffected by pH changes when the graph in Fig. 9 is inspected. It is observed that as the pH levels of the solutions go below 2.0, the electrode potential begins to rise dramatically. This can be explained by the fact that the selective composite begins to respond to increasing hydronium ions along with the copper ions. When the pH of the solution exceeds 6.5, the electrode potential begins rapidly decrease, as expected. We believe that this situation is related to the decrease in Cu(II) concentration through complex formation with OH^- ions of Cu^{2+} ions in the environment as the OH^- concentration increases.

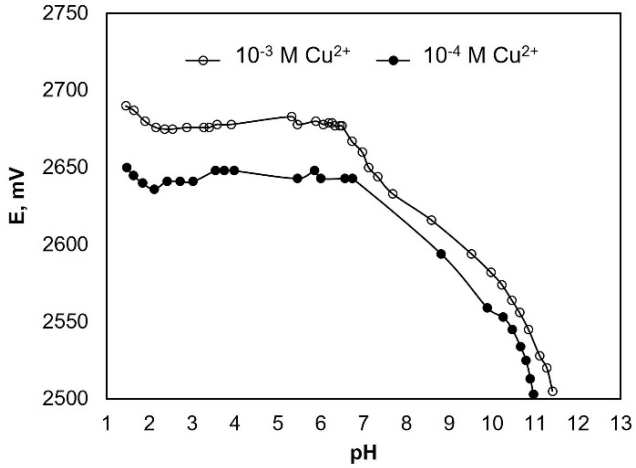

Fig. 9. Variation of the potentiometric response of the Cu^{2+}-selective electrode depending on the pH of the measurement medium.

It is preferable for any sensor's response to remain stable and constant as long as the conditions do not change. Based on this situation, we investigated the signal stability of the currently proposed sensor. The electrode and the reference electrode were immersed into 1.0×10^{-3} M Cu^{2+} solution and the potential of the electrochemical cell was recorded over time for 11 hours. The recorded potentials over time is demonstrated in Fig. 10. As can be seen, a total of 20.6 mV shift is observed in the potential of the electrode in 1.0×10^{-3} M Cu^{2+} solution at the end of the 11 hours period (1.85 mV/h). This magnitude of potential shift indicates that the sensor response is sufficiently stable. At this point, it should be emphasized that a potential shift of 1.85 mV per hour can lead to a significant error (approximately 3.0 % at logarithmic scale) in the determinations when the same calibration curve is used after one hour. This is valid when the electrode is constantly in contact with the solution for 1 hour. As a result, calibrating the electrode before each determination process will lead to more accurate and reliable analysis results.

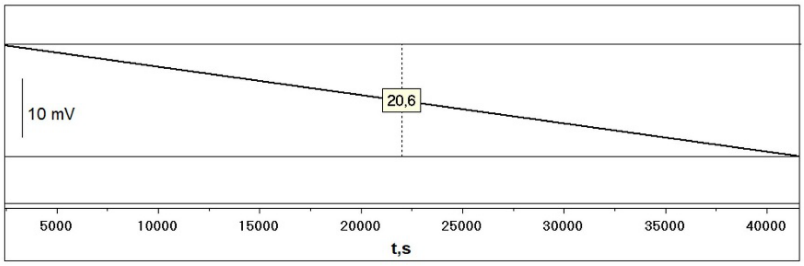

Fig. 10. The observed potential shift in the response of the Cu^{2+}-selective sensor over 11 hours in 1.0×10^{-3} M Cu^{2+} solution.

J. Mex. Chem. Soc. **2024**, *68*(2)
Regular Issue

ISSN-e 2594-0317

The slope of the potentiometric response in the concentration range of 5.0×10^{-6}-1.0×10^{-1} M was monitored daily to determine the useful life-time of the proposed sensor. Fig. 11 depicts the changes in the calculated slope values depending on time. The slope value of the sensor (19.0 mV/ten-fold concentration change) fell below 70 % of the initial slope value (31.1 mV/ten-fold concentration change) after the 14th day, as seen in the graph. Thereof, the life-time of a new surface on the composite sensor is about 2 weeks. This value is approximate and may vary depending on frequency of use. The lifetime of the sensor may seem very short, but the fact that the surface of the composite sensor prepared in this study is constantly renewed by removing a thin section from the surface. This way of use can provide a much longer operational life-time for an existing sensor. This is one of the most significant benefits of the proposed composite membrane sensor.

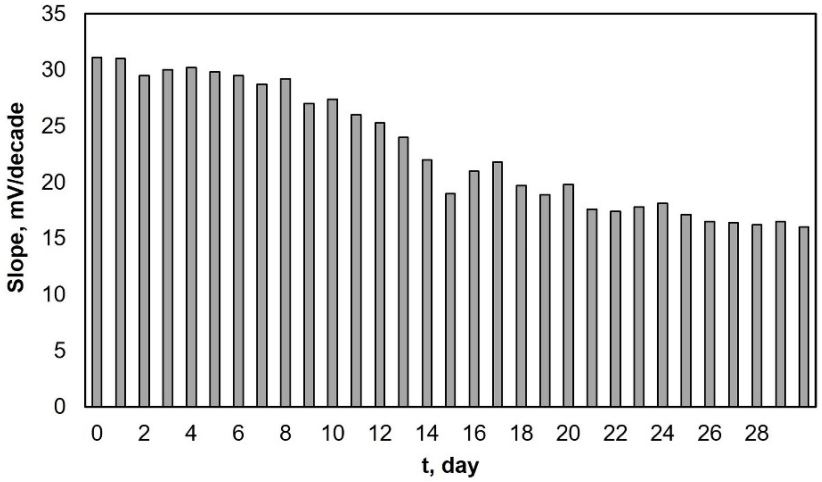

Fig. 11. Time-dependent change in the slope of the Cu^{2+}-selective sensor in the linear working range.

Analytical applications

Several analytical applications of the recommended sensor were performed to demonstrate its analytical usefulness. The sensor was initially used as an indicator electrode for the titration of Cu^{2+} ions with EDTA. Throughout the titration process, the measured potential values of the solution were recorded by the potentiometric system while slowly adding 1.0×10^{-2} M EDTA solution in small volumes to continuously stirred 1.0×10^{-3} M 25 mL Cu^{2+} solution. The obtained titration curve was illustrated in Fig. 12. Because the Cu^{2+} ion concentration decreased in the medium with each addition of EDTA to the solution, as a consequence of the complexation reaction, the potential values gradually decreased in the later stages of titration process. Using the portion of the titration curve where the sudden drop in potential occurred, the potentiometric end-point of the titration was calculated as 2.6 mL. ($V_{theoretical}$=2.5 mL).

J. Mex. Chem. Soc. **2024**, *68*(2)
Regular Issue

ISSN-e 2594-0317

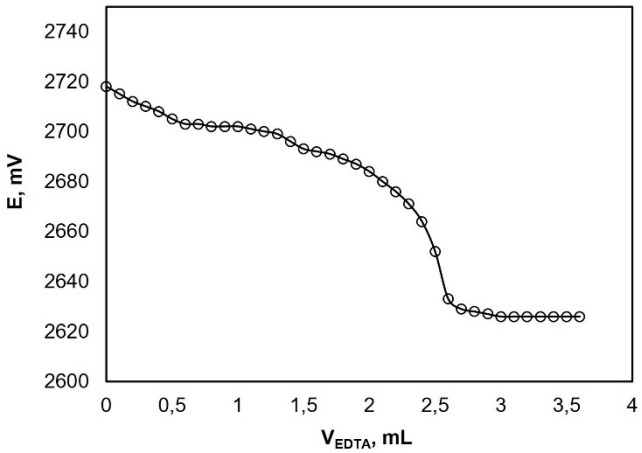

Fig. 12. Titration curve obtained from potentiometric titration of 25 mL 1.0×10^{-3} M Cu^{2+} solution with 1.0×10^{-2} M EDTA solution.

In another analytical application of the present sensor, Cu(II) determinations were carried out directly in tap water samples into which Cu(II) ions were spiked at concentrations ranging between 1.0×10^{-1}-1.0×10^{-4} M. The actual Cu^{2+} concentrations in the solutions, the estimated Cu^{2+} concentrations by the potentiometric method and regarding recovery values were given in Table 4. As can be seen, fairly good recovery values ranging from 98-111 % were obtained.

Table 4. Direct potentiometric determinations of Cu^{2+} ions in spiked tap water samples by the proposed electrode.

Water samples	**Actual [Cu^{2+}], M**	**Estimated [Cu^{2+}], M (N=3)**	**% RSD**	**Recovery**
1	4.0×10^{-4}	$4.5\pm0.3\times10^{-4}$	7.8	111
2	2.0×10^{-3}	$2.1\pm0.1\times10^{-3}$	4.4	103
3	3.0×10^{-3}	$3.1\pm0.1\times10^{-3}$	3.9	104
4	4.0×10^{-2}	$3.9\pm0.2\times10^{-2}$	4.6	98
5	6.0×10^{-2}	$6.2\pm0.1\times10^{-2}$	2.3	102

With regard to the final analytical use of the sensor, the copper percentage of a Turkish coin (25 kuruş, year: 2009) was determined by using the proposed sensor. For this purpose, initially, about 0.4 g of coin was completely dissolved in 10 mL of concentrated nitric acid, the resulting mixture was heated to dryness and then diluted to a final volume of 1000 mL with de-ionized water. Sample solution prepared by diluting the main sample solution in appropriate proportion was implemented for the determinations carried out by potentiometry and ICP-MS. Before the potentiometric determination, pH of the analysed solution was adjusted to 5.0 with the addition of small amount of NaOH solution. Standard addition method was used in the potentiometric determination to eliminate errors brought on by the matrix. While the reported theoretical Cu percent by weight is 60.0, the determined Cu percent for potentiometry and ICP-MS are 61.3±0.3 and 59.7±0.2, respectively for 5 replications. In this case, the calculated recovery % value for potentiometric determination with respect to

J. Mex. Chem. Soc. **2024**, *68*(2)
Regular Issue

ISSN-e 2594-0317

ICP-MS determination is 102.7. The most striking and impressive aspect of these results is that the standard deviation values of the ICP-MS results and the potentiometric results are almost the same. This shows that the repeatability of potentiometric measurements in this application is almost at the same level as that of ICP-MS measurements. These results verify that the recently recommended all-solid-state composite Cu^{2+}-selective sensor can be successfully and practically used for Cu^{2+} determination in this sort of real samples as an alternative to more sophisticated systems.

Conclusions

To some up, a novel potentiometric all-solid-state composite Cu^{2+}-selective sensor based on a thiourea derivative symmetric Schiff base, (1E,3E)-1,3-bis(5-bromo-2-hydroxybenzylidene)thiourea, was favourably developed and employed for Cu^{2+} determinations. Along the study, it was shown that the sensor had a high affinity to Cu^{2+} ions in a wide linear range with a well-nigh Nernstian behaviour. In terms of stability, response time, life-time, pH range and selectivity, very satisfactory potentiometric performance characteristics were obtained. The proposed sensor was successfully applied as the indicator electrode for the determination of Cu^{2+} ions by the titration of EDTA. It was also satisfactorily used for the determination of Cu^{2+} contents of some spiked tap water samples and (w/w) Cu% content of Turkish coins. One of the most striking advantages of the sensor is that the regeneration of the sensor surface can be achieved by the removal of a thin section from the sensing surface and can be used time and again, due to its structural nature. The sensor is sufficiently robust and particularly ideal for miniaturization purposes. The proposed sensor can be preferred for rapid, accurate, practical and cheap determinations of Cu^{2+} levels at various sample types in the future.

Acknowledgements

The authors express their deep gratitude to the Menagement of Faculty of Arts and Sciences (Erzincan Binali Yildirim University) because of the provided facilities and opportunities to achieve the study.

References

1. Jaishankar, M.; Tseten, T.; Anbalagan, N.; Mathew, B.B.; Beeregowda, K.N. *Interdiscip. Toxicol.* **2014**, *7*, 60–72. DOI: https://doi.org/10.2478/intox-2014-0009.
2. Richardson, H.W., in: *Handbook of Copper Compounds and Applications.* Marcel Dekker, New York, **1997**.
3. Institute of Medicine (US) Panel on Micronutrients. Dietary Reference Intakes for Vitamin A, Vitamin K, Arsenic, Boron, Chromium, Copper, Iodine, Iron, Manganese, Molybdenum, Nickel, Silicon, Vanadium, and Zinc. Washington (DC): National Academies Press (US); 2001. 7, Copper. Available from: https://www.ncbi.nlm.nih.gov/books/NBK222312/
4. Hordyjewska, A.; Popiolek, L.; Kocot, J. *Biometals.* **2014**, *27*, 611–621. DOI: https://doi.org/10.1007/s10534-014-9736-5.
5. Schaefer, M.; Gitlin, G. D. *Am. J. Physiol. Gastrointest. Liver Physiol.* **1999**, *276*, G311–G314. DOI: https://doi.org/10.1152/ajpgi.1999.276.2.G311.
6. Ali, A.; Shen, H.; Yin, X. *Anal. Chim. Acta.* **1998**, *369*, 215–223. DOI: https://doi.org/10.1016/S0003-2670(98)00252-9.
7. Bruno, P.; Caselli, M.; Daresta, B. E.; de Gennaro G.; de Pinto, V.; Ielpo, P.; Placentino C. M. *J. Liq. Chromatogr. Relat. Technol.* **2007**, *30*, 477–487. DOI: https://doi.org/10.1080/10826070601093762.
8. Yaseen, S.; Qasim, B.; Al-lame, N. *Egypt. J. Chem.* **2021**, *64*, 673–691. DOI: https://doi.org/10.21608/ejchem.2019.13907.1861.

J. Mex. Chem. Soc. **2024**, *68*(2)
Regular Issue

ISSN-e 2594-0317

9. Babayeva, K.; Demir, S.; Andac, M. *J. Taibah Univ. Sci.*, **2017**, *11*, 808–814. DOI: https://doi.org/10.1016/j.jtusci.2017.02.001.
10. Arpa Şahin, Ç.; Tokgöz, İ. *Anal. Chim. Acta* **2010,** *667*, 83–87. DOI: https://doi.org/10.1016/j.aca.2010.04.012.
11. Bagherian, G.; Arab Chamjangali, M.; Shariati Evari, H.; Ashrafi, M. *J. Anal. Sci. Technol.* **2019**, *10*, 3. DOI: https://doi.org/10.1186/s40543-019-0164-6.
12. Neri, T. S.; Rocha, D. P.; Muñoz, R. A. A.; Coelho, N. M. M.; Batista, A. D. *Microchem. J.,* **2019**, *147*, 894–898. DOI: https://doi.org/10.1016/j.microc.2019.04.014.
13. Erdoğan, H. *Düzce Üniversitesi Bilim ve Teknoloji Dergisi*. **2021**, *9,* 1469–1482. DOI: https://doi.org/10.29130/dubited.884511.
14. Poosinuntakul, N.; Parnklang, T.; Sitiwed, T.; Chaiyo, S.; Kladsomboon, S.; Chailapakul, O.; Apilux, *Microchem. J.,* **2020**, *158,* 105101. DOI: https://doi.org/10.1016/j.microc.2020.105101.
15. Clark, A. C.; Zhang, X.; Kontoudakis, N. *Aust. J. Grape Wine Res.* **2020**, *26*, 399–409. https://doi.org/10.1111/ajgw.12450.
16. Vasimalai, N.; Prabhakarn, A.; Abraham John, S. *Nanotechnology*. **2013**, *24,* 505503. DOI: https://doi.org/10.1088/0957-4484/24/50/505503.
17. He, L.; Bao, Z.; Zhang, K.; Yang, D.; Sheng, B.; Huang, R.; Zhao, T.; Liang, X.; Yang, X.; Yang, A.; Zhang, C.; Cui, P.; Zapien, J. A.; Zhou, H. *Microchim. Acta.* **2018**, *185*, 511. DOI: https://doi.org/10.1007/s00604-018-3043-8.
18. Chrastný, V.; Komárek, M. *Chem. Pap.* **2009**, *63*, 512–519. DOI: https://doi.org/10.2478/s11696-009-0057-z.
19. Yilmaz, V.; Arslan, Z.; Hazer, O.; Yilmaz, H. *Microchem. J.* **2014**, *114*, 66–72. DOI: https://doi.org/10.1016/j.microc.2013.12.002.
20. Ferreira, S. L.; Santos, H. C.; Ferreira, J. R.; Araujo, N. M.; Costa, A. C.; Jesus, D. S. *J. Braz. Chem. Soc.* **1998**, *9*, 525–530. DOI: https://doi.org/10.1590/S0103-50531998000600004.
21. Basheer, C.; Lee, H. K.; *Electrophoresis.* **2007**, *28*, 3520–3525. DOI: https://doi.org/10.1002/elps.200700248.
22. Ergün, E. G. C., Kenar, A. *Turk. J. Chem.* **2018**, *42,* 257–263. DOI: https://doi.org/10.3906/kim-1703-83.
23. Uesugi, K.; Kumagai, T.; Wada, S. *Microchem. J.* **1986**, *33,* 204–208. DOI: https://doi.org/10.1016/0026-265X(86)90056-1.
24. Musa, D.; Sha'Ato, R.; Eneji, I.; Itodo, A. *Open Access Library Journal*. **2018**, *5,* 1–14. DOI: https://doi.org/10.4236/oalib.1104446.
25. Topcu, C.; Lacin, G.; Yilmaz, V.; Coldur, F.; Caglar, B.; Cubuk, O.; Isildak, I. *Anal.Lett.* **2018**, *51,* 1890–1910. DOI: 10.1080/00032719.2017.1395035.
26. Mohammadi, S.; Taher, M. A.; Beitollahi, H. *Russ. J. Electrochem.* **2021**, *57*, 1175–1185. DOI: https://doi.org/10.1134/S1023193521100098.
27. Cui, Y.; Yang, C., in: *3rd International Conference on Bioinformatics and Biomedical Engineering*, **2009**, 1–4. DOI: https://doi.org/10.1109/ICBBE.2009.5162761.
28. Romero-Cano, L. A.; Zárate-Guzmán, A. I.; Carrasco-Marín, F.; González-Gutiérrez, L. V. *J. Electroanal. Chem.* **2019**, *837*, 22–29. DOI: https://doi.org/10.1016/j.jelechem.2019.02.005.
29. Chong, J. M., Nor, A. Y., Shahrul Ainliah, A. A. *Chemosensors.* **2021**, *9*, 157. DOI: https://doi.org/10.3390/chemosensors9070157.
30. Khalil, S.; El-Sharnouby, M. *Chemosensors.* **2021**, *9*, 86. DOI: https://doi.org/10.3390/chemosensors9050086.
31. Mashhadizadeh, M. H.; Sheikhshoaie, I. *Talanta*. **2003**, *60*, 73–80. DOI: https://doi.org/10.1016/S0039-9140(03)00036-5.
32. Ganjali, M. R.; Emami, M.; Rezapour, M.; Shamsipur, M.; Maddah, M.; Salavat-Niasari, M.; Hosseini, M.; Talebpour, Z. *Anal. Chim. Acta.* **2003**, *495,* 51–59. DOI: https://doi.org/10.1016/S0003-2670(03)00921-8.
33. Malinowska, E. *Analyst.* **1990**, *115,* 1085–1087. DOI: https://doi.org/10.1039/AN9901501085.
34. Ganjali, M. R.; Roubollahi, A.; Mardan, A. R.; Hamzeloo, M.; Mogimi, A.; Shamsipur, M. *Microchem. J.* **1998**, *60*, 122–133. DOI: https://doi.org/10.1006/mchj.1998.1642.
35. Su, C. C.; Chang, M. C.; Liu, L. K. *Anal. Chim. Acta.* **2001**, *423*, 261–267. DOI: https://doi.org/10.1016/S0003-2670(00)01375-1.

J. Mex. Chem. Soc. **2024**, *68*(2)
Regular Issue

ISSN-e 2594-0317

36. Gupta, V. K.; Mangla, R.; Aggarwal, S. *Electroanalysis.* **2002**, *14,* 1127. DOI: https://doi.org/10.1002/1521-4109(200208)14:15/16<1127::AID-ELAN1127>3.0.CO;2-7
37. Bhat, V. S.; Ijeri, V. S.; Srivastava, A. K. *Sens. Actuat.* **2004**, *99*, 98–105. DOI: https://doi.org/10.1016/j.snb.2003.11.001.
38. Amini, M. K.; Mazloum, M.; Ensafi, A. A. *Fresenius J. Anal. Chem.* **1999**, *364*, 690–693. DOI: https://doi.org/10.1007/s002160051415.
39. Srivastava, S. K.; Gupta, V. K.; Jain, S. *Anal. Chem.* **1996**, *68*, 1272–1275. DOI: https://doi.org/10.1021/ac9507000.
40. Ardakani, M. M.; Dehghani, H.; Jalayer, M. S.; Zare, H. R. *Anal. Sci.* **2004**, *20*, 1667–1672. DOI: https://doi.org/10.2116/analsci.20.1667.
41. Yagi, Y.; Masaki, S.; Iwata, T.; Nakane, D.; Yasui, T.; Yuchi, A. *Anal. Chem.* **2017**, *89*, 3937–3942. DOI: 10.1021/acs.analchem.6b03754.
42. Jain, A. K.; Singh, R. K.; Jain, S.; Raisoni, J. *Transition Met. Chem.* **2008**, *33*, 243–249. DOI: https://doi.org/10.1007/s11243-007-9022-2.
43. Schiff, H. *Justus Liebigs Ann. Chem.* **1864**, *131*, 118–119. DOI: https://doi.org/10.1002/jlac.18641310113.
44. Issaadi, S.; Douadi, T.; Zouaoui, A.; Chafaa, S.; Khan, M. A.; Bouet, G. *Corros. Sci.* **2011**, *53*, 1484–1488. DOI: https://doi.org/10.1016/j.corsci.2011.01.022.
45. Lashgari, M.; Arshadi, M. R.; Miandari, S. *Electrochim. Acta.* **2010**, *55*, 6058–6063. DOI: https://doi.org/10.1016/j.electacta.2010.05.066.
46. Papic, S.; Koprivanac, N.; Grabaric, Z.; Parac-Osterman, D. *Dyes Pigment.* **1994**, *25,* 299–240. DOI: https://doi.org/10.1016/0143-7208(94)85012-7.
47. Dhar, D. N.; Taploo, C. L. *J. Sci. Ind. Res*. **1982**, *41*, 501–506.
48. Gupta, V. K.; Goyal R. N.; Pal, M. K.; Sharma, R. A. *Anal. Chim. Acta.* **2009**, *653*, 161–166. DOI: https://doi.org/10.1016/j.aca.2009.09.008.
49. Chaudhari, T. D.; Subnis, S. S. *Bull. Haskine Inst.* **1986**, *4*, 85–88.
50. Sharma, P. K.; Dubey, S. N. *Ind. J.Chem.* **2002**, *33A,* 1113–1115.
51. Ali, M. M.; Jesmin, M.; Salam, S. M. A.; Khanam, J. A.; Islam, M. F.; Islam, M. N. *J. Sci. Res.* **2009,** *1,* 641–646. DOI: https://doi.org/10.3329/jsr.v1i3.2585.
52. Fontana, R.; Marconi, P. C. R.; Caputo, A.; Gavalyan, V.B. *Molecules.* **2022**, *27*, 2740. DOI: https://doi.org/10.3390/molecules27092740.
53. Irawan, C.; Islamiyati, D.; Utami, A.; Putri, I. D.; Perdana Putri, R.; Wibowo, S. *Orient. J. Chem.* **2020**, *36*, 577–580. DOI: http://dx.doi.org/10.13005/ojc/360332.
54. Chaudhary, A.; Singh, A. *Int. J. Curr. Res. Med. Sci.* **2017**, *3*, 60–74. DOI: http://dx.doi.org10.22192/ijcrms.2017.03.06.009.
55. Crespo, G. A.; Macho, S.; Rius, F. X. *Anal. Chem.* **2008**, *80,* 1316–1322. DOI: https://doi.org/10.1021/ac071156l.
56. Parra, E. J.; Crespo, G. A.; Riu, J.; Ruiz, A.; Rius, F. X. *Analyst.* **2009**, *134,* 1905–1910. DOI: https://doi.org/10.1039/B908224G.
57. Xinde, Z.; Chenggang, W.; Zhiping, L.; Zhifeng, L.; Zishen, W. *Synth. React. Inorg. Met.-Org. Chem.* **1996**, *26,* 955–966. DOI: https://doi.org/10.1080/00945719608004346.
58. Buck, R. P.; Lindner, E. *Pure Appl. Chem.* **1994**, *66*, 2527–2536. DOI: https://doi.org/10.1351/pac199466122527.
59. Umezawa, Y.; Buhlmann, P.; Umezawa, K.; Tohda, K.; Amemiya, S. *Pure Appl. Chem.* **2000**, *72,* 1851–2082. DOI: https://doi.org/10.1351/pac200274060923.

Article

J. Mex. Chem. Soc. **2024**, *68*(2)
Regular Issue

ISSN-e 2594-0317

Theoretical Investigation Non-covalent Interactions of *N*-(diphenylphosphinothioyl)-2-pyrazinecarboxamide

Masoud Rashidi, Niloufar Dorosti*, Alireza Gholipour

Department of Chemistry, Faculty of Science, Lorestan University, 68135-465, Khorramabad, Iran.

***Corresponding author:** Niloufar Dorosti, email: dorosti.n@lu.ac.ir; nilufardorosti@gmail.com

Received December 26th, 2022; Accepted August 26th, 2023.

DOI: http://dx.doi.org/10.29356/jmcs.v68i2.1936

Abstract. Phosphine chalcogenides can form reliable and reproducible supramolecular synthons through noncovalent interactions that can be employed for designing high dimensional supramolecular architectures. Here, we systematically study the influence of non-covalent interactions in the fabrication of these synthons and the stability of the crystalline structure of $(N_2C_4H_3)C(O)NHP(S)(C_6H_5)_2$ (**1**) through non-covalent interactions (NCI) analysis, molecular Hirshfeld surfaces and the corresponding two-dimensional (2D) fingerprint plots. The theoretical studies were employed to further confirm the presence of these synthons by comparing the stabilization energies of the dimers and monomers. The nature and electronic structure of the phosphor-chalcogenid bond in $(N_2C_4H_3)C(O)NHP(E)(OC_6H_5)_2$(E = S(**1**), O(**2**), and Se (**3**)) have also been evaluated by QTAIM, NBO, MEP, and HOMO-LUMO energy gaps.
Keywords: Phosphine chalcogenide; Non-covalent interaction; NCI analysis; Hirshfeld; QTAIM; NBO.

Resumen. Los calcogenuros de fosfina pueden formar sintones moleculares confiables y reproducibles por medio de interacciones nocovalentes que se pueden utilizar para diseñar arquitecturas supramoleculares de alta dimensionalidad. En este trabajo estudiamos sistemáticamente la influencia de las interacciones nocovalentes en la preparación de estos sintones y en la estabilidad de la estructura cristalina de $N_2C_4H_3)C(O)NHP(S)(C_6H_5)_2$ **(1)**, usando el análisis NCI de interacciones nocovalentes, las superficies moleculares de Hirshfeld y sus correspondientes gráficas bidimensionales (2D). Los estudios teóricos se usaron para confirmar la presencia de estos sintones al comparar las energías de estabilización de los dímeros y monómeros. La naturaleza y estructura electrónica del enlace fósforo-calcogenuro en $(N_2C_4H_3)C(O)NHP(E)(OC_6H_5)_2$(E = S(**1**), O(**2**), y Se (**3**)) también se estudiaron con QTAIM, NBO, MEP y el gap de energía HOMO-LUMO.
Palabras clave: Calcogenuros de fosfina; interacciones nocovalentes; análisis NCI; Hirshfeld; QTAIM; NBO.

Introduction

Understanding directional and nondirectional intermolecular interactions in the crystal lattice and its application to design supramolecular architectures with favorite chemical and physical features is the finaltarget of crystal engineering. The crystal engineering of inorganic/organic compounds *via* intermolecular forces is considered a traditional synthesis against novel synthesis through covalent bonds [1-4]. Crystal engineering is a research area with goal of designing synthons that conserve intact from one lattice structure to another, which guarantees predict ability and generality [5-7]. To justify the design of new supramolecular structures and methodologies for crystal synthesis, non-covalent interactions including hydrogen bonds [8-10], halogen bonds [11-13], the $\pi\cdots\pi$stacking

J. Mex. Chem. Soc. **2024**, *68*(2)
Regular Issue

ISSN-e 2594-0317

[14], C − H ⋯ π, cation/anion···π, and lone-pair···π [15] play essential roles in formation and stabilization of solid-state architectures. Thus, recently, "non-classical" interactionshave become a noteworthysubject for study as they have been proven to be equal or even dominating contributors to inorganic-organic crystal structure construction.

Tertiary phosphine chalcogenides having an O, S, or Se donor atom are considerable interestin the various areas as coordination chemistry [16], chalcogen-transfer reactions [17], and organometallic chemistry [18]. These substances are useful as startingcompounds for catalysis [19] and metal chalcogenide NPs [20]. Also, the synthesis, characterization and crystalstructure of a lot of them have been investigated [21]. Phosphine chalcogenides containing N-H and P=E groupscan act as a ligand to provide distinct complexing [22] with therapeutic [23] properties as well as participate in non-covalent interactions as diverse types of hydrogen bonds. The characterization of intermolecular forces involving N-H and P=E groups can clarify their critical roles in various processes as interacting drug design [24]. On the other hand, density functional theory (DFT) is a complementary theoretical approach for the experimental methods nearly all fields of chemistry [25]. Understanding diverse intermolecular forces present in structure crystals of phosphoramidates and their metal complexes has been contributed by Gholivand *et al.*[10,26]. Recently, we investigated intermolecular interactions in a triorganotin (IV) cocrystal with a phosphoramide derivative both theoretically and experimentally [27]. In our previous studies, a tertiary phosphine chalcogenide with formula $(N_2C_4H_3)C(O)NHP(S)(C_6H_5)_2$(**1**) was synthesized [28]. It was found that there are few comprehensive studies about the role of the non-covalent interactions on the formation and stability of the crystal structures and diagnosis of the typical synthons of phosphine chalcogenides [29]. Hence, we determined to systematically study the various types of non-covalent forces inside the lattice and detect all the molecular discernment properties that lead to the supramolecular synthons and compare these findings with the theoretical results at the end. Subsequently, two other model compounds with formula $(N_2C_4H_3)C(O)NHP(E)(C_6H_5)_2$ (E = O (**2**) and Se (**3**)) were selected to obtain more knowledge into the nature of the P=E bond in phosphine chalcogenides, and the NBO and QTAIM analyses were carried out. The molecular electrostatic potential (MEP) and energy gap of HOMO-LUMO for the title compounds were calculated as well.

Experimental

The structure of *N*-(diphenylphosphinothioyl)-2-pyrazinecarboxamide, $(N_2C_4H_3)C(O)NHP(S)(C_6H_5)_2$ (**1**), was taken from the ccdc database (Fig. 1)[28].

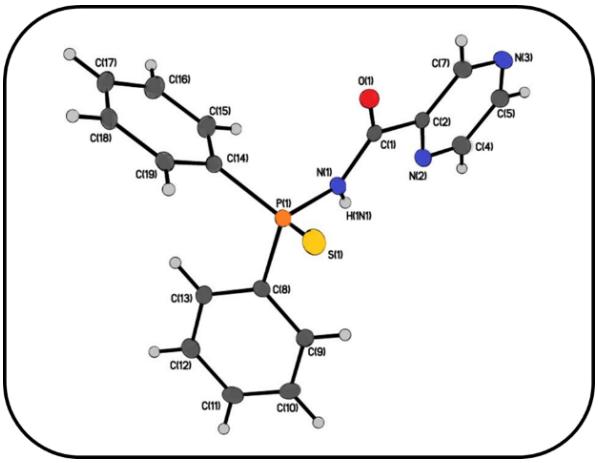

Fig. 1. Perspective view of compound **1** with displacement ellipsoid at the 50 % probability level.

Computational details

The geometry of molecule **1** was optimized by Cam-B3LYP [30] method with 6-311+G* basis set and compared with the obtained experimental data. The optimized geometries are also confirmed by frequency

J. Mex. Chem. Soc. **2024**, *68*(2)
Regular Issue

ISSN-e 2594-0317

analysis. To investigate the non-covalent interactions in solid-state structure, the X-ray structure of this compound was also applied as starting point for DFT studies in the gas phase. The crystal structure was modeled as dimers including two intermolecular-bonded phosphine chalcogenides. As X-ray crystallography cannot accurately determine the position of the H atoms, optimization of the H-atom positions was performed at the B3LYP/6-311G* level for the model clusters, while other atoms were kept frozen. The energies of intermolecular bonding were computed at the M062X/6-311G* level, based on ΔE between the dimer and its fragments, which are connected by the corresponding interaction as represented in the equation $\Delta E = E_{Total} - (E_{Frag1} + E_{Frag2})$, fragments 1 and 2 are two phosphine chalcogenide compounds **1**. The contact energies have been corrected for the error owing to the superposition of the basis set (BSSE) through the counterpoise procedure method [31]. Moreover, two selected model molecules were optimized at the same level. By QTAIM [32] analysis at the Cam-B3LYP/6-311+G*, the electronic structure of substances was evaluated. NBO analysis [33] was carried out at the same level of theory. Quantum chemical studies were performed by the Gaussian 09 [34] in the gas phase. Besides, the non-covalent interaction (NCI) and the reduced density gradient (RDG) analyses [35] were performed to identify the intermolecular interactions observed in $(N_2C_4H_3)C(O)NHP(S)(C_6H_5)_2$ crystal structure at the M062X/6-311G* level using Multiwfn [36] and VMD 1.9.2 [37] programs. The value of sign $(\lambda_2)\rho$ exhibits the color of the isosurfaces. Hydrogen bonding, vander Waals, and non-bonded interactions are described through blue, green, and red color codes. The Hirshfeld surface analysis was performed by Crystal Explorer 3.1 program [38]. The intermolecular interactions in the crystal structure are located by the normalized contact distance map, d_{norm}, and are quantified using the 2D fingerprint plots [39]. Further, DFT calculations have been carried out to predict E_{HOMO}, E_{LUMO}, and the electrostatic potential areas on the optimized geometry of all compounds at the Cam-B3LYP/6-311+G*.

Results and discussion

X-ray structure of $(N_2C_4H_3)C(O)NHP(S)(C_6H_5)_2$ (Fig. 1) was applied as starting point for theoretical studies and optimized by Cam-B3LYP/6-311+G* level. The selected crystallographic data [28] and the theoretical parameters are listed in Table S1. We have started by studying synthons $R_1^2(6)$, $R_2^2(12)$, and $R_2^2(18)$ described in Fig. 2, which form through C−H…S and C−H…O interactions, as well as the self-assembled dimmers where different supramolecular interactions ($C-H\ldots\pi$, C−H…N, N–H…N, and $\pi\ldots\pi$ stacking) are accountable for the fabrication of them and obtained these interaction energies. The studied dimers were obtained from the intermolecular interactions of the crystallographic structure of **1**. Different non-covalent interactions will be discussed in light of NCI, Hirshfeld surface analyses, and the corresponding 2D fingerprint plots.

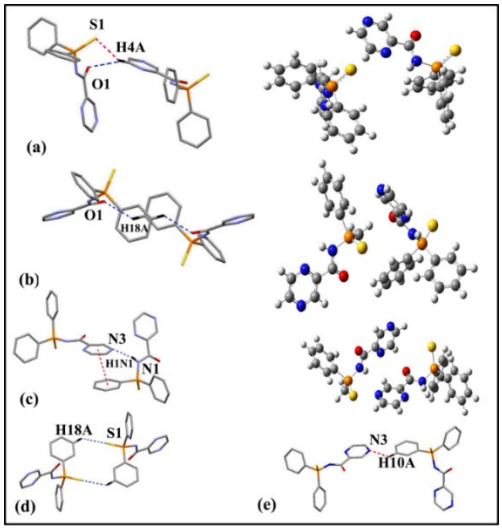

Fig. 2. Models used to evaluate several non-covalent interactions in $(N_2C_4H_3)C(O)NHP(S)(C_6H_5)_2$ (**1**).

J. Mex. Chem. Soc. **2024**, *68*(2)
Regular Issue

ISSN-e 2594-0317

Non-covalent binding energies

Binding energies of supramolecular interactions in the crystal packing (ΔE) were calculated at the M062X method with 6-311G* basis set. We used a series of models to evaluate interactions on the basis of the reported method in papers [9,25]. First, the interaction energy of the complete assembly of each dimer was calculated. After, in this method, in order to estimate the contribution of an individual interaction, a neutral theoretical model has been used where the molecules of other interaction have been replaced or eliminated. Consequently, enrgy proportion of desired interaction would obtain. Fig. 2 shows the computational model used to study non-covalent interactions. Dimer 2a connects *via* C−H…S and C−H…O interactions to create $R_1^2(6)$ synthon. The interaction energy of the complete assembly was calculated, and its value was -4.80 kcal mol^{-1}. To evaluate the share of both interactions (C−H…S and C−H…O), a model have been applied where the $O_{C=O}$ atom has been modified by a CH_2 group (Fig. 2**(a)**, right). The interaction energy is reduced to ΔE_2= –3.00 kcal/mol for C−H…S interaction, and as a result the C−H…O interaction energy was calculated -1.80 kcal mol^{-1}. A second model has also been utilized to measure C−H…O and C–H…π interactions in $R_2^2(18)$ synthon (Fig. 2**(b)**). H-bond arising between a soft acid CH and a soft base π-system exhibits a fundamental role in a variety of chemical phenomena [40,41]. Based on the information provided, many organic structures showed short contact between π-system and C–H bonds [42]. The total assembly has considerable interaction energy (ΔE_1 = −13.59 kcal mol^{-1}) that is diminished to ΔE_2= −11.30 kcal mol^{-1} for two C−H…O bonds, when the phenyl ring has been changed using the methyl group (Fig. 2**(b)**, right). The difference between both interaction energies (ΔE_1−ΔE_2) can be assigned to the contribution of both C–H…π contacts (nearly –1.147 kcal mol^{-1} for each C–H…π in agreement with distance; $d_{H...Cg}$ = 3.403 Å). Moreover, we have analyzed other self-assembly with N–H…N and π ...π interactions between Pyrazine and Phenyl rings, respectively (Fig. 2**(c)**). A theoretical model has been used to determine the energy of each kind of non-covalent interaction. Therefore, hydrogen bond of N–H…N can be approximately estimated –8.25 kcal mol^{-1} (Fig. 2**(c)**, right), and π ...π interaction ($d_{Cg...Cg}$ = -3.56 Å) roughly –3.83 kcal mol^{-1}. Several researchers have documented the role of π ...π stacking interactions in governing the structure of small compounds [14,43]. Finally, Fig. 2**(d)**, e is shown $R_2^2(12)$ synthon and the last self-assembly, where C–H…S and C–H…N interactions are formed between two neighboring molecules, respectively. The interaction energy obtained for these assemblies is ΔE = –1.80 kcal mol^{-1}and -0.38 kcal mol^{-1}.

NCI approach

Recently, the NCI-RDG theoretical method has been applied better than the AIM technique to characterize van der Waals (vdW) interactions, repulsive steric interactions, and hydrogen bonds [44]. The NCI and the RDG *S* vs. (sign λ_2)ρ plots are generated to investigate the existence of these interactions, where (sign λ_2)ρ is the electron density multiplied by the sign of the second Hessian eigenvalue (λ_2) (Fig. 3, right). The (sign λ_2)ρ value is useful helps in anticipation interaction nature. (sign λ_2)ρ < 0 correspond to attractive interaction like hydrogen bonds, whereas sign(λ_2)ρ ≈ 0 and (signλ_2)ρ>0 correlate to the weak vdW types, and non-bonded regions, respectively. In every dimer, the spikes at the zero region show van der Waals forces (-0.01 <sign(λ_2)ρ < +0.01 a.u.). Several peaks at positive signs can related to the non-bonded interactions with ρ critical values of 0.017 and 0.025 a.u. due to the pyrazine and phenyl moieties. Besides, a broad spike of density at values between -0.02 and -0.01 a.u. is observed in RDG graph, which demonstrates C–H…S, C–H···N, C–H…O, and N–H…N interactions. Fig. 3, left, exhibits the 3D plots of π···π stacking and C–H···π interactions in crystal structure. The pill-shaped and flat isosurfaces shows the importance of these interactions which cause to stable crystal packing.

J. Mex. Chem. Soc. **2024**, *68*(2)
Regular Issue

ISSN-e 2594-0317

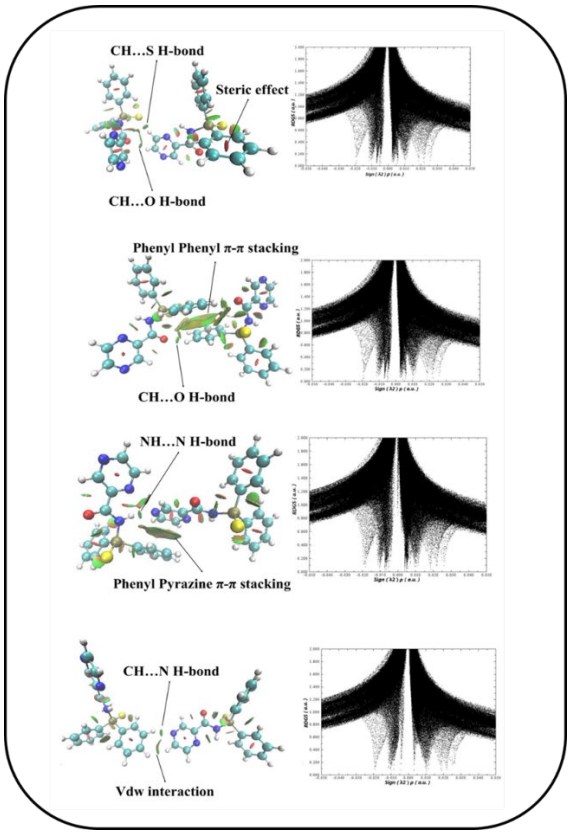

Fig. 3. Right: The NCI-RDG s *vs.* sign(λ_2)ρ plots for dimers of compound **1**.Left: Coloured RDG-based NCI isosurfaces for these dimers.

Hirshfeld surface analysis

The Hirshfeld surface analysis was used to characterize the non-covalent interactions [45] in molecular structure of *N*-(diphenylphosphinothioyl)-2-pyrazinecarboxamide (**1**). The Hirshfeld surfaces (HS) mapped with shape index range of -1.0 to 1.0 Å, d_{norm} range of -0.353 to 1.407 Å, the overall fingerprint plots (FPs) and the decomposed ones for the most significant contacts 2D fingerprint plots for **1** are shown in Figures 4 and 5. Pairs of blue and red triangles with bow tie pattern (on the surface mapped with shape index) observed in Fig. 4**(a)**, are characteristic of π…π stacking interactions. On the Hirshfeld surfaces (d_{norm}) of **1**, two deep red sites exhibit the intermolecular N…H-N interactions (labeled as 1 and 2 in Fig. 4**(b)**). Moreover, intermolecular C-H…S interactions are identified by light red areas near thiophenyl group and piprazine ring, labeled as 3 and 4 in Fig. 4**(b)**. The C–H…S and C–H…O contacts are viewed as the pale red spots (labeled as 5 and 6). The decomposed FPs of the selected compound clarify the effect of the S…H, C…H, O…H, N…H, C…C, and H…H intermolecular interactions on the title molecular structures. Fig. 5 illustrates the contribution of all non-covalent intermolecular interactions in the selected crystal. The N…H–N hydrogen bond reveals two long sharp spikes on the 2D fingerprint plots of **1**, containing 10.7 % of the total Hirshfeld surface area of substance (Fig. 5**(b)**, left). The lower spike relates to the hydrogen bond donor (where $d_e<d_i$), and the upper spike correlates with the H-bond acceptor (where $d_e>d_i$), with d_e+d_i~2.2 Å. The O…H–C and S…H–C interactions appear as shorter spikes in Fig. 5**(b)** (middle, right) with $d_e + d_i$~2.5 Å and 2.68, respectively. The broadness of them may be corresponded to the presence of different O…H–C and S…H–C interactions. Further, H…H contacts view as a very distinguished spike on the diagonal of the plot in Fig. 5**(c)**, left with $d_e + d_i$~2.36Å and 38.9 % in 2D graphs. The share of C…H/H…C contacts corresponding to C–H…π interactions is the most significant interactions after H…H contacts (Fig. 5**(c)**, middle). They have the value of *d*e + *d*i in molecule **1** (2.36 Å). 5 % of the total Hirshfeld

J. Mex. Chem. Soc. **2024**, *68*(2)
Regular Issue

ISSN-e 2594-0317

surface area is related to the $\pi \cdots \pi$ stacking interaction which indicated as a small segment in (Fig. 5**(c)**, right). A similar result was reported by Gholivand *et al.* in the case of the crystal structure of organotin (IV) with phosphoramides [46]. The lowest share of the total Hirshfeld surface in structure **1** is from H…O/H…O interactions at 8.1 %. All these interactions display the leading role in directing the crystal structure. [46,47].

Subsequently, we selected two model compounds with formula $(N_2C_4H_3)C(O)NHP(E)(OC_6H_5)_2$(E = O (**2**), Se (**3**)) and investigated the electronic structure and nature of P=E bond, which may be connected with electronic and steric effects, by DFT calculation, AIM, and NBO analyses. Although understanding the P=E bond features is key to optimizing their coordination to metalcations and their usein biological activities, a limited number of computational and experimental studies probe this issue.

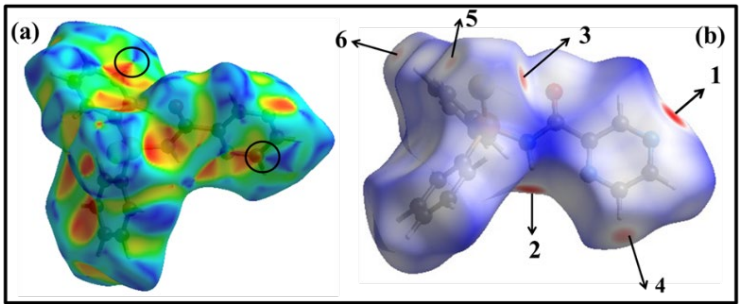

Fig. 4. Hirshfeld surfaces mapped with **(a)** shape index and **(b)** d_{norm} of $(N_2C_4H_3)C(O)NHP(S)(C_6H_5)_2$.

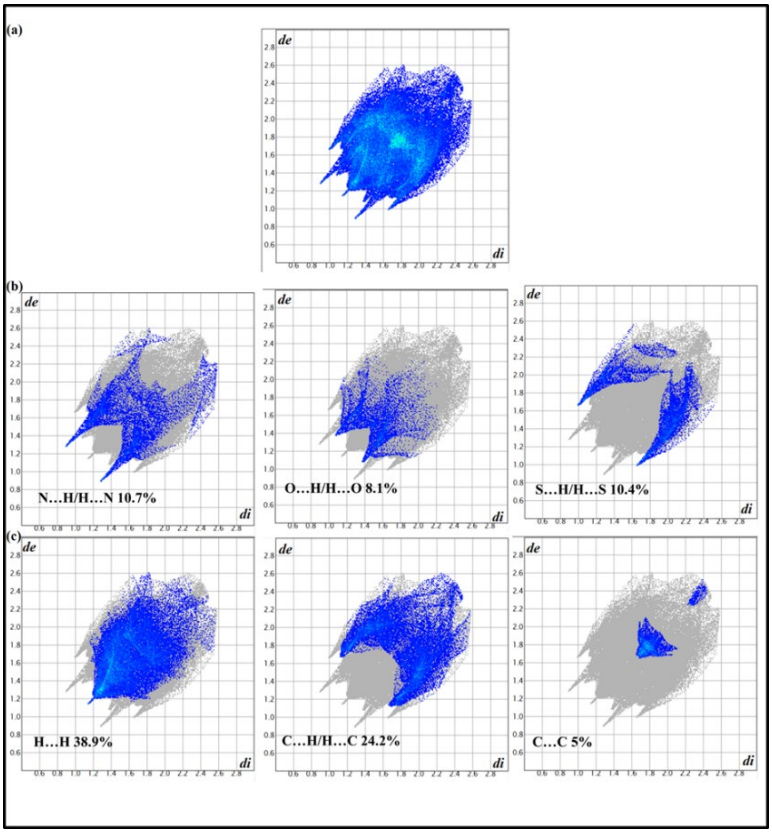

Fig. 5. 2D fingerprint plots, full and resolved into NH/HN, OH/HO, SH/HS, H/H, CH/HC, and C/C contacts showing percentages ofcontacts contributed to the total Hirshfeld surface area of molecule.

J. Mex. Chem. Soc. **2024**, *68*(2)
Regular Issue

ISSN-e 2594-0317

Molecular electrostatic potential (MEP)

The electrostatic potential is broadly applied to characterize their activity, molecular stability and to distinguish the reactive sites of compound in nucleophilic/electrophili creactions and H-bonding interactions. Considering the overall molecular charge distribution, every area of the surface is demonstrated by different colors. Here, the blue and red maps display the electropositive and the electronegative potentials. The green exhibits the potential halfway between these two atmos [48].

In Fig. 6, the negative potential areas are enclosed over the chalcogenid atoms (S, O, and Se), $O_{C=O}$, and $N_{Pyrazine}$. Thus, these sites are the most desirable areas for electrophilic attack in molecules. The appearance of the localized negative potential areas situated at the title regions is in agreement with the published experimental findings, which identified these areas as a reactive and coordinating part to the metal ions by coordination modes asmono, bridge, and bidentate ligand through $N_{pyrazine}$, $E_{P=E}$, and $O_{C=O}$ donor sites [49]. To explain this issue, the electronic features of the N=C and P=E bonds in these molecules will be investigated in the following sections.

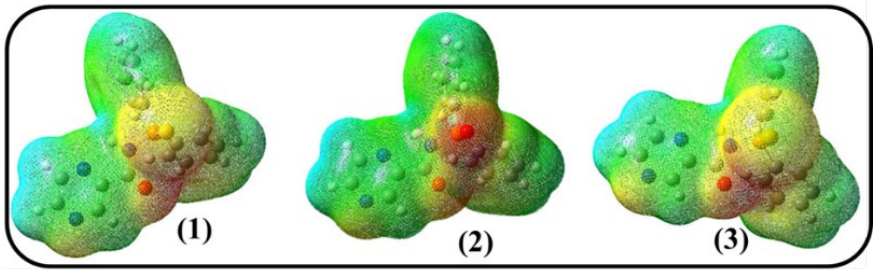

Fig. 6. MEP surfaces of $(N_2C_4H_3)C(O)NHP(S)(C_6H_5)_2$ (E = S (**1**), O (**2**), and Se (**3**)).

QTAIM analysis

The values of electron density ρ(r), the electronic energy density H(r), and the Laplacian of the electron density $\nu^2\rho(r)$ at the bond critical points (BCP) of P = E paths are presented in Table 2. The $\nabla^2\rho$ values at the P = E BCPs are in ranging from -0.045 to 1.44 a.u and negative except that of phosphine chalcogenide **2**, and the ρ values at the P = E BCPs are in the range of 0.135 - 0.232 au. Based on the calculated BCPs for P = E group (E = S and Se) in compounds **1** and **3** (H(r) < 0 and $\nabla^2\rho < 0$), the results show the strong interaction of P=S and P=Se bonds with the covalent bond property (Table 1). Further, the calculated charge density value at P=O BCP of **2** was determined to be 0.232 au, and the corresponding $\nabla^2\rho_{BCP}$ value is positive, with amount to 1.44 au, which characteristic the principally closed-shell interactions [32, 50]. For compound containing P=O group, despite being positive $\nabla^2\rho$, H(r) is negative, and its value is -0.175 au, which indicates that this interaction is electrostatic with some covalent properties [51].

Table 1. Calculated QTAIM parameters (electron density, ρ, its Laplacian,$\nabla^2\rho$, and total electronic energy density, *H(r)*) at the critical point of P=E bond (E = S (**1**), O (**2**), and Se (**3**)).

Compound	**P=E**				
	ρ	**$\nabla^2\rho$**	**V(r)**	**G(r)**	**H(r)**
1	0.172	-0.298	-0.1899	0.0577	-0.132
2	0.232	1.439	-0.7094	0.5346	-0.175
3	0.136	-0.046	-0.1387	0.0636	-0.075

J. Mex. Chem. Soc. **2024**, *68*(2)
Regular Issue

ISSN-e 2594-0317

Table 2. The values of $\Sigma E^{(2)}$ from lone pair (LP) of E (= S, O, and Se) to P=X (X = N and C) antibonding (BD*) instudied compounds **1**- **3** at Cam-B3LYP/6-311+G* levelof theory.

Compound	Donor	Acceptor	$E^{(2)a}$	$\Sigma E^{(2)}$
1	LP (1) S 2	BD* (1) P1 – N4	0.83	
	LP (3) S 2	BD* (1) P1 – N4	27.35	28.18
	LP (1) S 2	BD* (1) P1 – C15	0.92	
	LP (2) S 2	BD* (1) P1 – C15	14.65	
	LP (3) S 2	BD* (1) P1 – C15	5.08	20.65
	LP (1) S 2	BD* (1) P1 – C26	1.01	
	LP (2) S 2	BD* (1) P1 – C26	15.24	
	LP (3) S 2	BD* (1) P1 – C26	3.47	19.72
2	LP (1) O 2	BD* (1) P1 – N4	0.88	
	LP (3) O 2	BD* (1) P1 – N4	29.65	30.53
	LP (1) O 2	BD* (1) P1 – C15	1.01	
	LP (2) O 2	BD* (1) P1 – C15	18.16	
	LP (3) O 2	BD* (1) P1 – C15	4.33	23.5
	LP (1) O 2	BD* (1) P1 – C26	1.14	
	LP (2) O 2	BD* (1) P1 – C26	18.67	
	LP (3) O 2	BD* (1) P1 – C26	2.80	22.61
3	LP (1) Se 2	BD* (1) P1 – N4	0.87	
	LP (3) Se 2	BD* (1) P1 – N4	25.14	26.01
	LP (1) Se 2	BD* (1) P1 – C15	0.95	
	LP (2) Se 2	BD* (1) P1 – C15	12.3	
	LP (3) Se 2	BD* (1) P1 – C15	4.32	17.57
	LP (1) Se 2	BD* (1) P1 – C26	1.02	
	LP (2) Se 2	BD* (1) P1 – C26	12.92	
	LP (3) Se 2	BD* (1) P1 – C26	2.87	16.81

[a]The values are reported in Kcal•mol^{-1}.

J. Mex. Chem. Soc. **2024**, *68*(2)
Regular Issue

ISSN-e 2594-0317

NBO analysis

The natural hybrid orbitals (NHOs) of the P=E (E=O, S, Se) bonds in compounds **1** - **3** yielded the following composition: $\sigma_{PS}=0.7090(sp^{2.37}d^{0.02})_P+0.7052(sp^{4.84}d^{0.03})_S$, $\sigma_{PO}=0.5179(sp^{2.15}d^{0.05})_P+0.8554(sp^{1.73})_O$, and $\sigma_{PSe}=0.7398(sp^{2.45}d^{0.02})_P+0.6728(sp^{6.68}d^{0.08})_{Se}$. Therefore, the phosphorus hybridization is between sp^2 and sp^3 in the studied compounds and the d-orbital share to P=E bonding is negligible. Analysis by second-order perturbation theory exhibited significant interactions between the P-C_{ipso} and P-N antibonding orbitals and the electron lone pairs on the chalcogen atoms in derivatives **1** – **3** (Table 2). Here, each lone pair interacts with two P-C_{ipso} and one P-N antibonding orbitals. More delocalization of the oxygen lone pairs lead tostronger interaction in **2**. The same trend was observed for the stabilization energies of the reported phosphine chalcogenide [17]. This can be described by the stronger electron-withdrawing feature of the amido moietyas canbe viewed from the higher value of the polarization coefficient of the P atom in the NHOs presented above. Also, the NBO analysis exhibits that the $LP(E) \rightarrow \sigma^*(P-X; X=C,N)$ interaction among the subunits within compounds. The stabilization energies E^2 of $LP(E) \rightarrow \sigma^*(P-N)$ interaction are 28.18, 30.53, and 26.01 kcal/mol, and that of $LP(E) \rightarrow \sigma^*(P-C)$ interactions are 20.65, 19.72; 23.50, 22.61; 17.57, 16.81 in compounds **1**-**3**, respectively (Table 2). This electronic delocalization causes the weakening of the P – X bond in order **2**>**1**>**3**.

HOMO and LUMO

The energies of the lowest unoccupied molecular orbital (LUMO) and the highest occupied molecular orbital (HOMO) for derivatives **1**-**3** were computed by Cam-B3LYP method with 6–311G* basis set [52]. Fig. 7 display isodensity surface plot of HOMO and LUMO and the energy gap for these substances. As shown in Fig. 7, the LUMO electrons in all molecules are mainly delocalized on the pyrazine ring, C=O, and N-H moieties. For the phosphine chalcogenide **1**, the HOMO electrons are delocalized over the phenyl rings, as well as, sulfide and oxygen atoms, while these electrons are delocalized over the phenyl rings and oxygen atom of carbonyl group for **2** and Se atom for **3** only. Molecule **2** with P═O group shows the highest energy gap and hardness with the calculated values of 7.51 and 0.138, respectively. And in contrast to **3** with the P═Se group, shows less energy gap and hardness than the other two chalcogenides (**1** and **2**). Using E_{HOMO} and E_{LUMO}, electron affinity (EA) and ionization potential (IP) can be also estimated as $E_A \sim -E_{LUMO}$, $IP \sim -E_{HOMO}$ [53]. The chemical softness (S) = 1/2η [52] and chemical hardness (η) = (IP- EA)/2 [54] values were calculated and were presented in Table 3. It is well known, softness (S) indicates the tendency of a molecule to react. According to the information in Table 3, hardness values determined for derivatives **1**, **2**, and **3** are 0.122, 0.138, and 0.113. Consequently, the hardness of material decreases with increase in the atomic size: Se>S>O. The trend observed is in agreement with the softness of the reported compounds [18a, 55].

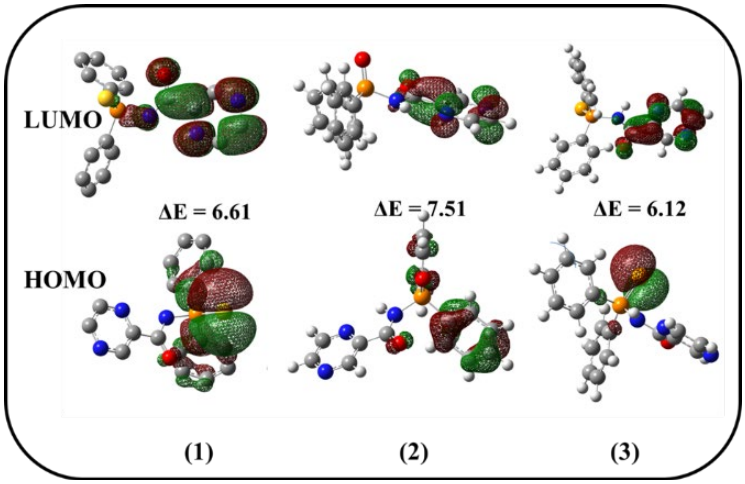

Fig. 7. Plots of the HOMO, LUMO orbitals and *ΔE* (the energy gap between HOMO and LUMO (eV)) of the compounds **1**, **2**, and **3**.

J. Mex. Chem. Soc. **2024**, *68*(2)
Regular Issue

ISSN-e 2594-0317

Table 3. Quantum chemical descriptors for derivatives **1** – **3** at Cam-B3LYP/6-311+G* level.

Compound	E_{HOMO}	E_{LUMO}	ΔE (ev)	$\eta = (E_{HOMO}-E_{LUMO})/2$	$S = 1/\eta$
1	-0.282	-0.039	6.61	0.122	8.23
2	-0.314	-0.038	7.51	0.138	7.25
3	-0.264	-0.039	6.12	0.113	8.89

Quantum chemical descriptors include energy of highest occupied and lowest unoccupied molecular orbital (E_{HOMO} and E_{LUMO}), energy difference between the LUMO and HOMO (ΔE_{L-H}), chemical hardness (η), and softness (S).

Conclusions

The presence of structure-directing interactions in packing crystal of $(N_2C_4H_3)C(O)NHP(S)(C_6H_5)_2$(**1**) have been investigated by NCI plot index, Hirshfeld surface, and finger plot analysis, as well as interaction energies were computed by theoretical calculation. A distinguishing character of the crystal structure in the monomeric substances is the fabrication of the dimeric motifs *via* H-bonding and interaction with aromatic clouds. N−H…N interaction can be identified as an effective interaction to detect the alignment of compounds in supramolecular assemblies. Go along with common hydrogen bonds, non-classical hydrogen bondings including C−H ...S, C−H ...O, C−H…N, and C–H…π further stabilize the packing structures so thatenergy of them is within a range of −0.38 (C−H…N) to −8.25 (N−H…N) kJ.mol^{-1}. Pyrazine and phenyl rings have a main role in directing the supramolecular assembly of the studied phosphine chalcogenideusing establishing C–H…π and $\pi \cdots \pi$ interactions. Besides, the electronic structure and strength of other two model derivatives with P=E functional group (E = O (**2**) and Se (**3**)) were optimized and investigated. The QTAIM analysis demonstrates P=O bond with electrostatic feature and a small amount of covalent overlap compared to P=E (S, Se) bondings with the nature of covalent. Further, the HOMO-LUMO energy gap of the studied compounds shows the effect of E atomic size on molecular softness. The NBO analysis exhibits that the $LP(E) \rightarrow \sigma^*(P-X; X = C, N)$ electronic delocalization weakens the P–X bond in compounds **1- 3** in order **2**>**1**>**3**.

Acknowledgements

The financial support of this work by Lorestan University is gratefully acknowledged.

References

1. Mirzaei, M.; Eshghi, H.; Akhlaghi Bagherjeri, F.; Mirzaei, M.; Farhadipour, A. *J. Mol. Struct.* **2018**, *1163*, 316-326.
2. Desiraju, G. R. *Angew. Chem. Int. Edit.* **1995**, *34*, 2311-2327.
3. Desiraju, G. R. in: *The Design of Organic Solids*: Elsevier: Amsterdam, **1989**.
4. Desiraju, G. R. *Angew. Chem. Int. Edit.* **2007**, 46, 8342–8356.
5. Seth, S. K.; Bauza, A.; Frontera, A. *Cryst. Eng. Comm.* **2018**, *20*, 746-754.
6. Khavasi, H. R.; Gholami, A.; Hosseini, M.; Nikpoor, L.; Eskandari, K. *Cryst. Growth. Des.* **2020**, *20*, 2266-2274.
7. Ray Choudhury, S.; Gamez, P.; Robertazzi, A.; Chen, C.Y.; Lee, H. M.; Mukhopadhyay, S. *Cryst. Growth. Des.* **2008**, *8*, 3773-3784.

J. Mex. Chem. Soc. **2024**, *68*(2)
Regular Issue

ISSN-e 2594-0317

8. Sathiyaraj, E.; Thirumaran, S.; Selvanayagam, S.; Sridhar, B.; Ciattini, S. *J. Mol. Struct.* **2018**, *1159*, 156-166.
9. Mitra, M.; Manna, P.; Bauza, A.; Ballester, P.; Seth, S-k.; Choudhury, S. R.; Frontera, A.; Mukhopadhyay, S. *J. Phys. Chem. B.* **2014**, *118*, 14713-14726.
10. Gholivand, K.; Hosseini, M.; Ebrahimi Valmoozi, A. A.; Farshadfar, K. *Cryst. Eng. Comm.* **2017**, 19, 2536-2548.
11. Khavasi, H. R.; AzhdariTehrani, A. *Inorg. Chem.* **2013**, *52*, 2891–2905.
12. Metrangolo, P.; Resnati, G. in: *Halogen bonding, fundamentals and applications*, Springer. **2008**.
13. Piltan, M.; Farshadfar, K.; Mark Roe, S. *Eur. J. Inorg. Chem.* **2017**, *2017*, 2723-2726.
14. (a) Khavasi, H. R.; Azizpoor Fard, M. *Cryst. Growth. Des*. **2010**, *10*, 1892-1896. (b) Field J. S.; Munro, Q. Q.; Waldron, B. P. *Dalton. Trans.* **2012**, 41, 5486−5496. (c) He, L.; Ma, D.; Duan, L.; Wei, Y.; Qiao, J.; Zhang, D.; Dong, G.; Wang, L.; Qiu, Y. *Inorg. Chem.* **2012**, *51*, 4502−4510. (d) Derikvand, Z.; Azadbakht, A.; AmiriRudbari, H. *J. Inorg. Organomet. Polym. Mater.* **2019**, *29*, 502–516.
15. (a) Janssen, F. F. B. J.; Gelde, R. G. Rowan, A. E. *Cryst. Growth. Des.* **2011**, *11*, 4326−4333. (b) Tiekink, E. R. T.; Zukerman-Schpector, J. *Cryst.Eng. Comm*. **2009**, *11*, 1176-1186. (c) Hay, B. P.; Bryantsev, V. S. *Chem. Commun*. **2008**, 2417−2428. (d) Mooibroek, T. J.; Gamez, P.; Reedijk, J. *Cryst. Eng. Comm.* **2008**, *10*, 1501−1515. (e) Schottel, B. L.; Chifotides, H. T.; Dunbar, K. R. *Chem. Soc. Rev*. **2008**, 37, 68−83. (f) Orvay, F.; Bauza, A.; Barcelo-Oliver, M.; Raso, A. G.; Fiol, J. J.; Costa, A.; Molins, E.; Mata, E.; Frontera, A. *Cryst. Eng. Comm*. **2014**, *16*, 9043-9053.
16. Popescu, A. P.; Laromaine, A.; Teixidor, F.; Sillanpaa, R.; Kivekas, R.; Liambias, J. I.; Vinas, C. *Chem. Eur. J.* **2011**, *17*, 4429 - 4443.
17. Davies, R. in: *Chalcogen-phosphorus (and heavier congeners) chemistry*, Chapter 5 of handbook of chalcogen chemistry, RSC Publishing, **2007**.
18. (a) Cook, J. B.; Nicholson, B. K.; Smith, D. W. *J. Organomet. Chem*. **2004**, *689*, 860-869 (b) Chutia, P.; Kumari, N.; Sharma, M.; Woollins, J. D.; Slawin, A. M. Z.; Dutta, D. K. *Polyhedron*. **2004**, *23*, 1657-1661.
19. Glueck, D. S. *Chem. Eur. J.* **2008**, *14*, 7108 - 7117.
20. (a) Koh, W. K.; Yoon,Y.; Murray, C. B. *Chem. Mater.* **2011**, *23*, 1825-1829. (b) Evans, C. M.; Evans, M. E.; Krauss, T.D. *J. Am. Chem. Soc*. **2010**, *132*, 10973-10975. (c) Liu, H.; Owen, J. S.; Alivisatos, A. P. *J. Am. Chem. Soc*. **2007**, *129*, 305-312. (d) Arachchige, I. U.; Brock, S. L. Acc. *Chem. Res.* **2007**, 40, 801 - 809.
21. (a) Gholivand, K.; Madani Alizadehgan, A.; Mojahed, F.; Soleimani, P. *Polyhedron*. **2008**, 27, 1639-1649 (b) Gholivand, K.; Shariatinia, Z.; Mashhadi, S. M.; Daeepour, F.; Farshidnasab, N.; Mahzouni, H.R.; Taheri, N.; Amiri, S.; Ansar, S. *Polyhedron*. **2009**, *28*, 307–321. (c) Shi, M.; Shi, J. W. *Tetrahedron: Asymmetry.* **2007**, *18*, 645–650.
22. Gholivand, K.; Gholami, A.; Ebrahimi, A. A. V.; Abolghasemi, S. T.; Esrafili, M. D.; Fadaei, F. T.; Schenk, K. J. *Rsc. Adv.* **2015**, 5, 17482-17492.
23. Gholivand, K.; Farshadian, S.; Hosseini, Z.; Khajeh, K.; Akbari, N. *Appl. Organomet. Chem.* **2010**, *24*, 700–707.
24. (a) Eini Roumiani, M.; Dorosti,N. *Ultrason. Sonochem.* **2019**, *55*, 207-216. (b) Nikpour, S.; Dorosti, N.; Afshar, F.; Kubicki, M. *Appl. Organomet. Chem.* **2020**, e5724. (c) Gholivand, K.; Hosseini, Z.; Farshadian, S.; Naderi Manesh, H. *Eur. J. Med. Chem.* **2010**, *45*, 5130-5139.
25. Manna, P.; Ray Choudhury, S.; Mitraa, M.; Seth, S.K.; Helliwell, M.; Bauza, A.; Frontera, A.; Mukhopadhyay, S. A. *J. Solid. State. Chem.* **2014**, *220*, 149-156. (b) Mirzaei, M.; Eshtiagh-Hosseini, H.; Karrabi, Z.; Notash, B.; Bauza, A.; Frontera, A.; Habibi, M.; Ardalani, M.; Shamsipur, M.; *J. Mol. Stru*. **2015**, *1079*, 78-86.
26. (a) Gholivand, K.; Hosseini, M.; Maghsoud, Y.; Valenta, J.; Ebrahimi Valmuzi, A.A.; Owczarzak, A.; Kubicki, M.; Jamshidi, M.; Kahnouji, M. Inorg. Chem. **2019**, *58*, 9, 5630–5645. (b) Gholivand, K.; Farshadfar, K.; Roe, S.M.; Hosseini, M.; Gholami, A. *Cryst. Eng. Comm.***2016**, 18, 7104-7115.

J. Mex. Chem. Soc. **2024**, *68*(2)
Regular Issue

ISSN-e 2594-0317

27. Dorosti, N.; Nikpour, S.; Molaei, F.; Kubicki, M. *Chem. Pap.* **2021**, *75*, 2503-2516.
28. Gholivand, K.; Dorosti, N. *Monatsh. Chem*. **2013**, *144*, 1417-1425.
29. Alvarado, S. R.; Shortt, I. A.; Fan, H. I.; Vela, J. *Organometallics*. **2015**, *34*, 4023-4031.
30. Yanai, T.; Tew, D. P.; Handy, N. C. *Chem. Phys. Lett.* **2004**, *393*, 51–57.
31. Boys, S. F.; Bernardi, F. *Mol. Phys.***1970**, *19*, 553–566.
32. Bader, R. F. W. *Chem. Rev.***1991**, *91*, 893-928.
33. Reed, A. E.; Curtiss, L. A.; Weinhold, F. *Chem. Rev.***1988**, *88*, 899–926.
34. Frisch, M. J.; Trucks, G. W.; Schlegel, H. B.; Scuseria, M. A.; Robb, J. R.; Cheeseman, G.;*et al. Gaussian 09, Revision D.01. Gaussian, Inc*. Wallingford, **2009**.
35. Johnson, E. R.; Keinan, S.; Mori-Sanchez, P.; Contreras-Garcia, J.; Cohen, A. J.; Yang, W. J. *Am. Chem. Soc*. **2010**, *132*, 6498–6506.
36. Lu, T.; Chen, F. J. *Theor. Comput. Chem*. **2012**, *11*, 163-183.
37. Humphrey, W.; Dalke, A.; Schulten, K. *J. Mol. Graphics.***1996**, *14*, 33–38.
38. Wolff, S. K.; Grimwood, D. J.; McKinnon, J. J.; Turner, M. J.; Jayatilaka, D.; Spackman, M. A. *Crystalexplorer 3.0,* University of Western Australia, Perth, Australia, **2012**.
39. Spackman, M. A.; McKinnon, J. *J. Cryst. Eng. Comm.* **2002**, *4*, 378–392.
40. Nishio, M. *Cryst. Eng. Comm*. **2004**, *6*, 130–158.
41. Nishio, M. *Phys. Chem. Chem. Phys.* **2011**, *13*, 13873–13900.
42. (a) Umezawa, Y.; Tsuboyama, S.; Takahashi, H.; Uzawa, J.; Nishio, M. *Tetrahedron.* **1999**, *5*, 10047–10056. (b) Mirdya, S.; Roy, S.; Chatterjee, S.; Bauza, A.; Frontera, A.; Chattopadhyay, S. *Cryst. Growth. Des*. **2019**, *19*, 5869-5881.
43. Kim, K. S.; Tarakeshwar, P.; Lee, J. Y. *Chem. Rev*. **2000**, *100*, 4145-4185.
44. (a) Gabriele, S.; Gatti, C.; Lo Presti, L.; Garcia, J. C. *Chem. Eur. J.* **2012**, *18*, 15523–15536. (b) Lande, D. N.; Bhadane, S. A.; Gejji, S. P. *J. Phys. Chem.* **2017**, 121, 1814–1824.
45. Spackman, M. A.; Byrom, P. G. *Chem. Phys. Lett*. **1997**, *267*, 215–220.
46. Gholivand, K.; Azadbakht, M.; Maghsoud, Y.; Hosseini, M. *J. Organomet. Chem*. **2019**, *879*, 27-39.
47. Taghizadeh, L.; Montazerozohori, M.; Masoudiasl, A.; Joohari, S.; White, J. M. *Mater. Sci. Eng. C.* **2017**, *77*, 229–244. (b) Bejaoui, C.; Ameur, I.; Derbel, N.; Linden, A.; Abid, S. *J. Mol. Struct.* **2018**, *1166*, 7-14. (c) Binzet, G.; Gumus, I.; Dogen, A.; Florke, U.; Kulku, N.; Arslan, H. *J. Mol. Struct*. **2018**, *1161*, 519-529.
48. Politzer, P.; Murray, J. S. *Theor. Chem. Acc.* **2002**, *108*, 134–142
49. (a) Gholivand, K.; Mahzouni, H. R.; Pourayoubi, M.; Amiri, S. *Inorg. Chim. Acta.* **2010**, *363*, 2318–2324. (b) Gholivand, K.; Oroujzadeh, N.; Afshar, F. *J. Organomet. Chem.* **2010**, *695*, 1383–1391. (c) Torabi Farkhani, E.; Pourayoubi, M.; Izadyar, M.; Andreev, P. V.; Shchegravina, E. S. Dalton. Trans. **2019**, *48*, 17908-17918. (d) Taherzadeh, M.; Pourayoubi,M.; Nečas, M. *Phosphorus. Sulfur*. **2019**, *194*, 39-46.
50. Bader, R. F. W. Oxford University Press, New York, **1990**.
51. Dobado, J. A.; Martínez-García, H.; Molina, J.M.; Sundberg, M. R. *J. Am. Chem. Soc.***1998**, *120*, 33, 8461-8471.
52. Jamroz, M. H. in: *Vibrational energy distribution analysis*, VEDA 4 computer program, Poland, **2004**.
53. Zhou, Z.; Navangul, H. V. *J. Phys. Org. Chem*. **1990**, *3*, 784-788.
54. Senet, P. *Chem. Phys. Lett*. **1997**, *275*, 527-532.
55. Sarıoz, O.; Oznergiz, S.; Kandemirli, F. *Syn. React. Inorg. Met. Org. Chem.* **2013**, *43*, 185–195.

Article

J. Mex. Chem. Soc. **2024**, *68*(2)
Regular Issue

ISSN-e 2594-0317

Synthesis and NMR characterization of Bile Acid Derivatives Bearing Ugi 4CR-Modified Side Chains

Josué Vazquez-Chavez, Brian A. Verdeja-Perdomo, Martin A. Iglesias-Arteaga*

Facultad de Química, Universidad Nacional Autónoma de México. CDMX, 04510, México

***Corresponding author:** Martin A. Iglesias-Arteaga, email: martin.iglesias@unam.mx

Received May 4th, 2023; Accepted August 28th, 2023.

DOI: http://dx.doi.org/10.29356/jmcs.v68i2.2061

Abstract. The application of the four-component Ugi reaction for the synthesis of five bile acid derivatives bearing modified side chains is described. The unambiguous structural characterization and assignment of the functional ^{1}H NMR signals and all ^{13}C{^{1}H} NMR chemical shifts are presented.
Keywords: Bile acids; Ugi 4CR; ^{1}H NMR; ^{13}C{^{1}H} NMR.

Resumen. Se describe la aplicación de la reacción de cuatro componentes de Ugi a la síntesis de cinco derivados de ácidos biliares que portan cadenas laterales modificadas. Se presenta la caracterización estructural inequívoca y la asignación de las señales funcionales de ^{1}H RMN y de todos los desplazamientos químicos de ^{13}C{^{1}H} RMN.
Palabras clave: Ácidos biliares; Ugi 4CR; ^{1}H RMN; ^{13}C{^{1}H} RMN.

Introduction

Bile acids (BA) are synthesized in the liver and play an important role in digestion and other physiological processes.[1] Their structure consists of a tetracyclic rigid framework, with a lipophilic β-side bearing methyl groups attached to positions C-10 and C-13, and a hydrophilic α-side that bears hydroxyl groups at different positions of the steroid core. A side chain that ends in a carboxylic group is attached to position C-17.

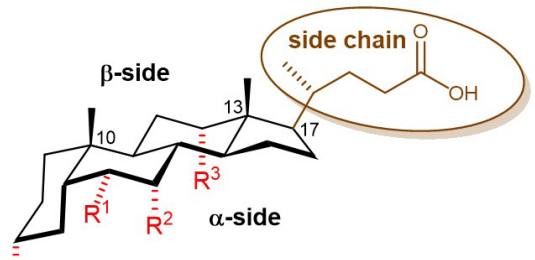

1a) $R_1 = R_2 = R_3 = H$, lithocholic acid
1b) R_1= OH, $R_2 = R_3 = H$, hyodeoxycholic acid
1c) $R_1 = R_3 = H$, R_2 = OH, chenodeoxycholic acid
1d) $R_1 = R_2$, = H, R_3 = OH, deoxycholic acid
1e) R_1 = H, $R_2 = R_3$ = OH, cholic acid

Fig. 1. Structure of some of most common bile acids.

J. Mex. Chem. Soc. **2024**, *68*(2)
Regular Issue

ISSN-e 2594-0317

In addition to the wide variety of pharmacological applications of naturally occurring bile acids and their synthetic derivatives that have been described, multiple applications of this family of compounds have been developed based on their amphiphilic nature.[2] Thus, monomeric, dimeric and trimeric bile acid derivatives have been reported as molecular pockets,[3] anion receptors and transporters,[4] and gelators,[5] amongst others. In particular, the modification of the structure of BA has been found to produce dramatic changes in their aggregation properties [6] and crystal habits.[7]

Multicomponent Reactions (MCRs) allow the assemblage of three or more compounds into more complex structures bearing a wide range of functional groups and substituents. Excellent reviews and books have covered the development and application of these powerful diversity-oriented synthetic tools.[8] MCRs have been employed for the derivatization of the skeleton and the side chain of a wide spectrum of steroids triggering the generation of new physical, biological, and chemical properties.[9a] In particular, Rivera and Wessjohann described an interestin application of the four component Ugi reaction (Ugi 4CR) to synthesis of macrolactones derived from bile acids [9b].

The Ugi 4CR has revealed as a powerful and straightforward tool to develop structural diversity.[11] The simple exchange of components allows the rapid development of compound libraries useful for the systematic screening of properties.

As a part of our ongoing projects on the application of MCR to the generation of new steroid materials [10] we have decided to the setup procedures for the synthesis and characterization of side chain-modified bile acids derived from the four component Ugi reaction (Ugi 4CR) with formaldehyde, aniline and ethyl isocyanoacetate, that will serve as models for the construction and characterization of more complex structures.

Herein we report on the synthesis of five different bile acid derivatives bearing modified side chains (Scheme 1, *vide infra*). The unambiguous structural characterization and assignment of the functional ^{1}H NMR signals and all $^{13}C\{^{1}H\}$ NMR chemical shifts are presented.

Experimental

Chemistry

General procedures. Reactions were monitored by TLC on ALUGRAM® SIL G/UV254 plates from MACHEREY-NAGEL. Chromatographic plates were sprayed with a 1 % solution of vanillin in 50 % $HClO_4$ and heated until color developed. Melting points were measured on a Melt-Temp II apparatus. Mass spectra were registered in a Thermo-Electron and Jeol- SX102A spectrometers. NMR spectra were registered in $CDCl_3$ solutions in a JEOL JNM-ECZ600R spectrometer using the solvent signal as reference. NMR signals assignments were carried out with the aid of a combination of 1D and 2D NMR techniques that included ^{1}H, ^{13}C, ^{1}H-^{1}H Correlated Spectroscopy (COSY), Nuclear Overhauser Effect Spectroscopy (NOESY), Heteronuclear Single Quantum Coherence (HSQC) and Heteronuclear Multiple Bond Correlation (HMBC). All 2D NMR spectra were recorded using the standard pulse sequences and parameters recommended by the manufacturer and were processed employing the MestreNova NMR processing program [See http://mestrelab.com/]. For copies of the NMR spectra see Supporting Information.

General procedure for Ugi 4CR

Aniline (100 µL, 1.1 mmol, 1.1 equiv) and 37 % aq. formaldehyde solution (96 µL, 1.18 mmol, 1.18 equiv.) were added to a suspension of the acetylated bile acid (1 mmol) in anhydrous CH_3OH (6 mL) and 1,2-dichloroethane (2 mL) and the mixture was stirred at room temperature for 15 min. Ethyl isocyanoacetate (120 µL, 1.1 mmol, 2.2 equiv.) was added and the mixture was stirred under reflux until the starting steroid was consumed (TLC). The solvent was evaporated in vacuo and the residue was submitted to a chromatographic column packed with silica gel (35 g), that was eluted with hexane/acetone mixture (85:15) to afford the desired adduct.

Ugi adduct 3a: Reaction time 29 h. Amorphous white solid (453 mg, 0.711 mmol, 71.3 % yield). **^{1}H NMR** (400 MHz, $CDCl_3$) δ: 7.42–7.24 (m, 5H, H-32, H-33, H-34, H-35, H-36), 6.91 (t, J = 5.5 Hz, NH), 4.68 (tt, J = 11.3, 4.8 Hz, 1H, H-3), 4.30 (d, J = 2.0 Hz, 1H, H-25), 4.19 (q, J = 7.1 Hz, 2H, H-29), 4.01 (d, J = 5.5 Hz, 1H, H-27), 2.16 (ddd, J = 14.8, 10.8, 4.6 Hz, 1H, H-23a), 1.99 (s, 3H. CH_3 acetyl), 1.26 (t, J = 7.2 Hz, 3H, H-30),

J. Mex. Chem. Soc. **2024**, *68*(2)
Regular Issue

ISSN-e 2594-0317

0.88 (s, 3H, H-19), 0.68 (d, *J* = 5.8 Hz, 3H, H-21), 0.55 (s, 3H, H-18). **^{13}C{^{1}H} NMR** (100.53 MHz, $CDCl_3$) δ: 35.0 C-1, 26.3 C-2, 74.3 C-3, 32.2 C-4, 41.8 C-5, 27.0 C-6, 26.6 C-7, 35.7 C-8, 40.3 C-9, 34.5 C-10, 20.8 C-11, 40.0 C-12, 42.6 C-13, 56.4 C-14, 24.1 C-15, 28.1 C-16, 56.0 C-17, 11.9 C-18, 23.3 C-19, 35.4 C-20, 18.2 C-21, 31.5 C-22, 31.0 C-23, 175.0 C-24, 53.9 C-25, 169.2 C-26, 41.2 C-27, 169.7 C-28, 61.4 C-29, 14.1 C-30, 142.8 C-31, 127.8 C-32 C36, 129.9 C-33 C-35, 128.4 C-34, 21.4 CH_3 acetyl, 170.6 C=O acetyl. **HRMS** (APCI) *m/z*: $[M+H]^+$ calcd for $C_{38}H_{57}N_2O_6$ 637.4211; found 637.42292.

Ugi adduct 3b: Reaction time 25 h. Amorphous white solid (558 mg, 0.802 mmol, 80.4 % yield). **^{1}H NMR** (400 MHz, $CDCl_3$) δ: 7.44–7.28 (m, 5H, H-32, H-33, H-34, H-35, H-36), 6.96 (t, *J* = 5.5 Hz, 1H, NH), 5.11 (dt, *J* = 12.3, 4.8 Hz, 1H, H-6), 4.67 (tt, *J* = 11.3, 4.7 Hz, 1H, H-3), 4.31 (d, *J* = 2.2 Hz, 2H, H-25), 4.20 (q, *J* = 7.2 Hz, 2H, H-29), 4.02 (d, *J* = 5.5 Hz, 2H, H-27), 2.17 (ddd, *J* =17.0, 10.5, 4.4 Hz, 1H, H-23a), 2.02 (s, 3H, CH_3 acetyl), 1.99 (s, 3H, CH_3 acetyl), 1.27 (t, *J* = 7.2 Hz, 3H, H-30), 0.93 (s, 3H, H-19), 0.69 (d, *J* = 5.7 Hz, H-21), 0.56 (s, 3H, H-18). **^{13}C{^{1}H} NMR** (100.53 MHz, $CDCl_3$) δ: 35.0 C-1, 26.4 C-2, 73.6 C-3, 26.2 C-4, 45.3 C-5, 70.9 C-6, 31.2 C-7, 34.5 C-8, 39.8 C-9, 36.0 C-10, 20.6 C-11, 39.8 C-12, 42.8 C-13, 56.0 C-14, 24.0 C-15, 27.9 C-16, 55.9 C-17, 11.9 C-18, 23.2 C-19, 35.3 C-20, 18.2 C-21, 31.5 C-22, 31.0 C-23, 175.0 C-24, 53.9 C-25, 169.1 C-26, 41.2 C-27, 169.8 C-28, 61.4 C-29, 14.1 C-30, 142.8 C-31, 127.8 C-32 C-36, 129.9 H-33 C-35, 128.4 H-34, 170.4 2xC=O acetyl, 21.3 2xCH_3 acetyl. **HRMS** (APCI) *m/z*: $[M+H]^+$ calcd for $C_{40}H_{59}N_2O_8$ 695.4266; found 695.42787.

Ugi adduct 3c: Reaction time 24 h. Amorphous white solid (612 mg, 0.880 mmol, 88.2 % yield). **^{1}H NMR** (400 MHz, $CDCl_3$) δ: 7.34-7.28 (m, 5H, H-32, H-33, H-34, H-35, H-36), 4.84 (q, *J* = 3.1 Hz, 1H, H-7), 4.56 (tt, *J* = 11.3, 4.5 Hz, 1H, H-3), 4.31 (d, *J* = 4.6 Hz, 2H, H-25), 4.20 (q, *J* = 7.2 Hz, 2H, H-29), 4.02 (d, *J* = 5.4 Hz, 2H, H-27), 2.03 (s, 3H, CH_3 acetyl), 2.01 (s, 3H, CH_3 acetyl), 1.27 (t, *J* = 7.2 Hz, 3H, H-30), 0.89 (s, 3H, H-19), 0.70 (d, *J* = 5.9 Hz, 3H, H-21), 0.56 (s, 3H, H-18). **^{13}C{^{1}H} NMR** (100.53 MHz, $CDCl_3$) δ: 34.6 C-1, 26.7 C-2, 74.1 C-3, 34.8 C-4, 40.9 C-5, 31.3 C-6, 71.2 C-7, 37.8 C-8, 34.0 C-9, 34.7 C-10, 20.6 C-11, 39.4 C-12, 42.6 C-13, 50.3 C-14, 23.5 C-15, 27.9 C-16, 55.8 C-17, 11.6 C-18, 22.6 C-19, 35.3 C-20, 18.2 C-21, 31.5 C-22, 31.0 C-23, 174.9 C-24, 53.9 C-25, 169.1 C-26, 41.2 C-27, 169.8 C-28, 61.4 C-29, 14.2 C-30, 142.8 C-31, 127.8 C-32 C-36, 129.8 C-33 C-35, 128.3 C-34, 21.5, 21.4 CH_3 acetyl, 170.5, 170.4 C=O acetyl. **HRMS** (APCI) *m/z*: $[M+H]^+$ calcd for $C_{40}H_{59}N_2O_8$ 695.4266; found 695.42884.

Ugi adduct 3d: Reaction time 30 h. Amorphous white solid (592 mg, 0.851 mmol, 85.3 % yield). **^{1}H NMR** (400 MHz, $CDCl_3$) δ: 7.43-7.28 (m, 5H, H-32, H-33, H-34, H-35, H-36), 6.95-6.86 (m, 1H, NH), 5.01-4.94 (m, 1H, H-12), 4.67 (tt, *J* = 11.2, 4.6 Hz, 1H, H-3), 4.31 (d, *J* = 5.8 Hz, 2H, H-25), 4.20 (q, *J* = 7.1Hz, 2H, H-29), 4.03 (d, *J* = 5.3 Hz, 2H, H-27), 2.22-2.08 (m, 1H, H-23a), 2.01 (s, 3H, CH_3 acetyl), 2.00 (s, 3H, CH_3 acetyl), 1.27 (t, *J* = 7.1 Hz, 3H, H-30), 0.87 (s, 3H, H-19), 0.64 (s, 3H, H-18), 0.58 (d, *J* = 5.7 Hz, 3H, H-21). **^{13}C{^{1}H} NMR** (100.53 MHz, $CDCl_3$) δ: 34.7 C-1, 26.6 C-2, 71.2 C-3, 32.2 C-4, 41.8 C-5, 27.2 C-6, 25.8 C-7, 35.6 C-8, 34.3 C-9, 34.0 C-10, 26.8 C-11, 75.8 C-12, 44.9 C-13, 49.3 C-14, 23.4 C-15, 25.6 C-16, 47.5 C-17, 12.3 C-18, 23.0 C-19, 34.6 C-20, 17.4 C-21, 31.2 C-22, 30.9 C-23, 174.8 C-24, 53.9 C-25, 169.1 C-26, 41.2 C-27, 169.8 C-28, 61.5 C-29, 14.1 C-30, 142.7 C-31, 127.8 C-32 C-36, 129.9 C-33 C-35, 128.4 C-34, 21.4, 21.3 CH_3 acetyl, 170.5, 170.4 C=O acetyl. **HRMS** (APCI) *m/z*: $[M+H]^+$ calcd for $C_{40}H_{59}N_2O_8$ 695.4266; found 695.4278.

Ugi adduct 3e: Reaction time 30 h. Amorphous white solid (665 mg, 0.883 mmol, 88.3 % yield). **^{1}H NMR** (400 MHz, $CDCl_3$) δ: 7.43-7.27 (m, 5H, H-32, H-33, H-34, H-35, H-36), 6.87 (t, *J* = 5.5 Hz, NH), 5.00–4.97 (m, 1H, H-12), 4.87 (q, *J* = 3.1 Hz, 1H, H-7), 4.55 (tt, *J* = 11.4, 4.3 Hz, 1H, H-3), 4.30 (q, *J* = 15.3 Hz, 1H, H-25), 4.21 (q, *J* = 7.2 Hz, 2H, H-29), 4.03 (d, *J* = 5.0 Hz, 2H, H-27), 2.07 (s, 3H, CH_3 acetyl), 2.04 (s, 3H, CH_3 acetyl), 2.03 (s, 3H, CH_3 acetyl), 1.28 (t, *J* = 7.2 Hz, 3H, H-30), 0.88 (s, 3H, H-19), 0.65 (s, 3H. H-18), 0.59 (d, *J* = 5.7 Hz, 3H, H-21). **^{13}C{^{1}H} NMR** (100.53 MHz, $CDCl_3$) δ: 34.6 C-1, 27.1 C-2, 74.0 C-3, 34.6 C-4, 40.9 C-5, 31.2 C-6, 70.7 C-7, 37.8 C-8, 28.9 C-9, 34.3 C-10, 26.8 C-11, 75.3 C-12, 45.0 C-13, 43.3 C-14, 22.8 C-15, 25.5 C-16, 47.4 C-17, 12.1 C-18, 22.5 C-19, 34.5 C-20, 17.4 C-21, 31.2 C-22, 30.9 C-23, 174.7 C-24, 53.8 C-25, 169.02 C-26, 41.2 C-27, 169.8 C-28, 61.5 C-29, 14.1 C-30, 142.7 C-31, 127.8 H-32 C-36, 129.9 C-33 C-35, 128.4 C-34, 21.6, 21.4, 21.3 CH_3 acetyl, 170.5, 170.4, 170.3 C=O acetyl. **HRMS** (APCI) *m/z*: $[M]^+$ calcd for $C_{42}H_{60}N_2O_{10}$ 752.4242; found 752.4265.

J. Mex. Chem. Soc. **2024**, *68*(2)
Regular Issue

ISSN-e 2594-0317

Results and discussion

Treatment of the acetylated lithocholic acid **2a** with 1.1 equivalents of aniline, formaldehyde and ethyl isocyanoacetate in methanol at room temperature afforded the desired Ugi adduct **3a** in poor yield (less than 50 %) after more than 24 hours. The same reaction in refluxing methanol afforded **3a** in 67.5 %. Refluxing **2a** in 3/1 anhydrous methanol/dichloroethane mixture increased the yield to 71.3 %. Thus, treatment of the parent acetylated bile acids **2b-e** un such conditions afforded the corresponding Ugi adducts **3b-e** in good yields (Scheme 1). This suggest that the low solubility of the staring material **2a**, hindered the reaction.

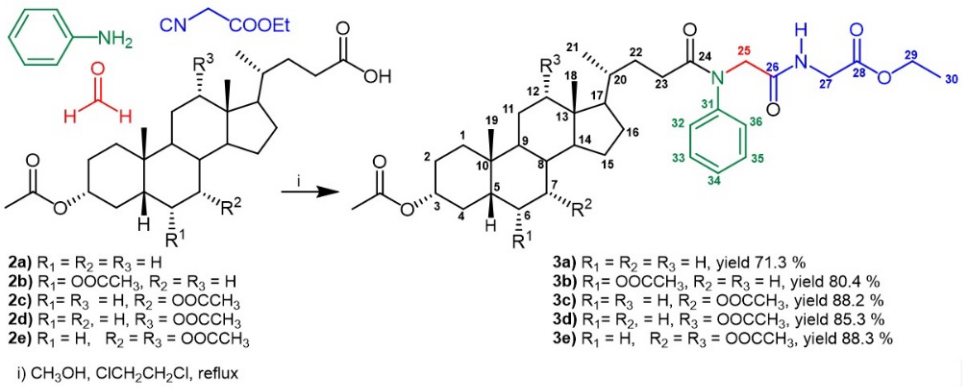

Scheme 1. Synthesis of modified side chain bile acid by Ugi 4CR reaction.

Combined 1D and 2D NMR techniques allowed the assignment of the observed chemicals shifts and the corroboration of the structures of the obtained Ugi adducts **3a-e**. In addition to the NMR signals associated to the functionality present in the steroid core of each bile acid, the most salient characteristics are the signals of the enlarged and highly functionalized side chain. Tables 1 and 2 respectively show ^{1}H and ^{13}C NMR signals of the side chain of the obtained compounds.

The signals of H-20, H-21 and H-23a,b corroborate the integrity of the fragment corresponding to the side chain of the starting bile acid. The addition of the new fragment is evinced by the signals of the protons of three new methylenes (H-25, H-27 and H-29) as well as that of the methyl group (H-30). Additionally, the chemical shifts of the NH group and the aromatic protons characterize the introduced fragment (Table 1).

Table 1. Selected ^{1}H NMR signals of the obtained compounds (δ ppm; *J* Hz).

	3a	**3b**	**3c**	**3d**	**3e**
H-21	0.68(δ, *J* = 5.8)	0.69(δ, *J* = 5.7)	0.70(δ, *J* = 5.9)	0.58(δ, *J* = 5.7)	0.59(δ, *J* = 5.7)
H-23a	2.16(δ, *J* = 14.8, 10.8, 4.6)	2.17(δ, *J* = 17.0, 10.5, 4.4)	2.18 (δ, *J* = 14.8, 11.5, 4.4)	2.15 (δ, *J*= 15.1, 11.2, 4.3)	2.15 (m)
H-23b	2.03 (m)	2.01 (m)	2.02 (m)	2.01 (m)	2.01 (m)
H-25	4.30(δ, *J* = 2.0)	4.31(δ, *J* = 2.2)	4.31(δ, *J* = 4.6)	4.31(δ, *J* = 5.8)	4.30(δ, *J* = 15.3)
H-27	4.01(δ, *J* = 5.5)	4.02(δ, *J* = 5.5)	4.02(δ, *J* = 5.4)	4.03(δ, *J* = 5.3)	4.03(δ, *J* = 5.0)
H-29	4.19(δ, *J* = 7.1)	4.20(δ, *J* = 7.2)	4.20(δ, *J* = 7.2)	4.20(δ, *J* = 7.1)	4.21(δ, *J* = 7.2)

J. Mex. Chem. Soc. **2024**, *68*(2)
Regular Issue

ISSN-e 2594-0317

H-30	1.26(δ, *J* = 7.2)	1.27(δ, *J*=7.2)	1.27(δ, *J* = 7.2)	1.27(δ, *J* = 7.1)	1.28(δ, *J* = 7.2)
H (Ar)	7.42–7.24(m)	7.44–7.28(m)	7.34-7.28(m)	7.43-7.28(m)	7.43-7.27(m)
NH	6.91(δ, *J* = 5.5)	6.96(δ, *J* = 5.5)	6.93(δ, *J* = 5.5)	6.91(δ, *J* = 5.5)	6.87(δ, *J* = 5.5)

The connectivity in the enlarged side chain can verified by HMBC correlations. The combined HSQC and NOE correlations also corroborate the signal assignment and the connectivity (Fig. 2).

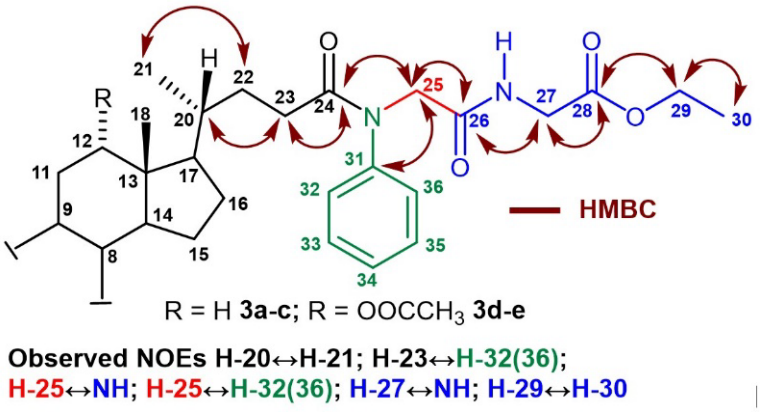

Fig. 2. Structure and 2D NMR correlations in the side chain of the obtained Ugi adducts.

The signals of carbons C-20 to C-24 account for the integrity of the fragment of the side chain coming for the bile acid. The acetylated hydroxyl group at position C-12α in compounds **3d** and **3e**, exert minor shielding effects on the signals of C-20 and C-21, compared to those in compounds **3a-c** (*vide supra*, Figure 2). The introduced fragment is characterized by the signals of the C=O groups of the amide and ester moieties installed at positions C-26 and C-28 respectively. In addition to the signals of the carbons of the ethyl group (C-29 and C-30) of the ester at C-28, the chemical shifts of the methylenes C-25 and C-27 respectively attached to the nitrogen atoms, also characterize the enlarged side chain. Additionally, the NMR signals associated to the aromatic ring corroborate the introduction of the aniline fragment (Table 2).

Table 2. $^{13}C\{^{1}H\}$ signals of the obtained compounds (δ ppm).

	3a	**3b**	**3c**	**3d**	**3e**
C-20	35.4	35.3	35.3	34.6	34.5
C-21	18.2	18.2	18.2	17.4	17.4
C-22	31.5	31.5	31.5	31.2	31.2
C-23	31.0	31.0	31.0	30.9	30.9
C-24	175.0	175.0	174.9	174.8	174.7
C-25	53.9	53.9	53.9	53.9	53.8

J. Mex. Chem. Soc. **2024**, *68*(2)
Regular Issue

ISSN-e 2594-0317

C-26	169.2	169.1	169.1	169.1	169.0
C-27	41.2	41.2	41.2	41.2	41.2
C-28	169.7	169.8	169.8	169.8	169.8
C-29	61.4	61.4	61.4	61.5	61.5
C-30	14.1	14.1	14.2	14.1	14.1
C-31	142.8	142.8	142.8	142.7	142.7
C-32, C-36	127.8	127.8	127.8	127.8	127.8
C-33, C-35	129.9	129.9	129.8	129.9	129.9
C-34	128.4	128.4	128.3	128.4	128.4

Conclusions

We have set up optimal conditions for the four-component Ugi Reaction involving five different acetylated bile acids, formaldehyde, aniline and ethyl isocyanoacetate that affords the corresponding adducts in 71 to 88 % yield. Combined 1D and 2D NMR techniques allowed the unambiguous structural characterization and assignment of the functional ^{1}H NMR signals and all ^{13}C{^{1}H} NMR chemical shifts.

Acknowledgements

The authors acknowledge financial support provided by *Dirección General de Asuntos del Personal Académico* (Grant IN204323), CONACyT (Grant A1-S-8019) and the Faculty of Chemistry UNAM (PAIP-5000-9063). The authors thank Nayeli Balbiaux and Jessica Amacosta (USAII-FQ) for registering NMR and HRMS spectra. JVC thanks CONACyT for the Postdoctoral Fellowship granted.

References

1. Monte, M. J.; Marin, J. J.; Antelo, A.; Vazquez-Tato, J. *World J. Gastroenterol.* **2009**, *15*, 804−816. DOI: dx.doi.org/10.3748/wjg.15.804.
2. Virtanen, E.; Kolehmainen, E. *Eur. J. Org. Chem.* **2004**, 3385−3399. DOI: doi.org/10.1002/ejoc.200300699.
3. (a) Luo, J.; Chem, Y.; Zhu, X.X. *Langmuir.* **2009**, *25*, 10913–10917. DOI: doi.org/10.1021/la9013703. (b) Maitra, U.; Mukhopadhyay, S.; Sarkar, A.; Rao, P.; Indi, S. S. *Angew. Chem., Int. Ed.* **2001**, *40*, 2281−2283. DOI: doi.org/10.1002/1521-3773(20010618)40:12<2281::AID-ANIE2281>3.0.CO;2-L . (c) Zhang, J.; Luo, J.; Zhu, X.X.; Junk, M. J. N.; Hinderberger, D. *Langmuir.* **2010**, *26*, 2958–2962. DOI: doi.org/10.1021/la9028996.
4. Brotherhood, P. R.; Davis, A. P. *Chem. Soc. Rev.,* **2010**, *39*, 3633–3647. DOI: doi.org/10.1039/B926225N.
5. Zhang, M.; Strandman, S.; Waldron, K. C.; Zhu, X. X. *J. Mater. Chem. B,* **2016**, *4*, 7506–7520. DOI: doi.org/10.1039/C6TB02270G.

J. Mex. Chem. Soc. **2024**, *68*(2)
Regular Issue

ISSN-e 2594-0317

6. (a) Li, R.; Carpentier, E., Newell, E.D.; Olague L.M.; Heafey, E.; Yihwa, C. *Langmuir.* **2009**, *25,* 13800–13808. DOI: doi.org/10.1021/la901826y. (b) Santiago-Sampedro, G. I.; Aguilar-Granda, A.; Torres-Huerta, A.; Flores-Álamo, M.; Maldonado-Domínguez, M.; Rodríguez-Molina, B.; Iglesias-Arteaga, M. A. *J. Org. Chem.* **2022**, *87*, 2255−2266. DOI: doi.org/10.1021/acs.joc.1c01334.
7. Mayorquín-Torres, M.C.; Flores-Alamo, M.; Iglesias-Arteaga, M.A. Steroids, **2015**, 101, 21–27.
8. Selected references (a) Zhu, J.; Bienaymé, H. *Multicomponent Reactions*, 1st Ed. Wiley-VCH: Weinheim, Germany, **2005**, 1−468. (b) Dömling, A.; Wang, W.; Wang, K. *Chem. Rev.* **2012**, *112*, 3083–3185. DOI: doi.org/10.1021/cr100233r. (c) Rotstein, B. H.; Zaretsky, S.; Rai, V.; Yudin, A. K. *Chem. Rev.* **2014**, *114*, 8323−8359. DOI: doi.org/10.1021/cr400615v. (d) Sunderhaus, J. D.; Martin, S. F. *Chem. Eur. J.* **2009**, *15*, 1300–1308. DOI: doi.org/10.1002/chem.200802140. (e) Biggs-Houck, J. E.; Younai, A.; Shaw, J. T. *Curr. Op. Chem. Biol.* **2010**, *14*, 371−382. DOI: doi.org/10.1016/j.cbpa.2010.03.003. (f) Ulaczyk-Lesanko, A.; Hall, D. G. *Curr. Op. Chem. Biol.* **2005**, *9*, 266−276. DOI: doi.org/10.1016/j.cbpa.2005.04.003. (g) Cioc, R. C.; Ruijter, E.; Orru, R. V. A. *Green Chem.* **2014**, *16*, 2958–295. DOI: https://doi.org/10.1039/C4GC00013G. (h) Sunderhaus, J. D.; Martin, S. F. *Chem. Eur. J.* **2009**, *15*, 1300–1308. DOI: https://doi.org/10.1002/chem.200802140. (i) Cores, A.; Clerigué, J.; Orocio-Rodríguez, M.; Menéndez, J. C. *Pharmaceuticals.* **2022**, *15*, 1009. DOI: https://doi.org/10.3390/ph15081009.
9. (a) Reguera, L.; Attorresi, C. I.; Ramírez, J. A.; Rivera, D. G. *Beilstein J. Org. Chem.* **2019**, *15*, 1236–1256. DOI: doi.org/10.3762/bjoc.15.121. (a) Rivera, D. G.; Wessjohann, L. A.; *Molecules.* **2007**, **12**, 1890-1899. DOI: doi.org/10.3390/12081890.
10. (a) Mayorquín-Torres, M. C.; Flores-Álamo, M.; Iglesias-Arteaga, M. A. *Tetrahedron Lett.* **2017**, *58*, 3500–3504. DOI: doi.org/10.1016/j.tetlet.2017.07.081. (b) Mayorquín-Torres, M. C.; Navarro-Huerta, A.; Maldonado-Domínguez, M.; Flores-Álamo, M.; Rodríguez-Molina, B.; Iglesias-Arteaga, M. A. *J. Org. Chem.* **2021**, *86*, 4112−4120. DOI: doi.org/10.1021/acs.joc.0c02943.
11. Selected references: (a) Rocha, O.R.; Rodrigues M.O.; Neto. B.A.D. *ACS Omega.* **2020**, *5*, 972–979. DOI: doi.org/10.1021/acsomega.9b03684. (b) Foucad, M. A.; Abdel-Hamid, H.; Ayoup M. S. *RSC Adv.* **2020**, *10*, 42644–42681. DOI: doi.org/10.1039/D0RA07501A.

Article

J. Mex. Chem. Soc. **2024**, *68*(2)
Regular Issue

ISSN-e 2594-0317

Nanoencapsulation of Antifungal *Piper schlechtendalii* Extract in Poly(lactide-co-glycolic) Acid to Enhance Photostability

Felipe Barrera-Méndez[1,2]*, Laura Stefany Licona Velázquez[1], Diter Miranda-Sánchez[1], Aidée Jazmín Anguiano Hernández[3], Israel Bonilla-Landa[1], José Luis Olivares-Romero[1], Randy Ortíz Castro[1], Greta Hanako Rosas Saito[1], Juan Luis Monribot Villanueva[1], José Antonio Guerrero Analco[1], Oscar Carmona-Hernández[3], Juan Carlos Noa Carrazana[4]

[1]Red de Estudios Moleculares Avanzados, Instituto de Ecología AC, Xalapa, Veracruz, México.
[2]Investigador por México-CONAHCYT en el Instituto de Ecología AC, Xalapa, Veracruz, México.
[3]Facultad de Ciencias Agrícolas, Universidad Veracruzana. Xalapa, Veracruz, México.
[4]Instituto de Biotecnología y Ecología Aplicada, Universidad Veracruzana, Xalapa, Veracruz, México.

***Corresponding author:** Felipe Barrera-Méndez, email: felipe.barrera@inecol.mx

Received Febraury 3rd, 2023; Accepted September 4th, 2023.

DOI: http://dx.doi.org/10.29356/jmcs.v68i2.1964

Abstract. Synthetic fungicides are used to control fungal diseases in plants, such as those caused by members of the Fusarium genus. Nonetheless, the over-application of synthetic formulations can generate other problems, like phytotoxicity, or the pollution of water and soil. In this context, botanical extracts with antifungal properties can represent an environmentally friendly alternative to control fungal infections. The application of natural products in the form of crude extracts still requires the incorporation of toxic organic solvents to be used as vehicle. Nanotechnology allows the dispersion of hydroalcoholic extracts in water simply by the nanoencapsulation of the active molecules in a biodegradable polymer, with the advantage that no organic solvents are required while, at the same time, this polymer may protect the extract against photodegradation. The present study aims to encapsulate an antifungal Piper schlechtendalii crude extract in poly(lactide-co-glycolide) acid nanospheres, conferring good dispersion in water while protecting the active ingredients against degradation by solar irradiation. The particle size, zeta potential, and encapsulation efficiency obtained were 170 nm, -37 mV, and 33.7 %, respectively. The system obtained showed good dispersion in water, in the form of a colloidal suspension of polymeric nanospheres. After 24 h of exposure to UV-A radiation, crude extract only retained 58.35 % of its original Fusarium solani growth inhibition capacity, while the nanoencapsulated extract retained 70 %. The study concluded that the biodegradable polymer does confer photoprotection to the active ingredients in the antifungal Piper extract while simultaneously removing the necessity of organic solvents as vehicles, potentially reducing the environmental impact.
Keywords: Plant extract; biodegradable polymer; fusarium; pesticide; colloidal suspension.

Resumen. Los fungicidas sintéticos son usados para controlar enfermedades fúngicas en plantas, como aquellas causadas por el género Fusarium. Sin embargo, la aplicación desmedida de formulaciones sintéticas puede generar otros problemas, como fitotoxicidad, o contaminación de agua y suelos. En este contexto, extractos botánicos con propiedades antifúngicas representan una alternativa ecológicamente amigable para controlar infecciones fúngicas. La aplicación de productos naturales en forma de extractos crudos aún requiere la incorporación de disolventes orgánicos tóxicos para ser utilizados como vehículos. La nanotecnología permite la dispersión de extractos hidroalcóholicos en agua simplemente nanoencapsulando las moléculas activas en polímeros biodegradables, con la ventaja de que no requiere disolventes orgánicos mientras que, a la vez, dicho polímero protege al extracto contra fotodegradación. El presente estudio busca encapsular un extracto crudo antifúngico de Piper schlechtendalii en nanoesferas de poli(ácido láctico-co-glicólico), brindando buena dispersión en agua

J. Mex. Chem. Soc. **2024**, *68*(2)
Regular Issue

ISSN-e 2594-0317

mientras se protege a los ingredientes activos contra degradación por luz solar. El tamaño de partícula, potencial zeta, y eficiencia de encapsulación obtenidos fueron 170 nm, -37 mV, y 33.7 %, respectivamente. El sistema obtenido mostró buena dispersión en agua, en forma de una suspensión coloidal de nanoesferas poliméricas. Después de 24 h de exposición a radiación UV-A, el extracto crudo solo retuvo 58.35 % de su inhibición de crecimiento de Fusarium solani original mientras que el extracto nanoencapsulado retuvo el 70 %. El estudio concluyó que el polímero biodegradable logra brindar fotoprotección a los ingredientes activos del extracto de Piper mientras que, simultáneamente, remueve la necesidad de usar disolventes orgánicos como vehículo, reduciendo potencialmente el impacto ambiental.
Palabras clave: Extracto vegetal; polímero biodegradable; fusarium; suspensión coloidal.

Introduction

One of the most common alternatives to control fungal infections on plants, like those caused by fungi of the *Fusarium* genus, is the application of synthetic fungicides, but such pesticides have a few problems associated with them. Over 90% of the applied pesticides are unable to reach the target area required for effective pest control. [1] This is due to different factors including the application technique, physicochemical properties of the pesticides, and environmental conditions like wind speed, humidity, and temperature, influence the extent of loss during application. [2,3] The remaining losses are attributed to leaching, evaporation, deposition, being washed away, and degradation of the active ingredient by photolysis, hydrolysis, and microbial activity. [4] Given all these accumulated losses, the amount of pesticide in the target area is below the minimum effective concentration, and to achieve the desired biological response within a given period, it is necessary to increase the quantity of product applied, as well as the number of applications. This does not only increase the cost of the treatment, but also brings unfavorable outcomes either to plants or to the environment, including soil and water pollution, ultimately endangering human health. [4,5] In addition to the previously mentioned, there are reports that indicate that some synthetic fungicides, like the triazole fungicides, can provoke phytotoxicity in economically important crops, affecting the growth and development of seedlings and the root system, reducing the number of primary roots. [6]

As an environmentally friendly alternative, the search for natural products with applications related to pest management is currently very active. Plant extracts with antimicrobial properties that contain a wide spectrum of secondary or specialized metabolites, whose concentration of bioactive compounds and synergistic effects depend on the environmental conditions, have generated interest from the field of plant disease control. [7–9] In this regard, natural products in the form of extracts, fractions or pure compounds obtained from plants of the genus *Piper* have shown promising antifungal activities. [10] For example, extracts of *Piper capense* and *P. eriopodon* showed antifungal properties against filamentous fungi, such as mycotoxigenic species of the genus *Aspergillus*, *Fusarium*, and *Penicillium*. [11] *Piper divaricatum* also showed antifungal activity against *Fusarium* infection on black pepper, reaching up to 100% of growth inhibition.

[12] At the same time, hexanic extracts of *P. auritum* and *Piper holtonii* showed a relatively good antifungal activity against different phytopathogenic fungi, including *Collectotrichum acutatum, Collectotrichum gloeosporioides,* and *Botryodiplodia theobromae.* [13] Furthermore, isolated compounds obtained from *Piper spp.* extracts have demonstrated fungicide properties against *Fusarium spp.* [14] This biological activity of some of the genus *Piper* species is attributed to the presence of a wide variety of secondary metabolites, like alkaloids, amides, propenyl phenols, lignans, terpenes, flavonoids, among others. [15,16] Regarding the fungicidal activity (resistance to *Fusarium solani f sp piperis*), it is attributed to phenolic compounds specifically found in American *Piper* species. [17] Biological history says that American Piper had developed a mechanism of defense known as Systemic Acquired Resistance (SAR). [18,19] Phenols and flavonoids are overexpressed and act in the fungal wall and the plasmatic membrane, resulting in the disruption of the cell. [20] Some phenols and flavonoids with these characteristics present in Piper are: safrole, apiole, dillapiole, asebogenin, apigenin, quercetin, kaempferol, myricetin and epicatechin. [21]

However, the usage of plant extracts can be hampered by the high volatility and easy degradation of many of the active compounds. Furthermore, in many cases it is necessary to use toxic organic solvents as

J. Mex. Chem. Soc. **2024**, *68*(2)
Regular Issue

ISSN-e 2594-0317

vehicles to incorporate these extracts in the final formulation. So, the encapsulation in suitable nanostructures is a strategy for the preservation and controlled release of bioactive compounds, allowing a better dispersion in water and safer application. [22] Among the materials used to encapsulate the plant extracts, it was found that poly(lactide-co-glycolide) (PLGA) is a very promising one, due to being a biocompatible and biodegradable polymer that degrades by hydrolysis of the ester backbone into non-harmful and non-toxic compounds, and it has been used to enhance the antimicrobial activity of fruit extracts. [23-27] As an additional advantage, PLGA has been proven to bring photoprotection to nanoencapsulated active ingredients. [28] This is relevant given UV light may represent negative effects on natural extracts. The ethanolic extract of *Euphorbia herita* presented antifungal and antibacterial activity against experimental pathogens such as *Escherichia coli* and *Aspergillus niger*, but overexposure to ultraviolet light caused a gradual decrease in the antimicrobial capacity of this plant. [29]This study aims to encapsulate an antifungal crude extract obtained from the *Piper schlechtendalii,* a plant without previous antifungal activity studies and that is endemic to Mexico (with presence in the state of Veracruz), in PLGA nanospheres to protect the active ingredients from photolysis and to preserve their bioactivity when exposed to UV light, as well as to gain dispersion in water without the need of organic solvents.

Experimental

Reagents

G Hydrochloric acid (reagent grade, Sigma-Aldrich, USA), potato dextrose agar (PDA) (Difco, USA), ethanol (analytical-grade, Quimica Rique, Mexico), dichloromethane (DCM) (industrial-grade, Pochteca, Mexico), poly (lactic-co-glycolic) acid (PLGA) 85:15 (reagent grade, Mw 190,000- 240,000, Sigma-Aldrich, USA), acetone (industrial-grade, Pochteca, Mexico), poly vinyl alcohol (PVA) (reagent grade, Mw 89,000-98,000, Sigma-Aldrich, USA), sodium citrate tribasic (reagent grade, Sigma-Aldrich, USA), and type 1 distilled water, obtained by a Genpure water purification system (Thermo Scientific, USA). All organic solvents were purified by simple distillation before use. The industrial-grade solvents were previously distilled before being used in the experiments. The nanoencapsulation of the extract was performed using either the emulsification and solvent evaporation, or the diffusion and solvent evaporation techniques. [30] DCM and acetone were tested as the solvents for the organic phase, PLGA was tested as the biodegradable carrier, and sodium citrate and PVA were tested as the emulsion stabilizer.

Biological material

Plant material (stem and leaves) was collected in Zozocolco, Veracruz, Mexico (Lat 20.14186 Long -97.587901), on April 13, 2019. Only phenotypically similar specimens with healthy appearance were selected. For the bioassays, a phytopathogenic strain of *Fusarium solani* was used, donated by Dr. Mauricio Luna Rodríguez, researcher from the Faculty of Agronomy of the Universidad Veracruzana, Xalapa, Veracruz, Mexico. The strain was cultivated in Petri dishes with potato dextrose agar (PDA) at 27 ± 1°C with periodic reseeding.

Piper schlechtendalii crude extract obtention

The vegetable material was dried on the stove at 45 °C and then pulverized. The hydroalcoholic extract was obtained by maceration in ethanol solution/water solution (70:30), using a mass/volume (m/v) proportion of 1:10, and constant stirring (90 rpm) for 48 h at room temperature. Using only water as solvent could yield a much lower extraction when compared to ethanol or methanol, given these substances increase the solubility of organic material with lower polarity. [31] The solvent was then separated by vacuum filtration and eliminated by rotary evaporation (Büchi RII, Büchi, Switzerland), leaving a completely dry extract (PsE) that was stored in refrigeration until use.

Preparation of stock aqueous solutions

The aqueous phase in the experiments consisted of the dissolution of an emulsion stabilizer in type 1 distilled water. Two different stabilizers were tested, using either a 1 mM sodium citrate solution, or a 1 % w/v PVA solution, respectively. To avoid precipitation of the PLGA nanospheres during the washing process,

J. Mex. Chem. Soc. **2024**, *68*(2)
Regular Issue

ISSN-e 2594-0317

washing solutions were prepared by diluting the aqueous phase ten times, obtaining a concentration of 0.1 mM sodium citrate washing solution, and a 0.1 % w/v PVA washing solution.

Preparation of stock organic solutions

The organic phase consisted of the dissolution of PLGA 85:15 in an organic solvent, with a concentration of 5 mg/L. Two solvents were tested separately: acetone and DCM.

Emulsification and solvent evaporation technique

For each emulsion prepared, 10 mg of the extract previously dissolved in 1 mL of ethanol were added to 5 mL of the PLGA in DCM solution to conform the organic phase. Once homogenized by magnetic stirring, the organic phase was added to 15 mL of the aqueous phase, consisting in a solution of either sodium citrate, or PVA. The emulsion was obtained using an ultrasonic processor (Sonics & Materials, model VCX750-110V) applying 70 % of amplitude in three intervals of 10 seconds. To avoid boiling the DCM, the emulsion was rested in an ice bath for 10 seconds between each interval. Finally, the DCM was removed by rotary evaporation, obtaining solid nanospheres of PLGA suspended in water. Each encapsulation process was repeated 3 times.

Diffusion and solvent evaporation technique

Similarly to the steps performed with the emulsification and solvent evaporation technique, 10 mg of the extract was previously dissolved in 1 mL of ethanol and added to 5 mL of the PLGA solution, the difference being that acetone was used as the organic solvent instead of DCM. Once homogenized by magnetic stirring, the organic phase was poured to 15 mL of the aqueous phase (solution of either sodium citrate, or PVA) under heavy stirring. Since acetone is miscible with water, there was no need for the ultrasonic processor to homogenize both phases. Finally, the acetone was removed leaving the mixture in an extraction hood overnight. Each encapsulation process was repeated 3 times.

Washing of nanospheres

To remove the fraction of extract and stabilizer that remained outside of the PLGA, the nanospheres were washed by centrifugation at 5,000 x g for 30 minutes. Once the supernatant was discarded, the nanospheres were re-suspended in a similar volume of the washing solution, obtaining a colloidal suspension of PLGA nanospheres. This process was performed 3 times.

Characterization of nanospheres

The size and zeta potential were obtained using the dynamic light dispersion technique (DLS), while scanning electron microscopy (SEM) was used to observe the form of the nanoparticles, obtaining the images with a FEI Quanta 250 FEG (United States of America) scanning electron microscope in the Advanced Microscopy Unit (INECOL) To measure the amount of encapsulated extract, it had to be released from the nanospheres and then quantified. To achieve this, a known volume of nanospheres suspension was centrifuged at 5,000 x g to remove the water. Then, a 1 mL of ethanol was added, and the suspension was left in an ultrasonic bath for 30 minutes. After that, the nanospheres were centrifuged at 16,000 x g for 30 minutes. Finally, the ethanol was collected, and the amount of released extract was measured by UV-vis spectrophotometry (Thermo Scientific, Genesys 10S UV-Vis, United States of America). Given the chlorophyll presented the highest absorbance peak, and assuming that all the chemical species in the extract were captured and released in the same proportion, chlorophyll was used as the tracer to measure the concentration of the extract, at a wavelength of 279 nm.

The encapsulation efficiency (EE) was calculated using Equation 1.

$$EE(\%) = (EX_m / EX_0) * 100 \quad (1)$$

where EX_0 is the extract mass used in the encapsulation process and EX_m is the extract mass measured in the ethanol after being released.

J. Mex. Chem. Soc. **2024**, *68*(2)
Regular Issue

ISSN-e 2594-0317

P. schlechtendalii extract release tests

The release profile was obtained by dialyzing 1 mg of extract (either encapsulated or in crude form) in 100 mL of a water/ethanol mixture (90:10), using 10 cm segments of semipermeable cellulose tubes (45 mm flat, 12-14 kD). The pH of the release medium was adjusted to 5 with concentrated HCl, as this was the pH obtained for the PDA used in the antifungal activity tests. The extract was incorporated in 5 mL of the water/ethanol mixture and placed inside the tube (donor medium), while 95 mL of the same mixture was used as the receiving medium, adding a total volume of 100 mL. The dialyzes were performed in amber capped bottles, with constant magnetic stirring (60 rpm), shielded from light by using a cardboard box at room temperature. Samples were taken at different time lapses, and the volume withdrawn was replaced with fresh water/ethanol mixture. Finally, the extract concentration was measured by UV-Vis spectrophotometry. The experiment was performed 3 times for both the crude extract and the nanoencapsualted extract, respectively.

Photodegradation assay

To measure if there is any photoprotection given by the PLGA, 1 mg of extract in crude and nanoencapsulated forms, respectively, were placed in individual glass vials and then irradiated using a UV-A lamp (λ = 354 nm), receiving an irradiance of 13.73 ± 0.035 mW/cm^2 for 24 h.

Antifungal activity of the crude and encapsulate *P. schlechtendalii* extracts

For antifungal characterization of the extracts, 3 µL of conidia suspension of *F. solani* were inoculated in the center of the wells of 12-well culture plates with 1 mL of solid PDA, adjusting the final concentration to 5x10^6 spores/mL, approximately. To test the treatments, the *Piper* extract, either in the crude form or nanoencapsulated form, was incorporated to the PDA up to a concentration of 1 mg/mL. The plates were incubated at 28 ± 1 °C in complete darkness for 5 days. PDA culture media with 5% of ethanol was used as negative control (C-), while solid PDA culture media supplemented with commercial fungicide (Prozan ®) 0.5 µL was used as positive control (C+). The 5% of ethanol present in the control is due this solvent was used as a vehicle for the crude extract. Empty PLGA nanoparticles were tested to evaluate the antifungal activity of the encapsulating polymer, both before and after being exposed to UV-light for 24 h (P and UP, respectively). The concentration of empty PLGA nanoparticles was the same as that of the PLGA present in the nanospheres that contain 1 mg of encapsulated extract. The treatments tested consisted in the extract in its crude and nanoencapsulated forms, before and after been exposed to UV light for 24 h; crude extract (E), nanoencapsulated extract (N), UV irradiated extract (UE), and UV irradiated nanospheres with extract (UN). A treatment consisting in the encapsulation of previously irradiated extract was tested as well (N-UE). The experiments were performed with 5 replicates. The antifungal activity was recorded at 7 days after the inoculation and the area of fungus growth were obtained with image analysis software Image J®. The growth inhibition percentage (GIP) was calculated using Equation 2.

$$GIP\ (\%) = 100 - (A_i/A_c) * 100 \quad (2)$$

where A_c is the growth area of the fungus in the negative control well (full growth), and A_i is the growth area of the fungus in the well exposed to the treatment.

Comparative chemical profiling of the extract

An untargeted metabolomic analysis was performed on the extract before and after been exposed to the 24 h of UV-light ($n \geq 6$), using an ultra-high performance liquid chromatography (UPLC) system (Waters, model Acquity class I), coupled to a quadrupole time-of-flight (QTOF) mass spectrometer (Waters, model Synapt G2-Si HDMi), as proposed by Monribot-Villanueva et al. [32] The chromatography was carried out on an Acquity BEH column (1.7 µm, 2.1 x 50 mm) with a column and sample temperatures of 40 °C and 15 °C, respectively. The mobile phase consisted of (A) water and (B) acetonitrile, both with 0.1 % of formic acid (SIGMA). The gradient conditions of the mobile phases were 0-20 min a linear gradient from 1 to 99 % of B, 20-24 min 99 % of B, 24-25 min a linear gradient from 99 to 1 % of B (total run time 30 min). The flow rate was 0.3 mL/min and 5 µL of extract was injected. The mass spectrometric analysis was performed with an electrospray ionization source in positive mode with a capillary, sampling cone and source offset voltages of 3000, 40 and 80 V, respectively. The

J. Mex. Chem. Soc. **2024**, *68*(2)
Regular Issue

ISSN-e 2594-0317

source temperature was 100 °C and the desolvation temperature was 20 °C. The desolvation gas flow was 600 L/h and the nebulizer pressure was 6.5 Bar. Leucine-enkephalin was used as the lock mass (556.2771, $[M+H]^+$). The conditions used for MSe analysis were mass range 50-1200 Da, Function 1 CE, 6 V, function 2 CER 10-30 V, scan time 0.5 sec. The data were acquired and processed with MassLynx (version 4.1) and MarkerLynx (version 4.1) software respectively. All statistical analysis (Hierarchical clustering, t-test and Fold Change analysis) were performed in the bioinformatic MetaboAnalyst platform. [33]

Results and discussion

Characterization of nanospheres and selection of encapsulating systems

Table 1 shows the hydrodynamic particle diameter, zeta potential, and encapsulating efficiency for the four encapsulating systems tested. Both particle size and zeta potential were obtained using a Malvern Zetasizer, model Nano ZS90 (England).

Table 1. Parameters of the different encapsulating systems.

Solvent	Stabilizer	Size (nm)	Zeta potential (mV)	Encapsulating Efficiency (%)
Acetone	PVA	201.5 ± 5.82	25.63 ± 3.18	20.02 ± 2.54
Acetone	Sodium Citrate	147.7 ± 3.05	37.67 ± 4.93	24.95 ± 3.49
DCM	PVA	269.73 ± 3.75	27.77 ± 0.63	4.19 ± 1.36
DCM	Sodium Citrate	259.16 ± 3.31	35.37 ± 1.5	2.93 ± 0.81

It can be observed that the emulsion stabilizer used in the encapsulation influences the size and the zeta potential of the nanospheres, resulting in both a smaller diameter and a higher stability of the particles when using sodium citrate. Fig. 1 shows the SEM images of the particles of each of the four encapsulating systems, where spherical particles with smooth surfaces can be observed.

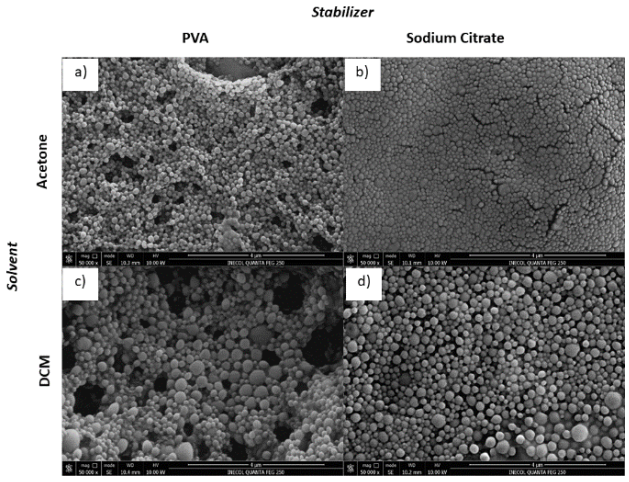

Fig. 1. Morphology of the nanospheres obtained using different solvents and stabilizers at 50 000 X: **(a)** Acetone + PVA, **(b)** Acetone + Sodium Citrate, **(c)** DCM + PVA, **(d)** DCM + Sodium Citrate.

J. Mex. Chem. Soc. **2024**, *68*(2)
Regular Issue

ISSN-e 2594-0317

Since smaller particles can achieve better penetration of the active substance into tissues with reduced consumption rates, and a higher zeta potential denotes better dispersion of the particles in water for longer times, sodium citrate was chosen as the best stabilizer to use in the nanoencapsulation of the extract. [34] On the other hand, the solvent presents an important effect on the encapsulation efficiency, given that the systems that used DCM only achieved percentages under 5 %, while the systems that used acetone managed to reach encapsulations over the 20 %, making the acetone the better solvent to use in the extract encapsulation. In addition to the previously mentioned, the system that used acetone and sodium citrate was the one that yielded the smallest particle size, higher zeta potential, and higher encapsulation efficiency, making it the best encapsulation system for the extract. The largest amount of extract is captured during the nanoemulsion step, with a capture percentage of 0.5 to 20 %, depending on the type of nanosystem. The capture efficiency values in PLGA nanoparticles are related to the solubility of the trapped material in water, since the hydrophilic compounds during the synthesis tend to pass from the organic phase to the aqueous phase, presenting weaker interactions with the polymer and resulting in lower capture efficiencies than the hydrophobic compounds. [29] Regarding the polymer matrix, PLGA degrades *in vivo* into harmless products. Its final degradation products are lactate (lactic acid salt form) and glycolate (glycolic acid salt form), and in *in vitro* systems it does so through hydrolysis of ester bonds, obtaining lactic acid and glycolic acid as final degradation products. [35]

Extract release profiles

It has been reported that the lipases from fungi of the *Candida, Mucor,* and *Rhizopus* geniuses have a significant effect on PLGA degradation by enzyme-catalysed cleavage of ester bonds of the polymer. [36] More specifically, studies have demonstrated that fungus of Fusarium genius would favor the degradation of PLGA copolymers by destroying the crystallization of poly lactide acid (PLA) segments. [37] However, this process was completed over a relative long time (15 weeks) compared to the 6 days that took the release profile experiment. Given this, it is safely to asume that the extract is releases mainly by molecular difussion and not by erotion of the polymer matrix. Preliminary results showed that the extract would not be released into distilled water due to its low solubility, while a liberation in pure ethanol proved to be too fast, dialyzing 100 % of the extract in a few hours, regardless of whether it was in its crude or nanoencapsulated form. Fig. 2 shows the release profiles obtained for the crude extract and the nanoencapsulated extract in water/ethanol (90:10) medium, adjusted at pH 5.

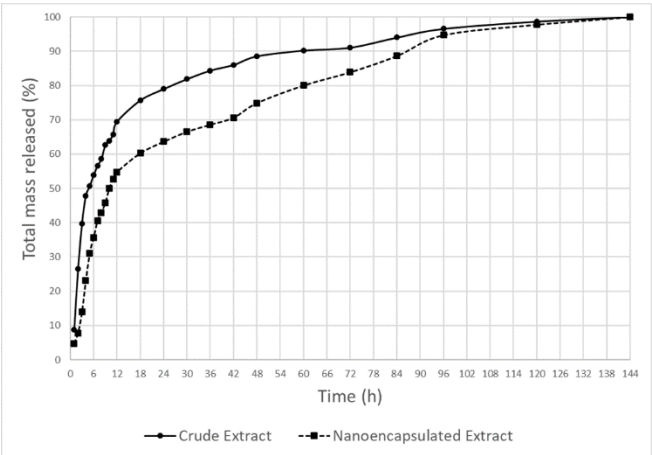

Fig. 2. Percentage of mass of *Piper* extract released in the water/ethanol (90:10) receiving medium.

At first sight, the nanoencapsulated extract is dialyzed slower than its crude form. This is congruent with the literature, and is explained by the molecular diffusion, a relative slow mechanism of mass transport that the extract must endure to travel from the PLGA polymer matrix of the nanospheres to the donor medium inside the cellulose tube, and finally, from the donor medium to the receiving medium. [16] While the crude extract has dialyzed 50 % of its mass in 5 hours, the nanoencapsulated extract took 11 hours to reach that

J. Mex. Chem. Soc. **2024**, *68*(2)
Regular Issue

ISSN-e 2594-0317

percentage. Another important point is at hour 48, having almost reached 90% of the crude extract mass release while the nanospheres still conserve 25 % of the extract load.

Photodegradation assay

In order to determine the effect of UV exposition on PsE, an untargeted metabolomic analysis was performed comparing PsE exposed and non-exposed to UV radiation. The UV exposition clearly changes the chemical profile of the PsE (Fig. 3**(a)**). The hierarchical clustering by the Ward algorithm displayed in the top of Fig. 3**(a)** shows that UV treatment consistently affect the chemical composition of the *Piper* extract. The compounds tentatively identified in the PsE exposed and non-exposed to UV radiation were grouped mainly in seven metabolic pathways (Fig. 3**(b)**) which exhibited the highest pathway impact values. Detailed information about all metabolic pathways and the tentatively identified compounds is shown in Supplementary Material. When it is performed a comparative fold change (FC) analysis using a threshold value of 1.5 joined to a *t*-test analysis between PsE exposed and non-exposed to UV radiation, the intensity of 294 features (mass/charge-retention times pairs) remain unchanged, while the intensity of 20 and 58 features increased and decreased after UV treatment, respectively (Fig. 3**(c)**). The compounds methyl-hexyl caffeate (FC=3.63) and linolenic acid (FC=3.03) increased their content after UV treatment. On the other hand, the compounds feruloyltyramine (FC=0.63), pyridoxine (FC=0.59), pantetheine phosphate (FC=0.59), apiole (FC=0.50), aceteugenol (FC=0.50), methyl-trimethoxycinnamate (FC=0.48), eugenyl benzoate (FC=0.48), (2E,6E)-piperamide-C7:2 (FC=0.48), sphinganine (FC=0.44), methyl 3-(3,4-dimethoxyphenyl)propanoate (FC=0.30), 3-hydroxy-4-methoxy-2-(3,7,11-trimethyldodeca-2,6,10-trienyl)benzoic acid (FC=0.26), ethyl 3-(3,4-dimethoxyphenyl)propanoate (FC=0.25) and acetoxychavicol acetate (FC=0.08) decrease their content after UV exposition (Fig. 3**(c)**). Detailed information about the tentatively identified compounds is shown in Supplementary Material.

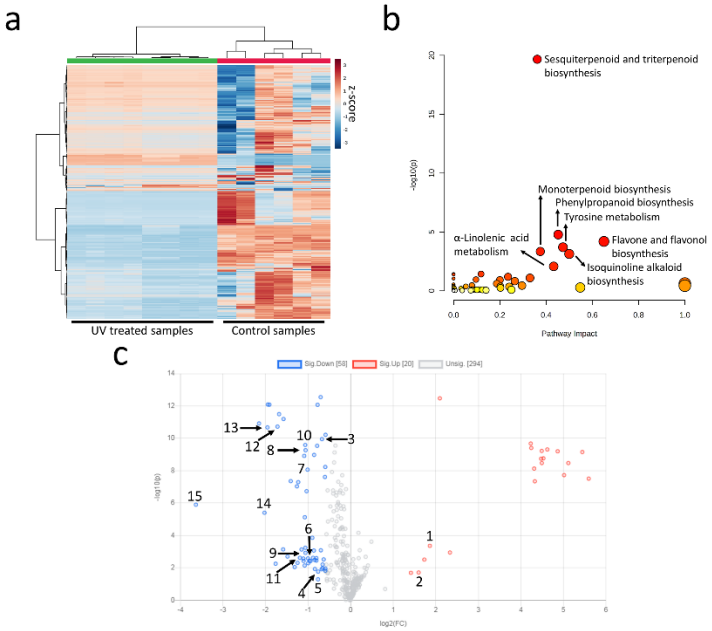

Fig. 3. Comparative metabolomic analysis of PsE before and after UV treatment. **(a)** Heatmap showing the 372 features detected in the extract before (Control) and after UV treatment (UV treated). **(b)** Pathway impact of the tentatively identified compounds. **(c)** Volcano plot of the features intensity of UV treated/Control samples. 1: Methyl-hexyl caffeate; 2: Linolenic acid; 3: Feruloyltyramine; 4: Pyridoxine; 5: Pantetheine phosphate; 6: Apiole; 7: Aceteugenol; 8: Methyl-trimethoxycinnamate; 9: Eugenyl benzoate; 10: (2E,6E)-Piperamide-C7:2; 11: Sphinganine; 12: Methyl 3-(3,4-dimethoxyphenyl)propanoate; 13: 3-Hydroxy-4-methoxy-2-(3,7,11-trimethyldodeca-2,6,10-trienyl)benzoic acid; 14: Ethyl 3-(3,4-dimethoxyphenyl)propanoate; 15: Acetoxychavicol acetate.

J. Mex. Chem. Soc. **2024**, *68*(2)
Regular Issue

ISSN-e 2594-0317

Antifungal activity

The fungal growth in the well plates at the time the experiment was concluded is shown in Fig. 4. It can be perceived that the PLGA nanospheres, both before and after exposure to UV light, have very little antifungal activity, and it's close to the one presented by the negative control. Concerning the antifungal activity of the crude PsE, it is comparable to the one reported for other plants of the *Piper* genius when tested *in vitro* against fungi of the *Fusarium* genius. For example, *Piper sarmentosum* extracts exhibited inhibition activity against *F. graminearum* at concentrations of 1 and 2 mg/mL. [38] This behavior is not limited to the *Piper* extracts, since experiments using essential oils, such of the obtained from *Piper auritum,* demonstrated growth inhibition against *Fusarium oxysporum* and *Fusarium equiseti*. [39]

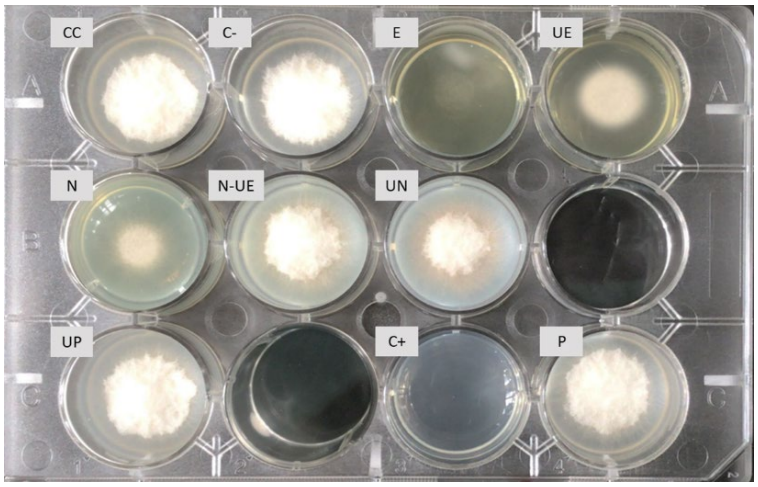

Fig. 4. Representative image of the *F. solani* growth detected in the well plates with the different treatments; crude extract (E), nanoencapsulated extract (N), UV irradiated extract (UE), UV irradiated nanospheres with extract (UN), encapsulation of a previously irradiated extract (N-UE), growth control (CC), positive control (C+), and negative control (C-).

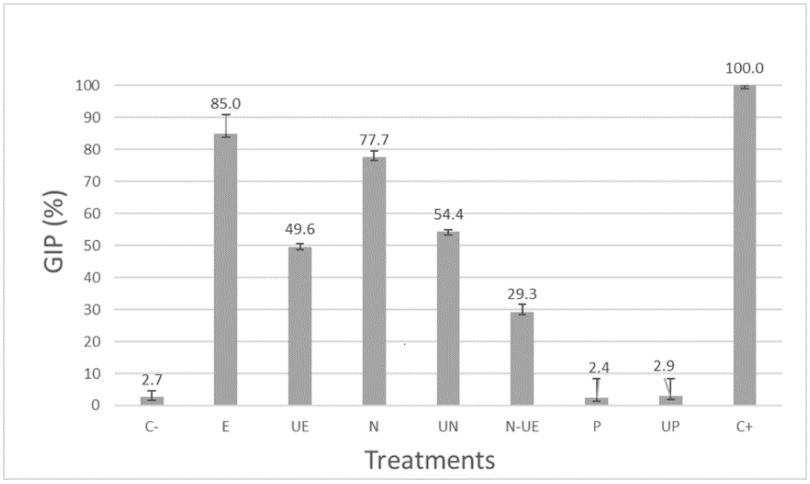

Fig. 5. Growth inhibition potential (GIP) values with standard deviation for the different treatments tested; crude extract (E), nanoencapsulated extract (N), UV irradiated extract (UE), UV irradiated nanospheres with extract (UN), encapsulation of a previously irradiated extract (N-UE), PLGA nanospheres (P), irradiated PLGA nanospheres (UP), positive control (C+), and negative control (C-).

J. Mex. Chem. Soc. **2024**, *68*(2)
Regular Issue

ISSN-e 2594-0317

The GIP for the different treatments tested are shown in Fig. 5. The antifungal activity decrease exhibited by PsE exposed to UV radiation compared to non-exposed treatment (UE vs E) can be explained by the decrease in the content of the metabolites showed previously (Fig. 3**(c)**). Acetoxychavicol acetate, which exhibited the largest decrease (FC=0.08) after UV treatment, has been reported in *Piper cubeba* [40] and it has shown antifungal activity against *Trichophyton mentagrophytes*, *Trichophyton rubrum*, *Trichophyton concentricum*, *Epidermophyton floccosum*, *Rhizopus stolonifer*, *Penicillium expansum*, *Aspergillus niger* and *Candida albicans*. [41] Also, acetoxychavicol acetate inhibited the growth of *Alternaria porri*, *Colletotrichum gloesporioides*, *Fusarium oxysporum* and *Phytophthora nicotianae*. [42]

It is important to mention that the PsE lost some growth inhibition capacity (about 7 %) when encapsulated in the nanospheres. It happens because, at the start of the experiment, there is less availability of the bioactive molecules in the extract, given they must be released from the PLGA matrix to the PDA medium, while the E treatment has the 100 % of the active molecules available from the beginning. Nevertheless, after being exposed from 24 h to UV light, the crude extract growth inhibition capacity was diminished down to 58.35 % of its original, while the nanoencapsulated extract retained up to 70 % of its original. In addition to this, globally, the UN treatment achieved close to a 5 % more GIP than the UE. Finally, the N-UE treatment yielded the lowest GIP, confirming that the PLGA is absorbing a portion of the UV radiation. Previous studies have tested the photoprotective efficiency of PLGA nanoparticles to reduce the adverse biological interactions of photo-degradation products of curcumin upon the exposure of UVA and UVB. The results demonstrated that a significant DNA damage in the cells was due to free curcumin exposed to UV light, while the PLGA nanoparticles with curcumin were totally photosafe. [43] Other studies have used PLA as wall material to protect the photosensitive molecules of spinosad and emamectin benzoate, reaching a significantly higher long-term toxicity to *Plutella xylostella*, as well as a reduction in the photolysis and hydrolysis of these insecticides. [44]

Conclusions

The *Piper schlechtendalii* extract was successfully encapsulated in a PLGA nanospheres system, with particle sizes under 150 nm, having a good dispersion in water, removing the necessity of organic solvents as vehicle for the antifungal natural product. Using acetone as solvent for the organic phase proved to yield the best encapsulation efficiencies, while using the sodium citrate solution as the aqueous phase yielded the best particle size and Zeta potential. The dialysis experiments show that the encapsulated extract is released at a much slower rate as compared to the crude extract. The advantage of this release profile lies in the fact that the whole load of extract would not be exposed to sunlight at the same time (as in the case of the crude extract treatment), but it is released fast enough to be able to control the in vitro growth of the *Fusarium solani* fungus tested. *In vivo,* tests are needed in order to determinate if there is a decrease in the antifungal activity due to a very slow release of PsE in a medium lacking any organic solvent. Finally, even when the nanoencapsulated extract was not as effective, compared to its crude form at the beginning of the experiment, once the treatments were exposed to UV light, the PLGA probed to partially absorb the radiation, protecting the active ingredients in the extract, and reaching a higher inhibition than the one yielded by the crude extract. This difference was only 5 % but could grow if the treatments were exposed to the UV radiation for longer times. This nanoencapsulated system has potential as a mean to protect the extract from photodegradation and perhaps represents, in the future, an environmentally friendly alternative for the application of the antifungal *Piper schlechtendalii* extract.

Acknowledgements

This work was supported by the FORDECyT (Fondo Institucional de Fomento Regional para el Desarrollo Científico, Tecnológico y de Innovación) of CONAHCyT (Consejo Nacional de Humanidades, Ciencias y Tecnologías) under Grant 292399 and PRONACES-CONAHCyT under Grant 316998.

J. Mex. Chem. Soc. **2024**, *68*(2)
Regular Issue

ISSN-e 2594-0317

References

1. Ghormade, V.; Deshpande, M. V.; Paknikar, K. M. *Biotechnol. Adv.* **2011**, *29*, 792−803. DOI: http://dx.doi.org/10.1016/j.biotechadv.2011.06.007.
2. Van den Berg, F.: Kubiak, R.; Benjey, W. G.; Majewski. M. S.; Yates, S. R.; Reeves, G. L.; Smelt, J. H.; Van der Linden, A. M. A. *Water, Air, Soil. Pollut.* **1999,** *115*, 195−218. DOI: https://doi.org/10.1023/A:1005234329622.
3. Bedos, C.; Cellier, P.; Calvet, R.; Barriuso, E. *Agronomie.* **2002,** *22*, 35−49. DOI: http://dx.doi.org/10.1051/agro:2001004.
4. Mogul, M. G.; Akin, H.; Hasirci, N.; Trantolo, D. J.; Gresser, D.; Wise, D. L. *Resour. Conserv. Recy.* **1996**, *16*, 289−320.
5. Nair, R.; Varghese, S. H.; Nair, B. G.; Maekawa, T.; Yoshida, Y.; Kumar, D. S. Nanoparticulate material delivery to plants. *Plant. Sci.* **2010**, *179*, 154−163. DOI: http://dx.doi.org/10.1016/j.plantsci.2010.04.012.
6. Korsukova, A. V.; Gornostai, T. G.; Grabeinych, O. I.; Dorofeev, N. V.; Pobezhimova, T. P.; Sokolova, N. A.; Dudareva, L. V.; Voinikov, V. K. *J. Stress Physiol. Biochem.* **2016**, *12*, 72–79.
7. Balakumar, S.; Rajan, S.; Thirunalasundari, T.; Jeeva, S. *Asian Pac. J. Trop. Biomed.* **2011**, *1*, 309-12. DOI: http://dx.doi.org/10.1016/S2221-1691(11)60049-X.
8. Gahukar, R. T. *Crop Prot.* **2012,** *42*, 202-9. DOI: http://dx.doi.org/10.1016/j.cropro.2012.07.026.
9. Gillitzer, P.; Martin, A. C.; Kantar, M.; Kauppi, K.; Dahlberg, S.; Lis, D.; Kurle, J.; Sheaffer, C.; Wyse, D. *J. Med. Plants Res.* **2012,** *6,* 938-49. DOI: http://dx.doi.org/10.5897/JMPR10.710.
10. Tangarife-Castaño, V.; Correa-Royero, J. B.; Roa-Linares, V. C.; Pino-Benitez, N.; Betancur-Galvis, L. A.; Durán, D. C.; Mesa-Arango, A. C. *J. Essent. Oil Res.* **2014,** *26*, 221-227. DOI: https://doi.org/10.1080/10412905.2014.882279.
11. Matasyoh, J. C., Wagara, I. N.; Nakavuma, J. L.; Chepkorir, R. *Int. J. Biol. Chem.* **2013,** *7,* 1441-1451. DOI: http://dx.doi.org/10.4314/ijbcs.v7i4.2.
12. Da Silva, J. K. R.; Silva, J. R. A.; Nascimento, S. B.; Da Luz, S. F.; Meireles, E. N.; Alves, C. N.; Maia, J. G. S. *Molecules*. **2014**, *19*, 17926-17942. DOI: https://doi.org/10.3390/molecules191117926.
13. Pineda, R.; Vizcaíno, S.; García C. M., Gil J. H.; Durango, D. L. *Chil. J. Agric. Res*. **2012**, *72*, 507-515.
14. Parra, J. E.; Delgado, W. A.; Cuca, L. E. *Phytochem. Lett.* **2011,** *4*, 280-282. DOI: 10.1016/j.phytol.2011.04.015.
15. Ee, G. C.; Lim, C. M.; Lim, C. K.; Rahmani, M.; Shaari, K.; Bong, C. F. J. *Nat. Prod. Res.* **2009,** *23*, 1416–1423. DOI: http://dx.doi.org/10.1080/14786410902757998.
16. Scott, I. M.; Puniani, E.; Jensen, H.; Livesey, J. F.; Poveda, L.; Sanchez-Vindas, P.; Durst, T.; Arnason, J. T. *J. Agric. Food Chem.* **2005**, *53*, 1907–1913. DOI: http://dx.doi.org/10.1021/jf048305a.
17. Meireles, E.; Xavier, L. *J. Plant Pathol. Microbiol*. **2016**, *7*. DOI: https://doi.org/10.4172/2157-7471.1000333.
18. Nascimento, S.; de Mattos Cascardo, J.; de Menezes, I.; Reis Duarte, M.; Darnet, S.; Harada, M.; de Souza, C. *Protein Pept. Lett*. **2009**, *16*, 1429–1434. DOI: https://doi.org/10.2174/092986609789839368.
19. Fernández, M. D. S.; Hernández-Ochoa, F.; Carmona-Hernández, O.; Luna-Rodríguez, M.; Barrientos-Salcedo, C.; Asselin, H.; Lozada-García, J. A. *Rev. Mex. Fitopatol*. **2020**, *39*, 198–206. DOI: https://doi.org/10.18781/r.mex.fit.2006-6.
20. Al Aboody, M. S.; Mickymaray, S. *Antibiotics (Basel)* **2020**, *9*, 45. DOI: https://doi.org/10.3390/antibiotics9020045.
21. Parmar, V. S.; Jain, S. C.; Bisht, K. S.; Jain, R.; Taneja, P.; Jha, A.; Tyagi, O. D.; Prasad, A. K.; Wengel, J.; Olsen, C. E.; Boll, P. M. *Phytochemistry.* **1997**, *46*, 597–673. DOI: https://doi.org/10.1016/s0031-9422(97)00328-2.
22. Nuruzzaman, M.; Mahmudur, M. M.; Liu, Y.; Naidu, R. *Agric. Food Chem.* **2016**, *64,* 1447−1483. DOI: http://dx.doi.org/10.1021/acs.jafc.5b05214.
23. Anderson, J. M.; Shive, M. S. *Adv. Drug Deliv. Rev.* **1997**, *28*, 5–24. DOI: http://dx.doi.org/10.1016/s0169-409x(97)00048-3.
24. Astete, C. E.; Sabliov, C. M. *J. Biomater. Sci. Polym. Ed.* **2006**, *17*, 247–289. DOI: http://dx.doi.org/10.1163/156856206775997322.

J. Mex. Chem. Soc. **2024**, *68*(2)
Regular Issue

ISSN-e 2594-0317

25. Park, T. G. *Biomaterials.* **1995**, *16*, 1123–1130. DOI: http://dx.doi.org/10.1016/0142-9612(95)93575-x.
26. Stevanovic, M. M.; Uskokovic, D. P. *Curr. Nanosci*. **2009**, *5,* 1–14. DOI: 10.2174/157341309787314566.
27. Oliveira, D. A.; Angonese, M.; Ferreira, S. R. S.; Gomes, C. L. *Food Bioprod. Process*. **2017**, *104*, 137–146. DOI: http://dx.doi.org/10.1016/j.fbp.2017.05.009.
28. Chopra, D.; Ray, L.; Dwivedi, A.; Tiwari, S. K.; Singh, J.; Singh, K. P.; Kushwaha, H. N.; Jahan, S.; Pandey, A.; Gupta, S. K.; Chaturvedi, R. K.; Pant, A. B.; Ray, R. S.; Gupta, K. C. *Biomaterials*. **2016**, *84*, 25-41. DOI: http://dx.doi.org/10.1016/j.biomaterials.2016.01.018.
29. Ahmad, W.; Kumar, P.; Chaturvedi, A. K. *J. Pharm. Phytochem*. **2019**, *8*, 1737-1740.
30. Hwisa, N.; Katakam, P.; Rao, B.; Kumari, S. *VRI Biol. Med. Chem.* **2013**, *1*, 8-22. DOI: http://dx.doi.org/10.14259/bmc.v1i1.29.
31. Guntero, V. A.; Longo, M. B.; Ciparicci, S.; Martini, R. E.; Andreatta, A. E. in: *Comparison of extraction methods of polyphenols from waste from the wine industry*. CAIQ2015-VII Argentine Congress of chemical engineering. 3rd. Argentine Conference on process safety. **2015**
32. Monribot-Villanueva, J. L.; Elizalde-Contreras, J. M.; Aluja, M. Segura-Cabrera, A.; Birke, A.; Guerrero-Analco, J. A.; Ruiz-May, E. *Food Chem.* **2019**, *285*, 119–129. DOI: http://dx.doi.org/10.1016/j.foodchem.2019.01.136.
33. Pang, Z.; Chong, J.; Zhou, G.; Morais, D.; Chang, L.; Barrette, M.; Gauthier, C.; Jacques, P. E.; Li, S.; Xia, J. *Nucl. Acids Res*. **2021**, *49*, 388-396. DOI: http://dx.doi.org/10.1093/nar/gkab382.
34. Scharma, K. K.; Singh, U. S.; Sharma, P.; Kumar, A. *J. Appl. Nat. Sci.* **2015**, *7*, 521-539. DOI: http://dx.doi.org/https://doi.org/10.31018/jans.v7i1.641.
35. Vert, M.; Mauduit, J.; Li, S. *Biomaterials*. **1994**, *15*, 209-1213.
36. Kemme, M.; Prokesch, I.; Heinzel-Wieland, R. *Polym. Test.* **2011**, *30*, 743-748. DOI: https://doi.org/10.1016/j.polymertesting.2011.06.009.
37. Cai, Q.; Bei, J.; Luo, A.; Wang, S. *Polym. Degrad. Stab*. **2001**, *71*, 243-251. DOI: https://doi.org/10.1016/S0141-3910(00)00153-1.
38. Zhou, L.; Zhou, H.; Hou, G.; Ji, F.; Wang, D. *J. Appl. Microbiol.* **2023**, *134*, 1–8. DOI: https://doi.org/10.1093/jambio/lxad019.
39. Chacón, C.; Bojórquez-Quintal, E.; Caamal-Chan, G.; Ruíz-Valdiviezo, V. M.; Montes-Molina, J.A.; Garrido-Ramírez, E.R.; Rojas-Abarca, L.M.; Ruiz-Lau, N. *Agronomy.* **2021**, *11*, 1098. DOI: https://doi.org/10.3390/agronomy11061098.
40. Aboul-Enein, H. Y.; Kładna, A.; Kruk, I. *Luminescence.* **2011**, *26*, 202-207. DOI: https://doi.org/10.1002/bio.1209.
41. Janssen, A. M.; Scheffer, J. J. C. *Planta medica.* **1985**, *51*, 507-511. DOI: https://doi.org/10.1055/s-2007-969577.
42. Mongkol, R.; Chavasiri, W.; Ishida, M.; Matsuda, K.; Morimoto, M. *Weed Biol. Manag.* **2015**, *15*, 87-93. DOI: https://doi.org/10.1111/wbm.12071.
43. Chopra, D.; Ray, L.; Dwivedi, A.; Tiwari, S. K.; Singh, J.; Singh K. P.; Kushwaha, H. N.; Jahan, S.; Pandey, A.; Gupta, S. K.; Chaturvedi, R. K.; Pant, A. B.; Ray, R. S.; Gupta, K. C. *Biomaterials.* **2016,** *84*, 25-41. DOI: https://doi.org/10.1016/j.biomaterials.2016.01.018.
44. Huang, B. B.; Zhang, S. F.; Chen, P.H.; Wu, G. *Sci. Rep.* **2017**, *7*, 10864. DOI: https://doi.org/10.1038/s41598-017-11419-2.

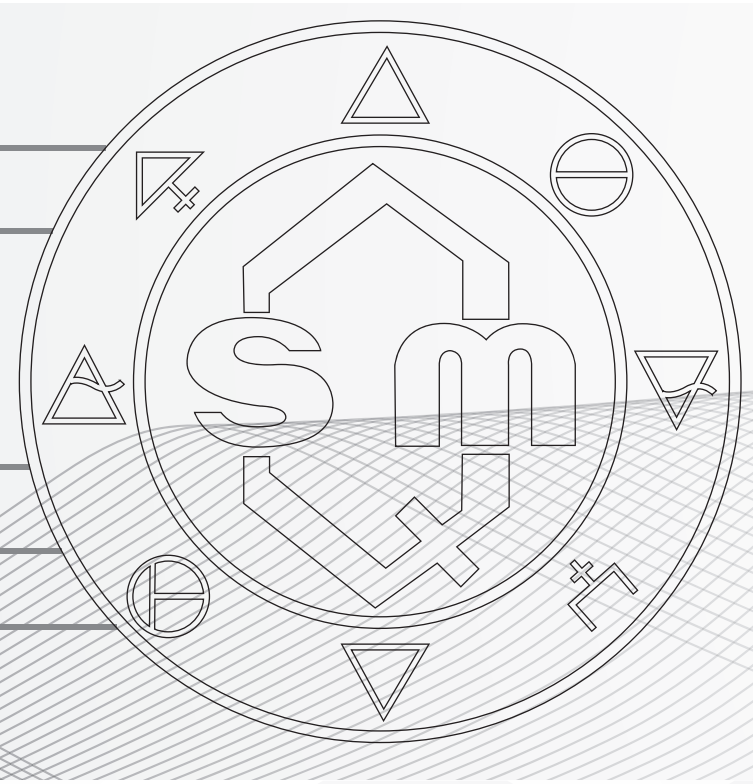

Journal of the Mexican Chemical Society **(*J. Mex. Chem. Soc.*) *Vol 68, No 2 (2024). Quarterly publication (April-June).*** Edited and distributed by ***Sociedad Química de México, A.C.*** Barranca del Muerto 26, Col. Crédito Constructor, Alc. Benito Juárez, Zip Code 03940, Mexico City. Phone: +5255 56626837; +5255 56626823 Contact: soquimex@sqm.org.mx, https://www.sqm.org.mx ***Editor-in-Chief: Prof. Alberto Vela***. Indexed Journal. Certificate of reserved rights granted by the Instituto Nacional del Derecho de Autor (INDAUTOR): 04-2005-052710530600-102. Certificate of lawful title and content: Under procedure. ISSN-e granted by the Instituto Nacional del Derecho de Autor (INDAUTOR): 2594-0317. ISSN granted by the Instituto Nacional del Derecho de Autor (INDAUTOR): 1870-249X. Postal registration of printed matter deposited by editors or agents granted by SEPOMEX: IM09-0312 Published online (***https://www.jmcs.org.mx/***) April 1st, 2024 by Adriana Vázquez and Alejandro Nava (editorial assistants, ***e-mail: jmcs@sqm.org.mx***), ***J. Mex. Chem. Soc., Sociedad Química de México, A.C.***

Journal of the Mexican Chemical Society **(*J. Mex. Chem. Soc.*) *Vol 68, No 2 (2024). Quarterly publication (April-June).*** Edited and distributed by ***Sociedad Química de México, A.C.*** Barranca del Muerto 26, Col. Crédito Constructor, Alc. Benito Juárez, Zip Code 03940, Mexico City. Phone: +5255 56626837; +5255 56626823 Contact: soquimex@sqm.org.mx, https://www.sqm.org.mx ***Editor-in-Chief: Prof. Alberto Vela***. Indexed Journal. Certificate of reserved rights granted by the Instituto Nacional del Derecho de Autor (INDAUTOR): 04-2005-052710530600-102. Certificate of lawful title and content: Under procedure. ISSN-e granted by the Instituto Nacional del Derecho de Autor (INDAUTOR): 2594-0317. ISSN granted by the Instituto Nacional del Derecho de Autor (INDAUTOR): 1870-249X. Postal registration of printed matter deposited by editors or agents granted by SEPOMEX: IM09-0312 Published online (***https://www.jmcs.org.mx/***) April 1st, 2024 by Adriana Vázquez and Alejandro Nava (editorial assistants, ***e-mail: jmcs@sqm.org.mx***). ***J. Mex. Chem. Soc. Sociedad Química de México, A.C.***